Theoretical description of electron-driven processes in astrophysical and technological plasmas: Applications for development of materials, waste treatment processes, and atmospheric depollution

Mehdi Ayouz

UPMC SORBONNE UNIVERSITÉS

CentraleSupélec

Habilitation à Diriger des Recherches

Spécialité : Physique

présentée par

Mehdi Adrien Ayouz

Sujet :

Theoretical description of electron-driven processes in astrophysical and technological plasmas: Applications for development of materials, waste treatment processes, and atmospheric depollution

soutenue le 14 décembre 2020

devant le jury composé de :

M.	Alexander ALIJAH	Rapporteur
M.	Alexandre FAURE	Rapporteur
M^{me}	Evelyne ROUEFF	Rapporteur
M.	Arnaud BULTEL	Examinateur
M.	Christophe LAUX	Examinateur
M.	François PUEL	Examinateur
M.	Viatcheslav KOKOOULINE	Invité
M.	Ioan SCHNEIDER	Invité

SCIENCES SORBONNE UNIVERSITÉ

Titre: Description théorique des processus de collisions électroniques dans les plasmas astrophysiques et technologiques: applications pour le développement de matériaux, les processus de traitement des déchets et la dépollution atmosphérique

Mots clés: Théorie du défaut quantique, méthode R-matrice, collisions électron-molécules, transformations de repère, excitation rovibronique, recombinaison dissociative, applications plasmas

Résumé: Les collisions électron-molécule jouent un rôle important dans différents domaines de recherche allant de l'ingénierie au plasma. Ce mémoire s'efforce de retracer mes activités de recherche axées sur l'étude (i) des mécanismes de destruction des ions moléculaires en astrophysique et pour le traitement des déchets, (ii) le rôle des collisions impliquant électron-molécules neutres et électron-radicaux pour les procédés de dépollution atmosphérique et (iii) la formation de molécules fluorées pour la conception de matériaux. Avec mes doctorants, nous avons développé des méthodes théoriques basées sur les premiers principes pour calculer les sections efficaces et les constantes de vitesse pour les processus d'excitations rotationnelles, vibrationnelles et électroniques ainsi que la recombinaison dissociative de diverses molécules. Ces résultats pourraient être utilisés ultérieurement dans la modélisation des plasmas afin d'améliorer les performances des procédés utilisant ces mêmes plasmas.

Dans le cadre de mes activités d'enseignement, nous avons développé avec mes collègues un cours complet de mécanique quantique de premier cycle basé sur des expériences numériques, dont la version beta est disponible sur http://prd-mecaqu.centralesupelec.fr/index.html. Cet outil pédagogique est actuellement testé à Centralesupélec et à l'Université of Central Florida. Enfin, je présenterai mon programme de recherche pour les 4 années à venir. Ce programme s'inscrit dans la continuité des travaux précédemment entrepris.

Title: Theoretical description of electron-driven processes in astrophysical and technological plasmas: Applications for development of materials, waste treatment processes, and atmospheric depollution

Keywords: Quantum defect theory, R-matrix method, electron-molecules scattering, rovibronic frame transformation, rovibronic excitation, dissociative recombination, plasma applications

Abstract: Electron-molecule collisions are of fundamental importance in a plethora of research fields ranging from engineering to plasma. The present habilitation compiles my achievements and contributions within each of the following research axis: (i) mechanisms of destruction of molecular ions in astrophysics and waste treatment, (ii) role of collisions involving electron-neutral molecules and electron-radicals for atmospheric depollution process and (iii) formation of fluorine based-molecules in the development of materials. We developed theoretical approaches based on first principles to compute cross sections and related rate coefficients for electron-impact rotational, vibrational and electronic excitations as well as dissociative recombination of various molecules. These outcomes could be used later in plasma kinetics modeling in order to improve the performance of a process.

Another contribution within the physics education axis will be also outlined in this habilitation. We developed a complete course of undergraduate quantum mechanics based on numerical experiments, whose the beta version is available on http://prd-mecaqu.centralesupelec.fr/index.html. This pedagogical tool is currently tested at Centralesupélec and at the University of Central Florida. Finally, I sketch the planned research work for the next 4-year period. This work is a continuation of the above research items.

Contents

Overview of research works

After a MsC degree in Applied Physics from the Université Pierre et Marie Curie (2007) and a Ph.D. in fundamental physics from the Université Paris-sud (2010), I worked as a post-doctoral associate at the Marquette University (US) studying dynamics of destruction of the ozone molecule (2011) and, after one year, also as a post-doc at LSPM-CNRS (2012) modelling electron-molecule collisions for plasma applications. I joined Laboratory LGPM of CentraleSupélec as an assistant professor in 2012 and started modeling fundamental elementary processes and performing numerical simulations for various applications ranging from engineering to plasma.

My research activities are mainly focused on describing elementary fundamental processes involving electron, atoms and molecules. In many fields of research and applications, it is essential to have accurate cross sections for different processes taking place in collisions between molecules and electrons. Among such processes are electron-impact rotational (RE), vibrational (VE), or electronic (EE) excitation of molecules, dissociative recombination (DR), dissociative electron attachment (DEA). Over the last years, I focused on (1) studying simplest diatomic systems to benchmark our developed theoretical models, afterwards (2) extending these models to large molecular ions and (3) to the neutral species.

- Starting with the HeH^+ molecular ion, one of the simplest molecular ion formed in the early universe, we developed a theoretical approach that combines the multi-channel quantum defect theory (MQDT), vibrational-frame-transformation (VFT) and the UK R-matrix code to compute electron-impact VE of HeH^+. In ISM, the temperature is not high, such that only the ground state vibrational state of HeH^+ is significantly populated. Hence, knowledge of rate coefficients of rotational transitions may be also of great importance for the analysis of experimental and astronomical spectra. Thus, we generalized our model to include RE process for its isotopologues.

- Another important species relevant in ISM is CH^+. Theoretical description of low-energy $e^- - CH^+$ collisions is complicated due to the presence of a low-energy electronic resonance and several low-energy excited electronic states of CH^+. In this situation, the standard VFT approach, used in many theoretical studies on electron-molecule collisions, is not well adapted due to the energy-dependence of the scattering matrix. We improved our model on HeH^+ by adapting the VFT to CH^+ with the help of "closed-channel elimination" procedure (CCE-MQDT). Cross sections for vibronic excitations (VE+EE) and DR of CH^+ were computed.

- Equipped with the theoretical method developed on diatomic molecules, we have applied it to more complicated systems and computed DR and VE cross sections of polyatomic ions of astrophysical ($CH_2NH_2^+$, NH_2CHOH^+) and material development (BF_2^+) interests. Additional approximation of the theoretical method was introduced: the use of the normal mode approximation (NMA) for vibrational states of the target molecules. Our theoretical studies have allowed us, on one hand, to provide an upper limit for the total rate coefficient of DR, where data are not available, on the other hand, to confirm previous calculations.

- More recent studies include neutral molecules, especially, NO_x molecules that have a number of applications in engineering and science. Similarly, cross sections for electron-impact vibrational excitation of NO_2 and N_2O were calculated for the first time.

My research activities also encompass other applications such as (a) describing the formation of MnO oxides on a Fe-Mn alloy surface and (b) thermal and mass characterizations of bio-materials using the Lattice Boltzmann methods (based on the kinetic theory of gases). Both applications either requires *ab initio* calculations or are based on methods similar to those developed in quantum physics. It should be stressed that the above research were carried out in close collaboration with experimentalists and modelers in plasma and material fields.

Last but not least, my experience in numerical simulation and programming allowed me to develop a complete course of undergraduate quantum mechanics (QM) based on numerical experiments, whose the beta version is available on http://prd-mecaqu.centralesupelec.fr/index.html. This tool was tested this semester on the 1st-year students of Centralesupélec and is currently used at the University of Central Florida from August 2020 in QM course, given by Prof. V. Kokoouline.

Introduction

Over the last decades, low-temperature plasma science and technology has attracted the attention of many research groups due to a plethora of applications ranging from material development (semi-conductor and photovoltaic industries [Duchaine et al., 2012, Gonzatti et al., 2010, Bartschat and Kushner, 2016] for instance), to waste treatment ([Bundaleska et al., 2013]), to air pollution control (atmospheric depollution [M and E, 1993, Baeva et al., 2002]) and to astrophysical environments (interstellar medium [Lepp et al., 2002, Millar et al., 2017]), nay to nuclei fusions reactors ([Hagelaar et al., 2011, Boeuf et al., 2011]) and to the biomedical ([Boudaïffa et al., 2000, Shomali et al., 2015b]) or recently to food processing [Misra et al., 2016].

The above applications and advances were supported by significant efforts in understanding the mechanisms governing the plasma sources, especially those involving collisions between electron, atoms and molecules. Numerical plasma simulations require two main ingredients: (i) a physical model for describing the discharge plasma and (ii) a numerical algorithm for solving the set of equations for different species. In modeling plasma, there are two approaches: kinetic (atomistic) and fluid (hydrodynamic). In the former approach, one tracks the position and velocity of each particle of plasma, or more exactly a macroparticle representing a large number of particles of a given specie, by solving either the equations of motion (Newton's Law) or kinetic equation, viz. the Boltzmann or Vlasov– if collisions are ignored– equation, for a space-time distributions of the charged species energy or velocity distribution probabilities. As an example of kinetic models, we can cite the Particle In Cell with Monte-Carlo Collisions (PIC-MCC) which is commonly adopted to simulate the plasmas immersion ion implantation (PIII) for material development (see paper .7 dealing with the study of BF_2^+).

On the other hand, in the fluid description, the plasma is considered as a continuous medium (macroscopic picture) where average quantities such density, temperature and mean velocity are of great interests. A set of equations for conservation of species mass, momentum and energy, derived form the Boltzmann equation, is then solved. Each approach has its own advantages and drawbacks. When some species are described with the kinetic approach and the others with the fluid one, we have the hybrid model. To describe the plasma chemistry, a 'reactive flow' model that describes the coupled phenomena of chemistry and diffusion-convection transport of chemical species is combined with the kinetic or continuum discharge model. For a self-consistent plasma simulation, it is ought to determine the self consistent electromagnetic field taking into account the plasma sheath space charges and/or the high frequency plasma oscillation using either Poisson's (electrostatic approximation) or Maxwell equations. As it is beyond the scope of this habilitation (Habilitation à Diriger des Recherches) to discuss details on plasma models and numerical algorithms, find here an interesting reviews

[van Dijk et al., 2009], [Samukawa et al., 2012] and [Adamovich et al., 2017], that give a detailed snapshot of the state of the art in this field.

As hinted above, characterizing the plasma chemistry, in order to improve the performance of a process, requires tremendous amount of data from atomic and molecular processes. Typically, atomic and molecular processes can be classified into surface reactions and gas-phase reactions. The former are characterized by the adsorption process of a reactant, a chemical process between two adsorbed species or an adsorbed species and a gas phase species, and desorption of a product from the surfaces of small grains. It is generally acknowledged that surface reactions are responsible for formation of complex organic molecules in space [Garrod et al., 2008]. As for gas-phase reactions, we can categorize them into one-, two- or three-body reactions. For example, an excitation/dissociation of molecules by electrons impact, $e + M \rightarrow M^*$, is a two-body reaction. The rate equations of species M that experience such reactions may be written

$$\frac{\partial n_{M^*}}{\partial t} + \nabla \cdot (n_{M^*} \mathbf{v}_{M^*}) = \Gamma_{M^*} \tag{.1}$$

where $\mathbf{v}_{M^*}$ is the velocity of specie M^* and n_{M^*} its density. Above, Γ_{M^*} designates the rate production of M^* per unit of time and volume. Note that solving the above equation, with the transport flux term (involving diffusion and convection) in the left-hand side (the second term), could be accomplished if the velocity $\mathbf{v}_{M^*}$ is well known. The latter can be obtained from solving the specie momentum equation.

The most striking feature of Eq.(.1) is the presence of Γ_{M^*}, which can take the following simplified form

$$\Gamma_{M^*} = \alpha n_e n_M \tag{.2}$$

with α or k (in $\mathrm{cm}^3 \cdot \mathrm{s}^{-1}$) being the rate coefficient of the two-body reaction. As we will see in the next chapters, this coefficient is a macroscopic quantity depending on the cross section collision and the energy distribution probabilities of the colliding particles (see Equation I.31 in Chapter I). The challenge here lies in the determination of this rate coefficient which serves as input parameters in computer simulations of plasmas. Moreover, accuracy in the rate coefficients is very important since the uncertainty could affect the prediction of simulations. This HDR attempts to address these issues, at least, partially for certain fundamental elementary processes that are relevant at low-energy collision.

In this context, my main research interests are largely motivated by the lack of reliable data for atomic and molecular reactions especially those involving electron-molecule collisions at low-energy. In low-temperature and pressure plasmas, characterized by electron energies of the order of ionization potential of atoms/molecules ($\sim$ 10 eV) and pressure of few Pa, electron-molecule collisions are dominant because electrons interact with electromagnetic fields and collide with the gas to produce radicals and excited neutral species in chemical reactions [Kolobov, 2009]. Availability of accurate cross sections and related rate coefficients for processes such as (i) rotational, vibrational and electronic excitations (RE,VE,EE), (ii) dissociative recombination (DR) and (iii) dissociative electron attachment (DEA) is crucial for plasmas modeling, as discussed above. Studies in this field can be conducted only in close

collaboration with plasma experimentalists and modellers (see list of collaborations in CV).

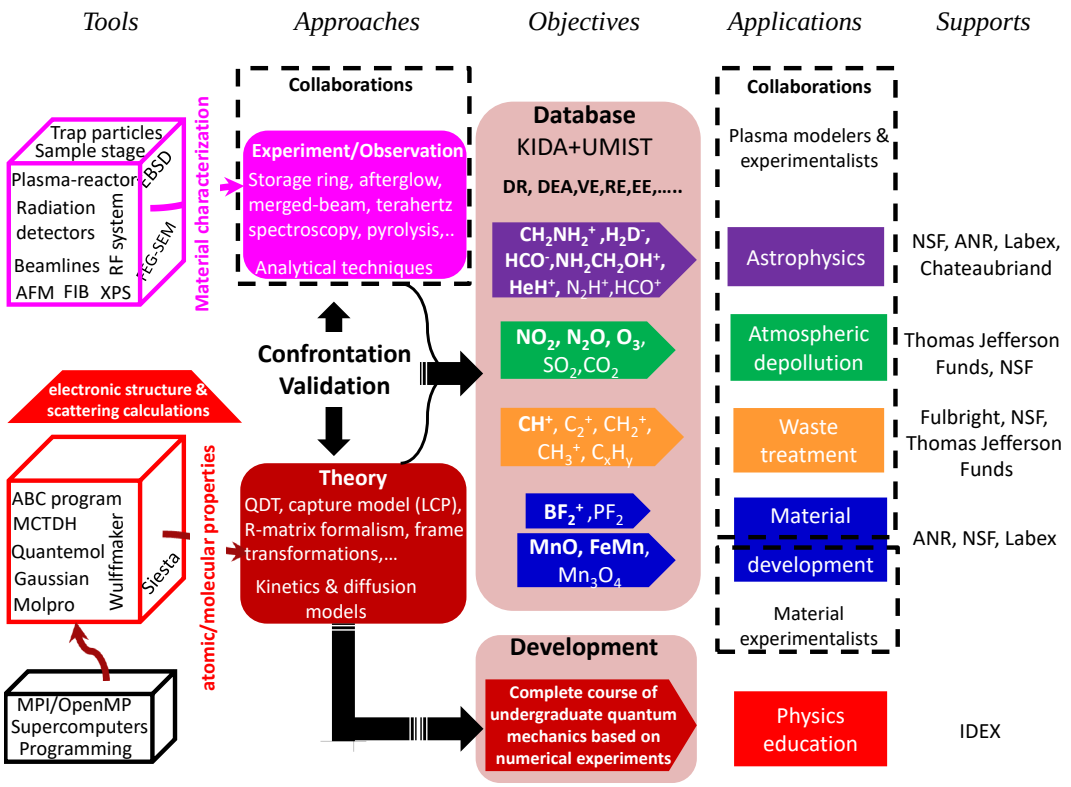

Figure .1: *Schematic diagram summarizing the research activities performed over the previous years. Note that the molecules drawn in bold have already been studied while the others are in progress to date. It should be stressed that certain molecules could play different role in various applications.*

This report presents an overview of my research works as assistant professor at LGPM (from 2012 to 2020). Figure .1 resumes my achievements as well as the motivations regarding to applications in low-temperature plasma science. Over the last years, LGPM acquired a large expertise in chemical-based processes for environmental applications and *in situ* analysis of molecules of astrophysical interest (through the MSL-Curiosity mission in collaboration with NASA). My research fits into this context and is mainly focused on the development of theoretical approaches to study processes relevant for material science, waste treatment, and atmospheric depollution. This field of research is part of the LGPM project, proposed to the HCERES committee, in which the modelling of materials at different scales is one of the two target areas of excellence for the next five-year period.

The recent key achievements were motivated by the following:

- need of understanding basic mechanisms in plasma kinetics in laboratory, in the interstellar medium (ISM), or in technological applications;
- identify key elementary processes needed in plasma modeling;

- develop theoretical approaches for the identified processes, especially, those involving polyatomic molecules for which experimental and theoretical data are sparse;

- in theoretical modelling of the processes, the need of taking into account that the presence of low-energy electronic resonances in electron-molecule collisions;

- an importance of uncertainty estimations of the theoretical models when experiential data are not available, especially, for processes involving excited-state ions or such ions as radicals. These excited-state ions and radicals are unstable in collisions with other species present nearby;

- the use of theoretical approaches as complement of experimental data;

- improvement and validation of theoretical models by building collaborations with plasma experimentalists and modelers;

- enrich KIDA, IAEA and LxCat databases for atomic and molecular reactions needed in various applications.

Within this wide context, the main goal is to develop and improve theoretical methods dictated not only by the lack of the fundamental understanding, but very practical interests in applications in plasma engineering, plasma-depollution technologies, space sciences and technologies (see Figure.1). Considering the cross-discipline importance of these applications (in physics, chemistry, astrophysics, plasma physics, materials), it is necessary to build an approach combining (i) the identification of the role of atomic and molecular species and key processes leading to their formation and destruction, (ii) development and improvement of theoretical models describing these processes, and (iii) experimental and theoretical validations with the help of collaborations.

The above lead to the following main research axes:

I Mechanisms of destruction of molecular ions (in astrophysics and waste treatment).

II Role of collisions involving electron-neutral molecules and electron-radicals (in atmospheric depollution).

III Formation of fluorine based-molecules and oxide particles (in the development of materials).

Besides the above research items, I would like to report in this manuscript my contribution in the field of physics education. I will further describe our initiative of transforming the traditional undergraduate and graduate quantum mechanics (QM) courses of Centralesupélec (CS) and the University of Central Florida (UCF) into actively engaging studio-mode styles. This pedagogical initiative led to the following achievement :

IV Toolkit for teaching quantum mechanics.

Over my experience of teaching QM and computational physics at CS, I have noticed the difficulties that students encounter in understanding the QM concepts. Typically, QM is taught as a pure math course or a descriptive phenomenological discipline, in which different

core concepts of quantum physics appear to students to be disconnected from each other and from their real-life experience. Initially, the students are curious and participate in a course but very quickly, the more the course progresses, the more they lose their motivation and interest in studying QM. Nowadays, there is a broad consensus that the use of multimedia in QM classes helps to make teaching QM more efficient. This conclusion highlights the link between teaching and numerical tools as well as theoretical methods, developed in the above three main research axes for describing and understanding different fundamental elementary processes.

The present document compiles my achievements and contributions within each above items. Since details on the employed theoretical approaches and the obtained results have been published (see list of publication in Appendix V.2.C), I will restrict myself to underlining the major ideas, sometimes with the inclusion of a few illustrations or tests. This manuscript is organized as follows.

In Chapter I, I will present briefly my works on a variety of molecular ions, namely, HeH^+, CH^+, $CH_2NH_2^+$ and NH_2CHOH^+. My main contribution to this topic is the development of theoretical methods to compute DR and VE cross sections of molecular ions relevant in astrophysics and waste treatment. The presented works were carried out in the context of two thesis: Dr. Xianwu Jiang at CS and Dr. Chi Hong Yuen through a long term collaboration with UCF.

Chapter II is devoted to neutral molecules and radicals. Equipped with the theoretical methods developed on molecular ions, I extended them to neutral systems and computed VE cross sections of NO_2 and N_2O that play an essential role in the atmospheric depollution processes. The outcomes were obtained in the context of Dr. Hainan Liu thesis at CS.

It is important to note that my past research also encompasses other applications such as metallic material and bio-material characterizations. For the sake of clarity, I will expose in Chapter III only the works on BF_2^+, playing a role in development of materials, since the study of metallic materials lies rather on describing experimentally/theoretically the formation of MnO oxides on a Fe-Mn alloy surface whereas the second one focuses on thermal and mass characterizations of bio-materials using the Lattice Boltzmann methods (based on the kinetic theory of gases). Both studies either require *ab initio* calculations (Li Gong's PhD on the determination of surface energy) or are based on methods similar to those developed in quantum physics (Mathilde Louërat and Huan Du PhDs on the calculation of thermal and mass diffusion coefficients). It should be stressed that the above research were carried out in close collaboration with experimentalists and modelers in plasma and material fields. Moreover, the BF_2^+ study has enabled to develop and formulate ideas for further applications in particular for the HCO^+ and N_2H^+ molecular ions in the context of Dr. Abdillah Abdoulanziz's thesis, co-supervised with Prof. Ioan Schneider at Université du Havre.

On the strength of my experience in numerical simulation and programming, I attempted to contribute to physics education by developing a set of PYTHON numerical codes (published in textbooks. See Appendix V.2.C) and designing a graphical interface allowing students to prepare and run numerically-simulated experiments demonstrating all basic concepts taught in QM course. An overview of the performed work, conducted in the context of the post-doc

of Dr. Alexander Korovin and in collaboration with Prof. Viatcheslav Kokoouline at UCF, is given in Chapter IV.

Finally, Chapter V concludes this report and sketches the planned research work for the next 4-year period. Contributions within each of the above items and communications are also given. Most relevant published papers related to each above items are provided in Appendix.

I – Mechanisms of destruction of molecular ions

I.1 Context and Motivations

A number of process can occur when an electron collides with molecular ions. In low-temperature ionized environments such as interstellar medium (ISM), planetary atmospheres and technological plasmas (see Figure .1) (where the pressure is low and the electron density is high), the main route for the ions destruction is the dissociative recombination (DR). This results in stable and metastable small species and/or radicals that are in turn the basis of chain of reactions leading to more complex species. Furthermore, DR competes with transitions between the rotational, vibrational and electronic states of the target ions. Hence, detailed knowledge of DR and competitive processes is necessary for modeling very cold and rarefied environments, often in non-equilibrium.

In this chapter, I will present my works on two types of ions: (i) those with low-energy electronic resonances appearing for geometries near the equilibrium of the target ion (in a fixed-nuclei picture) and (ii) the ions without such low-energy electronic resonances. Two theoretical treatments were developed in Section I.3 to be applied in Section I.5 to systems relevant in ISM as HeH^+, example of ions of the first type, and in technological plasmas (as well as ISM) such as CH^+, that have the two first excited electronic state at a relatively low energy, below 5 eV. With some additions, the theoretical method developed for ions of the first type was extended to more complicated systems with several vibrational degrees of freedom, such as NH_2CHOH^+ or $CH_2NH_2^+$ (illustrated below) of planetary atmospheres interest. The theoretical method was initially introduced for BF_2^+ with few vibrational degrees of freedom, viz. four-folded. This theory will be described in details in Chapter IV. The basics of theoretical approaches developed for both diatomics and polyatomics are similar and exposed in the next Section I.2.

Cross-sections and related rate coefficients of the electron-induced dissociation and/or excitation of molecular cations presented in this chapter were obtained in the context of collaboration with Prof. V. Kokoouline at the University of Central Florida (UCF) and two dissertations: Dr. Xianwu Jiang at Centralesupélec (CS) and Dr. Yuen Chi Hong at UCF. The following works have been published in different papers. Only relevant studies and related articles are included in Appendix V.2.C, with the inclusion of some illustrations or tests. The obtained results could serve in kinetic modeling of ionized media such as cold plasmas and

interstellar clouds.

I.2 The basics of the theoretical approaches

Generally, electron-molecule scattering calculations are performed either in the laboratory-frame (with respect to which the molecule rotates) in the framework of the *Close-Coupling* (CC) theory [Arthurs et al., 1960] or in the body-fixed frame making use of the *Fixed-Nuclei* (FN) theory [Chase, 1956].

In CC theory, a set of coupled second-order ordinary differential equations is solved for one-electron wave function where the total wave function is expanded on the unperturbed states of the isolated molecule, typically, via the products of functions of the internal states of the molecule (called a *channel*) with angular functions (often spherical harmonics) describing the rotation of electron around the molecule. The scattering (or reaction) matrix can be deduced when matching the propagated one-electron wave function, from the internal region to a distance where the potential is negligible, to a well know asymptotic form [Lane, 1980]. This method was applied for studying electron-atom/molecule and atom/molecule-molecule collisions [mot, 1966, McGuire and Kouri, 1974, Green, 1975, Bohr et al., 2014, Mukherjee and Mukherjee, 2015, Zammit et al., 2017]. However, including the rovibrational states into CC equations introduces complications into the calculation, which is especially the case for polar molecules where the long-range nature of the dipole potential requires a large number of partial waves to be considered [Sanz et al., 2012]. This leads to a strong rotational coupling in the equations and, consequently, slow numerical convergence because the laboratory-frame, where the scattered electron is referred, is not appropriate at small electron-molecule separation, where the electron is close to the molecule. This discussion will be completed in Section II.4 on the NO_2 study. More details can be found in Ref.[Lane, 1980].

On the other hand, FN theory adopts the philosophy of the Born-Oppenheimer approximation (BO) [Born and Oppenheimer, 1927] in which the motion of nuclei can be separated from that of electrons because they are munch lighter (about 2000 times) and, hence, move faster than nuclei in a molecule. Performing bound states (electronic structure) calculations is thus possible and one can find the energy spacing of electronic, vibrational, and rotational levels of the order of 1000, 100, and 1 meV, respectively. The energy-time uncertainty principle enables to obtain the respective time scales 10^{-17}, 10^{-16}, and 10^{-14} s. This result reveals that time scale for electronic processes is usually much shorter (about 10 or 100 times) than the nuclei motion, in agreement with the BO consideration. In a similar spirit, the motion of electrons in the continuum, in the framework of FN approximation, is fast in such a way that the nuclei can be viewed as fixed during the scattering process. This assumption, however, break downs when the scattering electron energies are close to excitation thresholds or to a narrow and long-lived resonance, where the collision time becomes long. As for CC, collision with a polar molecule, characterized by a strong long-range interaction potential, is also a circumstance for which FN approximation can not be readily applied.

In this context, the *Frame Transformation* (FT) approach of [Fano, 1970] takes the advantage of both representations by exploiting the features of electron-molecule interaction

in accordance with the electron scattering distance. Indeed, close to the nuclei, the electron undergoes a strong Coulomb acceleration and acquires a high velocity such that nuclei can be viewed as being stationary, justifying the use of FN approach in the framework of BO approximation. The electron nearby the nuclei form together a new complex that should be treated as many-electron system. The rising exchange and electron-electron correlation interactions lead to a strong coupling between the angular momentum of the scattered electron and the internuclear axis (the angular momentum component is constant of motion in case of diatomic molecules). In such situation, the body-frame representation is more appropriate than the laboratory-frame. On the contrary, when the electron is far from nuclei, its collision energy becomes comparable to the energy of nuclei motion and their respective angular momenta remain uncoupled. Consequently, nuclear Hamiltonian has now to be introduced to take into account the effects of the rotational/vibrational molecule making thus the laboratory-frame more appropriate. In this representation, vibrational and rotational quantum numbers of the target molecule, in addition to the angular momentum of the scattered electron are utilized. The total angular momentum is here a collision constant.

The theoretical methods developed on diatomic (described in next section) and polyatomic molecules (described in next chapters) employs the above approach where once the scattering matrices are obtained in the framework of FN approximation, FT is performed for describing interactions between rovibronic channels of the target molecules induced by the incident electron. Nowadays, there are two types of computational approaches in the FN approximation that are the most employed; variational approaches and bound states approaches. The Kohn Complex Kohn Variational method [Schneider and Rescigno, 1988] is based on the variational principle, where the $T-$matrix is chosen as the variational quantities instead of the $K-$matrix [Takatsuka and McKoy, 1981]. Some recent applications making use of this method could be found in [Douguet et al., 2015a, Douguet et al., 2015c]. A second approach is the Schwinger Multichannel Method which is based on the Schwinger variational principle for obtaining the scattering amplitude [Schwinger, 1947]. This method utilizes the Green's function matrix element and the electron-molecule interaction method. Details on this approach can be found in Ref.[da Costa et al., 2015] and references therein.

The *ab initio* R-matrix methods, to which we further direct our main attention, are other methods based on variational or on bound states approach [Burke, 2011]. They adopt the philosophy of the FT procedure by considering two regions of space in agreement with the interaction nature between an electron and a molecule. Compared to the above variational approaches, R-matrix method has a great advantage that the inner region problem is solved independently of the scattering electron energy. The dependence on that energy has only to be considered in the outer region where obtaining solutions is somewhat fast and straightforward. In practice, the employed inner region in FT approach is extended to a large distance and the whole problem can be thus solved in the framework of the body-fixed frame representation. This assumption called *Adiabatic Nuclei Approximation* is the central idea of R-matrix method. It is valid under certain circumstances, as stated above for the FN approximation, where electron energies are away from excitation thresholds or long-lived resonance and there are no significant long range interactions. The validity of these assumptions and, hence, of the theoretical models employed in the performed studies will be justified in the following section.

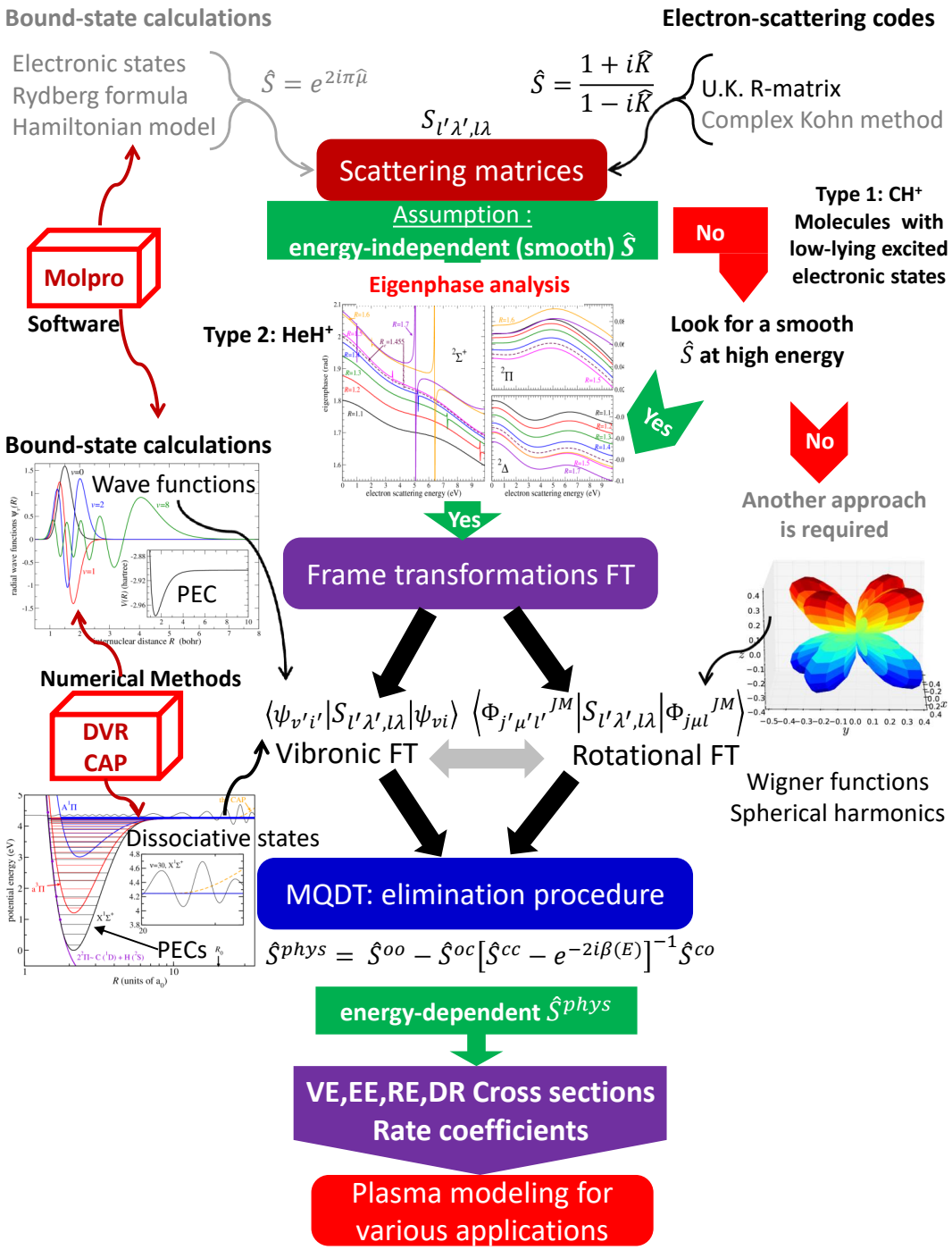

Figure I.1: The flow chart of different ingredients employed in the theoretical model developed for the description of rotational, vibrational and electronic (de-)excitation (RE,VE,EE) as well as dissociative recombination (DR) of diatomic molecular ions such as HeH^+ and CH^+. The following abbreviations are used. FT: frame transformation. PECs: potential energy curves. DVR: discrete variable representation. CAP: complex absorbing potential. Tasks or methods in non-bold text are not performed in this HDR yet.

I.3 Theoretical methods for collisions between electron and diatomic molecular ions

Theoretical models employed in the studies of Section I.5 are based on first-principles. They require three main ingredients summarized in Figure I.1. A brief description follows.

I.3.A The *ab initio* R-matrix method

Initially introduced by Wigner [Wigner, 1946, Wigner and Eisenbud, 1947] to treat nuclear reactions, R-matrix methods were early extended to study the scattering of electron-atom [Burke et al., 1971, Burke and Robb, 1976] and electron-molecule [Burke et al., 1977], based on the developments of Schneider [Schneider, 1975, Schneider and Hay, 1976]. A comprehensive reviews on the methodology and applications in atomic, molecular and optical processes can be found in [Burke and Tennyson, 2005, Burke et al., 2007].

In the following studies, the open-access UKRmol suite [Carr et al., 2012] with Quantemol-N interface [Tennyson et al., 2007] will be used. Recent applications can be found in [Loupas et al., 2018, Gupta et al., 2019, Loupas and Gorfinkiel, 2019]. The implemented R-matrix approach is drawn in Figure I.2. This method aims in calculating, as its name suggests, the R-matrix (in its simplest form):

$$\mathbf{R}(r,\epsilon) = \frac{\mathbf{F}(r)}{r\mathbf{F}'(r)}, \tag{I.1}$$

that relates the radial wave function $\mathbf{F}(r)$ to its derivative $\mathbf{F}'(r)$ at a radius r and for a specific scattering electron energy ϵ.

The above equation dictates the central idea of the R-matrix method: partition of configuration space into an inner and outer regions. The boundary is a sphere, with a radius noted $r = a$, centered at the center of mass of the molecule. This radius is chosen such as the electronic charge cloud of the target is negligible at the boundary. Usually in the inner part of configuration space, exchange and polarization interactions are dominant between N-electrons target and the scattering one. As a result, the collision problem within finite volume can be treated as a molecular bound state problem by constructing and diagonalizing an Hamiltonian matrix augmented with the Bloch operator (holding the Hermicity of the Hamiltonian) leading to solve a $N+1$ eigenvalue problem (see Eq.(8) of Ref [Tennyson, 2010]). The scattering wave function is constructed using close-coupling expansion where the scatterer spin is taken into account and the target wave function is represented through a Configuration Interaction (CI) expansion. A standard quantum chemistry methods are employed to obtain the variational parameters in the CC expansion.

In the outer region, asymptotic expansion such as a long range multipolar interactions between the scattering electron and the target is employed. For target ions, the dominant term is Coulomb potential of the separate charges, viz. $\alpha = 0$ in Eq.(II.12). Once the wave functions are generated in the inner region, the R-matrix is constructed at the boundary $r = a$ for a given incident energy ϵ and it is propagated to the outer region (see Eq.(23) of Ref [Tennyson, 2010]) where the radial scattering electron wave function can be matched at

the boundary $r = a_{asy} \simeq 70$ bohr (such that coupling potentials to be negligible) to Coulomb functions

$$F_{ij}^{\Gamma}(r) \sim \begin{cases} \frac{1}{\sqrt{k_i}} \left(\sin\theta_i(r)\delta_{ij} + \cos\theta_i(r) K_{ij}^{\Gamma}(R) \right) & \text{if } \epsilon_i \geq 0 \\ 0 & \text{otherwise} \end{cases} \tag{I.2}$$

where

$$\theta_i(r) = k_i r - \frac{l_i \pi}{2} + \frac{\ln(2k_i r)}{k_i} + \sigma_i, \qquad \sigma_i = \arg\Gamma\left(l_i + 1 - \frac{i}{\pi}\right), \tag{I.3}$$

and index i refers to the entrance channel before a collision and j refers to the outgoing channel after the collision. In the above equation, $K_{ij}^{\Gamma}(R)$ are the elements of the reactance matrix [Aymar et al., 1996, Tennyson, 2010] depending on the nuclei geometry, here the internuclear distance R, parametrically and obtained for each scattering electron energy ϵ. Above, Γ designates the constants of motion corresponding to the irreducible representation of the molecular point group, in particular the total angular momentum projections Λ of the electron-molecule system.

In the cross section calculation, the scattering matrix $\mathbf{S}^{\Gamma}(R)$ is needed, which is obtained from $\mathbf{K}^{\Gamma}(R)$ as

$$\mathbf{S}^{\Gamma}(R) = (\mathbf{1} + \imath\mathbf{K}^{\Gamma}(R))(\mathbf{1} - \imath\mathbf{K}^{\Gamma}(R))^{-1}. \tag{I.4}$$

The above matrices relate the amplitudes of the incoming and outgoing waves functions. Another observable defined from these scattering quantities is the eigenphase sums (analogous to the phase shift of potential scattering)

$$\delta^{\Gamma}(\epsilon, R) = \sum_i \arctan\left(K_{ii}^{\Gamma}\right) \qquad \text{or} \qquad \delta^{\Gamma}(\epsilon, R) = \sum_i \frac{\log\left(S_{ii}^{\Gamma}\right)}{2\imath}, \tag{I.5}$$

where K_{ii}^{Γ} (resp. S_{ii}^{Γ}) are the eigenvalues of the K-matrix (resp. S-matrix). We will see further that eigenphases are very helpful for testing the validity of the scattering models, identifying potential problems with calculations and studying the calculations convergence.

Table I.1: Correlation tables for $D_{\infty v} \to D_{2h}$ and $C_{\infty v} \to C_{2v}$ point groups for diatomic molecules. In the same rows, irreducible representations Γ of the same symmetry are provided.

$D_{\infty v}$	D_{2h}	$C_{\infty v}$	C_{2v}
Σ_g^+	A_g	Σ^+	A_1
Σ_u^+	B_{1u}	Σ^-	A_2
Σ_g^-	B_{1g}	Π	$B_1 \oplus B_2$
Σ_u^-	A_u	Δ	$A_1 \oplus A_2$
Π_g	$B_{2g} \oplus B_{3g}$		
Π_u	$B_{2u} \oplus B_{3u}$		
Δ_g	$A_g \oplus B_{1g}$		
Δ_u	$A_u \oplus B_{1u}$		

In practice, our calculations are performed in the abelian subgroups D_{2h}, C_{2v}, C_s or C_1 of the natural point groups of the molecules. Descent correlation tables for the most popular

point groups encountered in our studies are given in Table I.1. We choose a large R-matrix sphere of radius ranging from $a = 10$ to 14 bohrs, according to the size of the studied systems, and continuum Gaussian-type orbitals (real spherical harmonics for the angular part) with partial waves $l \leq 4$, viz. a total of 25 partial waves mapped to the irreducible representations of the abelian point groups in Table I.2. Thus, an element of the scattering matrix in Eq.(I.4) writes $S^{\Gamma}_{l'\lambda'i',l\lambda i}(R)$ where l, λ (noted sometimes m or Λ, in case of Σ electronic states of the target) and i enumerate, respectively, the electron angular momentum and its projections on the molecular axis Z, and the electronic state of the target molecule. This element represents the scattering amplitude when the electron scatters from one channel $(l\lambda i)$ to another $(l'\lambda' i')$, while the nuclei do not have time to move.

Table I.2: Mapping of spherical harmonics of partial waves $(l\lambda)$ in each irreducible representations Γ of the abelian point groups that are encountered in our studies.

C_1	A
	00,1-1,10,11
	2-2,2-1,20,21,22
	3-3,3-2,3-1,30,31,32,33
	4-4,4-3,4-2,4-1,40,41,42,43,44

C_s	A	A'
	00,1-1,11,2-2,20,22	10,2-1,21
	3-3,3-1,31,33,4-4,4-2,40,42,44	3-2,30,32,4-3,4-1,41,43

C_{2v}	A_1	B_1	B_2	A_2
	00,10,20,22	11,21	1-1,2-1	2-2
	30,32,40,42,44	31,33,41,43	3-3,3-1,4-3,4-1	3-2,4-4,4-2

D_{2h}	A_g	B_{1g}	B_{2g}	B_{3g}	A_u	B_{1u}	B_{2u}	B_{3u}
	00,20,22	2-2	21	2-1		10	1-1	11
	40,42,44	4-4,4-2	41,43	4-3,4-1	3-2	30,32	3-3,3-1	31,33

I.3.B Frame transformation

As stated in Section I.2, the theory of frame transformation connects the laboratory frame and the body-frame representations that are each suited for different ranges. This is based on the fact that the couplings between the scattering electron and the target are different according to the r regions.

Lower panel of Figure I.2 depicts these regions, namely, the $R-$region, $v-$region and the $j-$region. In the first region, the strength of couplings, induced by the scattering electron, between different vibrational and rotational states (v,j) of the target and the scatterer are small in comparison with the interaction potential $V(r)$, suffered by the incident electron. Therefore, the FN approximation is justified in this $R-$region (recall that R refers collectively to all nuclei coordinates) and the R-matrix calculations can then be performed where the scattering quantities (see above) depend on the nuclei geometry R parametrically. We will come back to this point in Section I.4 with more details.

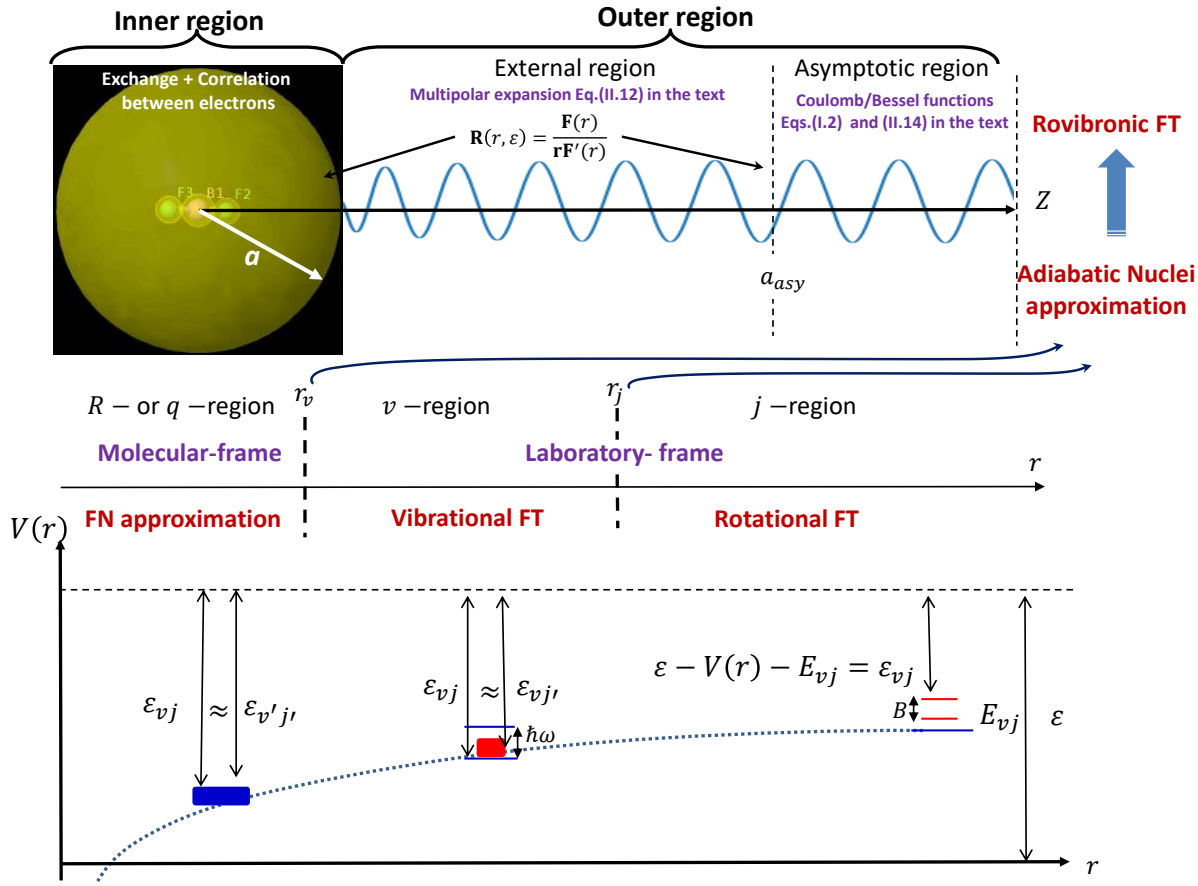

Figure I.2: Schematic diagrams for the R-matrix method (upper panel) as well as the R-/$q-$region, $v-$region and the $j-$region (lower panel) according to the local kinetic energy of the electron given in Eqs.(I.6) and (I.7). The frame transformation procedures (FT) connecting the molecular-frame to the laboratory-frame are also represented. Note that these transformations constitute the l-uncoupling transition from the Hund-coupling case b to case d [Chang and Fano, 1972].

Now, where the interaction potential $V(r)$ becomes comparable to the strength of couplings between different v and/or j, these later can not be neglected and hence *vibrational frame transformation* and *rotational frame transformation* need to be accomplished in $v-$region and $j-$region, respectively. Transitions between each regions can be estimated by defining the local kinetic energy

$$\epsilon_{vj} = \epsilon - V(r) - E_{vj}, \tag{I.6}$$

where ϵ is the scattering energy and $V(r)$ is the attractive potential. E_{vj} is the rovibrational energy of the target that can be expressed as

$$E_{vj} = \hbar\omega \left(v + \frac{1}{2}\right) + Bj(j+1), \tag{I.7}$$

white ω and B being respectively the vibrational frequency and the rotational constant of the target in the harmonic and rigid rotator approximations.

Making use of the above expressions, the values r_v and r_j in Figure I.2 can be estimated for $\epsilon - V(r_v) \simeq \hbar\omega$ and $\epsilon - V(r_j) \simeq B$. It follows that, when $r < r_v$, one can apply a *vibrational frame transformation* (nay full frame transformation) assuming then $\epsilon_{vj} \approx \epsilon_{v'j'}$; while for $r < r_j$, only *rotational frame transformation* can be applied with the assumption $\epsilon_{vj} \approx \epsilon_{vj'}$. In the region $r > r_j$, FN approximation is no longer valid because the nuclei and electrons have to be treated on a more equal footing, justifying the laboratory-frame description. These considerations are the basis of the theoretical models described below.

Vibrational Frame Transformation

Once the matrix element $S^{\Gamma}_{l'\lambda',l\lambda}(R)$ is obtained from the R-matrix calculations for a given geometry R and each symmetry (one of the irreducible representation Γ of the point group corresponding to a given projection Λ of the total angular momentum of the electron-molecule complex), one can employ the procedure of frame transformation

$$\mathcal{S}^{\Lambda}_{\lambda'v'l',\lambda vl} = \left\langle \psi_{v'}(R) \left| S^{\Lambda}_{\lambda'l',\lambda l}(R) \right| \psi_v(R) \right\rangle , \qquad S^{\Lambda}_{\lambda'l',\lambda l}(R)\delta(R'-R) = \left\langle R';\lambda'l' \right| \hat{S} \left| R;\lambda l \right\rangle , \quad \text{(I.8)}$$

where the brackets above imply an integration over the vibrational coordinates which requires the vibrational wave functions.

Bound vibrational wave functions: We calculated vibrational wave functions $\psi_v(R)$ above and related energies E_v by solving the Schrödinger equation for vibrational motion along R,

$$\left[-\frac{\hbar^2}{2\mu}\frac{\partial^2}{\partial R^2} + V(R) \right] \psi_v(R) = E_v \psi_v(R) , \quad \text{(I.9)}$$

where μ the reduced mass and $V(R)$ is the internal potential of the considered molecule. The above equation is solved using a DVR-type method, described in details in Section IV.2.B. In the numerical calculation, the distance R is discretized on a grid, on which the potential energy $V(R)$ is calculated with the *ab initio* methods (plus a basis set) with the help of Molpro package [Werner et al., 2008].

Dissociative vibrational wave functions: To compute dissociative recombination (DR) cross section of CH^+, for instance, the vibrational continua states need to be considered. They could be discretized by the outgoing-wave basis functions defined by a complex absorbing potential (CAP). Similar to the technique of Siegert pseudostates calculations [Tolstikhin et al., 1998], a purely imaginary potential (CAP) is added to the above Schrödinger equation (I.9) in order to simulate an infinite grid. Different shapes of CAPs are described in the literature [Vibok and Balint-Kurti, 1992], we choose an exponential form

$$W(R) = \begin{cases} A_5 \exp\left(-\frac{2L}{R-R_{CAP}}\right) & R \geq R_{CAP} \\ 0 & R < R_{CAP} \end{cases} , \quad \text{(I.10)}$$

where A_5 is the CAP strength and R_{CAP} its starting point. L specifies the entire grid length of the internal potential $V(R)$ of CH^+. These parameters will be adjusted

in the studies to reduce the uncertainty on the obtained DR cross sections.

Applying CAP, the Hamiltonian becomes non-Hermitian and eigenenergies turn to be complex (as eigenfunctions. See Figure I.14 for instance)

$$E_v = E_v - \imath\frac{\gamma}{2}, \tag{I.11}$$

where E_v and γ are the position and width (inversely proportional to half-time $\tau = \frac{\hbar}{\gamma}$) of the dissociative state.

When plugging the dissociative vibrational wave functions into Eq.(I.8), the obtained scattering matrix appears to be subunitary in the bound and dissociative states basis. This defect of unitarity, i.e. loss of flux, can be identified with the dissociative flux.

Finally, summations over the partial waves $(l\lambda)$ and $(l'\lambda')$ yield the transition amplitude $S_{v'v}$ from one vibrational level v to another v'. This latter is used to compute the vibrational (de-)excitation (VE,VdE) cross sections.

Rovibrational Frame Transformation

As a second step, the rotational frame transformation is accomplished using the matrix elements of the above S-matrix, leading to the laboratory-frame scattering matrix

$$\mathcal{S}^J_{j'\mu'l'v',j\mu lv} = \sum_{\lambda\lambda'}(-1)^{l'+\lambda'+l+\lambda} C^{j'\mu'}_{l'-\lambda' J\Lambda'} C^{j\mu}_{l-\lambda J\Lambda} \mathcal{S}^{\Lambda}_{l'\lambda'v',l\lambda v}\,, \tag{I.12}$$

where J is the total angular momentum of the e^--ion system, j, μ and j', μ' are the angular momenta with their projections on the molecular axis of the target before and after the rotational excitation of the projectile, and $C^{j'\mu'}_{l'-\lambda' J\Lambda'}$ and $C^{j\mu}_{l-\lambda J\Lambda}$ are Clebsch-Gordan coefficients. Note that J is specified in the above S-matrix because j is defined from the Clebsch-Gordan coefficients. Summing over l, l' and J leads to the rovibrational (de-)excitation (RVE,RVdE) cross sections. A detailed derivation of Equation (I.12) and ensued cross section are given in Appendix of paper .4.

Note that when several electronic states of the target are involved in the calculations, *rovibronic frame transformation* has to be accomplished, with some careful attention for target states of $\mu \neq 0$, where an extra indices (i', i) in Eq.(I.12) standing for the electronic state should be added. This development would a part of further works (see Section V).

The most striking features of Eqs.(I.8) and (I.12) is the presence of vibrational and rotational levels, initially absent in the nuclei-fixed S-matrix. The transition amplitude $S^{\Lambda}_{\lambda' l',\lambda l}(R)$ is obtained for a scattering electron energy ϵ computed with respect to the ground electronic state energy of the target, i.e. the entering channel, provided that the electron energy is not large enough to excite the target electronically. Consequently, performing frame transformation procedures give rise to uncertainty in the choice of the energy origin in the S-matrix which can resolved if $S^{\Lambda}_{\lambda' l',\lambda l}(R)$ is independent on the scattering energy within the spacing of rotational and vibrational levels. This is in fact consistent with the above approximation $\epsilon_{vj} \approx \epsilon_{v'j'}$ on

which the R-matrix calculations are carried out. Further discussion is postponed to Section I.4.

As a result, one can apply frame transformations as long as $S(R, \epsilon_{vj}) \approx S(R, \epsilon_{v'j'})$, where ϵ_{vj} is given by Eq.(I.6). This assumption could be verified by a detailed analysis of eigenpahse sums of Eqs.(I.5), as we will see in the applications.

I.3.C Elements of the Multi-channel quantum defect theory

Brief introduction

The quantum defect (QDT) theory was initially introduced by Ham [Ham, 1955] in solid physics and then reformulated by Seaton [Seaton, 1966, Seaton, 1983] for atomic physics. This theory is somewhat equivalent to the R-matrix or FT theories, described above, since the $r-$region space is divided in accordance with the interaction between an electron and a nuclei in an alkali atom. More specially, QDT deals with the properties of an excited electron of Rydberg surrounding an ionic core (nuclei+core electrons). The basic idea is to assume that beyond some distance from nuclei $r > r_0$, the electron undergoes a purely Coulombic field created by a positive point charge. Eigenenergies of that excited (Rydberg) electron can be described by a phenomenological extension of the hydrogen expression, as formulated by Rydberg [Rydberg, 1890].

Exploiting the spherical symmetry of the atom, one needs only to solve the radial the Schrödinger equation whose the solution can be written as a linear combination of regular, $f_l(r)$, and irregular, $g_l(r)$, Coulomb functions

$$F_l(r) = f_l(r)\cos\pi\mu_l - g_l(r)\sin\pi\mu_l \qquad r > r_0, \tag{I.13}$$

where μ_l denotes the *quantum defect* depending only on the angular momentum quantum number l and accounting for the corrections to the pure attractive Coulomb potential by the core electrons. Notice that for the diatomic molecules, one should add to the angular momentum l its projection along the Z axis of the molecule λ (sometimes noted m).

Making use of the asymptotic solutions of the above Coulomb functions, one can write Eq.(I.13), at any negative energy $E = -\frac{1}{2\nu^2}$, as follows (see Eq.(2.12) of Ref.[Aymar et al., 1996]):

$$F_l(r) \underset{r\to\infty}{\sim} \frac{1}{\sqrt{k}}\left[\sin\left(\pi(\nu - l + \mu_l)\right) D^{-1} r^{-\nu} e^{kr} - \cos\left(\pi(\nu - l + \mu_l)\right) D r^{\nu} e^{-kr}\right] \tag{I.14}$$

where ν is the *effective quantum* and D is a constant depending on the gamma function. As one is interested here by bound states, the exponential growth at infinity in Eq.(I.14) needs thus to be killed which leads to $\sin\left(\pi(\nu - l + \mu_l)\right) = 0$ or $\nu - l + \mu_l = n_r$, an integer. Putting the principal quantum number $n \equiv n_r + l$ and using the energy definition of the hydrogen atom, we fall back into the famous *Rydberg formula* of the allowed energy values (in atomic units)

$$E_{nl} = \mathcal{I} - \frac{1}{2(n - \mu_l)^2} \tag{I.15}$$

with $\mathcal{I}$ being the ionization energy (often set to zero). Equation (I.15) indicates that a series of resonant states can be formed with an excited ionic core. This series of resonances is called *Rydberg series* whose the energies are provided from the above formula. Therefore, the excited states of atoms with a large principle quantum number, leading to a very large electric dipole moments, are known as *Rydberg atoms*. In such atoms, the Rydberg electron is weakly bound to the ionic core which makes it sensitive to external perturbations resulting in a wide range of applications as in plasmas.

From Eq.(I.2) (by omitting here K-matrix), the radial wave function of the Rydberg electron can be expressed as follows

$$F_l(r) \underset{r\to\infty}{\sim} \frac{1}{\sqrt{k_l}} \sin\left[\theta_l(r) + \pi\mu_l\right], \tag{I.16}$$

where $\theta_l(r)$ is given by Eq.(I.3). $\pi\mu_l$ appears as an additional phase shift with respect to Coulomb functions. Quantum defect μ_l contains the information about short-range interaction between the outermost electron and the ionic core.

A key result above is the smooth manner in which the quantum defect can be extrapolated from below-threshold in Eq.(I.14) to above-threshold in Eq.(I.16) throughout a phase shifts

$$\delta_l = \pi\mu_l. \tag{I.17}$$

This is usually expressed as the Seaton's theorem [Seaton, 1966]. Reshaping Eq.(I.15) yields $\mu_{nl} = n - \sqrt{-\frac{1}{2E_{nl}}}$ and hence μ_{nl} depicts a weak dependence on n, in particular, on energy E_{nl}. We fall back here on the circumstance mentioned in the preceding section: the use of smooth S-matrix in the frame transformation procedure since

$$S_l = e^{2\imath\delta_l} \underset{\text{Eq.(I.17)}}{=} e^{2\imath\pi\mu_l}. \tag{I.18}$$

When several channels of electron excitation, distinguished by different core levels, or different orbital momenta are taken into account in the calculations, one has the multichannel QDT, noted MQDT. Generalizing QDT to include not specially Coulomb potentials, like molecular ones, arises with a more complicated relation between energies and quantum defects that can be described by the generalized quantum-defect theory GMQDT. More details can be found in [Greene et al., 1979].

The quantum defect approach briefly discussed above has been widely used in the literature for studying different systems, from diatomic to polyatomic molecules, and processes (VE,RE,DR) [Mezei et al., 2015, Moulane, Y. et al., 2018, Chakrabarti et al., 2018b, Douguet et al., 2012b, Mikhailov et al., 2006a, Douguet et al., 2008a, Douguet et al., 2009a, Kokoouline and Greene, 2001, Novotný et al., 2009, J. B. A. Mitchell and A. I. Florescu-Mitchell, 2005]. As an example, DR cross sections of NH_2^+ and HCO^+ were computed by [Fonseca dos Santos et al., 2014b] using a theoretical approach based on the computation of the scattering matrix, via the complex Kohn variational technique, just above the ionization threshold and enables the explicit determination of all diabatic electronic couplings responsible for DR. In addition, authors used MQDT to demonstrate the precision of the scattering matrix by reproducing

accurately *ab initio* Rydberg state energies of the neutral molecules, obtained from the Rydberg formula of Eq.(I.15). As a result, complex Kohn variational technique reproduced quantum defects calculated from bound state calculations, verifying Eq.(I.17). A very good agreement with the experiments was found.

Closed-channel-elimination procedure

Going back to S-matrices, obtained previously after the frame transformation procedures, with the above considerations, one can notice that the scattering matrices $\mathcal{S}$ of Eqs.(I.8) or (I.12) can be used for cross sections calculations only if the total energy of the system is high enough for all collision channels to be open for ionization. When some channels are closed, the scattering matrix should be modified applying the "closed-channel-elimination" procedure and producing matrix $\mathcal{S}^{phys}(E)$ according to

$$\mathcal{S}^{phys}(E) = \mathcal{S}^{oo} - \mathcal{S}^{oc}\left[\mathcal{S}^{cc} - e^{-2i\beta(E)}\right]^{-1}\mathcal{S}^{co}\,. \tag{I.19}$$

Mathematically speaking, the above partition consists of eliminating exponential growth in closed channels to impose the correct physical behavior in solutions of Eq.(2.42) of Ref.[Aymar et al., 1996].

The matrix $\mathcal{S}^{phys}(E)$ has $N_o \times N_o$ dimension, N_o being the number of channels open for ionization for a given total energy E of the system. The total energy could be written as a sum of the energy of the entrance channel E_i (rovibrational channel, E_{vj}) and the relative kinetic energy ϵ_{vj}, see Eq.(I.6), of electron and the target ion: $E = E_i + \epsilon_{vj}$. In the above equation, the matrices $\mathcal{S}^{oo}$, $\mathcal{S}^{oc}$, $\mathcal{S}^{cc}$ and $\mathcal{S}^{co}$ are submatrices of the original matrix $\mathcal{S}$ [Seaton, 1983, Aymar et al., 1996], partitioned as

$$\mathcal{S} = \begin{pmatrix} \mathcal{S}^{oo} & \mathcal{S}^{oc} \\ \mathcal{S}^{co} & \mathcal{S}^{cc} \end{pmatrix}, \tag{I.20}$$

where the partition of the matrix elements in the "o"- and "c"-parts is made on the basis whether the corresponding channel, i or i', is open or closed for ionization for a given total energy E. The quantity $\beta(E)$ is a diagonal $N_c \times N_c$ matrix

$$\beta_{i'i}(E) = \frac{\pi}{\sqrt{2(E_i - E)}}\delta_{i'i}\,, \tag{I.21}$$

where E_i refers to energy of the corresponding closed channel i (rotational, vibrational and/or electronic channels) and $N_c = N - N_o$ is the number of closed channels. It relies on the effective quantum numbers, aside from π factor, of Eq.(I.15) with $\mathcal{I}$ being the closed ionization channel E_i.

In summary, the first term in Eq.(I.19) is restricted to the open channels and the second takes into account their mixing with the closed ones. The denominator is responsible for the resonant patterns in the shape of the cross section when

$$\det\left|\mathcal{S}^{cc} - e^{-2i\beta(E_r)}\right| \text{ has a local minimum.} \tag{I.22}$$

This yields the position of Rydberg resonances (at first order if couplings between closed and open channels are neglected). According to the partition (I.19), the eignephase can be written as follows

$$\delta(E) = \delta_{bg} + \delta_r, \tag{I.23}$$

where $\delta_{bg} = \log \mathcal{S}^{oo}/2\imath$ is the background scattering phase shift contained in $\mathcal{S}^{oo}$ and δ_r is the resonant scattering phase shift given by the resonant S-matrix of the Breit-Wigner form

$$\exp(2\imath\delta_r) = \frac{E - E_r - \Delta - \imath\frac{\gamma}{2}}{E - E_r - \Delta + \imath\frac{\gamma}{2}}, \tag{I.24}$$

with γ and Δ being, respectively, the width and shift, due to the couplings between closed and open channels.

I.4 Validity of the theoretical models

In most theoretical studies, there are two main identifiable sources of uncertainty [Chung et al., 2016]. The first one is related to the uncertainties of the theoretical model in which one often employs models with reduced dimensionality or neglecting competitive processes. The second type of uncertainties arises from the choice of parameters of the model such as the use of limited basis set or *ab initio*/fitted data. Both uncertainties will be assessed for each studied system in Section I.5.

Besides the uncertainties stated above, the validity of the models is based on the frame transformation approach underlying the R-matrix method employed throughout this manuscript. In the case of ionic target where attractive potential $V(r)$ decaying slower than the centrifugal barrier $l(l+1)/(2r^2)$, the local kinetic energy ϵ_{vj} of Eq.(I.6) depends on r at $r > 100$ bohr. At this distance, corresponding to the edge of the outer region in the R-matrix calculation, the kinetic energy of the scattering electron increases by about 0.27 eV which is larger than the spacing between vibrational levels. Hence, r_1 and r_2 in Figure I.2 are larger than 100 bohr and thus the whole region of r can be considered as the $R-$region with $\epsilon_{vj} \approx \epsilon_{v'j'}$. This conclusion is consistent with the main hypothesis: adiabatic nuclei approximation can be used in the R-matrix calculations and frame transformation can afterwards be carried out, if $S(R, \epsilon_{vj})$ is smooth with respect to ϵ_{vj}, at the end of the calculation when K-matrix has been computed.

The energy dependence of the scattering matrix at threshold for attractive Coulomb potentials lies on the presence of a large range region, namely *Coulomb zone*, where the Coulomb potential dominates over the kinetic energy ϵ. The reactance matrix is defined as follows (from first-order perturbation theory)[Aymar et al., 1996]

$$K_{i'i} \approx -\pi \langle \psi_{i'} | V_{sr} | \psi_i \rangle , \tag{I.25}$$

where $\psi_{i'}$ and ψ_i are respectively the initial and final wave functions of the scattering electron. One can see from the above equation that the matrix element of the short range potential V_{sr} is proportional to a corresponding element of the reaction matrix. Therefore, the scattering matrix, deduced from Eq.(I.4), depends on the amplitude of the electron wave function

which changes little (for a given normalization[1], i.e. usually a normalization per unit energy) with respect to the scattering energy ϵ at threshold since the local kinetic energy of (Eq.I.6) (thus the local wavelength) is governed by the Coulomb potential and not by the value of $\epsilon = \hbar^2 k^2/2m$. For $r_c > Z/\epsilon$ (obtained from $\epsilon = V(r_c) = Z/r_c$, in atomic units), the wave function oscillations are governed by the wavelength $1/k$. When $\epsilon \to 0$, one has $r_c \to \infty$ and the Coulomb zone covers now the entire asymptotic range resulting to an energy independence of the electron wave function, thus the reactance matrix of Eq.(I.25) and the related scattering matrix.

To conclude, frame transformation procedures can be applied to ionic targets even at low scattering energy. This will be the subject of applications in the next section.

I.5 Applications

This section concentrates on a few studies using the theoretical approaches described above. Mechanisms of molecular ion destruction relevant to astrophysics are briefly presented and discussed. More details are provided in the published papers, the most relevant of which, are included in this manuscript.

I.5.A Rovibrational excitation of HeH^+ molecule by electron impact

To benchmark our theoretical approach, we started applying it to the simplest molecular ion formed in the early universe, namely, HeH^+ [Lepp et al., 2002]. This cation is an important specie in the interstellar medium (ISM) [Roberge and Dalgarno, 1982] and in the chemistry of the planetary nebulae such as NGC7027 [Dabrowski and Herzberg, 1977, Black, 1978, Flower and Roueff, 1979]. In the ISM, it is mainly formed in the radiative association process of He and H^+ or of He^+ and H [Zygelman and Dalgarno, 1990, Kraemer et al., 1995]. Collisions of HeH^+ with electrons play a significant role, in particular, leading to dissociation (dissociative recombination) and rovibrational (de-)excitation of HeH^+[Jimenez-Serra et al., 2006], due to the relative abundance of electrons and HeH^+ in the ISM.

In this section, we focus on the rovibrational excitation and (de)-excitation (RVE,RVdE) process

$$e^- + HeH^+(v,j) \to e^- + HeH^+(v',j')\,, \tag{I.26}$$

where v, j and v', j' stand for the vibrational quantum number and angular momenta of the target before and after the rovibrational excitation of HeH^+.

Since the first electronically excited state $A^1\Sigma^+$, correlated with $H(1s)$ + $He^+(1s)$ is approximately 11 eV above the H^+ + $He(1s^2)$ dissociation limit for the $X^1\Sigma^+$ground state, the ground state of electronic configuration $1\sigma^2$ is isolated and non-adiabatic effects are expected to be small. Therefore, for low electron energy collisions (below 10 eV) only the lowest electronic state is open for ionization in e^- − HeH^+ collisions and the dimension of the geometry-fixed scattering matrix does not change with energy. Consequently, HeH^+ is

[1]The normalization should eliminate any energy dependence of the electron wave function amplitude arising from the normalization factor in Eq.(I.16).

an ion of the second type –having the first excited electronic state at a high energy– and we can thus directly apply our theoretical approach that combines the R-matrix code (the obtained S-matrix from Eq.(I.4)), the rovibrational frame transformation (Eq.(I.12)) and the elimination procedure in the sprite of MQDT (Eq.(I.19)).

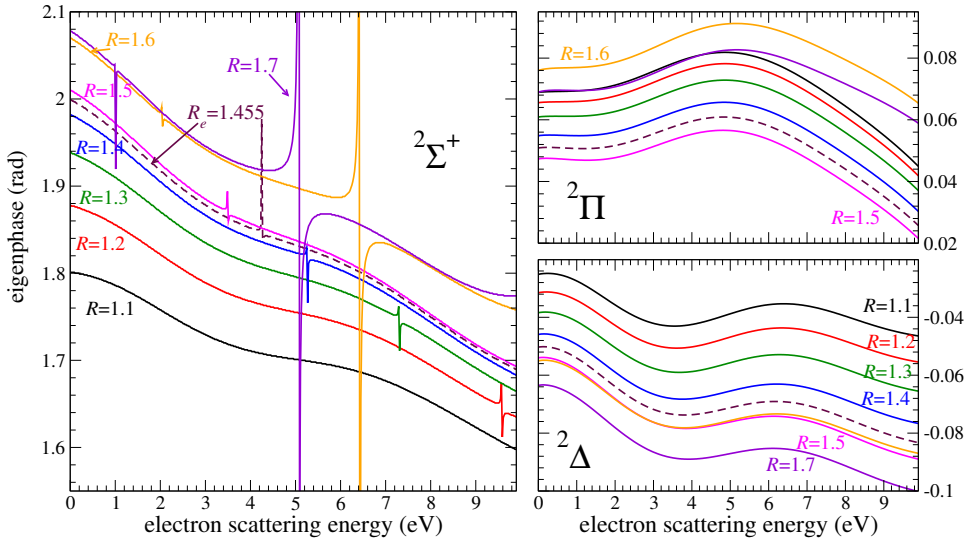

Figure I.3: Eigenphase sum as a function of the electron scattering energy E_{el} (in eV) for several internuclear distances R (in units of bohr) for the $^2\Sigma^+$ (left panel), $^2\Pi$ (right upper panel), and $^2\Delta$ (right bottom panel) symmetries. The color scheme used to label different values of R is the same for all three panels. The dashed line represents the equilibrium internuclear distance $R_e = 1.445$ bohrs [Rabadán et al., 1998] of HeH^+.

In the R-matrix calculations (carried out in C_{2v} which is subgroup of $C_{\infty v}$, natural point group of HeH^+), several basis sets, including `3-21G`, `DZP` and `6-311G*` as well as R-matrix sphere radii were tested to assess the uncertainties arising from the scattering model. Stability of the target properties such as dipole moment and ground state energy or positions of resonances have been investigated in order to select the adequate set of parameters for the final calculations. Moreover, in the calculations of the cross sections for reaction of Eq.(I.26), energies for vibrational and rotational transitions as well as vibrational wave functions of the target (in addition to its potential energy curve) are needed to perform the frame transformations of Eqs.(I.8) and (I.12). The obtained results are provided in papers .3 and .4 and compared with available data.

As widely discussed in the preceding sections, the application of frame transformations requires that $K(R)$ and $S(R)$ depend weakly on energy. A sharper energy-dependence is observed only at certain higher energies, corresponding to positions of Rydberg states attached to excited electronic states of the ion. A convenient way to represent a weak or a strong energy dependence of the matrices is the eigenphase sum of Eqs.I.5. Figure I.3 of paper .3 shows eigenphase sums for three symmetries ($^2\Sigma^+$, $^2\Pi$, and $^2\Delta$) of the e^- + HeH^+ system and for several internuclear distances in HeH^+. The chosen interval of internuclear distances corresponds to the Franck-Condon region of the lowest vibrational level of HeH^+.

The variation of the eigenphase sums for $^2\Pi$ and $^2\Delta$ is smooth for energies below 10 eV and does not change significantly with R. The $^2\Sigma^+$ eigenphase sums demonstrate a sharp energy dependence at certain energies, which corresponds to a resonant state of HeH with energy changing with the internuclear distance R.

Using the scattering matrix $\mathcal{S}^{phys}$ of Eq.(I.8), the cross section for purely vibrational transition $v \to v'$ is [Ayouz and Kokoouline, 2016]

$$\sigma_{v' \leftarrow v}(\epsilon) = \frac{\pi\hbar^2}{2m_e\epsilon} \sum_{\lambda' l' \lambda l} \left| \mathcal{S}^{phys}_{\lambda' l' v', \lambda l v} - \delta_{\lambda l v, \lambda' l' v'} \right|^2 , \tag{I.27}$$

where m_e is the reduced mass of the electron-ion system. Figure I.4 demonstrates, as examples, the cross sections of Equation (I.27) for the $v = 3 \to v' = 0, 1, 2, 4$ transitions. At very low scattering energies, below 0.02 eV, the de-excitation cross sections are smooth functions inversely proportional to the incident energy of the electron as predicted by the Wigner threshold law. But at higher energies, especially, just below the energy of the each excited threshold, $v' = 4, 5, \cdots$, the (de-)excitation cross sections and probabilities demonstrate series of Rydberg resonances, where they vary significantly.

The inelastic cross section for the rotational excitation or de-excitation process $j'\mu'v' \leftarrow j\mu v$ of a linear molecule by electron impact is obtained from the scattering matrix of Equation (I.12)

$$\sigma_{j'\mu'v' \leftarrow j\mu v}(\epsilon) = \frac{1}{2j+1} \frac{\pi\hbar^2}{2m_e\epsilon} \sum_{J,l,l'} (2J+1) \left| e^{i(l\pi/2+\sigma_l)} \mathcal{S}^{J,phys}_{j'\mu'l'v';j\mu l v} e^{-i(l'\pi/2+\sigma_{l'})} \right|^2 , \tag{I.28}$$

where σ_l is the Coulomb phase shift given in Eq.(I.3). In the above formula, the cross section is averaged over degeneracy of the initial rotational state j. Its derivation is given in paper .4. Note that in the ground electronic state of HeH^+, the projection μ of the electronic angular momentum on the molecular axis of the target is zero. Therefore, for scattering energies below the first excited electronic state $A^1\Sigma^+$ of HeH^+, $\mu = \mu' = 0$ in Eq.(I.28).

Cross sections for electron impact transitions between the lowest five $j, j' = 0-4$ rotational states of HeH^+ (without vibrational structure, i.e. a situation where the scattering electron is not energetic enough to excite the target vibrationally) are given in Figure I.5. Solid lines in the figure represent the results obtained using the complete theoretical approach, viz. the rotational frame transformation of Eq.(I.12) in combination with the closed-channels elimination procedure from Eq.(I.19). The cross sections exhibit a strong resonant character. The resonances are produced by closed rotational states of the target. These resonances are washed out when thermally-averaged rate coefficients are computed. Therefore, in the calculation of the rate coefficients, one can use cross sections averaged over the resonances. Such averaged cross sections can be computed directly from the energy-independent scattering matrix $\mathcal{S}^J$, replacing in Equation (I.28) the matrix elements $\mathcal{S}^{J,phys}_{j'\mu'l';j\mu l}$ of the physical scattering matrix with the corresponding elements $\mathcal{S}^J_{j'\mu'l';j\mu l}$ of the energy-independent matrix. The cross sections calculated using the energy-independent scattering matrix are shown by dotted lines in Figure I.5.

Furthermore, data relevant to the other isotopologues $^4HeD^+$, $^3HeH^+$, and $^3HeD^+$ could also be useful for plasma modeling. In this respect, cross sections as well as rate coefficients

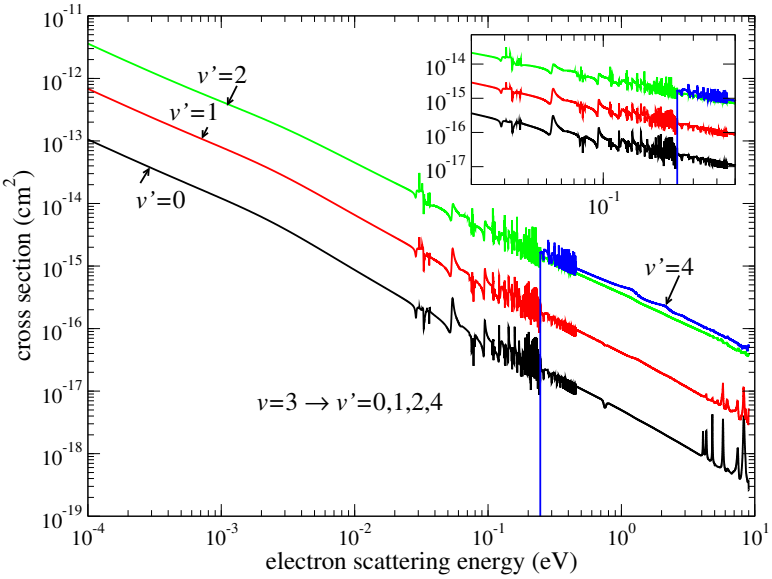

Figure I.4: Cross sections of vibrational (de-)excitation from the vibrational level $v = 3$ to several other levels v'. The inset enlarges the region of Rydberg series of resonances close to the $v' = 4$ and $v' = 5$ ionization thresholds, situated at energy of 0.2465 and 0.4533 eV, respectively, above the $v = 3$ threshold.

for collisions of the HeH^+ isotopologues with electrons were computed. Figure I.6 and I.7 are a result of a thermal Boltzmann convolution (see Eqs.(I.31) or (13) of paper .3) of the cross sections of $^4HeH^+$ molecule and its isotopologue $^4HeD^+$, for instance. The obtained results are in good agreement with the data available in literature. Due to the general $1/E_{el}$-dependence of cross sections of Eqs.(I.27) and (I.28), the calculated rate coefficients $\alpha_{v'j'\leftarrow vj}(T)$ behave as $1/\sqrt{T}$ for de-excitation and $\exp\left(-\Delta_{v'j'\ vj}/T\right)/\sqrt{T}$ for excitation transitions, where $\Delta_{v'j'\ v'} = E_{v'j'} - E_{v'}$ is the excitation energy. Therefore, similar to papers .3 and .4, for convenience of use, the rate coefficients were fitted to an analytical interpolation formulas with up to four parameters. See Eqs.(4), (5) and (8) in Ref.[Ayouz and Kokoouline, 2019].

To summarize, we reported in Refs.[Ayouz and Kokoouline, 2016, Khamesian et al., 2018, Ayouz and Kokoouline, 2019] and briefly in this section the cross sections and rate coefficients for rovibrational excitation of HeH^+ and its isotopologues by electron impact. These results were obtained in context of my collaboration with Prof. Viatcheslav Kokoouline and, at least, partially during the dissertation of Marjan Khamesian (first author of paper .3) at University of Central Florida (UCF), in which I was involved. Our data were included in the IAEA database https://www-amdis.iaea.org/DATASETS/e_HeH/. They could be used in modeling the hydrogen/helium plasma experiments as well as for modeling interstellar clouds and planetary atmospheres, where the HeH^+ ion is present.

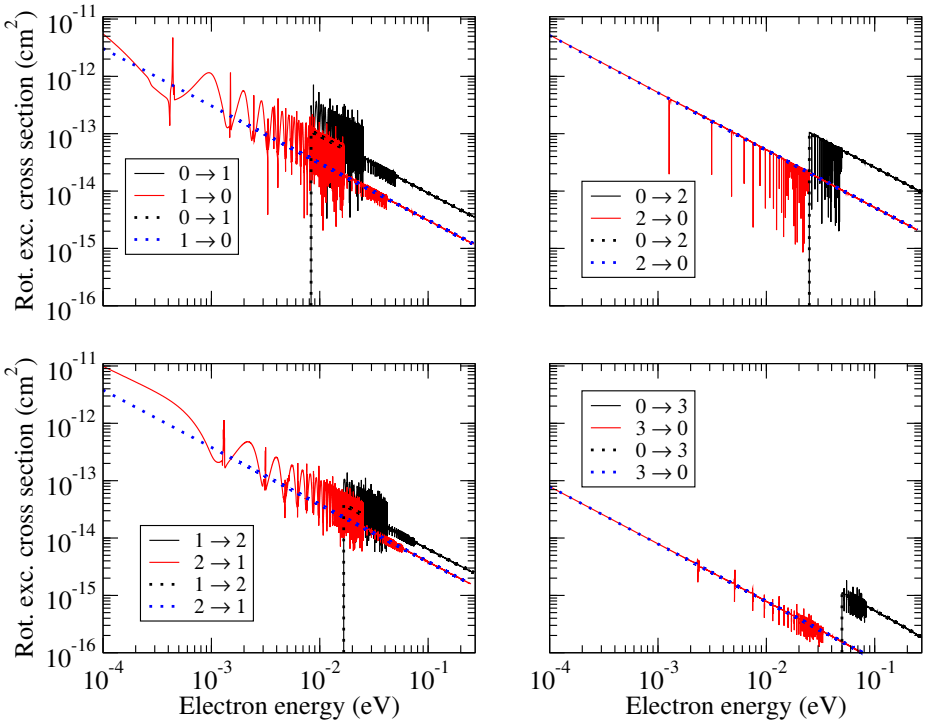

Figure I.5: Rotational (de-)excitation cross sections for transitions between the four lowest rotational states of HeH^+. Solid lines represent the results obtained with the applied closed-channel elimination procedure of Equation (I.19), while the dotted lines show the results for which the procedure was not applied.

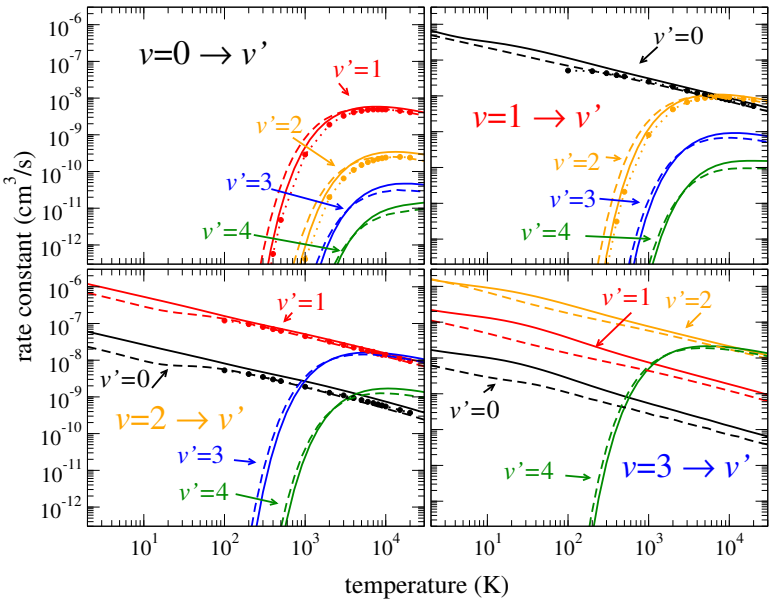

Figure I.6: Thermally averaged rate coefficients for several vibrational (de-)excitation transitions of $^4HeH^+$ (solid lines) and $^4HeD^+$ (dashed lines). Vibrational transition $v \rightarrow v'$ labels are shown in each panel. Results of a previous calculation [Rabadán et al., 1998] are shown in dotted lines with circles.

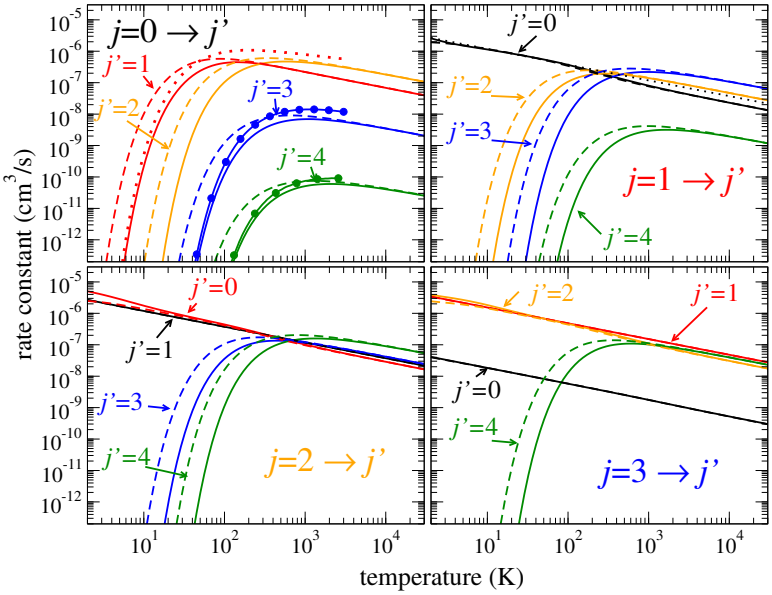

Figure I.7: Thermally averaged rate coefficients for several rotational (de-)excitation transitions of $^4HeH^+$ (solid lines) and $^4HeD^+$ (dashed lines). Dotted lines in the upper left panel are the calculations by Hamilton et al. [Hamilton et al., 2016], and lines with circles are those of Čurík and Greene [Čurík and Greene, 2017] for $^4HeH^+$.

I.5.B Vibronic excitation of CH^+ molecule by electron impact

Another important specie relevant in ISM is CH^+, first detected in cold ionized environments by Douglas and Herzberg [Douglas and Herzberg, 1941] in 1941 and later observed in many background stars. It is believed that its formation mechanism is governed by the collisions between C^+ and H_2. The main route for its destruction is the dissociative recombination (DR), in competition with the rovibronic (de-)excitations processes.

This section aims to study the vibronic excitation and (de-)excitation process

$$e^- + CH^+(i, v) \rightarrow e^- + CH^+(i', v') \,, \tag{I.29}$$

where v or v' corresponds to the number of vibrational quanta in initial i or final i' electronic state of the target ion. Rotational structure is neglected within this study. It will be considered in future work (see Chapter V).

Theoretical description of low-energy $e^- - CH^+$ collisions is complicated due to the presence of a low-energy electronic resonance and several low-energy excited electronic states of CH^+ which makes it an ion of the first type (see discussion in paper .5 and Ref.[Jiang et al., 2019]). The $a\,^3\Pi$ and $A\,^1\Pi$ curves above the ground state $X\,^1\Sigma^+$ of electronic configuration $1\sigma^2 2\sigma^2 3\sigma^2$, correlate with the $C^+\left(^2P\right) + H\left(^2S\right)$ dissociation limit at large internuclear distances (see Figure I.12). In this situation, the standard frame transformation approaches, used above for HeH^+ and in many theoretical studies on electron-molecule collisions, is not well adapted due to the energy-dependence of the scattering matrix. For this purpose, we improved our model

on HeH^+ by adapting the frame transformation procedures, described in Section I.3, to CH^+. The central idea of the developed theoretical approach is that the $e^- - CH^+$ scattering physics below the $A\,^1\Pi$ state can be represented using an energy independent multichannel scattering matrix evaluated at a higher energy, above the $A\,^1\Pi$ ionization limit in a combination with the closed-channel elimination.

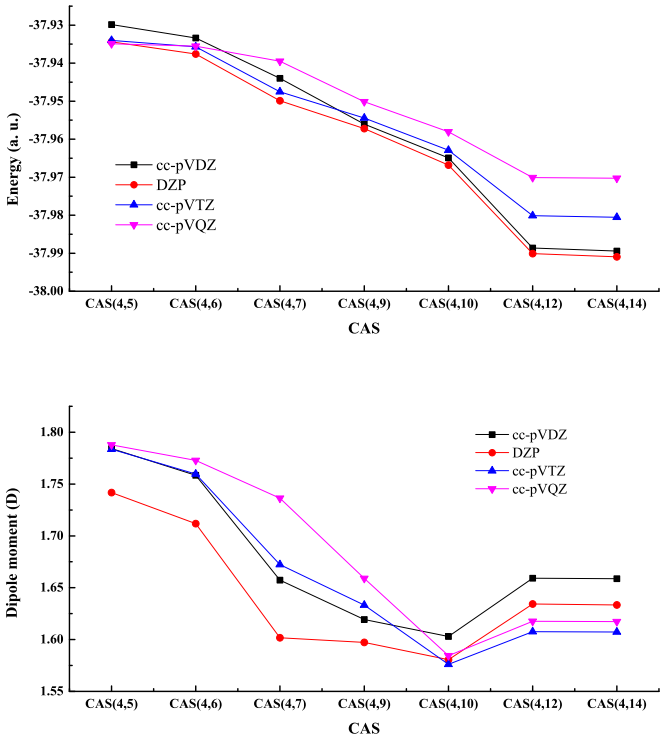

Figure I.8: Potential energy for the ground electronic state (upper panel) of CH^+ and its dipole moment(bottom panel) obtained with different CAS and basis sets at the equilibrium geometry $R_e = 2.137$ bohrs.

Again, our approach employs the fixed-nuclear R-matrix (S-matrix in Eq.(I.4) is obtained from calculations performed in C_{2v} which is subgroup of $C_{\infty v}$, natural point group of CH^+) with the vibronic frame transformation (in addition to electronic states) and the closed-channel elimination procedure in a spirit of MQDT (Eq.(I.19)). To perform frame transformation of Eq.(I.8), with the inclusion of the electronic states i and i', we take the (almost) energy-independent 3×3 electronic scattering matrix, obtained at an energy above the $A\,^1\Pi$ ionization limit, to produce $N \times N$ matrix with N vibronic (or rovibronic) channels. Such a vibronic scattering matrix is essentially energy-independent and a closed-channel elimination procedure should be performed to obtain the physical energy-dependent matrix, which can be used to compute cross sections and related rate coefficients.

Several parameters of the scattering model were first tested to investigate the stability

of the target properties. Figure I.8 depicts variation of the ground state energy and dipole moment of CH^+ regarding different basis sets and complete active spaces CAS(n_e,n_{ao}), viz. number of electrons n_e distributed in n_{ao} active orbitals. Considering the dipole moment 1.617 D obtained with `cc-pVQZ` is closer to the experimental value of 1.683 D, this basis with CAS(4, 12) and a R-matrix sphere of radius 13 bohrs were thus selected for the final calculations.

Another source of uncertainty is related to the model itself. The choice of the 3×3 scattering matrix used in the channel-elimination procedure is not unique, because the matrix depends on energy, even above the $A\,^1\Pi$ electronic state. To assess the result of uncertainty in the choice of the energy at which the 3×3 scattering matrix is taken, we plot in Figure I.9 eigenphase-sum derivatives obtained for 3×3 scattering matrices taken at three different energies above the $A\,^1\Pi$ state: at 3.413, 3.563, and 3.713 eV. Positions and the widths of the resonances are nearly the same in all three calculations.

To validate the developed model, we compare the fixed-nuclei electronic scattering matrices obtained (1) using the elimination procedure of the closed electronic states and by (2) a direct scattering R-matrix calculation at the same internuclear distance, viz. $R_e = 2.137$ bohrs. To do this, the physical scattering matrix $\mathcal{S}^{phys}(\epsilon, R_e)$ of Eq.(I.19) describing electronic transitions at R_e of CH^+, was used to compute the fixed-nuclei cross section of the electronic excitations from the $X\,^1\Sigma^+$ state to the $a\,^3\Pi$ state as

$$\sigma_{i' \leftarrow i}(\epsilon, R_e) = \frac{\pi\hbar^2}{2m_e\epsilon} \sum_{l'm',lm} \left| \mathcal{S}^{phys}_{l'm'i',lmi}(\epsilon, R_e) - \delta_{l'm'i',lmi} \right|^2, \tag{I.30}$$

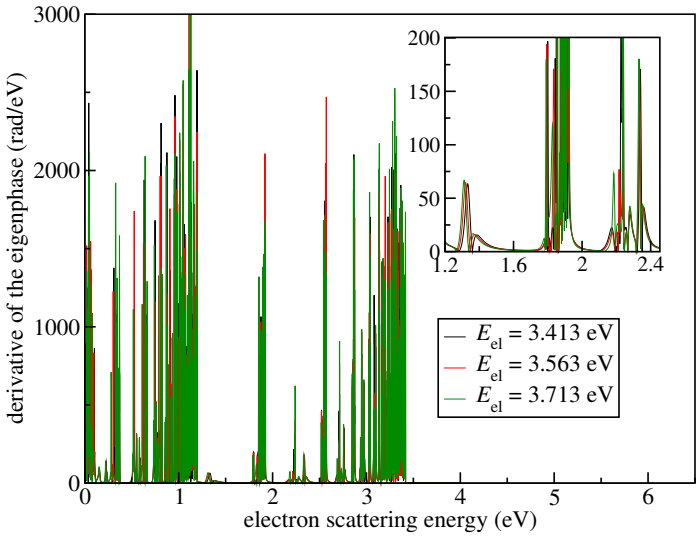

Figure I.9: Comparison of eigenphase-sum derivatives computed for a fixed CH^+ geometry using three different energy-independent 3×3 scattering matrices and the procedure of elimination of closed electronic channels. The three matrices are taken at energies 3.413 eV (black curve), 3.563 eV (red curve) and 3.713 eV (green curve). The inset shows an enlarged view for 1.2–2.4 eV energies.

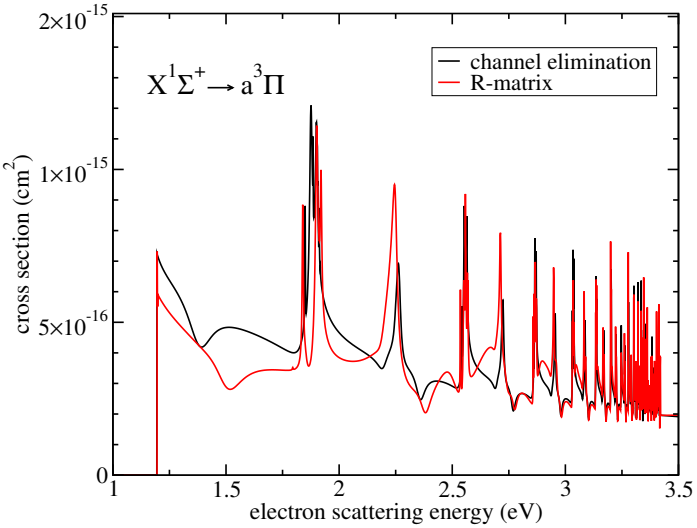

Figure I.10: Cross sections for the $X^1\Sigma^+ \to a^3\Pi$ electronic excitation of CH^+ at a fixed geometry R_e obtained in the direct R-matrix calculations (red curve) and using the QDT channel elimination procedure (black curve).

Figure I.10 compares the cross sections for the $X^1\Sigma^+ \to a^3\Pi$ transition obtained in the two approaches. The general agreement between the two curves is good, even for the widths of the resonances. One noticeable difference is in the position of the minimum near 1.5 eV: In the MQDT calculations it is shifted slightly to the left. The agreement is better at energies approaching the $a^3\Pi$ ionization limit.

Once the model is validated, a vibronic frame transformation of Eq.(I.8) can be performed in order to compute the cross sections for vibronic excitation or (de-)excitation of CH^+ using Eq.(I.27, where $\mathcal{S}^{phys}_{l'm'i',lmi}(\epsilon, R_e)$ is replaced with $\mathcal{S}^{phys}_{l'm'v'i',lmvi}(\epsilon)$. We noted here m as the project of the angular momentum quantum number on the molecular axis instead of λ. Figure I.11 illustrates cross sections obtained for different combinations of initial and final vibronic states. Panel (a) shows results for pure vibrational excitations between levels of the ground electronic state $X^1\Sigma^+$. As expected, the cross section for the transition with $\Delta v = 1$ is the largest one between inelastic processes. Panel (b) gives cross sections from the ground vibronic state $X^1\Sigma^+, v = 0$ to several vibrational levels of the $a^3\Pi$ state. Since the potential curves of the $X^1\Sigma^+$ and $a^3\Pi$ states have similar shapes near equilibrium, the largest $X^1\Sigma^+ \to a^3\Pi$ cross section is expected to be for $\Delta v = 0$, as the present calculation indeed demonstrated. Panel (c) gives cross sections for the de-excitation process $a^3\Pi, v = 0 \to X^1\Sigma^+, v' = 0 - 3$.

The obtained cross sections differ significantly from those of Ref.[Chakrabarti et al., 2018b]. These disagreements can be attributed to approximations employed in their study: (1) neglected differences in vibrational excitation threshold energies, (2) neglected dependence of $e^- - CH^+$ scattering parameters with the internuclear distance, and (3) the neglected resonances in closed vibronic channels. Thermally-averaged rate coefficients of the above vibronic (de-)excitations

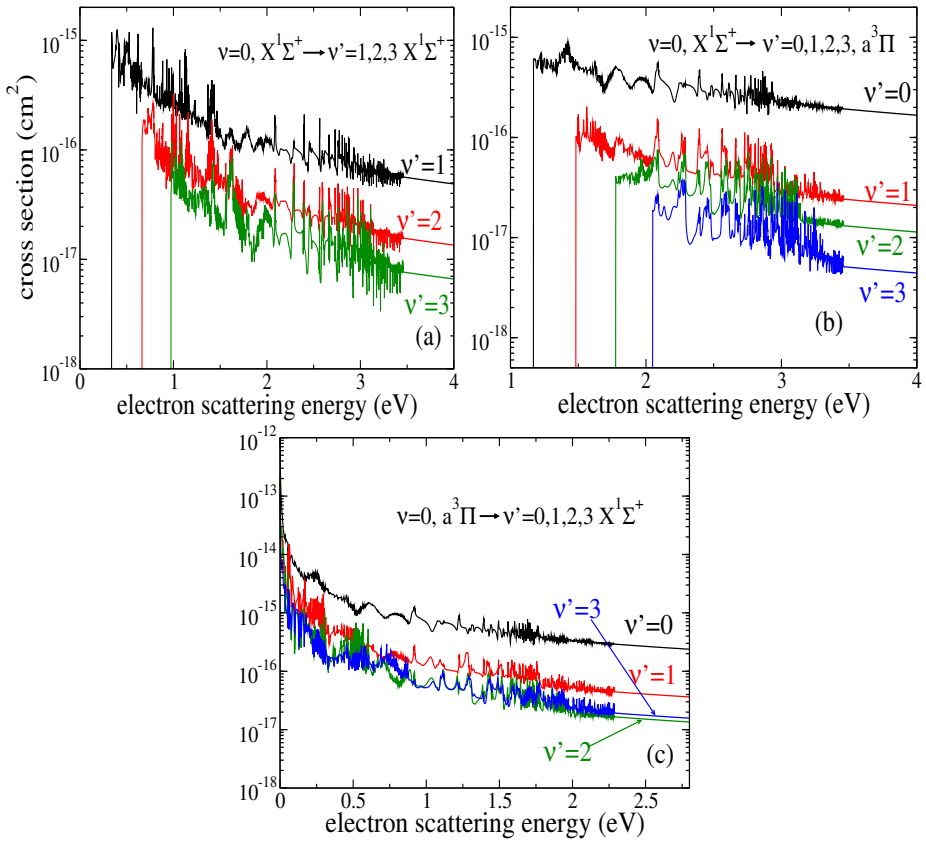

Figure I.11: Cross sections for vibronic excitations of CH^+ from the ground vibrational level $v = 0$ of the $X^1\Sigma^+$ state to $v = 1, 2, 3$ of the $X^1\Sigma^+$ state (left panel) , to $v = 0, 1, 2, 3$ of the $a^3\Pi$ state (middle panel), and for vibronic de-excitations from the ground vibrational level $v = 0$ of $a^3\Pi$ to $v = 0, 1, 2, 3$ of the $X^1\Sigma^+$ state (right panel).

$$\alpha_{i'v'\leftarrow iv}(T) = \frac{8\pi}{(2\pi k_b T)^{3/2}} \int_0^\infty \sigma_{i'v'\leftarrow iv}(\epsilon)\, e^{-\frac{\epsilon}{k_b T}}\, \epsilon\, d\epsilon, \tag{I.31}$$

are then computed and fitted to an analytical formula, analogously to HeH^+. More details and discussions can be found in paper .5.

Finally, we report in Ref[Jiang et al., 2019] and briefly in this section the cross sections for vibronic excitation and de-excitation of CH^+ by electron impact using only first principles. These outcomes were obtained in the context of Xianwu Jiang's dissertation at Centralesupélec and in collaboration with UCF. The developed theoretical approach can be applied to ions with low-energy excited states, known to be difficult to treat theoretically using previous theoretical methods. Our approach is quite general and can be applied also for a number of different processes such as dissociative recombination, which is the subject of the next section.

I.5.C Dissociative recombination of CH^+

In the continuation of the preceding study, we consider in this section the following dissociative recombination (DR) processes

$$e^- + CH^+(i,v) \rightarrow \begin{cases} CH^{**}(2\,^2\Pi) \rightarrow C\left(^1D\right) + H\left(^1S\right) & \text{direct DR} \\ CH^*(\text{Rydberg}) \rightarrow CH^{**}(2\,^2\Pi) \rightarrow C\left(^1D\right) + H\left(^1S\right) & \text{indirect DR} \end{cases} \tag{I.32}$$

where $CH^{**}(2\,^2\Pi)$ and CH^* are respectively the doubly-excited dissociative and singly excited bound Rydberg states.

The state $CH^{**}(2\,^2\Pi)$ is formed when the electron collision energy ϵ is not transferred directly into kinetic motion of the nuclei, but rather to the electronic ionic clouds resulting in the excitation of the target bound electrons. The striking feature of $CH^{**}(2\,^2\Pi)$ is that it is situated in the ionization-continuum of CH^+. The potential energy curve of the doubly-excited $CH^{**}(2\,^2\Pi)$ is repulsive and intersects the curve of $CH^+\left(X\,^1\Sigma^+\right)$ near the equilibrium geometry (see Figure I.12). The resonant state $CH^{**}(2\,^2\Pi)$ is unstable against autoionization, i.e. the re-emission of electron leading to vibronic excitations, because the excited electron has sufficient energy to escape from CH. Generally speaking, if the dissociative process happens fast enough so that the products of dissociation are already at a large distance from each other after a time equivalent to the order of the autoionizing lifetime, most of the collisional energy is already converted into nuclei kinetic energy and autionization becomes impossible. In such a case, the system irreversibly breakdowns in one of the dissociative channels. This is the direct dissociative recombination (DDR) process.

In contrast to the above situation, the indirect dissociative recombination (IDR) mechanism can be considered as the result of two non-radiation transitions. When the kinetic energy of the electron is transferred to the motion of nuclei, the electron then moves around a vibrationally (or rovibrationally in general) excited core in a hydrogenic-like orbital of CH with high principle quantum number (see Eq.(I.15)). The excited Rydberg state CH^* is in turn predissociated by the doubly-excited state $CH^{**}(2\,^2\Pi)$ leading to dissociation into $C\left(^1D\right) + H\left(^1S\right)$ through non-adiabatic couplings, i.e. breaking the BO approximation. The IDR process occurs very often in a closed shell ions, such as HeH^+ or $CH_2NH_2^+$ for example.

Both DDR and IDR in the reaction of Eq.(I.32) compete with the vibrionic excitation and (de-)excitation processes, investigated previously. Consequently, for a comprehensive study of mechanisms of destruction of CH^+ in ISM, for instance, one has to take into account the role of all these effects on the magnitude of the cross section at very low energy. As for the role of rotational effects, it has been postponed to a further study.

The theoretical approach employed in this section is similar to the one above for describing the VE and VdE processes. It combines the R-matrix code to compute electron-ion scattering matrices (Eq.(I.4)), the vibronic frame transformation (Eq.(I.8) with the inclusion of electron state indexes) and the closed-channel elimination procedure in a spirit of molecular quantum defect theory to construct an energy-dependent scattering matrix (Eq.(I.19)). The main difference here is the inclusion of vibrational continua states in addition to vibrational bound states (see Figure I.12). This can be accomplished throughout the outgoing-wave basis functions defined by a complex absorbing potential as described in Section I.3. Since the present work

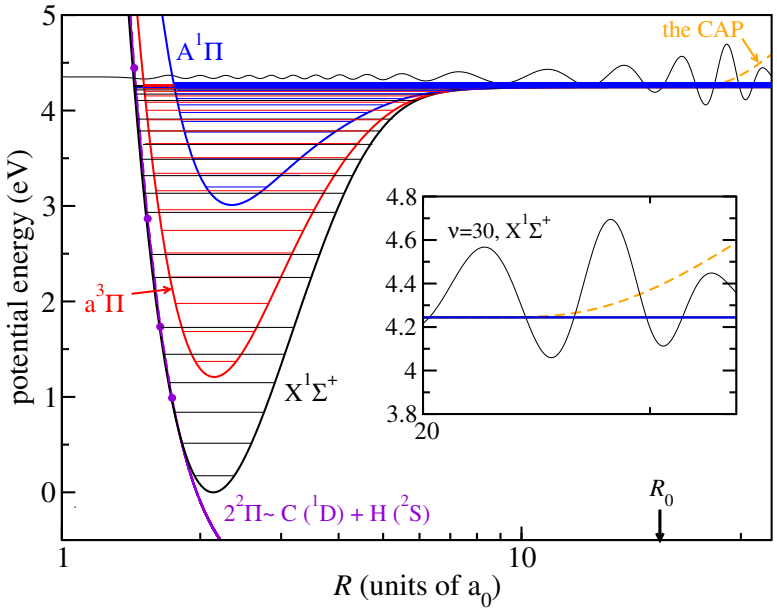

Figure I.12: Potential energy curves (PECs) of the three lowest $X^1\Sigma$ (black), $a^3\Pi$ (red) and $A^1\Pi$ (blue) electronic states taken from Ref.[Jiang et al., 2019]. The PEC of the $2^2\Pi$ resonance state (violet dotted curve) is obtained from the R-matrix calculations. For more clarity, an extrapolation was done below the ionic ground state (violet solid curve). 35 vibrational levels for each PEC are shown by horizontal thin lines where colors corresponding to each respective state. For illustration, the CAP is drawn in orange dashed curve while the vibrational wave function of level $v = 30$ in $X^1\Sigma^+$ (black solid curve) state is displayed in black solid curve. $R_{CAP} = 20$ bohr represents the starting point of the CAP of Eq.(I.10) and the inset shows the enlarged view of CAP region.

is still in development, I will only provide the first results below.

In figure I.12 displaying the potential energy curves of CH^+, the doubly-excited dissociative state $CH^{**}(2\,^2\Pi)$ crosses the ground electronic state $X\,^1\Sigma^+$ of CH^+ near the left turning point of the first excited vibrational state. This gives rise to a DR process according to Eq.(I.32). In the figure, 35 vibrational levels for each electronic states are drawn and the CAP of Eq.(I.10) is also represented. The insight depicts, as an example, the long-range behavior of a vibrational wave function of the discretized continuum.

Accurate description of DR in CH^+ of Eq.(I.32) requires including the $2\,^2\Pi$ resonant state in the MQDT treatment. So, performing the R-matrix calculations and selecting the 3×3 energy-independent scattering matrix (above the $A\,^1\Pi$ threshold) according to the procedure described in the preceding section, we can see in Figure I.13 the positions of the $2\,^2\Pi$ state at different geometries $R = 1.337$, 1.437, and 1.537 bohrs. The figure compares the positions, i.e. the derivative of eigenphase sum of $e^- - CH^+$ system, given directly from R-matrix to those obtained from the closed-channel elimination procedure of Eq.(I.19). Overall positions of the resonance are a little left shifted and the widths are slightly wider compared to that

of the R-matrix calculation. However, we expect that these discrepancies do not affect the final thermally-averaged rates coefficients as seen in calculations of vibrionic (de-)excitation of CH^+ in paper .5.

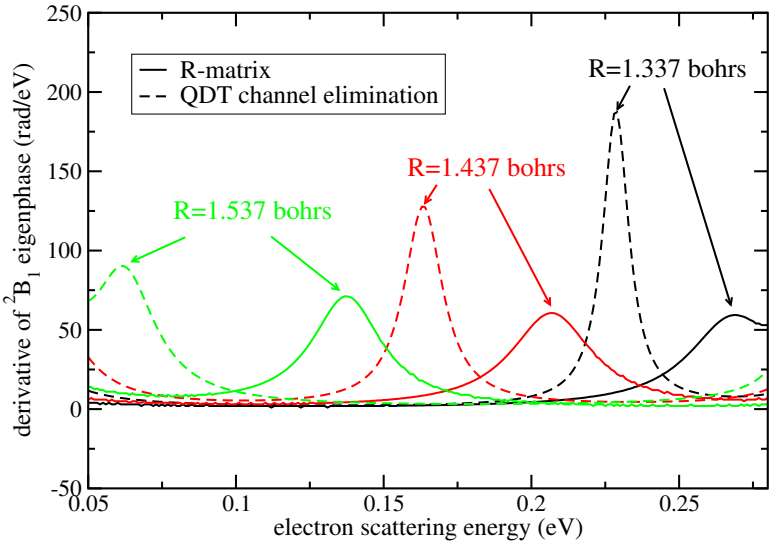

Figure I.13: Low-energy resonances corresponding to the doubly-excited $CH^{**}(2\,^2\Pi)$ obtained from the derivative of eigenphase sum of the $^2\Pi$ symmetry in R-matrix calculation (solid curves) and MQDT channel elimination procedure (dashed curves). Each color refer to different resonances obtained at R=1.337 (black), 1.437 (red), and 1.537 bohrs (green). Details of the R-matrix calculations could be found in paper .5.

In the present treatment, the dissociation proceeds through a number of excited Rydberg states, which are bound with respect to dissociation. MQDT treats such a system as a set of coupled vibrational states. As hinted in section I.3, the introduction of the CAP leads to simulate an infinite grid in which the vibrational continuum becomes discretized. To test parameters of the CAP in Eq.(I.10), we used the Fourier transformation (FT) technique and analyzed the vibrational wave functions in the momentum space.

In left panels of Figure I.14, we display wave functions of dissociative vibrational states (vibrational continua states), for instance, $v = 30$, $X\,^1\Sigma^+$ (black curve), $v = 26$, $a\,^3\Pi$ (red curve), and $v = 20$, $A\,^1\Pi$ (green curve) as functions of internuclear distance R. Right panels show the respective Fourier transform of that wave functions. The wave functions obtained with CAP calculations are given in solid lines whereas those without CAP are in dashed curves. The most striking feature in these figures is the absence of the second peak, corresponding to the incoming/reflected wave function, in the Fourier spectrum of the wave functions when the CAP is involved in the calculations. This indicates that the set of the CAP parameters, i.e. length and strength in Eq.(I.10 are appropriately chosen.

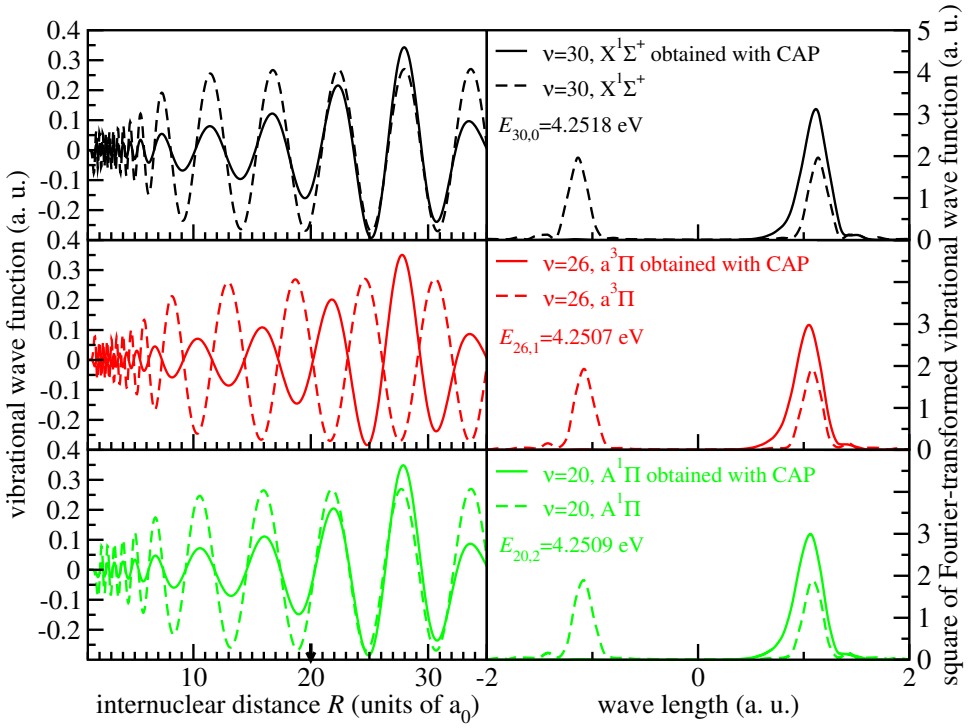

Figure I.14: Left panels show the vibrational wave function as function of R for v=30, $X^1\Sigma^+$ (in black), v=26, $a^3\Pi$ (in red), and v=20, $A^1\Pi$ (in green) obtained with (solid curve) and without CAP (dashed curve). Right panels display the Fourier transform of the corresponding vibrational wave functions. The starting point of the CAP, R_{CAP}, is drawn in the left lower panel.

After benchmarking the CAP parameters, the DR cross section can be computed from the following expression

$$\sigma_{vi}(\epsilon) = \frac{\pi\hbar^2}{2m_e\epsilon} \sum_{i'v'} \sum_{l'm',lm} \left(1 - \mathcal{S}^{phys}_{l'm'i'v',lmiv}(E)\, \mathcal{S}^{\dagger phys}_{l'm'i'v',lmiv}(E)\right) \tag{I.33}$$

where m_e is the reduced mass of e^-–CH^+ and $\epsilon_{vi} = E - E_{vi} \approx \epsilon_{v'i'} \approx \epsilon$ is the incident energy of the electron. $\mathcal{S}^{phys}_{l'm'i'v',lmiv}$ and $\mathcal{S}^{\dagger phys}_{l'm'i'v',lmiv}$ are calculated using the frame transformation of Eq.(I.8) with no complex conjugation for the vibrational states. In addition, performing the channel elimination procedure for $\mathcal{S}^\dagger : \mathcal{S}^\dagger \rightarrow \mathcal{S}^{\dagger phys}(E)$, one has to use the complex conjugate of $\beta(E)$ in Eq.(I.21). Recall that $\beta(E)$ is the effective quantum number for energy E in closed channel multiplied by π (see Eq.(I.17)). It is complex valued because the energy of the closed channel has a non-zero imaginary part, resulting from the boundary condition imposed by the CAP, related to the dissociation lifetime of the ionic channel. More details of this method can be found in Ref.[Kokoouline et al., 2011].

Figure I.15 shows the first result of the computed DR (including direct dn indirect routes) cross section of the ground vibronic state of CH^+, compared with different *ab initio* studies and experimental measurements available in the literature. To compare these results with

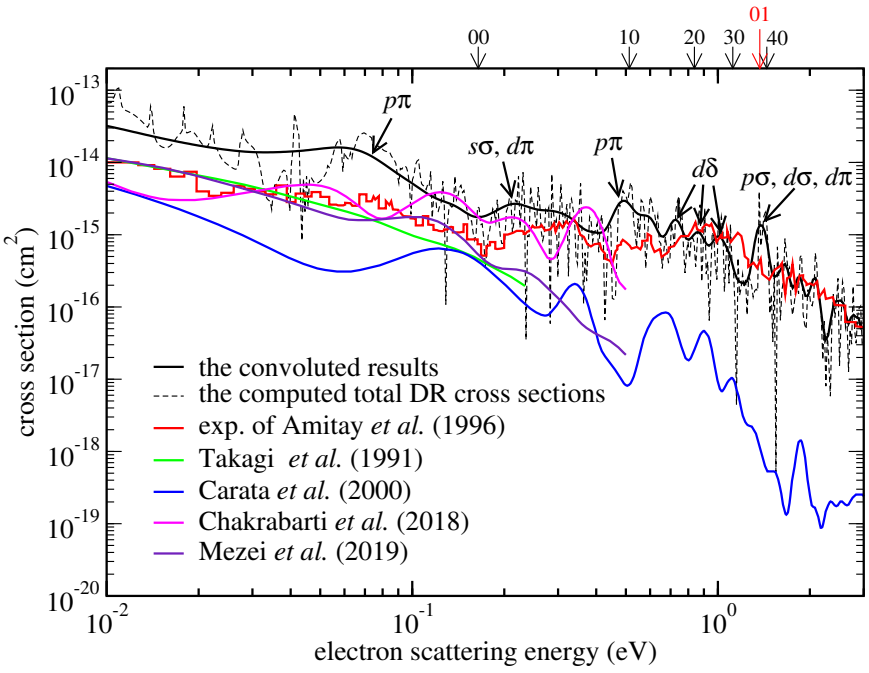

Figure I.15: Comparison of the DR cross section of the ground vibronic state of CH^+. The computed total DR cross section in the present work (black thin dashed curve) and the convoluted results (black solid curve) are compared with the experimental measurements of Ref.[Amitay et al., 1996] (red solid curve), theoretical results Ref.[Takagi et al., 1991] (green solid curve), Carata Ref.[Carata et al., 2000] (blue solid curve) and Ref.[Chakrabarti et al., 2018a] (magenta solid curve), and rotationally resolved DR cross section obtained by Ref.[Mezei et al., 2019] (violet solid curve). Partial waves of the incident electron are assigned to the prominent resonances by arrows. Energies of ground vibrational threshold in each electronic state are labeled with arrows and the corresponding vibrionic quantum numbers vi.

experimental data, the DR cross section, shown as a dashed curve, was averaged over the non-isotropic distribution throughout the formula of Eq.(2) of Ref.[Kokoouline and Greene, 2005], shown as a solid line. The parameter of the experimental energy distribution were picked from Ref.[Amitay et al., 1996]. This first result demonstrates a good agreement at high energy in contrast to the low-energy range. We attribute this discrepancy to the fact that the rotational structure in each vibrational level of CH^+ was neglected in the present study. Tests and improvements are ongoing to date.

I.5.D Dissociative recombination of polyatomic molecular ions: $CH_2NH_2^+$

This section presents an application of the simplified approach, described in Chapter III, on a population of some prebiotic molecules such as $CH_2NH_2^+$ and NH_2CHOH^+ that is largely influenced by the rate of dissociative recombination. Indeed, it has been shown that such molecules have a significant impact on chemical evolution in different astrophysical

environments. In the following, I will briefly report our work on $CH_2NH_2^+$ carried out in the context of the dissertation of Chi Hong Yuen at UCF. Details on NH_2CHOH^+ can be found in Ref.[Ayouz et al., 2019].

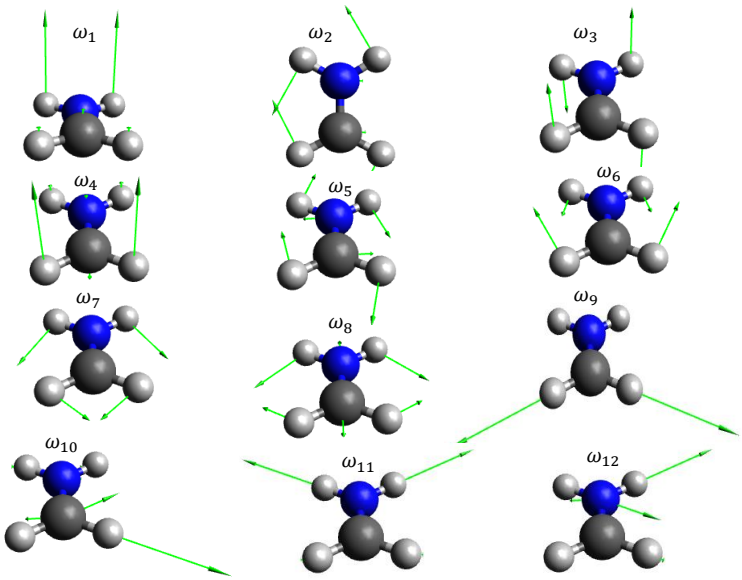

Figure I.16: Normal modes of $CH_2NH_2^+$. The arrows indicate the direction and magnitude of displacements for each mode. Note that arrowheads are not shown for the displacements of relatively large magnitudes. Vibrational frequencies and symmetries are listed in Table 2 of Ref.[Yuen et al., 2019].

Protonated methanimine $CH_2NH_2^+$ acts as a precursor of simple amino acids. It is formed in ISM after proton transfer reaction with methanimine CH_2NH_2 and HCO^+, H_3^+ or H_3O^+. Other $CH_2NH_2^+$ formation routes exist, such as the rapid reaction CH_2 with NH_3^+ giving [Anicich, 1993]. Methanimine and protonated methanimine are also important in the upper atmosphere of Titan, the massive moon of Saturn. It was detected by the Ion and Neutral Mass Spectrometer (INMS) on-board Cassini orbiter [Vuitton et al., 2006]. Once formed, $CH_2NH_2^+$ can undergo DR and, indeed, this is the only destruction pathway of $CH_2NH_2^+$ considered in the two most popular databases of astrochemical networks: KIDA [Wakelam et al., 2012] and UMIST [McElroy et al., 2013]. We are yet to obtain experimental or theoretical data about the DR of $CH_2NH_2^+$. The rate coefficient of this process was generally estimated using data on complex hydrocarbon ions. Consequently, a reliable value for the rate coefficient of the $CH_2NH_2^+$ DR is needed for chemical modeling.

Analogous to BF_2^+, $CH_2NH_2^+$ requires a highly-energetic incoming electron to form a doubly-excited resonant dissociative state of the neutral CH_2NH_2 throughout the process

$$e^- + CH_2NH_2^+ \rightarrow CH_2NH_2^* \rightarrow CH_2NH_2^{**} \rightarrow \begin{cases} CH_2NH + H \\ CH_2 + NH_2 \\ HCN + H_2 + H \\ CN + H_2 + H_2 \\ H_2CN + H + H \\ HNC + H + H_2 \end{cases}, \tag{I.34}$$

where a summary of the recommended rate coefficients and branching ratios for the above reactions is provided in Table 1 of Ref.[Yuen et al., 2019]. At low-energy, however, the electron is likely to be captured in a Rydberg level CH_2NH^*, strongly predissociated by CH_2NH^{**}, associated with a vibrationally excited state of CH_2NH^+. Again, in environments of low temperatures, such as ISM, the indirect process becomes dominant with the direct DR retaining negligible contributions to the total DR process. We will thus shift the focus on the IDR which is in competition with vibrational transitions

$$e^- + CH_2NH_2^+(v_i) \rightarrow e^- + CH_2NH_2^+(v_i'). \tag{I.35}$$

$CH_2NH_2^+$ is a closed-shell ion belonging to the C_{2v} point group at its equilibrium, with the ground state electronic configuration

$$X\ ^1A:\ 1a_1^2 2a_1^2 3a_1^2 4a_1^2 1b_2^2 5a_1^2 2b_2^2 1b_1^2. \tag{I.36}$$

Although there are 12 degrees of freedom for $CH_2NH_2^+$ internal motion (see Figure I.16), the formalism for indirect DR developed for BF_2^+ in Chapter III can be applied in a straightforward manner. Recall that the theoretical approach combines the normal modes approximation for the vibrational states of the target ion (described in Section II.2.A) and use of the R-matrix code to evaluate e^-−$CH_2NH_2^+$ scattering matrices, from Eq.(I.4), for fixed geometries of $CH_2NH_2^+$.

First, we computed the frequencies of the normal modes using a large active space CAS(12,10), i.e. 12 electrons distributed in 10 orbitals, and `cc-pVQZ` basis set. The obtained data such as frequencies and symmetries of the 12 vibrational modes are provided in [Yuen et al., 2019]. Secondly, we performed R-matrix calculations using identical parameters to the above and obtained the fixed-nuclei energy-independent scattering matrices, evaluated for two values of q_i keeping the other normal coordinates $q_{i'}$ fixed at $q_{i'} = 0$. Figure I.17 shows the eigenphases sums of the system e^-−$CH_2NH_2^+$ for different irreducible representations at the equilibrium position of the target ion. Eigenphases are smooth below 2.5 eV, where the first electronic resonance appears for the $^2A_1$ state. The absence of electronic resonances at low collision energies justifies the indirect DR approach.

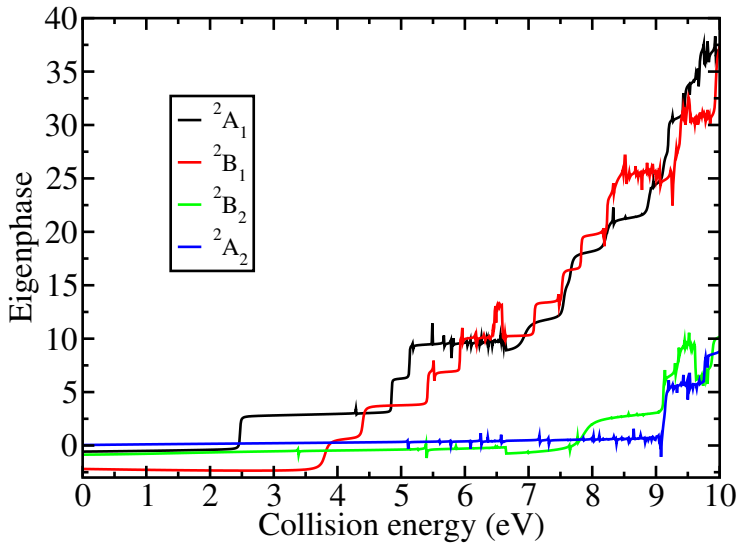

Figure I.17: Energy-dependence of eigenphases of different irreducible representations for the $CH_2NH_2^+ + e^-$ collisions.

With the formula of Eq.(III.12) and the summation extended to 12 normal modes, we calculated the DR cross section for $CH_2NH_2^+$ in its vibrationally ground state as a function of collision energy ϵ. Figure I.18 shows at low energies that the obtained DR cross section is featureless and behaves simply as $1/\epsilon$. This can be viewed as a DR cross-section averaged over the vibrational autoionizing resonances. Such a result could be justified by the fact that the experimental/observation resolutions (storage-ring or merged-beam experiments) are too low to resolve individual Rydberg resonances in the DR spectra. For energies above 0.1 eV, the cross section drops in stepwise manner because the scattering electron excites the vibrational level of the ionic target by one quanta and leaves with a smaller kinetic energy.

Fitting the probabilities of Figure 2 in Ref.[Yuen et al., 2019], rate coefficients can be computed analytically, assuming the collision energy follows Maxwell-Boltzmann distribution, as

$$\alpha_{v_i}^{VE}(T) = \sqrt{2\pi}(v_i+1)\frac{\hbar^2}{m_e^{3/2}}\left[\left(a_i + \hbar\omega_i b_i + (\hbar\omega_i)^2 c_i\right)/\sqrt{k_bT}\right.$$
$$\left. + \left(b_i + 2\hbar\omega_i c_i\right)\sqrt{k_bT} + 2c_i(k_bT)^{3/2}\right]\exp\left(-\frac{\hbar\omega_i}{k_bT}\right), \tag{I.37}$$

$$\alpha_{v_i}^{VdE}(T) = \sqrt{2\pi}v_i\frac{\hbar^2}{m_e^{3/2}}\left[\frac{a_i}{\sqrt{k_bT}} + b_i\sqrt{k_bT} + 2c_i(k_bT)^{3/2}\right], \tag{I.38}$$

and

$$\alpha_{v_i}^{DR}(T) = \sqrt{2\pi}\frac{\hbar^2}{m_e^{3/2}}\sum_i^{12}(v_i+1)\Bigg\{2c_i\left[1-\exp\left(-\frac{\hbar\omega_i}{k_bT}\right)\right](k_bT)^{3/2}$$
$$+\left[b_i-(b_i+2\hbar\omega_i c_i)\exp\left(-\frac{\hbar\omega_i}{k_bT}\right)\right]\sqrt{k_bT}$$
$$+\left[a_i-(a_i+\hbar\omega_i b_i+(\hbar\omega_i)^2 c_i)\exp\left(-\frac{\hbar\omega_i}{k_bT}\right)\right]/\sqrt{k_bT}\Bigg\}, \quad \text{(I.39)}$$

where a_i, b_i and c_i are the fitted parameters from Table 3 in the same reference.

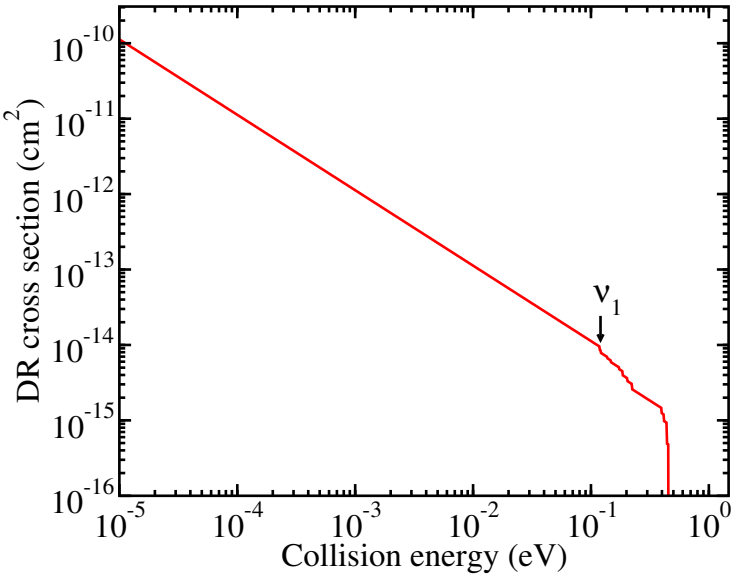

Figure I.18: The DR cross section as a function of the collision energy. For energies above 0.1 eV one or several vibrationally-excited channels are open. As a result, the DR cross section decreases in a stepwise manner.

Figure I.19 displays the thermally averaged VE and DR rate coefficients as functions of temperature for the initial ground vibrational state, $v_i = 0$. For low temperatures, $T < 400$ K, the rate coefficients behave as $1/\sqrt{T}$. Since the exponent factor $\exp(-\hbar\omega_i/k_bT)$ is much smaller than 1, the DR rate coefficient can be approximated as $4.65 \times 10^{-7}(300/T)^{0.5}$ cm^3/s.

As discussed previously, there are two main identifiable sources of uncertainty in the DR and VE rate coefficients obtained above. The most important source lies in the autoionization competitive process. Indeed, in our simplified model, once the electron is captured into a vibrational Rydberg resonance associated with a closed vibrationally-excited channel, the $e^- - CH_2NH_2^+$ system will dissociate rather than autoionize. In a previous studies dealing with smaller molecular ions such as H_3^+, HCO^+, NH_4^+, H_3O^+, CH^+ [Mikhailov et al., 2006b, Douguet et al., 2012b, Douguet et al., 2012a, Fonseca dos Santos et al., 2014], it was estimated that the probability of autoionization of vibrational Rydberg resonances in these closed-shell ions is of the order of 10-20% compared to the probability of dissociation. For

larger ions, the probability should be smaller and hence it is reasonable to assume that the corresponding uncertainty in the present DR calculations is below 20%.

To assess the second type of uncertainties related to the scattering model, we varied several parameters such as basis sets and complete active spaces. Table I.3 lists the three sets of parameters. The differences between results obtained in the three models are 1-2%. Therefore, the uncertainty due to the scattering model is negligible, with respect to the capture approximation and the overall uncertainty of the present theoretical rate coefficients, and is estimated to be below 20%.

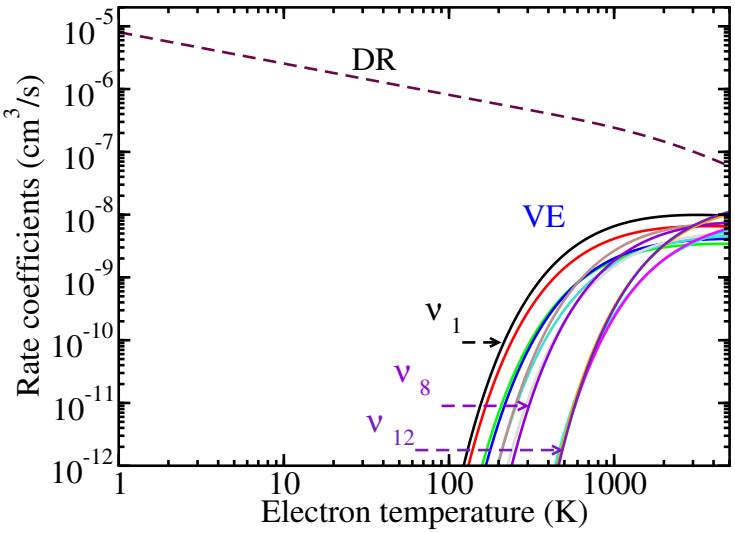

Figure I.19: The DR (dashed line) and VE (solid lines) rate coefficients for target ion $CH_2NH_2^+$ in the ground vibrational. To avoid overcrowded labeling in the figure, labels for three VE curves only are given. The lines for all VE rates cross the abscissa in the order of increasing number labeling the modes (and increasing energy) as in Table 2 of Ref.[Yuen et al., 2019]. For $T < 400$ K, the DR and VE rate coefficients behave as $T^{-1/2}$ and $T^{-1/2} \exp(-\hbar\omega_i/k_bT)$ respectively. At higher temperatures, as vibrational excitation becomes more probable, the DR rate coefficient decreases faster than $T^{-1/2}$.

To summarize, the first value for the total DR cross section and thermally averaged rate coefficient of $CH_2NH_2^+$ were briefly reported. The implications of the present calculations in the chemistry of extraterrestrial environments are important since the obtained value is consistent with the two most popular astrochemical data basis, KIDA, and UMIST but much smaller for $T < 400$ K than the value used in photochemical models of the upper atmosphere of Titan. This has in fact an impact on Titan ammonia abundance in the model. These results, however, provide an upper limit for the total rate coefficient of the $CH_2NH_2^+$ DR. See discussion in Ref.[Yuen et al., 2019].

Model	$C_1(\omega_3)$	$C_s(x=0)(\omega_2,\omega_5,\omega_{10},\omega_{12})$	$C_s(y=0)(\omega_1,\omega_4)$
1	cc-pVTZ	cc-pVQZ	cc-pVQZ
	$(5a\|6a)$	$(2a',0a''\|8a',2a'')$	$(2a',0a''\|7a',3a'')$
2	cc-pVTZ	cc-pVTZ	cc-pVTZ
	$(5a\|6a)$	$(2a',0a''\|8a',2a'')$	$(2a',0a''\|7a',3a'')$
3	cc-pVTZ	cc-pVQZ	cc-pVQZ
	$(5a\|6a)$	$(2a',0a''\|8a',2a'')$	$(2a',0a''\|7a',3a'')$

Model	$C_{2v}(\omega_6,\omega_7,\omega_8,\omega_9,\omega_{11})$
1	cc-pVQZ
	$(4a_1,0b_1,1b_2,0a_2\|2a_1,2b_1,2b_2,0a_1)$
2	cc-pVTZ
	$(4a_1,0b_1,1b_2,0a_2\|2a_1,2b_1,2b_2,0a_1)$
3	cc-pVQZ
	$(2a_1,0b_1,0b_2,0a_2\|5a_1,2b_1,3b_2,0a_1)$

Table I.3: Parameters of three different scattering models. Different basis and electronic configurations are used for normal modes with different point group symmetries. The symbols in the parenthesis indicates the number of frozen orbitals and number of active orbitals.

I.6 Concluding remarks

This chapter outlines my contribution to the study of the molecular ions destruction mechanisms in astrophysical environments. Two main developments were achieved within this research axis. First, a theoretical approach for electron-impact rovibrational excitation of molecular ions was developed and applied to the HeH^+ benchmark system. Second, this approach was adapted to molecular ions with low-lying excited electronic states like CH^+. With some additions whose details were deferred to Chapter III, these approaches were extended to more complicated systems such as prebiotic molecules NH_2CHOH^+ and $CH_2NH_2^+$ that play an important role in the chemistry of ISM and the upper planetary atmospheres.

Our theoretical studies have allowed us to investigate the main mechanisms of destruction and/or formation of these ions in low collisional energy, namely, direct and indirect DR that are in competition with autoionization, viz. rovibronic excitation and (de-)excitation processes. These studies have also enabled, on the one hand, to provide an upper limit for the total rate coefficient of DR, where data are not available ($CH_2NH_2^+$ case), on the other hand, to confirm previous calculations as for HeH^+ and CH^+. The obtained cross sections and related rate coefficients could be used in kinetic modeling of cold ionized media such as ISM.

The above works have been supported by different programs and funding listed in CV (see Appendix V.2.C). They have also been performed in the context of three thesis: Dr. Marjan Khamesian, Dr. Chi Hong Yuen and Dr. Xianwu Jiang. They result in at least height peer-reviewed articles. The following chapter pursues these studies to include neutral molecules.

II – Role of collisions involving electron-neutral molecules and electron-radicals

II.1 Context and Motivations

Neutral molecules and radicals play an important role in plasma discharges. They are mostly formed by surface processes on the walls and then involved in a volumetric chemical chain reactions with other species. Typically, neutral molecules are formed in excited states and radicals are well-known to be unstable in collisions with other species present nearby. Consequently, for both systems an experimental approach is difficult or impossible and data are needed for reactions taking place on the surfaces but also in the phase-gas [Pelicon and Razpet, 2003].

This chapter focuses on two type of neutral molecules NO_2 and N_2O. These species are involved in a number of different chemical pathways in the atmosphere leading to a large variety of species. They also play a role in a non-equilibrium kinetics of plasmas containing N_2 and O_2 that are used for plasma based technologies and depollution purposes. Understanding/validation of the fundamental kinetic mechanisms for these molecules remains limited. This relies partially on the availability of the cross-section data of elementary processes, in particular to the rovibrational-dependent electron impact excitation/(de-)excitation data, which is very sparse.

Our following studies aim to fill, at least partially, this gap and provide reliable cross sections for electron-induced vibrational excitation of NO_2 and NO_2. Cross sections and rate coefficients for transitions between different vibrational states of the targets are reported and compared to available experimental data. The rotational structure of each vibrational level of the targets was neglected which corresponds to the situation where rotational structure is not resolved in the initial and final states of the target molecule. A more comprehensive study will be considered in a near future (see Chapter V).

The main results of this chapter were obtained in the context of Dr. Hainan Liu's dissertation at Centralesupélec in collaboration with Prof. Viatcheslav Kokoouline at UCF and Dr. Samantha Fonseca Dos Santos at Rollins College. They have been published in two papers whose the one on N_2O is included in this manuscript.

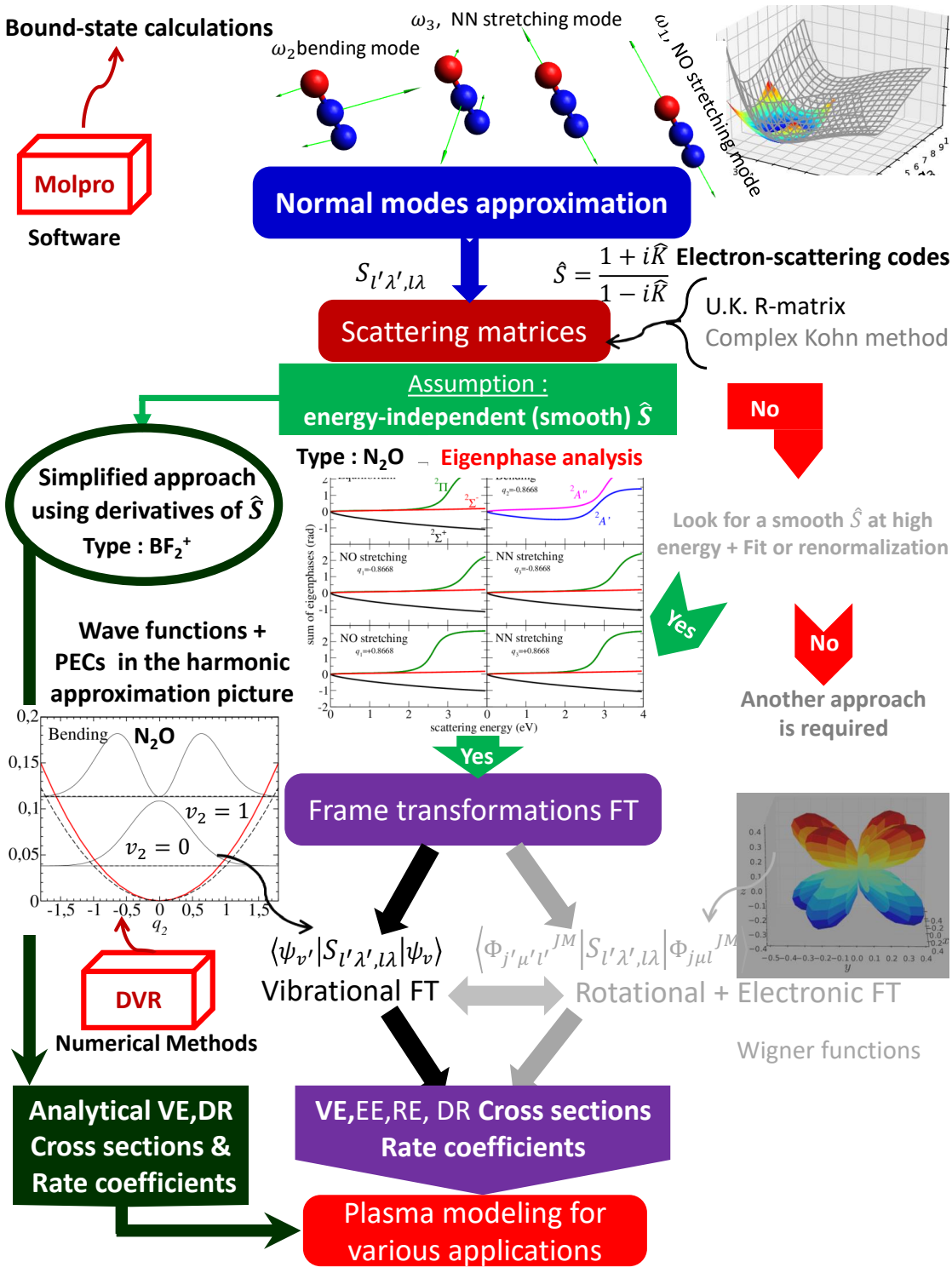

Figure II.1: The flow chart of different ingredients employed in the theoretical model developed for the description of vibrational (de-)excitation (VE) as well as dissociative recombination (DR) of polyatomic molecular ions such as NO_2, N_2O, $CH_2NH_2^+$ (described in Chapter I) and BF_2^+ (described in Chapter III). The following abbreviations are used. FT: frame transformation. DVR: discrete variable representation. Tasks or methods in non-bold text are not performed in this HDR yet.

II.2 Theoretical method developed on neutral molecules

Similar to molecular ions discussed in the preceding chapter, theoretical models employed in the studies of Section II.4 are based on first-principles. They require three main ingredients summarized in Figure II.1. A brief description is given below.

II.2.A Normal modes approximation

In calculations of the cross section for vibration (de-)excitation of Section II.4, one needs the vibrational wave functions of the target in order to construct elements of the scattering matrix for transition from one vibrational level v to another v'.

For polyatomic molecules, one can expand the potential energy V in a multi-dimensional Taylor expansion truncated at second order around equilibrium. The nuclear Schrödinger equation for an N atom system writes as

$$\left[-\sum_{i}^{3N}\frac{\hbar^2}{2m_i}\frac{\partial^2}{\partial x_i^2}+\frac{1}{2}\,{}^t(\mathbf{x}-\mathbf{x}_{\rm eq})\frac{\mathrm{d}^2V}{\mathrm{d}\mathbf{x}^2}(\mathbf{x}-\mathbf{x}_{\rm eq})\right]\psi(\mathbf{x})=E\psi(\mathbf{x}), \tag{II.1}$$

where N is the atoms number, m_i is the atomic mass and $\mathbf{x}=\{x_1x_2x_3\cdots x_{3N}\}$ is a vector containing the $3N$ components of coordinates of all nuclei. $\mathbf{x}_{\rm eq}$ defines the equilibrium structure and $\psi(\mathbf{x})$ is the nuclear wave function. Above, E stands for the total energy of the molecule, i.e. including translational, vibrational and rotational energies.

Defining the mass-weighted coordinates

$$\tilde{x}_i=\sqrt{m_i}\,(x_i-x_{eqi})\Rightarrow\frac{\partial^2}{\partial\tilde{x}_i^2}=\frac{1}{m_i}\frac{\partial^2}{\partial x_i^2}, \tag{II.2}$$

Equation (II.1) can be solved merely under the following form

$$\left[-\sum_{i}^{3N}\frac{\hbar^2}{2}\frac{\partial^2}{\partial\tilde{x}_i^2}+\sum_{i,j}^{3N}\frac{1}{2}\mathcal{H}_{ji}\tilde{x}_i\tilde{x}_j\right]\psi(\tilde{\mathbf{x}})=E\psi(\tilde{\mathbf{x}}). \tag{II.3}$$

where $\mathcal{H}_{ij}$ defines the mass-weighted Hessian, also called matrix of force constants:

$$\mathcal{H}_{ij}=\frac{1}{\sqrt{m_i}\sqrt{m_j}}\frac{\partial^2V}{\partial x_i\partial x_j}. \tag{II.4}$$

This matrix of the second derivatives of the potential energy plays a central role in energy minimization techniques.

Looking for a matrix $\mathbf{D}$ that diagonalizes the mass-weighted Hessian, the second term in the left-hand side of Equation (II.3) can be reshaped as

$$\sum_{i,j}^{3N}\frac{1}{2}\mathcal{H}_{ji}\tilde{x}_i\tilde{x}_j=\frac{1}{2}\,{}^t\mathbf{Q}\left(\mathbf{D}^{-1}\mathcal{H}\mathbf{D}\right)\mathbf{Q}, \tag{II.5}$$

where $\mathbf{Q}$ designates the set of $3N$ eigenvectors associated to $3N$ eigenvalues ω_i^2 [Janežič et al., 1995]. $\mathbf{D}$ above is a transformation matrix from mass-weighted Cartesian coordinates to a set of $3N$ coordinates including the translation, rotation and vibration degrees of freedom.

In quantum chemistry softwares such as Molpro or Gaussian, the eigenvectors $\mathbf{Q}$, i.e. the normal modes, are calculated after separating out the rotational and translational normal modes leaving $3N-6$ or $3N-5$ modes for vibrational analysis. The eigenvalues ω_i^2 are the fundamental frequencies of the molecule. For rotation and translation modes they should be close to zero. More details can be found in Ref.[Frisch, 2004].

Generally, it is convenient to introduce a new set of coordinates called *dimensionless normal coordinates* that are related to the length-unit normal coordinates Q_i as follows

$$q_i = Q_i \sqrt{\frac{\mu_i \omega_i}{\hbar}}. \tag{II.6}$$

where ω_i and μ_i are the frequency and reduced mass of the ith mode, respectively. Hence, Equation (II.3) can be written for vibrational normal modes as

$$\begin{array}{rcl} [T(\mathbf{q}) + V(\mathbf{q})]\,\psi(\mathbf{q}) & = & E\psi(\mathbf{q}) \\ \sum_i^{3N-6(5)} \frac{\hbar\omega_i}{2}\left[-\frac{\partial^2}{\partial q_i^2} + q_i^2\right]\psi(\mathbf{q}) & = & E\psi(\mathbf{q}), \end{array} \tag{II.7}$$

where E denotes here the vibrational energy of the molecule in the uncoupled harmonic-oscillator approximation

$$E = \sum_i^{3N-6(5)} \left(v_i + \frac{1}{2}\right)\hbar\omega_i, \tag{II.8}$$

associated to the following normalized wave function

$$\psi(\mathbf{q}) = \prod_i^{3N-6(5)} \eta_{v_i}(q_i), \tag{II.9}$$

with $\eta_{v_i}(q_i)$ representing the harmonic vibrational function with v_i quanta and corresponding vibrational frequency ω_i, reduced mass μ_i and dimensionless normal coordinate q_i.

With the above expressions in hand, we can perform the vibrational transformation in Eq.(II.17) according to the well-known formula

$$\eta_{v_i}(q_i) = \left(\frac{1}{\pi}\right)^{\frac{1}{4}} \frac{1}{\sqrt{2^{v_i} v_i!}} \mathrm{e}^{-\frac{{q_i}^2}{2}} H_{v_i}(q_i). \tag{II.10}$$

where H_{v_i} is the Hermite polynomials. For example, the normalized wave function of the ground vibrational state is

$$\eta_{v_i=0}(q_i) = \left(\frac{1}{\pi}\right)^{\frac{1}{4}} \mathrm{e}^{-\frac{{q_i}^2}{2}}, \tag{II.11}$$

associated to the zero-point energy $\frac{\hbar\omega_i}{2}$.

In our studies, we employed Molpro [Werner et al., 2008] to obtain the frequencies ω_i and the equilibrium geometry of the molecules throughout the Hessian matrix elements of Eq.(II.4). The matrix $\mathbf{D}$ enables to generate Cartesian displacements, $\mathbf{X} = \mathbf{Dq}$, along each normal coordinate that are used to perform scattering matrix calculations in the following section and then to compute the integral in Equation.(II.17). Permanent dipole moments of the molecules are also intermediate quantities useful to check the convergence of the final results, viz. cross sections and rate coefficients.

The normal mode approximation employed in this chapter is accurate for the lower vibrational levels. From the classical point of view, as v_i increases, the nuclei spend more time in regions far from their equilibrium separation. For such regions the potential energy deviates substantially from that of a harmonic oscillator and the harmonic-oscillator approximation tends to become poor. Therefore, the developed theoretical approach can be applied for vibrational transitions involving few quanta in each mode.

II.2.B The *ab initio* R-matrix method

Since a more detailed discussion on the R-matrix method is provided in Section I.3.A, I sketch below only the main difference.

Again, the R-matrix method (see upper panel of Figure I.2) involves the division of the configuration space into an inner region where a molecular ($N-$electrons targets+the scatterer) bound state is solved, and an outer region with an long range multipolar expansion of the form

$$V_{ij} = \sum_{\alpha=0} \frac{\mathcal{C}_{ij}^{(\alpha)}}{r^{\alpha+1}}, \tag{II.12}$$

where $\mathcal{C}_{ij}^{(\alpha)}$ is the asymptotic potential coefficient of order α between i and j channels. This coefficient is given by [Burke et al., 1977]:

$$\mathcal{C}_{ij}^{(\alpha)} = \sqrt{\frac{2l_i+1}{2l_j+1}} C_(l_i, \alpha, l_j; \lambda_i, \lambda_\alpha, \lambda_j) C(l_i, \alpha, l_j; 000) Q_{ij}^{(\alpha)}, \tag{II.13}$$

with l_j being the orbital angular momentum of the scattering electron for the ith channel and $C(l_i, \alpha, l_j; \lambda_i, \lambda_\alpha, \lambda_j)$ the Clebsch-Gordon coefficient. $Q_{ij}^{(\alpha)}$ is the target moment between the channels i and j such as if $i = j$, it corresponds to a permanent moment, and for $i \neq j$ it is a transition moment. In general, only the first few terms in the expansion over α play a significant role in the collision in the outer region. For neutral molecules such as NO_2 and N_2O, α is 1 which corresponds to the interaction between the charge of electron and the dipole moment of the target molecules.

Once the wave functions are generated in the inner region, the R-matrix is constructed at the boundary $r = a$ for a given scattering electron energy ϵ and it is propagated toward the outer region (see Eq.(23) of Ref [Tennyson, 2010]) where the radial scattering electron wave

function can be matched at the boundary $r = a_{asy} \simeq 70$ bohr (such that coupling potentials to be negligible) to Bessel functions

$$F_{ij}^{\Gamma}(r) \sim \begin{cases} \frac{1}{\sqrt{k_i}} \left(\sin\theta_i(r)\delta_{ij} + \cos\theta_i(r) K_{ij}^{\Gamma}(\mathbf{q}) \right) & \text{if } \epsilon_i \geq 0 \\ 0 & \text{otherwise} \end{cases} \tag{II.14}$$

where

$$\theta_i(r) = k_i r - \frac{l_i \pi}{2}, \tag{II.15}$$

and index i refers to the entrance channel before a collision and j refers to the outgoing channel after the collision. $K_{ij}^{\Gamma}(\mathbf{q})$ above are the elements of the reactance matrix [Aymar et al., 1996, Tennyson, 2010] depending on the dimensionless normal coordinates $\mathbf{q} = \{q_1, q_2, \cdots\}$ parametrically and obtained for each scattering electron energy ϵ. Recall, Γ denotes the constants of motion corresponding to the irreducible representation of the molecular point group, in particular the total angular momentum projections Λ of the anion system (electron-molecule).

Finally, in the cross section calculation, the scattering matrix $\mathbf{S}^{\Gamma}(\mathbf{q})$ is needed and can be obtained from

$$\mathbf{S}^{\Gamma}(\mathbf{q}) = (\mathbf{1} + \imath\mathbf{K}^{\Gamma}(\mathbf{q}))(\mathbf{1} - \imath\mathbf{K}^{\Gamma}(\mathbf{q}))^{-1}\,, \tag{II.16}$$

at a given geometry $\mathbf{q}$, similar to Eq.(I.4). The eigenphase sums is another observable, defined from these matrices through Eqs.(I.5), which is very useful for testing the validity of our theoretical approach. These key points will be discussed in Section II.3.

II.2.C Vibrational frame transformation

The application of the frame transformation procedures was discussed in Sections I.2 and I.3. It relies on the assumption that the strength of couplings between the scattering electron and vibrational states v of the target are small compared to the interaction potential $V(r)$ experienced by the incident electron. As we have seen, this assumption remains valid for ions even at low collisional energy because of Coulomb asymptotic behavior in $V(r)$. In case of neutral molecules, the situation is less obvious. More remarks are differed to the next section.

Assuming $\epsilon_v \approx \epsilon_{v'}$ and a smooth scattering matrices along each dimensionless normal coordinates, one can employ the procedure of frame transformation

$$\mathcal{S}_{v'v} = \sum_{\lambda' l', l\lambda} \left\langle \psi_{v'}(\mathbf{q}) \left| S^{\Lambda}_{\lambda' l', \lambda l}(\mathbf{q}) \right| \psi_v(\mathbf{q}) \right\rangle\,, \tag{II.17}$$

where the matrix element $S^{\Lambda}_{l'\lambda', l\lambda}(\mathbf{q})$ is obtained from the R-matrix calculations above, and v and v' denote the collection of initial and final vibrational quantum numbers of all the normal modes. The brackets in Eq.(II.17) imply an integration over the vibrational coordinates where the vibrational wave functions are given in the harmonic approximation picture by Eq.(II.9).

In the studied cases of Section II.4, the integral above is computed numerically using a Gaussian-Legendre quadrature with 10 points.

II.3 Validity of the theoretical model

As hinted in Section I.4, there are two main identifiable sources of uncertainty [Chung et al., 2016]. One is related to the uncertainties of the theoretical model often employing reduced dimensionality or neglecting competitive processes. A second type of uncertainties relies on the choice of parameters of the model such as the use of limited basis set or *ab initio*/fitted data. Both uncertainties will be assessed in NO_2 and N_2O studies of Section II.4.

In addition to the above uncertainties, the validity of the model developed for neutral molecules is mainly based on the circumstance of applying the frame transformation procedure in Eq.(II.17). Indeed, the attractive potential $V(r)$ decays faster than the centrifugal barrier, $\frac{l(l+1)}{2r^2}$ (in bohrs), in case of neutral targets, according to Eq.(II.15). In a such situation, the local kinetic energy of electron in Eq.(I.6) is independent on r at the edge of the R-matrix simulation box, i.e. $\epsilon_{vj} \sim 0.003$ eV at $r = 100$ bohrs for $V(r)$ behaving as $1/r^2$ for instance. Thus, $\epsilon_{vj} \approx \epsilon_{v'j'}$ can be fulfilled outside $r = 100$ bohrs only if the scattering energy is large enough, compared to the spacing between vibrational levels, such that the entire region of r can be considered here as the $q-$region (see lower panel of Figure I.2).

The above condition on ϵ_{vj} is consistent with an energy-independent scattering matrix. In general, $S(q)$ depends on the scattering energy especially for neutral targets. To overcome this difficulty, (1) one can use a smooth $S(q)$, if possible, as done in the preceding studies for target ions (HeH^+ or $CH_2NH_2^+$) or (2) choose a different normalization factor for the scattering wave function to remove the energy-dependence of $S(q)$ [Greene et al., 1979, Greene et al., 1982, Greene and Jungen, 1985]. This later suggestion is reserved for future study (see Chapter V).

In our following studies, the scattering electron energy is (i) chosen so as to not be so large to excite the target electronically and (ii) also below of electronic resonances appearing when the potential energy surface (PES) of the anionic molecule (electron-molecule system) crosses the neutral PES near the equilibrium geometry. Moreover, as we will see, a detailed analysis of enigenphase sums of e^-NO_2 and e^--N_2O collisions reveals that $S(q, \epsilon_v) \approx S(q, \epsilon_{v'})$. Hence, the vibrational frame transformation can be accomplished here directly without further development (refereed above as point (2)).

II.4 Applications

As a demonstration, we applied the theoretical approach described above to neutral species such as NO_2 and N_2O of atmospheric interest. Details on these studies, performed by Hainan Liu in her thesis at Centralesupélec, can be found in Refs.[Liu et al., 2019, Liu et al., 2020]. Below, I will underline only the major ideas and results in particular for the N_2O study whose the article is included to this manuscript as paper .6.

II.4.A Electron-induced vibrational excitation of NO_2

The nitrogen dioxide (NO_2) molecule has a number of applications in engineering and science. For instance, it is used in the sterilization of medical instruments [Shomali et al., 2015a]. It

plays a major role in the middle and upper atmosphere by the chemiluminescent emission process [Clough and Thrush, 1967]. NO_2 is also well-known to be an undesirable pollutant in the troposphere such as recent plasma technologies are used for its removal. Knowledge of physical and chemical processes taking place in NO_2 plasma especially collisions electrons and NO_2 molecules are of great importance in improving process efficiency in these technologies.

Electron collisions with the NO_2 molecule have been extensively investigated in the past, with initial studies focusing on the NO_2 ionization [Collin, 1959, Kiser and Hisatsune, 1961, Stephan et al., 1980]. In more recent studies, other processes in the e^-–NO_2 collisions were reported. We can cite, for example, the measurements of absolute total cross sections for electron-NO_2 collisions by Ref.[Szmytkowski and Krzysztofowicz, 1992] or those of dissociative electron attachment (DEA) to NO_2 as a mechanism on negative-ion formation from the groups [Fox, 1960] and [Rangwala et al., 2003]. Munjal *et al.* [Munjal et al., 2009] reported theoretical data on elastic integral, differential, momentum transfer cross sections, as well as electronic-excitation cross sections from the ground electronic state to the five lowest electronically excited states of NO_2.

As for electron-impact vibrational excitation (VE) of NO_2, only little information is available while this process plays an important role in plasma depollution because vibrationally excited NO_2 react differently, compared to the ground-state NO_2, with other species present in the plasma. To the best of our knowledge, there exist only one measurement on VE cross sections for energies $0.3 \sim 2.5$ eV by Benoit and Abouaf [Benoit and Abouaf, 1991]. No theoretical VE study of NO_2 has been reported until now. As excitation of different modes having almost the same fundamental frequencies cannot be separated experimentally, at least by the conventional technique, the theoretical treatment for the VE of NO_2 is indeed necessary.

Combining the normal mode approximation for vibrational states of the target molecule (Eq.(II.7)), fixed-nuclei electron-NO_2 scattering matrices (Eq.(II.16)) and the vibrational frame transformation (Eq.(II.17)) employed to evaluate the scattering matrix for vibrational transitions, we provided cross sections for VE,

$$e^- + NO_2(v_i) \rightarrow e^- + NO_2(v_i'), \tag{II.18}$$

and corresponding thermally-averaged rate coefficients. Above, the quantum number v_i and v_i' stand for the initial and final vibrational state of the target for normal mode i. The reaction channel for which $v_i = v_i'$ corresponds to elastic scattering. Systematic calculations were performed for the excitation of the 3 lowest excited vibrational levels in the ground electronic state of NO_2. For higher vibrational states, processes such as DEA become more predominant than vibrational excitation.

The *ab initio* calculations

NO_2 is an open-shell molecule belonging to the C_{2v} point group at its equilibrium, with the ground state electronic configuration

$$X^2A_1 : 1a_1^2 2a_1^2 1b_2^2 3a_1^2 2b_2^2 4a_1^2 5a_1^2 3b_2^2 1b_1^2 4b_2^2 1a_2^2 6a_1^1.$$

It is characterized by three normal modes of vibration: bending, symmetric stretching, and asymmetric stretching, displayed in Figure II.2. Displacements along the bending and symmetric stretching modes do not break the C_{2v} symmetry of the molecule, while the asymmetric stretching mode reduces the symmetry to the C_s group.

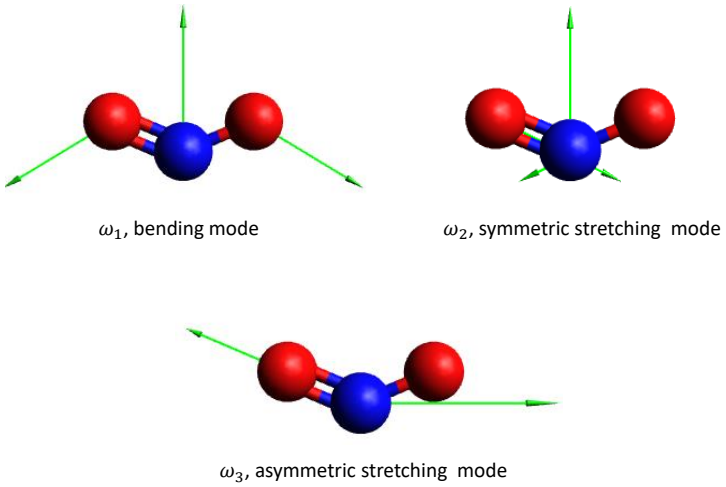

Figure II.2: Normal modes of NO_2. The arrows indicate the direction and magnitude of displacements for each mode. Note that arrowheads are not shown for the displacements of relatively large magnitudes. Vibrational frequencies and symmetries are listed in Table II.1.

The frequencies of the normal modes were computed with a complete active space self-consistent field method (CASSCF) of CAS(17,15), i.e. 17 electrons are distributed over 17 orbitals, and `cc-pVTZ` basis set using the *ab initio* quantum chemistry package Molpro [Molek et al., 2007]. Table II.1 lists the optimized geometry and vibrational frequencies obtained in the present calculation and compares the results with the available experimental data.

Table II.1: Structure and vibrational frequencies of NO_2 obtained in this study and compared with experimental data from Ref.[Johnson III, 2010]. ω_1, ω_2 and ω_3 are the frequencies of bending mode, symmetric stretching mode and asymmetric stretching mode, respectively.

	Bond (Å)	Angle(Degrees)	ω_1 (cm^{-1})	ω_2 (cm^{-1})	ω_3 (cm^{-1})
This work	1.204	133.95	756.66	1319.21	1625.86
Exp.	1.193	134.10	750.00	1318.00	1618.00

As the table demonstrates, the present results match excellently with the experiment. From the results of the frequencies calculation, we also obtained the transformation matrix, $\mathbf{D}$ of Eq.(II.5), between the normal and Cartesian coordinates. The matrix is needed to generate geometries input data from $\mathbf{X} = \mathbf{Dq}$ for electron-NO_2 scattering calculations.

Scattering calculations

In the scattering calculation, we used for several values of normal coordinates q_i an R-matrix sphere radius of 14 bohrs, the `cc-pVTZ` basis set and the complete active space configuration interaction (CAS-CI) method built on orbitals obtained from the same CASSCF calculation in Molpro. An accurate description of the target molecule is crucial in this model. Figure II.3 displays the potential energy surface of the ground state of NO_2 computed with the R-matrix code, where the surface is plotted along the three normal modes and compared with the harmonic potential energy. Almost no anharmonic contribution is observed for the bending (panel (a) in the figure) and asymmetric stretching (panel (c)) modes. The potential energy of the symmetric stretching mode is, however, slightly anharmonic as evident from panel (b) in the figure. The dipole moment of NO_2 obtained in this model is 0.317 D, which is in remarkably good agreement with the experimental value of 0.316 D [Leonardi et al., 1996].

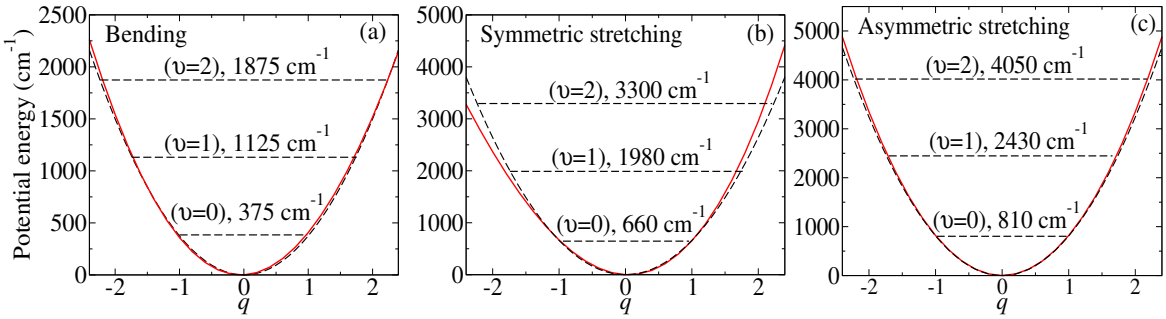

Figure II.3: Potential energy curves for the ground electronic state of NO_2 as a function of the (a) bending; (b) symmetric stretching; (c) asymmetric stretching modes. The abscissa axes in the figure represent dimensionless normal coordinates. In each panel, only one mode q_i is varied, while the other modes are kept fixed at their equilibrium positions $q_{i'} = 0$. Red solid curves are the actual potential energies obtained from the UKRmol suite, while black dashed curves represent energies calculated in the harmonic approximation. Horizontal dashed lines denote energies of vibrational states.

Cross sections and rate coefficients

Taking an average over initial rotational states and a sum over final rotational states in the process, i.e. neglecting the rotational structure of the molecule, the cross section for VE of the mode i is expressed as

$$\sigma_{v_i' \leftarrow v_i}(\epsilon) = \frac{\pi\hbar^2}{2m\epsilon} \left| \mathcal{S}_{v_i' v_i} - \delta_{v_i' v_i} \right|^2 , \tag{II.19}$$

where again ϵ is the energy of the incident electron and m is the mass of electron. The computation of the scattering matrix $\mathcal{S}_{v_i' v_i}$ for VE relies on the vibrational frame transformation of Eq.(II.17).

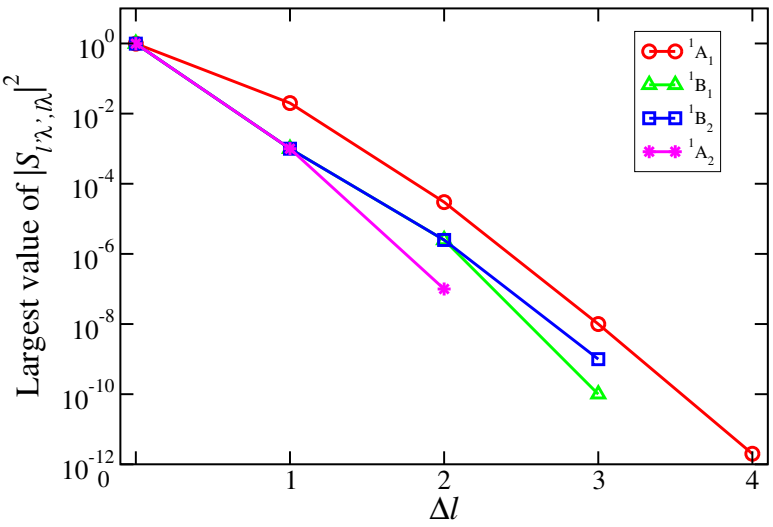

Figure II.4: The largest value of $\left|S_{l'\lambda',l\lambda}\right|^2$ with respect to all possible allowed combinations of $l\lambda, l'\lambda'$ as a function of the difference $\Delta l = l' - l$ for all four singlet irreps of the e^-–NO_2 complex. The lowest value of l is 0 for $^1A_1$, 1 for $^1B_1$ and $^1B_2$, 2 for $^1A_2$. For $^1A_1$ (solid red line with circles), the couplings between the s and f, s and g partial waves are very small. For $^1B_1$ (solid green line with triangles) and $^1B_2$ (solid blue line with squares), since s-wave scattering is forbidden by symmetry, only couplings between p, d, f and g partial waves is shown. For $^1A_2$ (solid pink line with stars), s and p partial waves scattering is not allowed.

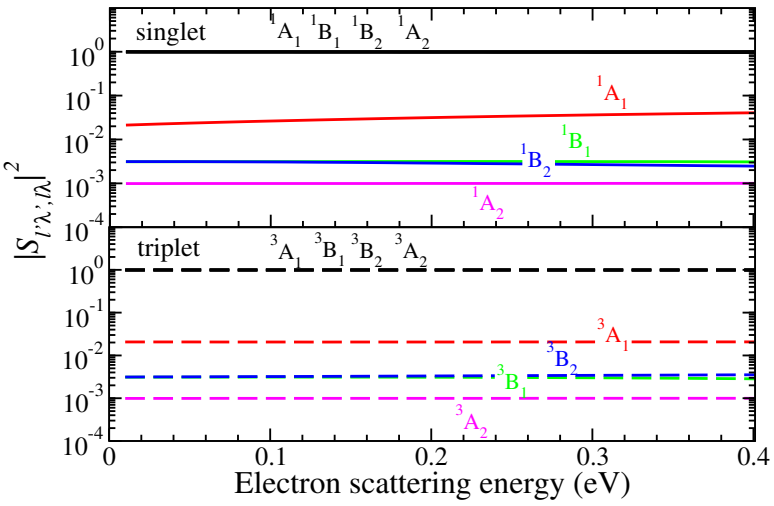

Figure II.5: The figures shows dominant (absolute value squared) elements $\left|S_{l'\lambda',l\lambda}\right|^2$ of the scattering matrix as a function of the electron scattering energy at the NO_2 equilibrium. Black lines: coupling between channels with $\Delta l = 0$. Color lines: coupling between channels with $\Delta l = 1$

As discussed in the preceding section, vibrational frame transformation treatment becomes feasible, at least in principle, only if the elements of the fixed-nuclei S-matrix for the $e^- - NO_2$ system are smooth with respect to the incident energy. Therefore, the treatment is not

appropriate if there are low-energy resonances in the $e^- - NO_2$ spectrum at low energies. In an attempt to analyze the behavior of S-matrix elements, we computed the absolute value squared $\left|S_{l'\lambda',l\lambda}\right|^2$ (Λ is omitted hereafter for the sake of simplicity) of the matrix elements as a function of the electron scattering energy at the equilibrium geometry. Figure II.4 gives an idea about couplings between different partial waves in the scattering process. Here, singlet states are chosen as an example. Although five partial waves is included in the computation, only couplings between channels with $\Delta l < 2$ are not negligible for inelastic scattering. The contribution from the $\Delta l \geq 2$ couplings is modest.

Notably, the $\left|S_{l'\lambda',l\lambda}\right|^2$ coupling producing the dominant contribution to the inelastic process for each symmetry depends only weakly on the scattering energy, as shown in Figure II.5. Therefore, it is reasonable to employ the vibrational frame transformation for the VE calculations.

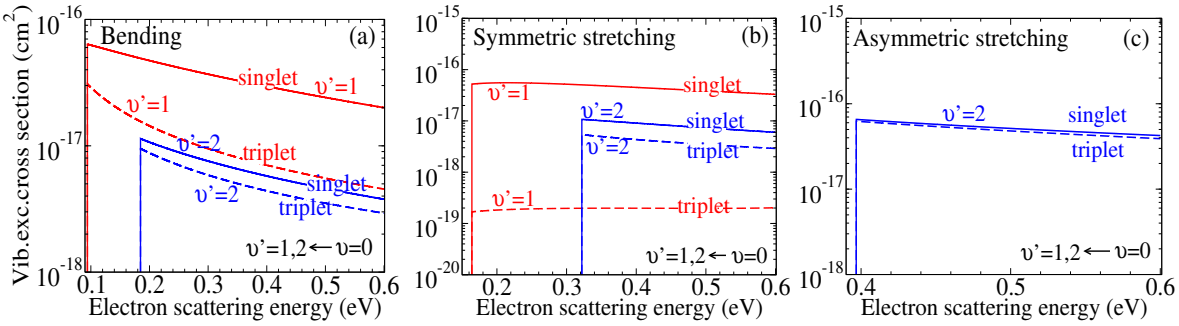

Figure II.6: Calculated cross sections as functions of the electron scattering energy for the vibrational excitation of NO_2 being initially in the lowest vibrational state $v = 0$ for the three normal modes (see the text for detailed discussion): (a) cross sections for $v' = 1, 2 \leftarrow v = 0$ transitions for bending mode; (b) for symmetric stretching mode; (c) for asymmetric stretching mode.

Figure II.6 displays the VE cross sections for the singlet and triplet states of the e^-–NO_2 complex with the target molecule being initially in the ground vibrational level. Not surprisingly, the $1 \leftarrow 0$ cross sections of the e^-–NO_2 singlet complex (solid red curves) are the largest compared to the triplet and $2 \leftarrow 0$ transitions. The $1 \leftarrow 0$ VE cross section for triplet (dashed red curve) bending mode has the same shape as that of the singlet. Its magnitude is smaller than that of the singlet by more than a factor of 4. For the symmetric stretching mode (see Figure 4 (b)), the $1 \leftarrow 0$ VE cross sections for both singlet and triplet depend very weakly on the scattering energy up to 0.6 eV. Note that the $1 \leftarrow 0$ VE cross sections for the asymmetric stretching mode are zero due to the symmetry of the scattering matrix with respect to positive and negative values of displacements along the mode. Furthermore, there is no significant difference in the magnitude of the cross sections for the symmetric stretching and asymmetric stretching modes due to the close fundamental frequencies (see Table II.1).

It should be stressed that the $\Delta v = 1$ transitions for asymmetric stretching mode are forbidden by symmetry. Indeed, Figure II.8 shows the dominant elements of S-matrix as function of asymmetric stretching mode at a given energy. As we can see, $\left|S_{l'\lambda',l\lambda}\right|^2$ is symmetric with respect to q_3 yielding a zero integral in Eq.(II.17) for one quanta transition.

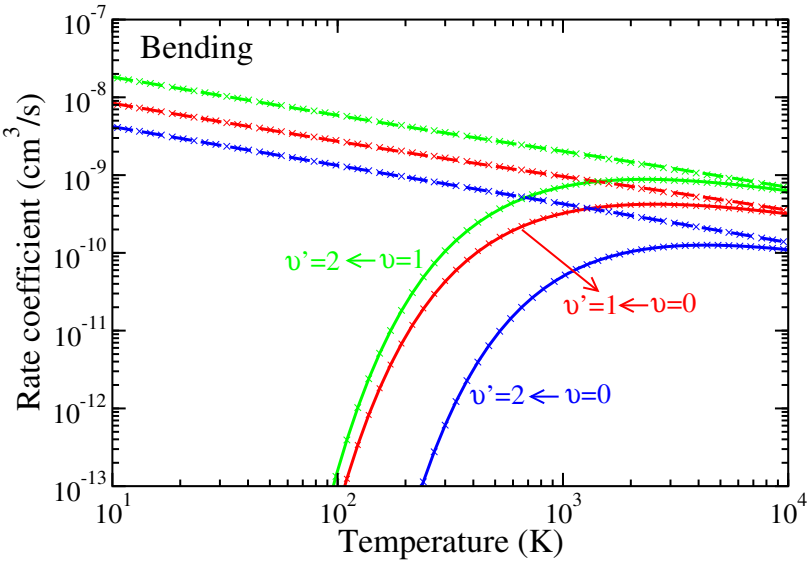

Figure II.7: Spin- and thermally-averaged rate coefficients for (de-)excitation transitions between the three lowest vibrational states of the bending mode. Vibrational excitations are labeled by $v' \leftarrow v$. Corresponding de-excitations are shown by dashed lines of the same color. The figure also demonstrates the quality of the fit of Equation (6) in Ref.[Liu et al., 2019]: Fitted curves are shown by stars with the same color for each transition.

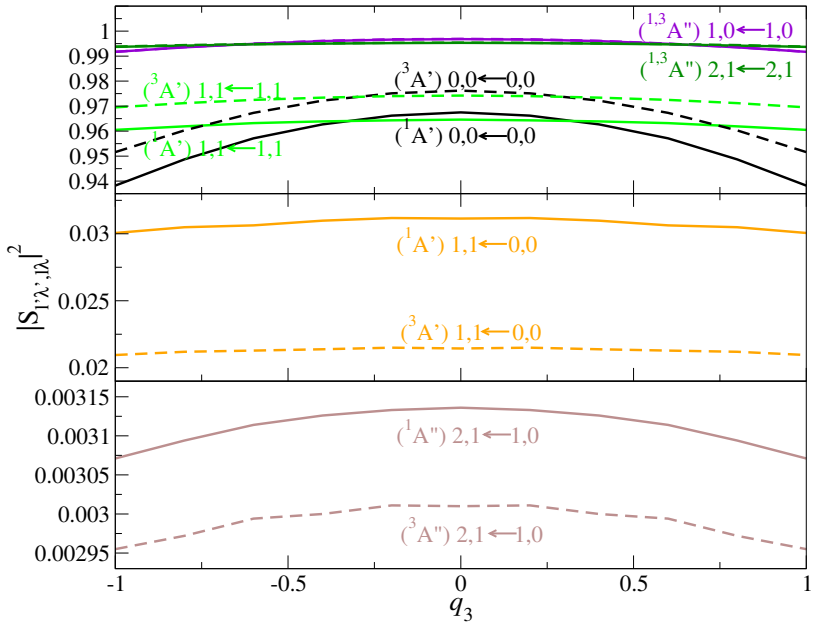

Figure II.8: Dominant (absolute value squared) elements $\left|S_{l'\lambda',l\lambda}\right|^2$ of the scattering matrix as a function of normal coordinate q_3 (asymmetric stretching mode) at 0.3 eV scattering energy. Solid curve: singlet for $NO_2 + e^-$ system. Dashed curve: triplet for $NO_2 + e^-$ system. The corresponding symmetry is indicated in parentheses. The mumbers indicate different partial waves $l'\lambda' \leftarrow l\lambda$.

The thermally averaged rate coefficient $\alpha_{v_i' \leftarrow v_i}(T)$ is obtained from the energy-dependent cross sections of Equation (I.28) according to Eq.(I.31). The rate coefficient is first calculated separately for singlet and triplet transitions and then the final rate coefficient is obtained by taking into account the corresponding statistical weights: 1/4 for singlet and 3/4 for triplet. Figure II.7 displays the spin- and thermally-averaged rate coefficients for (de-)excitation transitions between the three lowest vibrational states of the bending mode as an example. Similar to the previous studies for conveniently using the computed rate constants, we fitted the numerical spin- and thermally-averaged rate coefficients to an analytical formula. The fitted coefficients for each individual transitions are listed in Table 2 of Ref.[Liu et al., 2019].

Cross section obtained with a simplified approach

Making use of the simplified approach described in Chapter III, we computed the VE cross section for the change only one quanta form the analytical formula (III.9) and compared the result to the one obtained using the complete numerical treatment of Eq.(II.19).

Figure II.9 displays, as an example, the compared VE cross sections for the bending mode where the derivative of the scattering matrix in Eq.(III.6), employed in Eq.(III.9), was evaluated with two points $q_1 = 0.2$ and $q_1 = 1$. In the case of singlet, the VE cross section calculated with the simplified model (green solid curve) is larger than the presently calculated one (red solid curve) by about 30% while this deviation is less than 10% for triplet. To get an idea about these discrepancies, we plotted in Figures II.10 and II.11 the dominant fixed-nuclei S-matrix element $S_{l'\lambda',l\lambda}$ and the derivatives (for singlet only) as function of q_1.

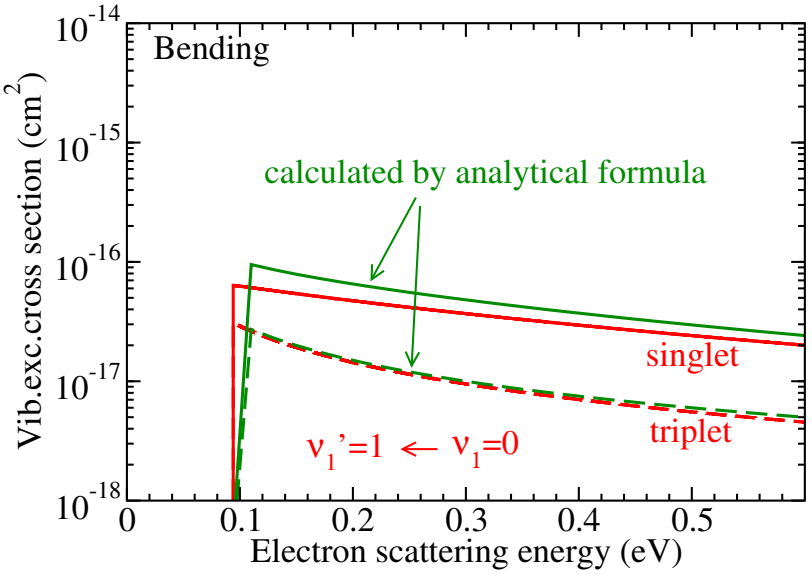

Figure II.9: Comparison between the presently calculated $v_1 = 0 \rightarrow v_1' = 1$ cross sections (red curves) for bending mode and that one calculated by Equation (III.9) (green curves) with two normal coordinates q_1 at 0.2 and 1 respectively.

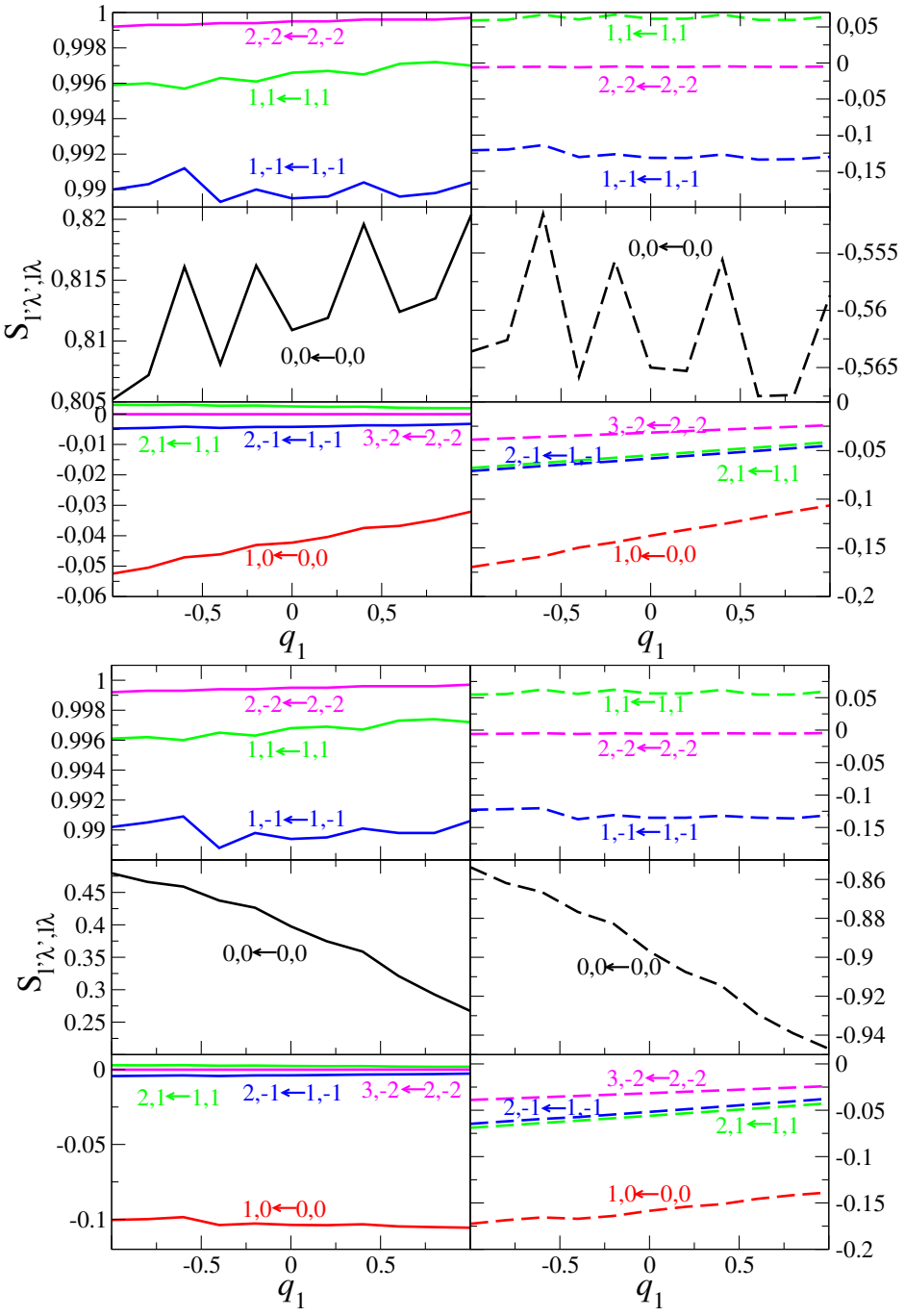

Figure II.10: Dominant elements $S_{l'\lambda',l\lambda}$ of the scattering matrix as a function of normal coordinate q_1 (bending mode) at 0.3 eV scattering energy. Upper figure: S-matrix elements for triplet . Bottom figure: S-matrix elements for singlet. The real (resp. imaginary) parts of the scattering matrix are given in solid curves in left panels (resp. dashed curves in right panels). The numbers indicate different partial waves $l'\lambda' \leftarrow l\lambda$.

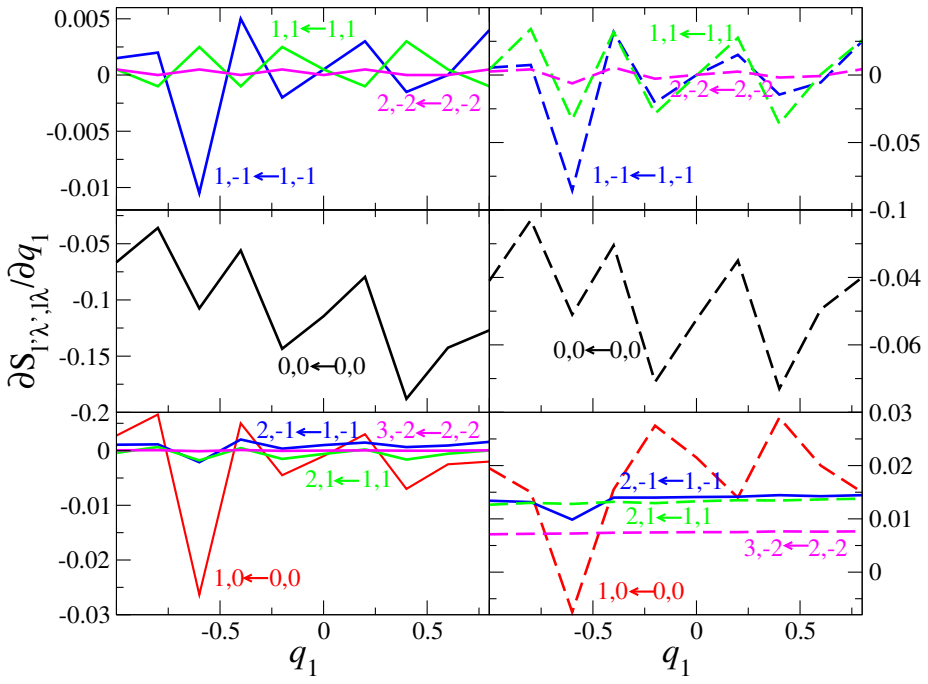

Figure II.11: Derivatives of dominant elements $S_{l'\lambda',l\lambda}$ as function of normal coordinate q_1 at 0.3 eV scattering energy, displayed in the lower Figure II.10. Recall that the real parts of the scattering matrix are given in left panels (solid curves) while the imaginary ones are in the right panels (dashed curves).

In the upper subfigure of Figure II.10, we can see small oscillations in the S-matrix elements of triplet state with a maximum amplitude of about 2%, for the middle panels ($S_{00,00}$ versus q_1). This implies that the S-matrix elements are in fact linear and hence the first derivative approximation for triplet is reasonable. As for singlet in the bottom subfigure of Figure II.10, the S-matrix elements seems smooth with respect to q_1 but a detailed analysis of the derivatives, displayed in Figure II.11, reveals that they depend on q_1. Consequently, the slop in Eq.(III.6) should be different according to the chosen points to evaluate it which can explain the overestimation observed in the obtained VE cross section. However, the simplified approach (III.9) apparently can provide an estimation of the VE probabilities used to compute the VE cross section for one quanta transition. In a better treatment higher orders in the Taylor expansion of the scattering matrix elements of Eq.(III.1) should be left.

Uncertainty estimations

In a similar manner to previous studies, there are sources of uncertainties in our calculations that need to be assessed. To our best knowledge, there exists no experimental or theoretical VE cross sections or rate coefficients data available in the literature. Hence, the uncertainties of the theoretical model can not be estimated since there is not other more accurate model to benchmark the present results. Nevertheless, for an *ab initio* study like this one, uncertainties could and should be provided by intermediate quantities as well as for final calculated observables, such as excitation and ionization energies, potential energy surfaces, dipole moments, polarizabilities, etc, that need to be stable regarding to parameters of the model.

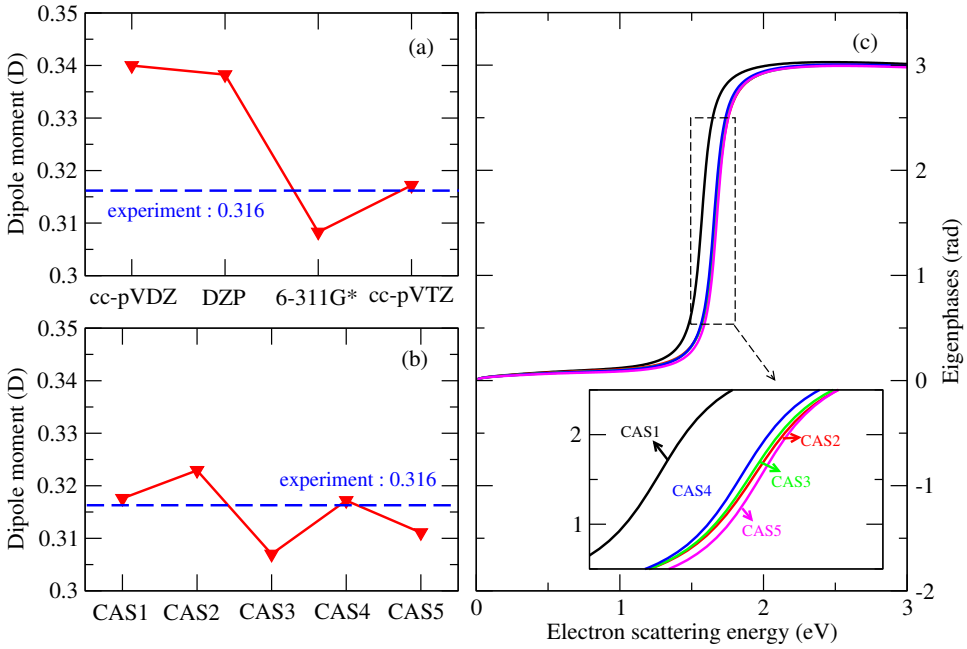

Figure II.12: Variation of the computed permanent dipole moment of NO_2 versus different basis sets (panel (a)) and CAS (panel (b)). CAS1: 7 electrons are kept free in the active space including 7 orbitals; CAS2: 9 electrons are kept free in the active space including 8 orbitals; CAS3: 11 electrons are kept free in the active space including 9 orbitals; CAS4 (CAS used in this paper): 13 electrons are kept free in the active space including 10 orbitals; CAS5: 15 electrons are kept free in the active space including 11 orbitals. The blue dashed line indicates the experimental value of the dipole moment of Ref [Leonardi et al., 1996]. (c) The eigenphase sums of scattering of the $^3B_1$ symmetry of the e^-–NO_2 complex as a function of the electron scattering energy for different CAS's. The inset enlarges the region where a sharper energy-dependence is observed around 1.6 eV corresponding to a resonance.

From a point of view of an electrostatic model potential for the electron-NO_2 collisions, the major contribution to the scattering amplitude for vibration excitation is expected to be caused by variations of the permanent dipole moment and the polarizabilities of NO_2 along the normal mode coordinates. We don't use the model potential method in the study: The accuracy of the final cross sections depends on the accuracy of wave functions of the target and the scattering electron. The accuracy of computed wave functions cannot be directly compared with previous results. However, comparing the dipole moment, evaluated from the wave functions of the target molecule, with the available accurate data can give an idea about the accuracy of computed wave functions used in the R-matrix calculations and, correspondingly, on the accuracy of the final cross sections.

Here, we investigate the stability of the dipole moment of target molecule as an example by performing a complete R-matrix calculation with different active spaces and basis sets, comparing the results with experimental data. We carried out two set of computations: (1) using the CAS (referred here as CAS4) mentioned above and increasing the size of basis sets; (2) increasing the complete active space (CAS) with the `cc-pVTZ` basis set. The obtained

results at the equilibrium geometry using the various parameters are illustrated in Figure II.12.

As one can see in Figure II.12(a), the dipole moment approaches the experimental value 0.316 D when we increase the basis set. Evidently, the dipole moment obtained by `cc-pVTZ` basis set used in this study agrees with the experimental data very well. Augmented (`aug-`) basis sets are not used as they would significantly extend outside the R-matrix sphere. Figure II.12(b) displays the variation of the dipole moment as a function of different CASs for the `cc-pVTZ` basis set. Obviously, the current CAS, i.e. CAS4 corresponds to the dipole moment closest to the experimental data. Therefore, we concluded that the target properties obtained by Quantemol-N are well converged and accurately represented. One might also provide uncertainties for other intermediate quantities computed in collisional studies, such as eigenphase sums. These are also shown in Figure II.12, panel (c). As shown in the figure, the small shift observed in calculations with different CASs indicates the convergence of the scattering data.

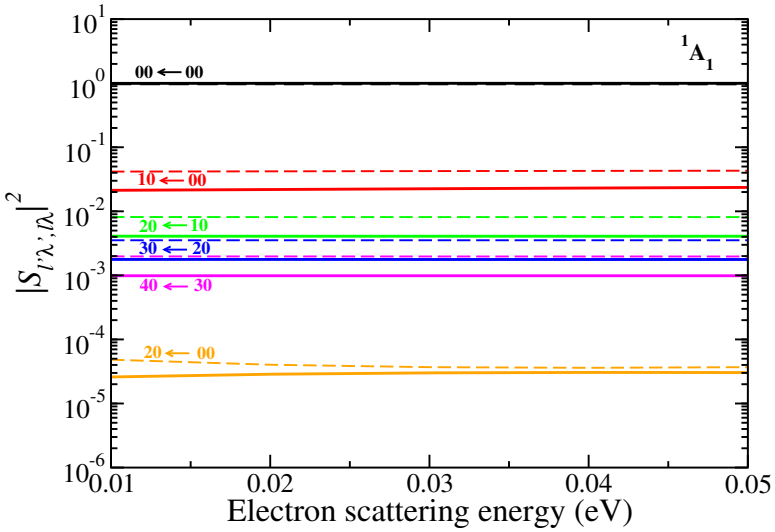

Figure II.13: The figure compares selected values of the $^1A_1$ scattering matrix elements (absolute value squared) before (solid color lines) and after (dashed lines of the same color) the unitary transformation that eliminates the long-range dipolar coupling between asymptotic channels in the e^-–NO_2 scattering matrix in the body frame. See the detailed discussion in the text. Each curve is labeled at the left of the figure with the pair of indexes $(l'\lambda' \leftarrow l\lambda)$, corresponding to the final channels and initial channel. The results for other irreps are not displayed but the situation is very similar to the $^1A_1$ symmetry.

Another source of uncertainty is the accuracy of the S-matrix derived from the R-matrix code, when the dipole term is included in the interaction. For the electron scattering by a nonpolar molecule, the electronic angular momenta l are decoupled at large distances from the target, such that l is a good quantum number for large separations between the electron and the molecule. However, for a dipolar molecule the electronic angular momenta l are coupled at long, as at short distances. The dipolar interaction exhibits the same long-range behavior as the centrifugal potential, thus, it is possible to combine the centrifugal and dipole interactions and obtain effective angular momentum. The Schrödinger equation for an electron in a dipole

field is given by (in atomic units)

$$\left(-\frac{1}{2}\frac{\mathrm{d}^2}{\mathrm{d}r^2}+\left(\frac{\hat{L}^2}{2r^2}-\frac{D\cos\theta}{r^2}\right)-E\right)\psi=0 \tag{II.20}$$

where $\hat{L}^2$ is the square of the orbital angular momentum, D is the dipole moment of NO_2, r and θ (polar angle) are the relevant spherical coordinates of the incident electron with respect to the center of mass of the target, E is the total (electronic) energy of the system. Note that the term $\frac{D\cos\theta}{r^2}$ in the above equation arises form Eq.(II.12) where D is given by Eq.(II.13).

In practice, expanding the angular part of the electron wave function ψ (the radial part is $F(r)$ whose the asymptotic form is given by Eqs.(II.14) and (II.15)) in the spherical harmonics basis and noting that $D\cos\theta = D\sqrt{\frac{4\pi}{3}}\mathcal{Y}_1^0$, Eq.(II.20) becomes an eigenvalue problem in which the elements

$$\left\langle l'\lambda'\right|\mathcal{Y}_1^0\left|l\lambda\right\rangle=\sqrt{\frac{(2l'+1)(2l+1)}{4\pi}}\begin{pmatrix} l' & 1 & l\\ 0 & 0 & 0\end{pmatrix}\begin{pmatrix} l' & 1 & l\\ \lambda' & 0 & \lambda\end{pmatrix}, \tag{II.21}$$

should be evaluated acknowledging that $\left\langle l'\lambda'\right|\hat{L}^2\left|l\lambda\right\rangle=\hbar^2 l(l+1)\delta_{ll'}\delta_{\lambda\lambda'}$. This can be accomplished using the Clebsch-Gordan coefficients or alliteratively the Wigner $3j$-symbol calculator.

Once all elements in Eq.(II.21) are obtained for $l\leq 4$ (recall that in the R-matrix calculations, continuum Gaussian-type orbitals was included up to $g-$wave), we find eigenvalues of the operator $\frac{\hat{L}^2}{2}-D\cos\theta$ corresponding to effective values of l. The eigenvectors of this operator are used to build the unitary matrix $\mathbf{U}$ to transform the scattering matrix in Eq.(II.16) into the effective angular momentum representation according to $\tilde{\mathbf{S}}=\mathbf{U}^{\dagger}\mathbf{S}\mathbf{U}$, where $\tilde{\mathbf{S}}$ designates a scattering matrix without long-range dipolar coupling. Therefore, the unitary transformation $\mathbf{U}$ allows eliminating the long-range dipolar coupling between asymptotic channels in the $e^-\!-\!NO_2$ scattering matrix in the body frame. The values of the effective angular momentum l could be noninteger and even complex. In our case, l are real such that $\mathbf{U}^{\dagger}=\mathbf{U^{-1}}$ and $\mathbf{U^{-1}}$ is orthogonal resulting in $\mathbf{U^{-1}}={}^{\mathbf{t}}\mathbf{U}$).

In the next step, we fitted the obtained S-matrix elements (absolute values squared) before $\left|S_{l'\lambda',l\lambda}\right|^2$ and after $\left|\tilde{S}_{l'\lambda',l\lambda}\right|^2$ the unitary transformation with power law: $\left|\mathrm{S}_{l'\lambda',l\lambda}\right|^2=\beta E^{\alpha}$ and $\left|\tilde{S}_{l'\lambda',l\lambda}\right|^2=\beta' E^{\alpha'}$, respectively, where α, β and α', $\beta'$are the fitted parameters. The obtained parameters are given in Table 3 of Ref [Liu et al., 2019]. Figure II.13 shows a few examples of scattering matrix elements of dominant channels ($\Delta l\leq 2$ and λ is zero) of the ${}^1A_1$ symmetry. The largest matrix element for the $00\leftarrow 00$ transition remains unchanged after the unitary transformation. It is the variation of this matrix element with respect to the normal coordinates that yields the largest contribution to the cross sections. Therefore, the uncoupling of the partial-wave channels at large distances would not produce a significant change in the final cross sections. This also means that the coupling between partial waves induced by the permanent dipole moment of the target has a minor effect on the final cross sections.

Assuming that the order of magnitude of the vibrational excitation cross sections is determined by the square of the derivatives of the permanent dipole moment and polarizabilities of the target with respect to the normal coordinates, and also assuming that the relative uncertainties of the derivatives are of the same order as the relative uncertainties of the dipole moment, we can estimate the uncertainty of the obtained cross sections with respect to the accuracy of the wave functions of the target. From panels (a) and (b) in Fig. II.12, we estimate that the uncertainty in the dipole moment of NO_2 is less than 2%, producing the uncertainty in cross sections less than 4%. Another source of uncertainty in the final cross sections is due to the variation of the geometry-fixed scattering matrix with energy. The choice of the energy at which the scattering matrix $\mathcal{S}_{l'\lambda',l\lambda}(\boldsymbol{q})$ in Eq. (II.17) is computed produces the corresponding uncertainty. Figure II.5 gives an idea about the energy variation of $\mathcal{S}_{l'\lambda',l\lambda}(\boldsymbol{q})$. The largest components with $\Delta l = 0$ vary for about 3% over the energy interval of 0.4 eV. It gives an uncertainty in the cross sections of the order of 6%. No other significant uncertainty sources were identified. Therefore, the overall uncertainty of the present calculations seems to be below 10%.

Summary

We reported in this section the first theoretical results on vibrational excitation and de-excitation of the NO_2 $\left(X\,^2A_1\right)$ molecule in collisions with a low-energy electron using first principles. Extensive uncertainty estimations were performed by changing parameters of the scattering model. Converged results for the target properties and eigenphase sums demonstrated the validity of the obtained results. We expect that the data reported in the present study could be valuable in kinetic studies of low-temperature NO_2-containing plasma.

II.4.B Vibrational excitation of N_2O by electron impact

As is the case with NO_2, nitrous oxide (N_2O) play an important role in a plethora of research fields ranging from astrochemistry [Ziurys et al., 1994, Jamieson et al., 2005, Wang and Sze, 1980] to low temperature plasma technology [Gherardi et al., 2000] and medicine [o20,]. To the best of our knowledge, no theoretical vibrational cross sections has been reported so far, while there are several experimental cross sections for electron-induced vibrational excitations complied in a recent review [Song et al., 2019].

In this section, we present the first theoretical vibrational (de-)excitation (VE) study of N_2O by electron impact. The studied process can be depicted by

$$e^- + N_2O(v_i) \rightarrow e^- + N_2O(v_i'), \tag{II.22}$$

in which v_i and and v_i' denoted the initial and final vibrational states of N_2O, respectively.

In a similar manner to the NO_2 study described above, we computed cross sections and rate coefficients for transitions between ground and first vibrational states of N_2O using an approach that employs the normal mode approximation for vibrational states of the target molecule (Eq.(II.7)), fixed-nuclei electron-NO_2 scattering matrices (Eq.(II.16)) and the vibrational frame transformation (Eq.(II.17)).

At its equilibrium geometry, N_2O (with 22 electrons) has a linear asymmetric "N–N–O" molecular structure, described by the $C_{\infty v}$ symmetry point group where a closed-shell electronic ground state configuration is given by

$$^1\Sigma^+ : 1\sigma^2 2\sigma^2 3\sigma^2 4\sigma^2 5\sigma^2 6\sigma^2 1\pi^4 7\sigma^2 2\pi^4. \tag{II.23}$$

N_2O has three normal modes of vibration, namely: NO stretching, the doubly degenerate bending mode, and NN stretching represented by v_1, v_2, and v_3, respectively. Figure I displays the normal modes of N_2O computed with Molpro using the complete active space self-consistent field (CASSCF) method with CAS(12,7), i.e. 12 electrons are distributed in 7 orbitals, and the `cc-pVTZ` basis set. Computational details and the obtained data on frequencies and equilibrium geometry are provided in paper .6 (see Table 1).

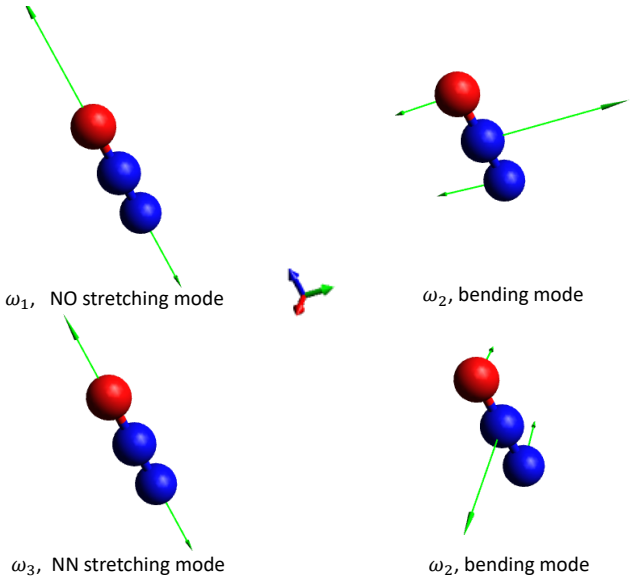

Figure II.14: Normal modes of N_2O. The arrows indicate the direction and magnitude of displacements for each mode. Note that arrowheads are not shown for the displacements of relatively large magnitudes. Vibrational frequencies and symmetries are listed in Table 1 of paper .6.

As a second step, we performed the scattering calculations in C_{2v} (a subgroup of $C_{\infty v}$ according to Table I.1) with the same basis set and CAS employed for the structure calculations. However, Quantemol-N does not have CASSCF built into it, a series of convergence tests using the available complete active space configuration interaction (CAS-CI) model with the Hartree-Fock orbitals built with Molpro were performed to investigate the stability of the target properties. We obtained with a R-matrix sphere radius of 11 bohrs a permanent electric dipole moment of the target molecule of 0.1 D, which is considered to be in satisfactory agreement with the experimental value, 0.16 D [Johnson III, 2010].

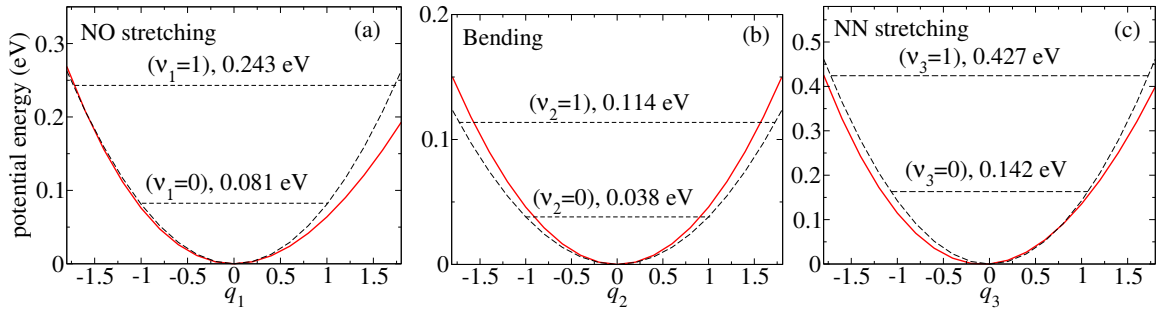

Figure II.15: Potential energy curves for the ground electronic state of N_2O as a function of the (a) NO stretching, (b) bending and (c) NN stretching normal-mode coordinates. The abscissa axes in the figures represent dimensionless normal mode coordinates. In each panel, only one mode is varied, while the other modes are kept fixed at their equilibrium positions. Red solid curves are the actual potential energies obtained from the R-matrix code, while black dashed curves represent energies calculated in the harmonic approximation, i.e. simply $\sim \frac{\hbar\omega_i}{2} q_i^2$. Horizontal dashed lines denote the energies of vibrational states.

Figure II.15 depicts the ground-state electronic potential energy curves of N_2O for each normal mode obtained with the R-matrix method and compared to the potential energy curves of harmonic oscillators generated with the frequencies provided by Molpro. As we can see the curves match reasonably well with each other but with small discrepancies that can be attributed to the anharmonicity of the actual N_2O potential.

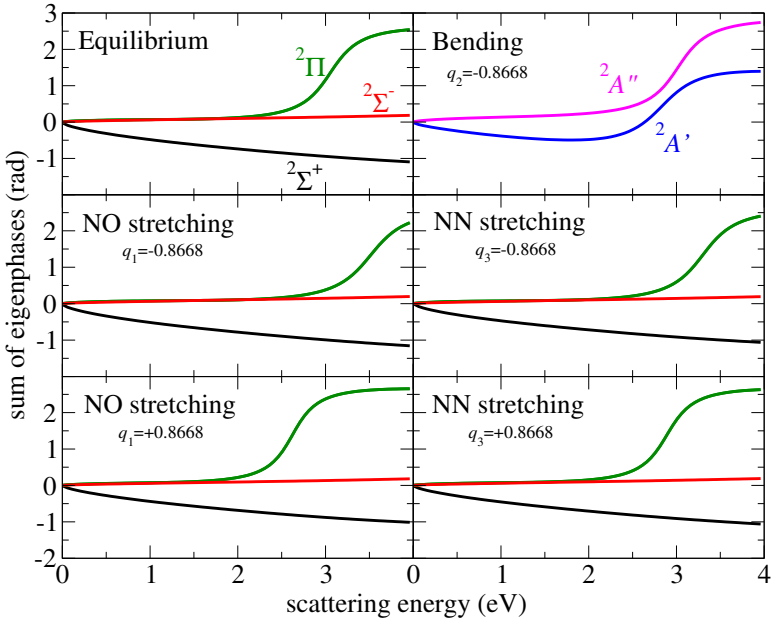

Figure II.16: The sum of eigenphases as a function of the electron scattering energy for equilibrium geometry and displacements $q_i = \pm 0.8668$ (dimensionless) along each normal mode. Due to the symmetry of bending mode, the eigenphase sums of $q_2 = +0.8668$ and $q_2 = -0.8668$ are the same. The curves are color coded according the different symmetries of the $e^- + N_2O$ system.

Again, the applicability of the theoretical approach described throughout this chapter is based on the fact that the scattering matrix should be smooth with respect to the collision energy. For this purpose, we plotted in Figure II.16 the eigenphase sums (from Eq.(I.5)) of different irreducible representations at equilibrium and at displacements away from the equilibrium along each normal mode coordinate. As we can see, the variation of the eigenphase sums is smooth for energies below 2.3 eV. Above this value, a sharp energy dependence at certain energies is observed due to the presence of electronic resonances $^2\Pi$ of the complex $e^- - N_2O$.

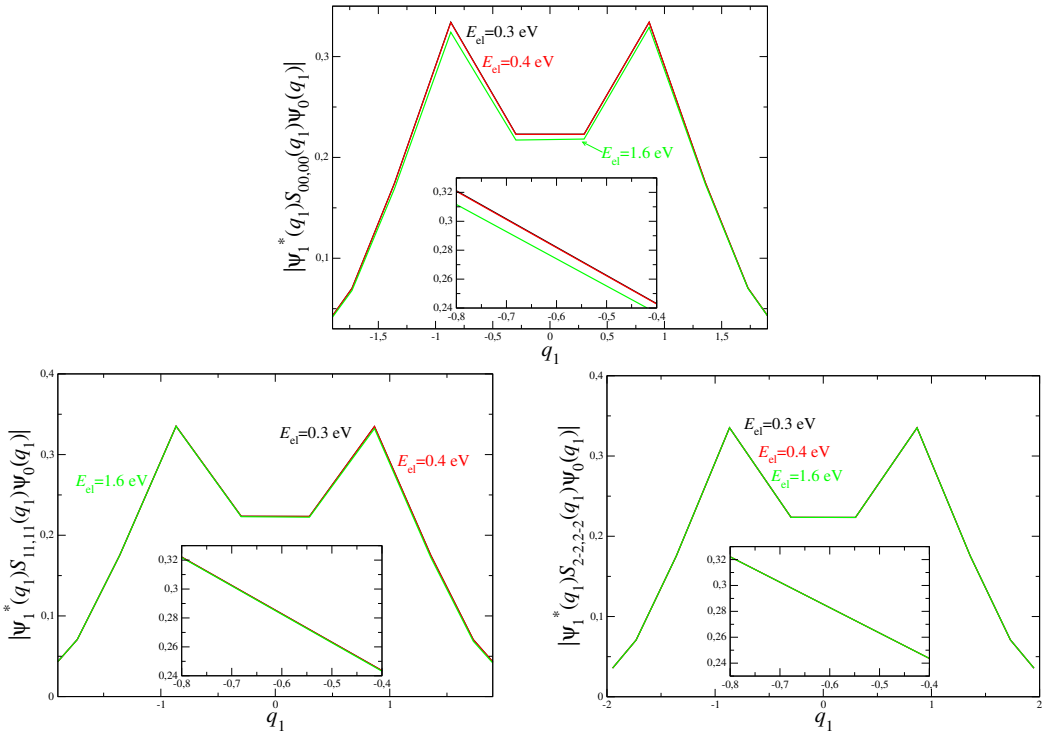

Figure II.17: The integrands of Equation (II.17) for the NO stretching mode for three among the largest matrix elements $00 \leftarrow 00$, $11 \leftarrow 11$ and $2-2 \leftarrow 2-2$ as an example. Each panel shows the integrand for one matrix element for three energies 0.3eV, 0.4eV and 1.6eV.

A second demonstration of the energy dependence is the analysis of the integrand in Eq.(II.17). Figure II.17 shows the integrands for the NO stretching mode for three among the largest matrix elements $00 \leftarrow 00$, $11 \leftarrow 11$ and $2-2 \leftarrow 2-2$. Each panel depicts the integrand for one matrix element for three energies 0.3eV, 0.4eV (which are just above the vibrational excitation threshold), and 1.6eV (the energy is well above the threshold). As one can see, the energy dependence is weak. For the $11 \leftarrow 11$ and $2-2 \leftarrow 2-2$ transitions drawn in the two lower panels, the curves for different energies are indistinguishable.

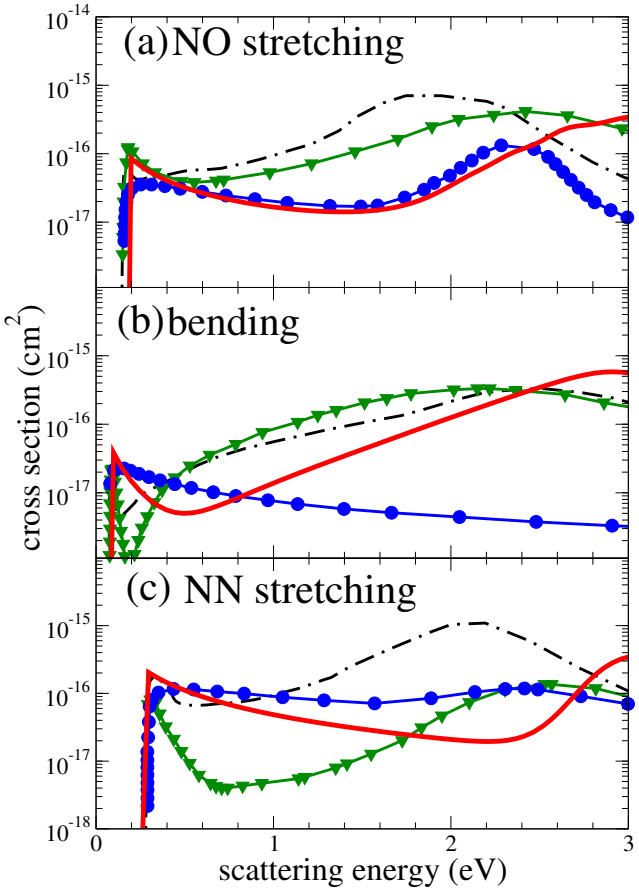

Figure II.18: Comparison of the present theoretical results with available experimental cross sections for the vibrational $v = 0 \rightarrow v' = 1$ excitation of the (a) NO stretching, (b) bending, and (c) NN stretching modes. The experimental results are taken from Hayashi [Hayashi and Akashi, 1992, Song et al., 2019] (solid line with circles), Allan and Skalický [Allan and Skalický, 2003] (solid line with triangles), and Nakamura[Nakamura, 2007] (dashed-dotted line).

With the above considerations, we calculated vibrational (de-)excitation cross sections for transitions between the ground and the first excited vibrational states for each of the normal modes using the formula of Eq.(II.19). Figure II.18 displays a comparison of the theoretical $1 \leftarrow 0$ VE cross sections with the available experimental data [Hayashi and Akashi, 1992, Allan and Skalický, 2003, Nakamura, 2007]. All three experimental data do not resolve the $v_1 = 1/v_2 = 2$ and $v_3 = 1/v_1 = 2$ thresholds, i.e. the experimental cross section for the excitation of the NO mode ($v_1 = 0 \rightarrow 1$) includes also a contribution for the transition $v_2 = 0 \rightarrow 2$, and the cross section for the excitation of the NN mode includes a contribution for the $v_1 = 0 \rightarrow 2$ transition. But these additional contributions are expected to be significantly smaller due to the vibrational propensity rule: The transitions with a change of only one vibrational quanta are the largest. There is a significant disagreement between the experimental data, up to a factor of 20-50 for certain energies. On the other hand, the theoretical results also don't agree better with one experiment or another: For

the NO stretching mode (panel a), the theory agrees better with the experiment by Hayashi [Hayashi and Akashi, 1992]. For the bending mode (panel b), the theory agrees better with the two other experiments, although the agreement is quite poor. Note that the presented integral cross sections by Allan and Skalický [Allan and Skalický, 2003] were obtained from the measured differential cross sections. Finally, for the NN stretching mode (panel c), the theory agrees better again with the data by Hayashi [Hayashi and Akashi, 1992].

The present theoretical cross sections are expected to be valid only for energies below the energy of the $^2\Pi$ resonance mentioned above, i.e. below 2.3 eV.

Thermally averaged rate coefficients $\alpha_{v_i' \leftarrow v_i}$ for vibrational excitation are obtained from the cross sections using the standard formula of Eq.(I.31). The computed rate coefficients were also fitted using an analytical formula employed in the preceding studies. The obtained coefficients are shown in Figure 6 and fitted parameters are listed in Table II of paper .6.

As in previous studies, we performed a number of calculations to assess the uncertainty of the obtained theoretical results. Once again, two main sources of uncertainty in the present theoretical approach can be identified. The first is the accuracy of the fixed-nuclei S-matrix elements computed for the polar molecule (with a small dipole moment) in the limited basis of spherical harmonics. This point has been discussed in the NO_2 study where the uncertainty associated with this approximation was estimated to be of the order of 6%. This uncertainty should not be larger for N_2O because it has a smaller dipole moment so that the couplings between partial waves induced by the permanent dipole moment of this molecule have a weaker effect on the final cross sections.

The second source of uncertainties is related to the particular scattering model used in the calculation. Performing a complete calculation with different parameters such as basis sets and CASs, uncertainty was assessed in paper .6. We found that the difference in the rate coefficients produced in by three models is about 6%. Consequently, the overall uncertainty of the present theoretical result is estimated below 12%.

One of the most striking features of this performed study is the role of Renner-Teller coupling in N_2O vibrational excitation by electron impact. The Renner-Teller coupling is a particular type of the non-Born-Oppenheimer (non-adiabatic) coupling leading to a coupling between the vibrational and the electronic motions. It has been discussed in several previous studies [Mikhailov et al., 2006b, Douguet et al., 2008b, Douguet et al., 2009b, Douguet et al., 2011, Douguet et al., 2015b, Fonseca dos Santos et al., 2014a]. For N_2O with a ground electronic state of $^1\Sigma^+$ symmetry, the Renner-Teller effect couples σ and π partial waves of the incident electron with degenerate bending mode of N_2O. It manifests itself by a linear dependence of the coupling between partial wave components for small displacements along the bending coordinate as displayed in Figure 6 of paper .6. Renner-Teller effect results in a bending configuration of the equilibrium geometry of the N_2O^- anion. More discussions can be found in [Hopper et al., 1976, Tschumper and Schaefer III, 1997] and [Liu et al., 2020] for N_2O.

Summarizing this section, we briefly reported the cross sections for vibrational (de-

)excitations of N_2O by a low-energy electron using first principles. The computed results show a reasonable agreement with experimental data for the NO and NN stretching modes while for the bending mode the agreement is rather poor at energies above 0.4 eV. It was found that Renner-Teller coupling is responsible for the excitation of the bending mode, as was expected from general theoretical considerations. These outcomes suggest that more measurement of vibrational excitation in N_2O, at least for a few energies, are needed. Current data could, however, be used in kinetic studies of low-temperature N_2O-containing plasma.

II.5 Concluding remarks

This chapter gives an overview of my contribution within the research axis on the role of collisions involving electron-neutral molecules in low-temperature plasma technology, used for atmospheric depollution purpose. A theoretical approach for the electron-impact vibrational excitation of neutral molecules was developed and applied to NO_2 and N_2O. Availability of accurate data for such process is believed to be crucial for plasma modeling. The study of electron-radicals collisions as well as taking into account for the rotational structure of each vibrational level of the targets were postponed to future works (see outlooks in Chapter V).

The present theoretical studies have allowed, on the one hand, to provide the first theoretical results on vibrational (de-)excitation of NO_2, on the other hand, to benchmark the obtained results with experimental data in case of N_2O. These studies have been carried out in the context of Hainan Liu dissertation at Centralesupélec and in close collaboration with UCF and Rollins College. These collaborations benefit from supports of NSF and the Thomas Jefferson Foundation, in addition to other programs listed in Appendix V.2.C.

Finally, it has to be stressed that the theoretical approach employed throughout this section handles a smooth scattering matrix with respect to the collision energy. This circumstance of energy-independent S-matrix was fortunately fulfilled for the performed studied. In general, S-matrix depends on the scattering energy for neutral molecules which requires a further development as proposed in Chapter V.

III – Formation of fluorine based-molecules

III.1 Context and Motivations

As stated in the introduction, this chapter investigates the formation/destruction mechanisms of fluorine based-molecules that play a vital role in plasma technologies used for the development of materials. For the sake of clarity, studies performed in the context of other projects such as the formation of MnO oxides on a Fe-Mn alloy surface or thermal/mass characterizations of bio-materials will not be reported here.

Currently, the non-equilibrium plasmas produced with electrical discharges in BF_3-containing feed gas have increasing been of interest for a large number of applications. In particular, BF_3 is frequently the boron carrier when plasmas are used for material processing [Sennikov et al., 2017, Torigoe et al., 2016, Gonzatti et al., 2010]. Basically, BF_3 plasmas are used either for (i) the synthesis of ultra-hard boron compounds, e.g. boron carbides [Sennikov et al., 2017], (ii) the deposition of boron nitride, an advanced material with a large number of functionalities [Torigoe et al., 2016], and (iii) p-type doping by boron in the semi-conductor and photovoltaic industries [Gonzatti et al., 2010, Duchaine et al., 2012]. As far as doping applications are concerned, plasma immersion ion implantation (PIII) processes are probably among the most promising in terms of cost and technical performance [Duchaine et al., 2012, Young et al., 2016]. These processes make use of very low pressure, very high density magnetized plasmas generated in a BF_3-containing feed gas.

Under such conditions, several ions as BF_3^+, BF^+, B^+ or F^- may be produced [M. Farber and Srivastava, 1984, Yong-Ki and Irikura, 2000] where the major one is BF_2^+ [Young et al., 2016]. In a typical PIII reactor, the positive ions losses are dominated by their dissociative recombination with electrons. Consequently, the investigation of DR of the major ion BF_2^+ and the competitive processes such as the vibrational (de-)excitation are of great importance for monitoring these plasmas.

The present study is motivated by the lack of data on $e^- - BF_2^+$ collisions. The theoretical model described in next Section III.2 is a simplified approach of the model employed for neutral molecules in Chapter II. With certain assumptions, we computed cross-sections for DR and electron-impact vibrational excitation of the BF_2^+ molecular ion in Section III.3. This study, performed in close collaboration with Prof. Viatcheslav Kokoouline at the University of

Central Florida (UCF), has also allowed for laying the theory for further applications in particular for the HCO^+ and N_2H^+ molecular ions in the context of Dr. Abdillah Abdoulanziz's thesis, co-supervised with Prof. Ioan Schneider at Université du Havre.

In the following, only main results are provided. More details can be found in paper .7 included to this manuscript.

III.2 Simplified theoretical approach

Similar to previous models of Chapters I and II, our theoretical approach combines the normal modes approximation for the vibrational states of the target ion and use of the UK R-matrix code to evaluate electron-ion scattering matrices for fixed geometries of the ion (see Figure II.1). The main difference here is that the vibrational frame transformation is evaluated analytically. Indeed, at low-energy collisions, the scattering matrix frequently depends, in a linear fashion, on the normal mode coordinate near the equilibrium geometry. Hence, from the mathematical point of view, one can expand $S^{\Lambda}_{\lambda' l',\lambda l}(\mathbf{q})$ of Eq.(II.17) to first order in the normal coordinates $\mathbf{q} = \{q_1, q_2, \cdots\}$ yielding

$$S^{\Lambda}_{\lambda' l',\lambda l}(\mathbf{q}) \approx S^{\Lambda}_{\lambda' l',\lambda l}(\mathbf{q}_0) + \sum_i \frac{\partial S^{\Lambda}_{\lambda' l',\lambda l}}{\partial q_i} dq_i, \tag{III.1}$$

where i is the index of different normal modes and $S^{\Lambda}_{l'\lambda',l\lambda}$ is the scattering amplitude when the electron scatters from one channel (λl) to another $(\lambda' l')$, l being still the electron angular momentum and λ its projections on the molecular axis. The partial derivative in Eq.(III.1) is taken at the equilibrium configuration $\mathbf{q}_0 = \{0\}$ of the ion, below BF_2^+ for instance.

Plugging the above expansion in Eq.(II.17), we arrive at

$$\mathcal{S}_{v_i' v_i} = \sum_{\lambda' l', l\lambda} S^{\Lambda}_{\lambda' l',\lambda l}(q_0)\delta_{v_i' v_i} + \frac{1}{\sqrt{2}} \sum_{\lambda' l', l\lambda} \frac{\partial S^{\Lambda}_{\lambda' l',\lambda l}}{\partial q_i} \left(\sqrt{v_i}\delta_{v_i' v_i - 1} + \sqrt{v_i + 1}\delta_{v_i' v_i + 1} \right), \tag{III.2}$$

for the mode i where we used the expressions of the vibrational wave functions in the harmonic approximation picture from Eq.(II.10) as well as the following identities

$$d\hat{q}_i = \frac{1}{\sqrt{2}} \left(\hat{a}_i + \hat{a}_i^{\dagger} \right) \tag{III.3}$$

$$\int dq_i \psi_{v_i'}(q_i) q_i \psi_{v_i}(q_i) = \sqrt{\frac{v_i}{2}}\delta_{v_i' v_i - 1} + \sqrt{\frac{v_i + 1}{2}}\delta_{v_i' v_i + 1} \tag{III.4}$$

$$\int dq_i \psi_{v_i'}(q_i) \psi_{v_i}(q_i) = \delta_{v_i' v_i}. \tag{III.5}$$

The second term on the right-hand side of Equation (III.2) implies that each normal mode is most likely (de-)excited by one quanta. As a result, performing the integral in Eq.(II.17) becomes an evaluation of the derivatives in Eq.(III.2) that can obtained using the finite difference method calculated from two values of q_i. The computational effort is thus significantly reduced.

For convenience, we introduce the quantities

$$\mathcal{P}_i = \frac{g_i}{2} \sum_{\lambda' l', l\lambda} \left| \frac{\partial S^{\Lambda}_{\lambda' l', \lambda l}}{\partial q_i} \right|^2 , \tag{III.6}$$

which could be interpreted as the probability of excitation of the vibrational mode i with g_i being its degeneracy.

Again, applying the vibrational frame transformation (FT) of Eq.(III.2) requires a smooth scattering matrices with respect to the incident electron energy and $\epsilon_{v_i} \approx \epsilon_{v_i'}$. Recall that FT theory extends the fixed-nuclei (FN) approximation by including the vibrational motion of the target adiabatically. As widely discussed in Chapter I (see Section I.4), this theory is powerful for ions without low-energy electronic resonances (doubly-excited dissociative states) appearing for geometries near their equilibrium and if the collision energy is not enough to excite the target ion electronically. The theory could also be applied to neutral targets if these assumptions are fulfilled (see Chapter II).

With the above considerations, if the doubly-excited dissociative states are not energetically accessible, one can only consider the indirect dissociative recombination (IDR) process in competition with rovibrational (de-)excitation. Based on the expansion of Eq.(III.2), the present theoretical model employs the following assumptions.

- The rotation of the molecule is neglected leading to a cross section without rotational structure. This is justified since these rotational resonances are washed out in the experimental cross sections.

- The cross section is averaged over the autoionizing resonances leading to a featureless curve. This procedure is justified because these resonances are not individually resolved in the experiment.

- For the indirect DR route, the autoionization lifetime is assumed to be much longer than the predissociation lifetime. The kinetic energy of the electron is quickly converted to vibrational motion of the ion just after the electron capture in a Rydberg resonant state.

This simplified approach allows to describe the vibrational (de-)excitation (VE,VdE) process in which the electron energy is enough to excite the ion in each normal mode q_i and then leave it. In contrast, if that energy is not sufficient to excite the ion, the present model suggests that the probability of excitation of the ion by the electron is described by the same physics, but instead of leaving the vibrationally excited ion, the electron is captured in a Rydberg resonance attached to that vibrational state, excited by the electron. If the electron is captured by the ion, the system will most likely dissociate, rather then autoionize, leading to the IDR process.

It should be finally stressed that the method implemented is based on ideas developed in previous studies [Mikhailov et al., 2006b, Douguet et al., 2008b, Douguet et al., 2012b]. The expansion of Eq.(III.2) was performed on the quantum defect matrix that is used afterwards

in Eq.(I.15) with a set of *ab initio* potential surfaces of the neutral molecule and of the corresponding molecular ion obtained numerically near the equilibrium position of the ion. In a later study [Fonseca dos Santos et al., 2014a], a scattering matrix approach was used through the complex Kohn variational method and has allowed reproducing accurately *ab initio* Rydberg state energies of the neutral molecule.

In the next section, the scattering matrix approach for indirect DR using this time around the R-matrix method will be employed to obtain the DR and VE/VdE rate coefficients for BF_2^+, as a benchmark system. This formalism was also applied in a straightforward manner to more complex molecules such as $CH_2NH_2^+$, described in Chapter I, or NH_2CHOH^+ investigated in Ref.[Ayouz et al., 2019]. Below, a brief description of the BF_2^+ study is given.

III.3 Application: DR cross section of BF_2^+

The ion BF_2^+ requires a highly-energetic incoming electron to form a doubly-excited resonant dissociative state of the neutral BF_2. Low energy electrons are more likely to be captured in a Rydberg level BF_2^* associated with a vibrationally excited state of BF_2^+. This Rydberg state BF_2^* is predissociated by BF_2^{**}. In this section, we aim to study the IDR and VE/VdE depicted by

$$e^- + BF_2^+(v_i) \rightarrow BF_2^*, BF_2^{**} \rightarrow \begin{cases} BF + F \\ F_2 + B \\ e^- + BF_2^+(v_i') \end{cases} \quad \text{(III.7)}$$

BF_2^+ is a linear molecule in its equilibrium geometry belonging to $D_{\infty h}$ point group. Its main electronic ground state configuration $^1\Sigma_g^+$ is (with 22 electrons)

$$\left(1\sigma_u^+\right)^2 \left(1\sigma_g^+\right)^2 \left(2\sigma_g^+\right)^2 \left(2\pi_u^+\right)^2 \left(3\sigma_g^+\right)^2 \left(4\sigma_g^+\right)^2 \left(3\pi_u^+\right)^2 \left(1\pi_u^-\right)^2 \left(1\sigma_u^+\right)^2 \left(1\pi_g^+\right)^2 \left(1\sigma_g^-\right)^2 \quad \text{(III.8)}$$

The structure calculations were performed using a coupled pair approximation CEPA(2) method and the `cc-pVTZ` basis via the Molpro suite of codes [Werner et al., 2008]. Two stretching modes v_1 and v_3 (asymmetric and symmetric) with respective frequencies ω_1 and ω_3 and corresponding coordinates q_1 and q_3, and a doubly degenerate transverse mode v_2 with a lower frequency ω_2 and coordinates (q_{2x}, q_{2y}) were found. Figure III.1 shows the vibrational frequencies listed in Table 1 of Ref.[Kokoouline et al., 2018].

The electron-scattering calculations were carried out using the UK R-Matrix [Tennyson, 2010] code in the abelian subgroup D_{2h} with a configuration of interaction (CI) model; a basis `cc-pVTZ` and a complete active space CAS(12,10), i.e. 12 electron are distributed in 10 orbitals. We choose a R-matrix sphere of radius 10 bohrs. It should be noted that bending and asymmetric stretching mode calculations were performed in the C_{2v} abelian subgroup, while for the symmetric mode the group D_{2h} was used in the calculations.

As discussed above and widely in the preceding chapters, at low collision energies the fixed-nuclei scattering matrix depends weakly on energy whereas a sharper energy-dependence is observed at certain relatively high energies, corresponding to positions of Rydberg states attached to the excited electronic states of the ion. To analyze the energy dependence of the

scattering matrix, we provide in Figure III.2 the eigenphase sums, obtained from Eqs.(I.5), for three different geometries corresponding to a small displacement from equilibrium along each normal mode of the BF_2^+ ion. As one can see, the variation of the eigenphase sums is smooth for energies below 6 eV. Above this value, a sharp energy dependence at certain energies is observed due to the presence of electronic Rydberg resonances attached to closed ionization limits.

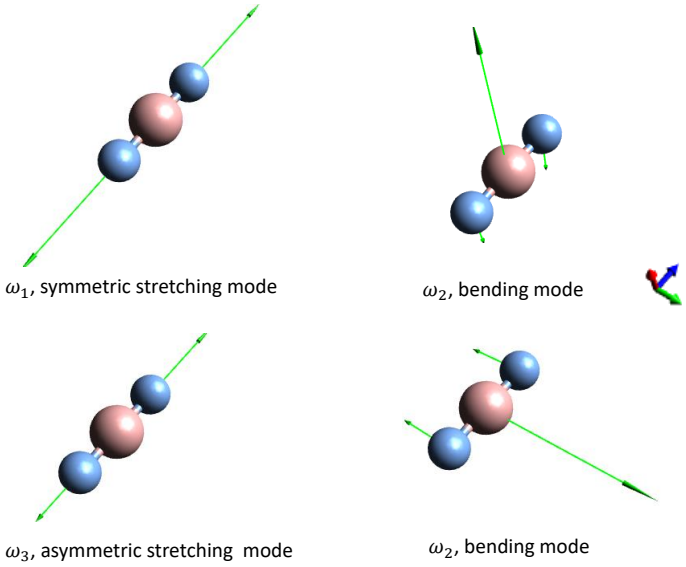

Figure III.1: Normal modes of BF_2^+. The arrows indicate the direction and magnitude of displacements for each mode. Note that arrowheads are not shown for the displacements of relatively large magnitudes. Vibrational frequencies and symmetries are listed in Table 1 of Ref.[Kokoouline et al., 2018].

Plotting the excitation probabilities defined from Eq.(III.6) for each normal mode, we found in Figure 2 of paper .7 that these quantities have a weak dependence on energy and, therefore, they could be used as constants in calculations of the cross sections and thermally-averaged rate coefficients.

Therefore, combining Eqs.(III.6) and (III.2), the cross sections[1] for VE and VdE of one quanta for normal mode i take the respective simplified forms

$$\sigma_{v_i+1\leftarrow v_i}(\epsilon) = \frac{\pi\hbar^2}{2m\epsilon}(v_i+1)\mathcal{P}_i\ \theta(\epsilon-\hbar\omega_i)\,, \tag{III.9}$$

$$\sigma_{v_i-1\leftarrow v_i}(\epsilon) = \frac{\pi\hbar^2}{2m\epsilon}v_i\mathcal{P}_i\,, \tag{III.10}$$

where m is the reduced mass of the electron-ion system, ϵ is the incident energy of the electron, $\hbar\omega_i$ and v_i are respectively the energy and the vibrational quantum of mode i. $\theta(\epsilon-\hbar\omega_i)$ denotes the Heaviside step function that opens the vibrational excitation channel when the collision energy is larger than one quanta of the vibrational energy for the ith normal mode.

[1]Definition of the cross section is $\sigma_{v_i'\leftarrow v_i}(\epsilon) = \frac{\pi\hbar^2}{2m\epsilon}\left|\mathcal{S}_{v_i'v_i} - \delta_{v_i'v_i}\right|^2$.

The formulas of Eqs.(III.9) and III.10 describe the situation where the electron excites or de-excites the ion and then leaves it.

With the assumptions stated in the preceding section, the DR cross section for capture of the electron by an ion initially on its vibrational level v_i via the temporary capture into a Rydberg state associated to the vibrational ionic level v_i' writes

$$\left\langle \sigma_{v_i}^{DR}(\epsilon) \right\rangle = \frac{\pi\hbar^2}{2m\epsilon}(v_i+1)\mathcal{P}_i\ \theta(\hbar\omega_i - \epsilon), \tag{III.11}$$

where the brackets $\langle\ \rangle$ symbolically refer to a cross section averaged over the Rydberg series of resonances associated with the same vibrational state $v_i' = v_i + 1$ (one quantum transitions) of the ion as well as over the rotational structure of the molecule [Douguet et al., 2012b].

Adding contributions from all normal modes q_i, yields the total DR cross section (accounting for only indirect route)

$$\left\langle \sigma_{\{v\}}^{DR}(\epsilon) \right\rangle = \frac{\pi\hbar^2}{2m\epsilon}\sum_i (v_i+1)\mathcal{P}_i\ \theta(\hbar\omega_i - \epsilon), \tag{III.12}$$

where $\{v\}$ denotes the collection of initial vibrational quantum numbers of all the normal modes. Above, the sum runs over the three modes of BF_2^+; two stretching modes and doubly degenerate transverse mode. The Heaviside step function in $\left\langle \sigma_{\{v\}}^{DR}(\epsilon) \right\rangle$ subtracts the contribution from the normal modes which are energetically allowed to excite. It results in a sharp drops in the cross section.

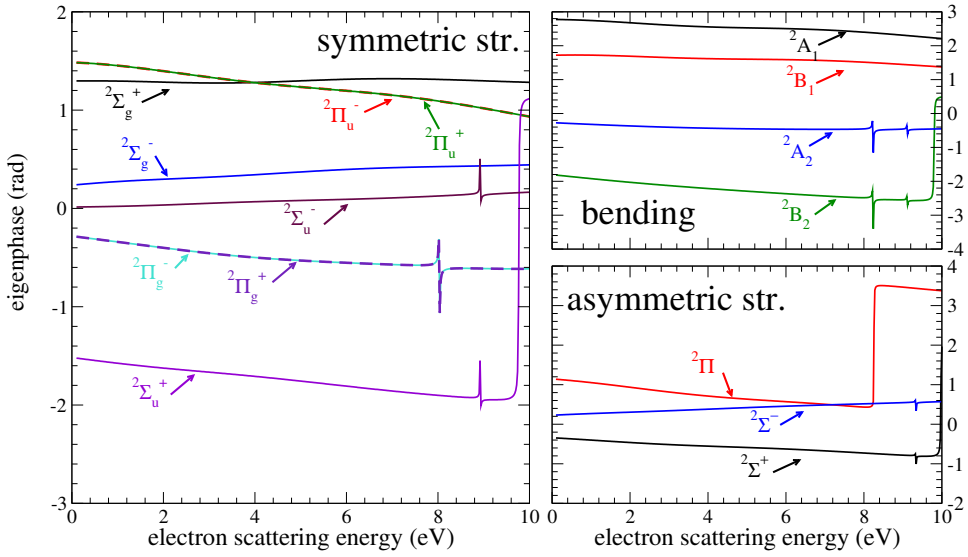

Figure III.2: Eigenphase sums as a function of the electron-scattering energy ϵ for $q_i = 0.01$ (dimensionless) for the symmetric stretching (left panel), bending (right upper panel), and asymmetric stretching (right bottom panel) modes. The curves of different color correspond to different symmetries of the $e^- - BF_2^+$ system.

Figure III.3 illustrates the DR cross-section $\left\langle \sigma^{DR}_{\{v\}}(\epsilon) \right\rangle$ assuming that the initial state of BF_2^+ is the ground vibrational level and thus the electron can only be captured in a Rydberg resonances attached to the first excited vibrational state of each normal mode, excited by the electron. At very low scattering energies, i.e. below 0.02 eV, the DR cross-section is a smooth function inversely proportional to the incident energy of the electron, as predicted by the Wigner threshold law, whereas at higher energies, it exhibits a drop at each vibrational threshold, as expected from Eq.(III.12). In the calculations, the derivatives of $\mathcal{P}_i$ in Eq.(III.12) were obtained using the finite difference method calculated from two values, $q_i = 0.01$ and 0.1, for the displacements in each mode.

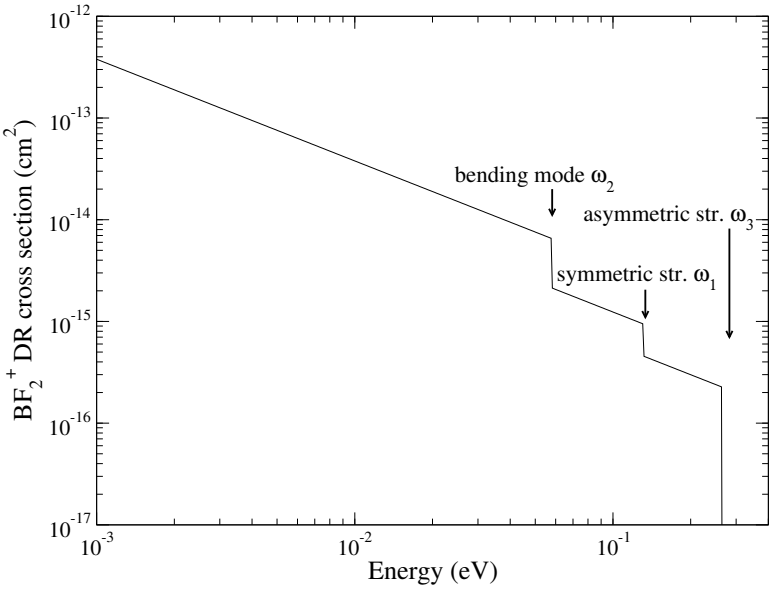

Figure III.3: Cross-section for the DR of BF_2^+. The lowest vibrational threshold of each normal mode is indicated by arrows.

Due to the simple analytical form of the cross-sections, the corresponding rate coefficients are readily evaluated from the general expression of Eq.(I.31) yielding

$$\alpha_{v_i}(T) = \sqrt{\frac{2\pi}{k_b T}} \frac{\hbar^2}{m^{3/2}} \begin{cases} (v_i+1)\mathcal{P}_i \exp\left(-\frac{\hbar\omega_i}{k_b T}\right) & \text{VE} \\ v_i \mathcal{P}_i & \text{VdE} \end{cases}, \tag{III.13}$$

$$\alpha^{DR}_{v_i}(T) = \sqrt{\frac{2\pi}{k_b T}} \frac{\hbar^2}{m^{3/2}} \sum_i (v_i+1)\mathcal{P}_i \left[1 - \exp\left(-\frac{\hbar\omega_i}{k_b T}\right)\right], \tag{III.14}$$

where k_b is the Boltzmann coefficient and T is the temperature. The thermally-averaged rate coefficients for DR and VE are shown in figure 4 of paper .7.

To check convergence of the obtained DR and VE/VdE rate coefficients, we have performed calculations for three sets of parameters (1) the $CAS_1(12,10)$ with the `cc-pVTZ` basis set; (2) a calculation (referred here as `cc-pVTZ` CAS_2) similar to (1) but with a smaller orbital space,

where 8 electrons are kept free in the active space; and (3) a calculation (referred here as `cc-pVQZ` CAS_1) similar to (1) but with the larger basis `cc-pVQZ`. The results are shown in Figure III.4. The difference between the rate coefficients produced in the three calculations for the DR process and the VE of the asymmetric stretching and bending modes is about 4%. The uncertainty of the rate coefficient for the VE of the symmetric stretching mode is larger, varying in the interval 10-40% for different temperatures.

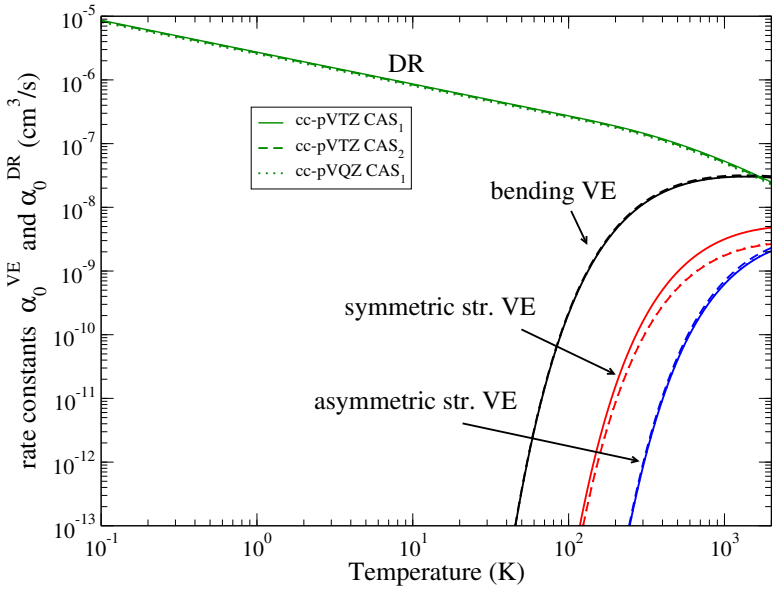

Figure III.4: Dissociative recombination and vibrational excitation of BF_2^+: rate coefficients - Eqs. (III.13) and (III.14). To give an idea about the uncertainty of the present results, we also plotted results of two calculations with the `cc-pVTZ` CAS_2 (dashed line) and the `cc-pVQZ` CAS_1 (dotted line) sets of parameters of the model. For the vibrational excitation of the symmetric stretching mode, the `cc-pVTZ` CAS_2 and `cc-pVQZ` CAS_1 curves are indistinguishable and slightly below the `cc-pVTZ` CAS_1 curve. For the remaining three processes, the three calculations produce the curves almost indistinguishable in the figure.

In addition to uncertainties related to the choice of the model parameters estimated above, the second source of uncertainty deals with the approximation (the capture model) that once the electron is captured into a vibrational Rydberg resonance associated with a closed vibrationally-excited channel, the $e^- - BF_2^+$ system will dissociate rather than autoionize. For small and medium-size polyatomic closed-shell ions such as HCO^+, NH_4^+ or H_3O^+ [Mikhailov et al., 2006b, Douguet et al., 2012b, Douguet et al., 2012a, Fonseca dos Santos et al., 2014a], it has been estimated that the probability of autoionization of vibrational Rydberg resonances is of the order of 10-20% compared to the probability of dissociation. Extending this result to BF_2^+, which is also a closed-shell ion, the overall uncertainty of the present theoretical rate coefficients is below 20-40%.

To test our simplified approach, we compared the cross sections obtained for the bending mode of BF_2^+ to those computed by the complete treatment described in Chapter II, i.e. cross section of Eq.(II.19) evaluated numerically with and/or without the inclusion of the

closed-channel elimination procedure of Eq.(I.19). As an example, Figure III.5 shows this comparison for transitions between the two lowest vibrational levels of bending mode of BF_2^+. The cross sections (solid lines) obtained using the complete theoretical approach exhibit a strong resonant character, absent in a treatment without elimination procedure (dashed lines). The resonances are produced by closed vibrational states of the target. These resonances are washed out when thermally-averaged rate coefficients are computed. Therefore, in the calculation of the rate coefficients, one can use cross sections averaged over the resonances obtained using the simplified approach (dotted lines). Figure III.6 displays the employed probabilities in Fig.III.5. The averaged probabilities obtained from a complete treatment are in good agreement with the one of the simplified approach given by Eq.(III.6).

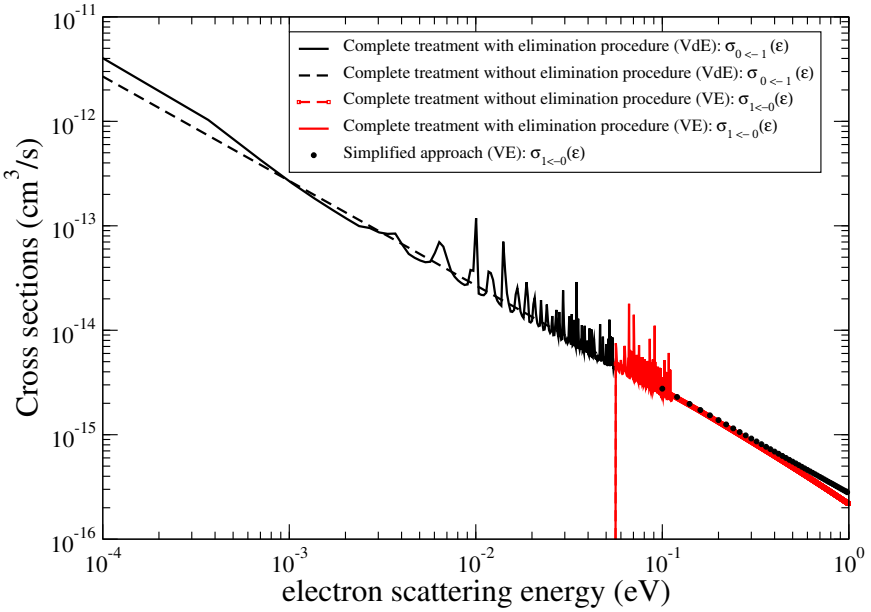

Figure III.5: Vibrational (de-)excitation cross sections for transitions between the two lowest vibrational levels of the bending mode of BF_2^+. Solid lines represent the results obtained using the complete treatment of Equation (II.19) in addition to the closed-channel elimination procedure of Equation (I.19) in dashed lines. Dotted lines show the results from the simplified approach of Equations (III.9) or (III.10).

III.4 Concluding remarks

Contribution within the research axis on the formation of fluorine based-molecules, in particular BF_2^+, was reported briefly in this chapter. A simplified theoretical approach using the normal modes approximation, the vibrational frame transformation and the UK R-matrix code was developed to compute cross-sections and rate coefficients for DR, VE and VdE of BF_2^+ by electron-impact. The thermally-averaged rate coefficients have a simple analytical form. Uncertainty estimations were performed by changing parameters of the scattering model. After benchmarking our model with the complete theoretical approach, we applied it to more complex systems in Chapter I.

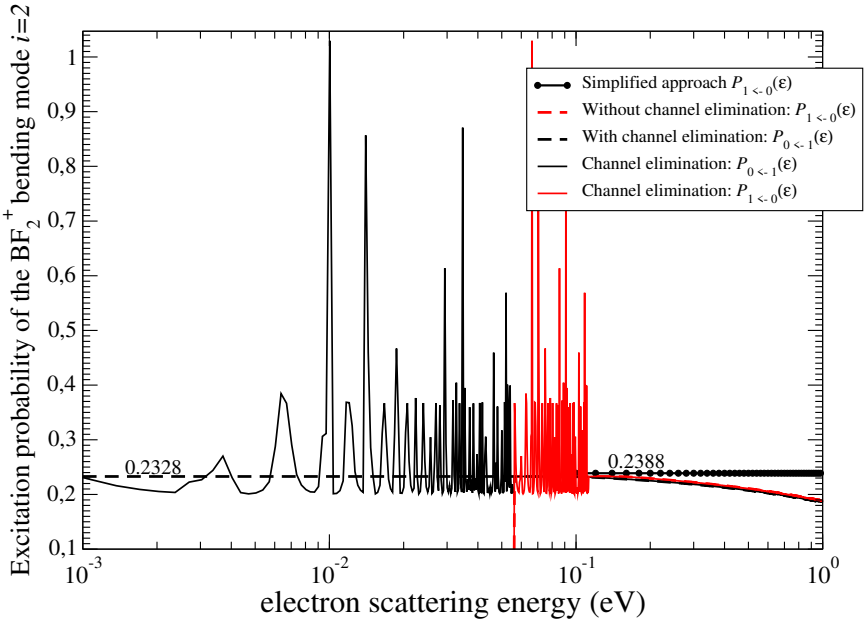

Figure III.6: Vibrational (de-)excitation probabilities, used in Fig.III.5, for transitions between the two lowest vibrational levels of the bending mode of BF_2^+. Solid lines represent the results obtained using the complete treatment in addition to the closed-channel elimination procedure in dashed lines. Dotted lines show the results from the simplified approach using Eq.(III.6).

The obtained thermally-averaged rate coefficients are relevant for the kinetic modeling of molecule based cold non-equilibrium plasmas, in the context of a complete lack of other theoretical or experimental data on these processes for this cation, and are ready to be used in the modeling of fluorine/boron plasma for etching or implantation processes.

The rotational structure of the target ion and of the neutral molecule was neglected in the present approach to be deferred in a further study (see outlooks in Chapter V). This implies that the obtained cross-sections and rate coefficients should be viewed as averaged over initial rotational states and summed over final rotational states of the corresponding initial and final vibrational levels (for VE) or dissociative states (for DR). Purely rotational transitions, i.e. without changing the vibrational state, might be useful to model very cold environments, below 40 K, which is not the case for the presently investigated BF_3 plasma. BF_2^+ has no permanent dipole, so the rotational transitions are likely to have very small cross-sections.

At low collision energies, if the doubly-excited states of the electron-ion system are not energetically accessible, the indirect DR is usually dominant. Therefore, our simplified approach can provide an *ab inito* estimation of the total DR cross section when other more accurate approaches are computationally expensive or not available for polyatomic ions. An implementation of the developed model as module in Quantemol-N is currently performed with Dr. Maria Tudorovskaya, scientific consultant form Quantemol team. The module could be used to compute DR cross sections of molecular ions relevant in the interstellar medium and planetary atmospheres or low-temperature plasma technologies.

Finally, the above work was published in Ref.[Kokoouline et al., 2018]. It has received supports from different programs listed in CV (see Appendix V.2.C). This study has also allowed to develop and formulate ideas for further applications in particular for the HCO^+ and N_2H^+ molecular ions in the context of Dr. Abdillah Abdoulanziz's thesis, co-supervised with Prof. Ioan Schneider at Université du Havre.

IV – Toolkit for teaching quantum mechanics

IV.1 Context and motivation

Since about 70 years, quantum physics is responsible for the technological advances that make modern life possible. For example, without quantum mechanics there would be no transistors, and hence no personal computers and smartphones; no lasers, and hence no Blu-ray players or modern TV; no atomic clocks, and hence no GPS navigation. A new and promising area of research in recent years, at the intersection of mathematics, computer science, and quantum physics, is quantum computers and quantum information [Shor, 1995, Britt and Humble, 2017]. The developed processes in this area, based on a novel way of information coding using the quantum-bit (qbit), are going to transform many sectors such as artificial intelligence [Cai et al., 2015], online security [Lucamarini et al., 2009], or drug development [Zhou et al., 2010]. To support these advances and further new technologies, based also on principles governing the microworld, knowledges of quantum mechanics are essential for future scientists, engineers, medical doctors, and many other professions.

Typically, quantum physics/mechanics (QM) is taught either as a pure math course or as a descriptive phenomenological discipline, in which different core concepts of quantum physics appear to students to be disconnected from each other and from their real-life experience. Moreover, designing laboratory experiments for a course of QM, as commonly made for the course topics in Newtonian mechanics and classical electromagnetism, is expensive or/and not available for the most of the core QM concepts [Singh and Marshman, 2015]. These difficulties make quantum mechanics to new students counter-intuitive, in contrast to other areas of physics that allow describing phenomena objectively observed in the real world, and hence uneasy to apprehend. Over the last two decades, several excellent physics-education studies reported this issue [Carr et al., 2009, McKagan et al., 2010, Deslauriers and Wieman, 2011, Zhu and Singh, 2012a, Zhu and Singh, 2012b, Sadaghiani and Pollock, 2015] and proposed solutions on how to improve teaching QM [Müller and Wiesner, 2002, McKagan et al., 2008, Kohnle et al., 2015, Krijtenburg-Lewerissa et al., 2017]. There is a general consensus that the use of multimedia in QM classes helps to make teaching QM more efficient. This conclusion consolidated me in the idea of integrating experiential learning in my QM classes (since 2016) at Centralesupélec (CS), taking the form of computer-simulated experiments.

For this purpose, with my colleague Prof. Viatcheslav Kokoouline from the University of

Central Florida (UCF), we have formulated and developed an initial version of a complete course of undergraduate quantum mechanics based on numerical experiments. The framework combines a set of PYTHON numerical codes and a graphical interface allowing students to prepare and run numerically-simulated experiments demonstrating all topics of a standard QM course, usually covered in a formal mathematical approach. The most of the codes are simplified versions of previous codes developed in my research activities in the area of atomic, molecular, and optical physics. These codes are published in two textbooks [Ayouz et al., 2020, Ayouz et al., 2022]. As for the graphical interface, it was designed in the context of a post-doc, Dr. Alexander Korovin, funded by IDEX Paris-Saclay.

In the following, I will provide the basic ingredients of the numerical experiments, i.e. programming language, mathematical techniques and the theoretical topics covered by simulations, as well as the two components of the developed digital learning environment.

IV.2 Basic ingredients

IV.2.A Programming language

For the purpose of the suggested transformation of our QM courses, PYTHON language was found convenient because it offers a wide range of operations and functions allowing to manipulate easily with vectors and matrices (product of matrices, diagonalization,...) as well as special mathematical functions (Legendre, Laguerre, Chebyshev, Hermite, Bessel and other functions). In addition, graphical representations can be produced almost directly-using the plot () function, unlike some languages, which require additional graphical software (C or FORTRAN for example). The plot can also be displayed at each iteration, which, for example, makes it easy to visualize the time-evolution of wave functions. The simplicity of the syntax, the great flexibility in the utilization and execution of the programs as well as the free access are also among the advantages.

The codes were developed in PYTHON under Spyder (via ANACONDA), which is a powerful interactive development environment for the Python language with advanced editing, interactive testing, debugging and introspection features.

IV.2.B Mathematical techniques

For computer modeling several numerical techniques will be employed. As hinted above, they are chosen with two objectives that (1) they provide an intuitive and visual picture of the QM concepts and processes and (2) they could be used in an actual research work for simple projects. The methods may not be extremely accurate for idealized situations (such as a purely theoretical δ-potential or the infinite square wall) due to discontinuities in idealized potential, but they are very accurate for realistic potentials, which usually don't have any discontinuities. Below, we will describe briefly the employed techniques.

Discrete variable representation method for solving the stationary Schrödinger equation

In the described numerical method, wave functions are mainly represented using the Fourier grid Hamiltonian method (FGH), which is widely used in different research areas, in particular, to describe quantum molecular dynamics [Kosloff, 1988] and to solve the stationary Schrödinger equation [Dulieu et al., 1997, Kokoouline et al., 1999, Ayouz and Kokoouline, 2016].

FGH is one of the variety of the Discrete Variable Representation (DVR) methods that uses a basis of complex exponent functions. The DVR methods were initially introduced by Harris *et al.* [Harris et al., 1965] for calculating matrix elements of complicated potential functions in a truncated basis set. Later, Dickinson and Certain [Dickinson and Certain, 1968] derived the transformation matrix with Gaussian quadrature for standard orthogonal polynomials. The DVR method is sometimes referred to as the Lagrange method [Baye, 2006], where the functions are usually represented on a coordinate grid or lattice. Analytical expressions for the matrix elements of operators in the DVR basis is an important advantage for the approach adopted here for numerical experiments: An explicit form of the kinetic energy operator allows one to avoid computing derivatives numerically using finite-difference approximations, as is the case for iterative methods such as Euler or Runge-Kutta. It therefore simplifies the structure of the codes, making them simple to handle by an inexperienced student. The main elements of the method used here are given below.

One of the core concepts of the non-relativistic QM is the equation of state: the stationary Schrödinger equation. Typically (in research or in QM courses), one needs to find solutions of the equation in one dimension

$$[\mathbf{T}(x) + \mathbf{V}(x)]\,\Psi(x) = \left[-\frac{\hbar^2}{2m}\frac{d^2}{dx^2} + \mathbf{V}(x)\right]\Psi(x) = E\Psi(x), \tag{IV.1}$$

where m is the mass of the particle. In general, FGH starts by defining a grid of N points over coordinate x such as

$$x_0 = x_0 + i\Delta x \qquad i = 0, 1, \cdots N-1, \tag{IV.2}$$

where

$$\Delta x = \frac{x_L - x_0}{N}, \tag{IV.3}$$

is the constant grid step and x_0 and x_L are respectively the initial and final grid points of the space interval where the equation is solved. It is assumed that outside of the interval the wave functions of interest are negligible within the required numerical accuracy.

The grid step Δx and the interval $[x_0, x_L]$ are the key parameters determining the accuracy of obtained numerical results, which are the energies E and wave functions $\Psi(x)$. The grid step Δx determines the largest possible momentum p_{grid}, which could be represented by the grid. If the largest and smallest values of the potential $V(x)$ are $V_{\max}$ and $V_{\min}$, respectively, the step should satisfy [Kokoouline et al., 1999]

$$\Delta x = \frac{\pi}{p_{\text{grid}}} \leq \frac{\pi}{\sqrt{2m(V_{\max} - V_{\min})}}. \tag{IV.4}$$

The wave function $\Psi(x)$ in this method is expanded in terms of the orthonormal DVR/FGH basis set functions as

$$\Psi(x) = \sum_i c_i \varphi_i(x), \qquad \langle \varphi_i | \varphi_i \rangle = \delta_{ii'} \,. \tag{IV.5}$$

The functions $\varphi_i(x)$ form an orthonormal set [Bulgac and Forbes, 2013]

$$\begin{aligned} \varphi_i(x) &= \sum_{k=-N/2}^{N/2-1} \frac{1}{L} \exp\left\{ \imath p_k (x - x_i) \right\} \\ &= \frac{1}{L} \sin\left[\frac{\pi(x-x_i)}{\Delta x} \right] \cot\left[\frac{\pi(x-x_i)}{L} \right], \end{aligned} \tag{IV.6}$$

with $p_k = \frac{2\pi k}{L}$ and $k \in \left(-\frac{N}{2}+1, -\frac{N}{2}+1, \cdots, \frac{N}{2}-1\right)$. Note that $p_{N/2} = p_{\rm grid}$. Examples of functions $\varphi_i(x)$ with $\Delta x = 1$ are shown in Figure IV.1 by solid lines.

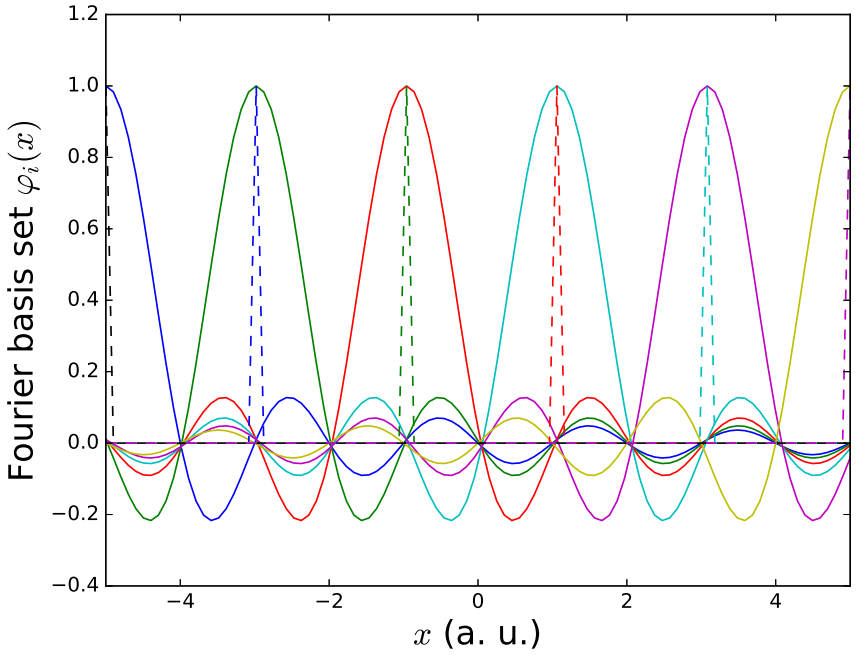

Figure IV.1: FGH basis functions $\varphi_i(x)$ for $N = 5$. Solid and dashed lines represent the basis functions of Eq.(IV.6) for $\Delta x = 1$ and $\Delta x \neq 1$, respectively.

In the basis of functions $\varphi_i(x)$, both operators $\mathbf{T}$ and $\mathbf{V}$ are represented by $N \times N$ matrices. The potential operator $\mathbf{V}$ is diagonal in this representation

$$V_{ii'} = \int dx \varphi_i^*(x) V(x) \varphi_{i'}(x) = V(x_i)\delta_{ii'}. \tag{IV.7}$$

The kinetic energy operator $\mathbf{T}$ is diagonal in the momentum representation, which enables one to evaluate the analytical form of matrix elements of $\mathbf{T}$ in the coordinate representation:

$$T_{ii'} = \int dx \varphi_i^*(x) T(x) \varphi_{i'}(x) = \begin{cases} \frac{\pi^2(N^2+2)}{6m(N\Delta x)^2} & i = i' \\ (-1)^{i-i'} \frac{\pi^2}{m(N\Delta x)^2} \frac{1}{\sin^2[(i-i')\pi/N]} & i \neq i' \end{cases} . \tag{IV.8}$$

A convenient property of the FGH representation is that the coefficients c_i of the expansion in Eq. (IV.5) give also the values of $\Psi(x)$ at the grid points $\Psi(x_i) = c_i/\sqrt{\Delta x}$.

Once the matrix elements of the potential and kinetic energy operators are obtained, the matrix of the Hamiltonian operator $\mathbf{T}+\mathbf{V}$ is written in the explicit form as

$$H_{ii'} = \left\{ \begin{array}{ll} \frac{\pi^2(N^2+2)}{6m(N\Delta x)^2} & i = i' \\ (-1)^{i-i'} \frac{\pi^2}{m(N\Delta x)^2} \frac{1}{\sin^2[(i-i')\pi/N]} & i \neq i' \end{array} \right\} + V(x_i)\delta_{ii'} \,, \tag{IV.9}$$

where N is assumed here to be an even integer.

Eigenvalues E_n and eigenfunctions $\Psi_n(x)$ of the Hamiltonian, $\mathbf{H} = \mathbf{T} + \mathbf{V}$, are obtained using numerical PYTHON routines of $N \times N$ matrix diagonalization. The diagonalization produces the eigenfunctions in terms of the coefficients c_i^n of expansion (IV.5). The normalization of the Ψ_n and c_i^n is such that

$$\int_{x_0}^{x_L} |\Psi_n(x)|^2 dx \approx \sum_{i=0}^{N-1} |\Psi_n(x_i)|^2 \Delta x = \sum_{i=0}^{N-1} |c_i^n|^2 = 1 \;\; \text{for all } n. \tag{IV.10}$$

It should be stressed that for a few case studies, we also use the DVR with basis functions constructed from sin, Legendre, Laguerre, or Chebyshev polynomials. Details on the form that should take the Hamiltonian (IV.9) in such basis can be found in Refs.[Szalay, 1993, Ayouz et al., 2020] and therein.

The Chebyshev polynomial expansion method for solving the time-dependent Schrödinger equation

When solving the one-dimensional time-dependent Schrödinger equation

$$\imath\hbar \frac{\partial \Psi(x,t)}{\partial t} = \mathbf{H}\Psi(x,t), \tag{IV.11}$$

in most cases one employs the second-order differences, split operator propagation, Chebyshev polynomial expansion or Lanczos method to represent the time variable. Among these methods, the propagation approach using the FGH method (introduced above) and the Chebyshev expansion (FGH-C) is one of numerous pseudo-spectral techniques for the time evolution problem. Details on this method and comparison with others have been reported in [Leforestier et al., 1991, Monnerville and Robbe, 1994, Kosloff, 1994].

For the sake of consistency with the DVR/FGH method employed in the stationary case, we choose FGH-C method in which the solution of Eq.(IV.11) is given by the operator $\exp\left(-\imath\frac{\mathbf{H}\Delta t}{\hbar}\right)$:

$$\Psi(x, t+\Delta t) = e^{-\imath\frac{\mathbf{H}\Delta t}{\hbar}} \Psi(x,t) \equiv \mathbf{U}(\Delta t)\Psi(x,t) \tag{IV.12}$$

Thus, the problem of the time propagation can be separated in two essential parts.

1. A choice of a basis of the representation of the wave function $\Psi(x,t)$; exponential function in FGH.

2. The procedure of evaluation of the propagation operator $e^{-\imath\frac{\mathbf{H}\Delta t}{\hbar}}$ on the wave function $\Psi(x,t)$: $\mathbf{U}(\Delta t)\Psi(x,t)$.

The propagation (IV.12) is carried out using an expansion of the propagation operator $\exp\left(-\imath\frac{\mathbf{H}\Delta t}{\hbar}\right)$ as a function of t in a series of Chebyshev polynomials:

$$\mathbf{U}(\Delta t) \approx \sum_{k=0}^{N_c} a_k g_k \left(-\imath\frac{\mathbf{H}\Delta t}{r}\right), \qquad a_k = e^{\imath(r+q)} C_k \beth_k(r), \tag{IV.13}$$

where $\beth_k(r)$ designates the Bessel function of order k and N_c is the number of expansion coefficients. The following abbreviations were also used

$$\frac{r}{\Delta t} = \frac{E_{\max} - E_{\min}}{2} \qquad \text{and} \qquad q = V_{\min}\Delta t, \tag{IV.14}$$

where $\frac{r}{\Delta t}$ denotes the half of Hamiltonian energy spectrum with $E_{\min} = V_{\min}$ and $E_{\max} = V_{\max} + \frac{p_{\max}^2}{2m}$ such as $p_{\max} = \hbar\pi/\Delta x$. Coefficients a_k are defined from the Bessel function $\beth_k(r)$ with $C_k = 1$ for $k = 1$ and $C_k = 2$ when $k > 1$. Finally, g_k functions are obtained making use of the recurrence relation

$$g_k(\hat{z}) = 2\hat{z}g_{k-1}(\hat{z}) + g_{k-2}(\hat{z}), \tag{IV.15}$$

where

$$\hat{z} = -\frac{\imath}{\hbar}\mathbf{H}\Delta t, \quad \forall\ \hat{z} \in [-1,1] \qquad \text{and} \qquad \begin{cases} g_0(\hat{z}) &= 1 \\ g_1(\hat{z}) &= z \end{cases}.$$

Note that the refinement of the scheme is based on increasing N_c and not the time step Δt, as usual. It is well known that the expansion by complex Chebyshev polynomials gives the best approximation among other possible expansions [Tal-Ezer and Kosloff, 1984]. Above, $\mathbf{H}\Delta t$ is $N \times N$ matrix operator where N being the number of grid points, defined above in Eq.(IV.3). Elements of the matrix $\mathbf{H} = \mathbf{T} + \mathbf{V}$ are given by Eq.(IV.9).

IV.2.C Theoretical topics

The main topics of the developed course are the same as in a standard undergraduate course of QM for physics and chemistry majors. The PYTHON codes solve elementary and more complex problems covering topics such as the piecewise potentials, measurements in QM, uncertainty and sperposition principles, WKB-approximation, $\alpha-$decay, harmonic oscillator, hydrogen atom, diatomic molecules, propagation of wave packets, methods of approximation, Hartree-Fock method, Spin, etc.

Demonstrating all topics listed above requires some additions to methods introduced in Section IV.2.B. The main elements are given below.

- To treat $\alpha-$decay in polonium, resonant states of the atom have to be determined. This can be accomplished making use of the complex absorbing potential (CAP) formalism, combined to the DVR methods. Again, the CAP formalism was developed in research work and employed, for instance, in computing the DR cross section of CH^+. Details on that method are given in Chapter I. Recall that by adding the CAP, the Hamiltonian matrix becomes non-Hermitian, requiring a special library for diagonalization. This latter, namely, LAPACK, is available in PYTHON without extra efforts.

- Extending Eq.(IV.9) to two (or three) dimensions is straightforward and reads

$$H_{i,j} = T_{ii'}\delta_{jj'} + T_{jj'}\delta_{ii'} + V(x_i, y_j)\delta_{ii'}\delta_{jj'} \,, \tag{IV.16}$$

  where $j-$index stands for $y-$coordinate.

- The rotational structure of a molecule can be taken into account using the spherical harmonics for representing the angular wave functions. It follows that a centrifugal barrier should be added into the radial Schrödinger equation. The potential in Eq.(IV.9) reshapes as

$$V(r_i)\delta_{ii'} \;\rightarrow\; \left(V(r_i) + \frac{\hbar^2 l(l+1)}{2mr_i^2}\right)\delta_{ii'} \,, \tag{IV.17}$$

  with l being the eigenvalues of the angular momentum operator.

- To obtain reflection and transmission coefficients of barriers, a projection method is employed in which the wave packet, obtained at the end of the propagation using Eq.(IV.12), is projected onto reflected or transmitted wave functions. Similar method will be used to compute branching ratios in DR of small polyatomic ions in Section V.2.C (planned research work).

- When a non-orthonormal basis sets (in contrast to those employed in the DVR methods) are used to represent the kinetic operator, such as atomic orbitals in Hartree-Fock methods, a generalized eigenvalue problem has to be solved: $\mathbf{H}\Psi = E\mathbf{S}\Psi$ where $\mathbf{S}$ is the overlap matrix. This latter rises from the non-orthogonality of the basis. In practice, an orthogonalization procedure (canonical, symmetric or Gram-Schmid) is performed to save time spent on calculation.

- Take into account the spin, of an electron for instance, is also straightforward in the DVR methods since the equation to be solved will be somewhat similar to Eq.(IV.16), where $j-$index now stands for the two possible projections of the spin $\pm 1/2$.

With the above additions, all major concepts of QM are covered by the developed digital learning environment and this is made possible due to the adopted DVR method. Indeed, this latter is easy to implement in computer modeling (differential operators have analytical expressions according to Eq.(IV.8)) and intuitive because it fully reconciles mathematical tools of QM and digital programming. Thus, mathematics that are employed, in general, heavily in explanations of postulates could be demonstrated with codes since students will be able to manipulate with matrices representing QM operators; inverting them, finding and analyzing their eigenvalues, analyzing eigenvectors and eigenfunctions, calculating expectation values of observables using dot/matrix products.

IV.3 Achievements: the digital learning environment

IV.3.A Python numerical codes

A standard code starts its execution by the variable "__name__" having the value "__main__" which represents the main program. In this program, we declare variables of the problem,

tables, constants, and the required libraries to be used during the execution. The called functions from the main program will return an operation or calculations such as the desired wave functions. Figure IV.2 displays the general structure of the majority of the codes dealing with the above topics. These codes are simplified versions of those developed in my research activities. Hence, they are use-friendly allowing a quick handling for further utilization: as tool, for instance, to teach the course of Computational Physics and test the approximation methods commonly thought in QM course for solving the Schrödinger equation. Note that atomic units for masses, energies, distances and times are adopted in the codes.

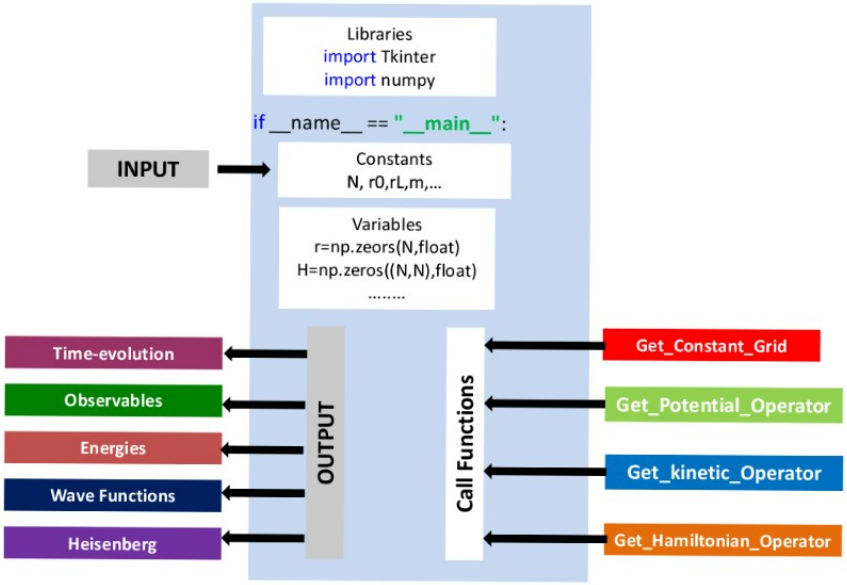

Figure IV.2: The general structure of the majority of the codes for modeling QM phenomena and demonstration of main QM concepts.

IV.3.B Graphical interface

In order to make the codes accessible to a large public, we have designed, in the context of post-doc of Dr. Alexander Korovin, a preliminary version of the graphical interface, that can be accessed at this address http://prd-mecaqu.centralesupelec.fr/. Currently, the interface works and contains draft versions of 10 chapters including most of the preceding discussed topics.

Figures IV.3 and IV.4 display two snapshots of the draft version of the web-interface. The snapshot (Fig.IV.3) of the front page of the preliminary version of the learning environment looks like a table of content of a book (in the spirit of published textbooks). Links to different chapters lead to web-pages of corresponding topics of the class. Figure IV.4 shows the logical structure of the interface of the learning environment as well as an example of in-class activities on the topic of the harmonic oscillator. In the figure, the following abbreviations are used. CGI: Computer-generated imagery. It is a computer graphics application to create images.

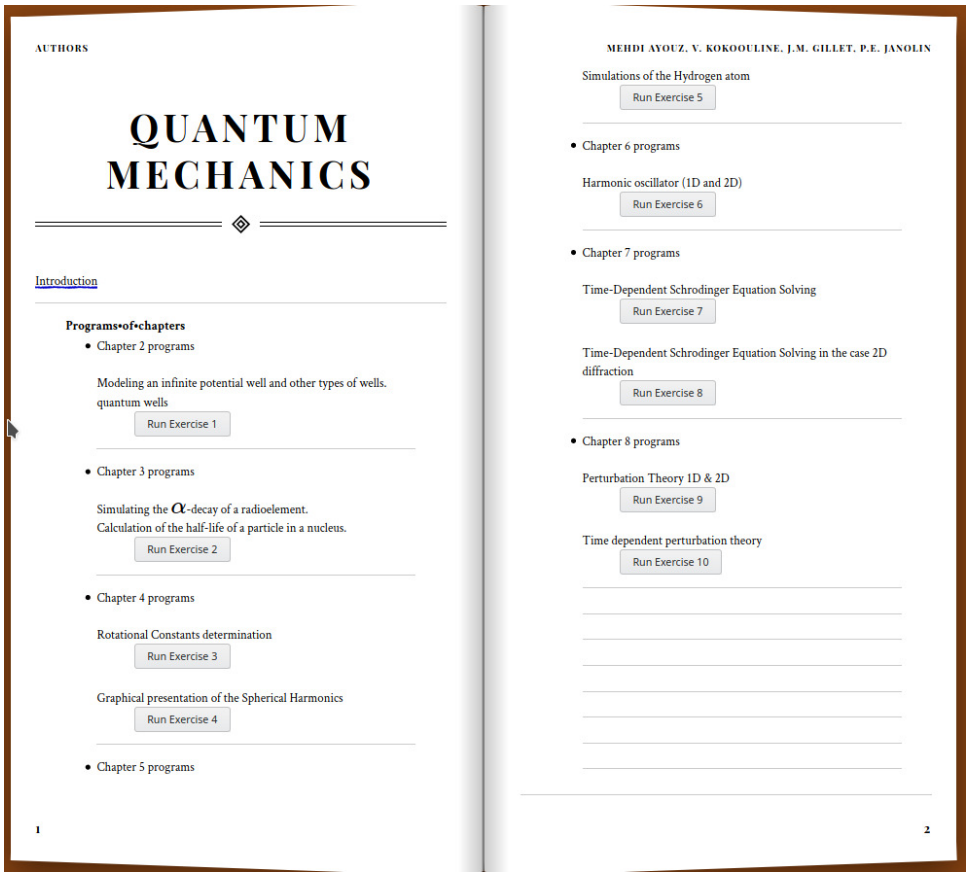

Figure IV.3: The front page of the draft version of the QM learning environment under development.

NGINX: a web server used as a reverse mail proxy and HTTP cache. AJAX: Asynchronous JavaScript + XML programming languages used to create web applications. JSON: is an open-standard file and data interchange format that uses human-readable text to transmit data objects consisting of attribute-value pairs and array data types. js - JavaScript: a high-level programming language used for web applications.

Figure IV.5 demonstrates a draft version of the interface for material on the time-dependent Schrödinger equation, for instance. Various functionalities are available in the web-interface for the other topics:

- Upload potential energy data.
- Choose one of the "standard" potentials (step-like, square well, etc.).
- Enter an analytical formula for a potential energy or a physical disturbance, in studying methods of approximation, especially, for the perturbation theory.
- Modify the input parameters,

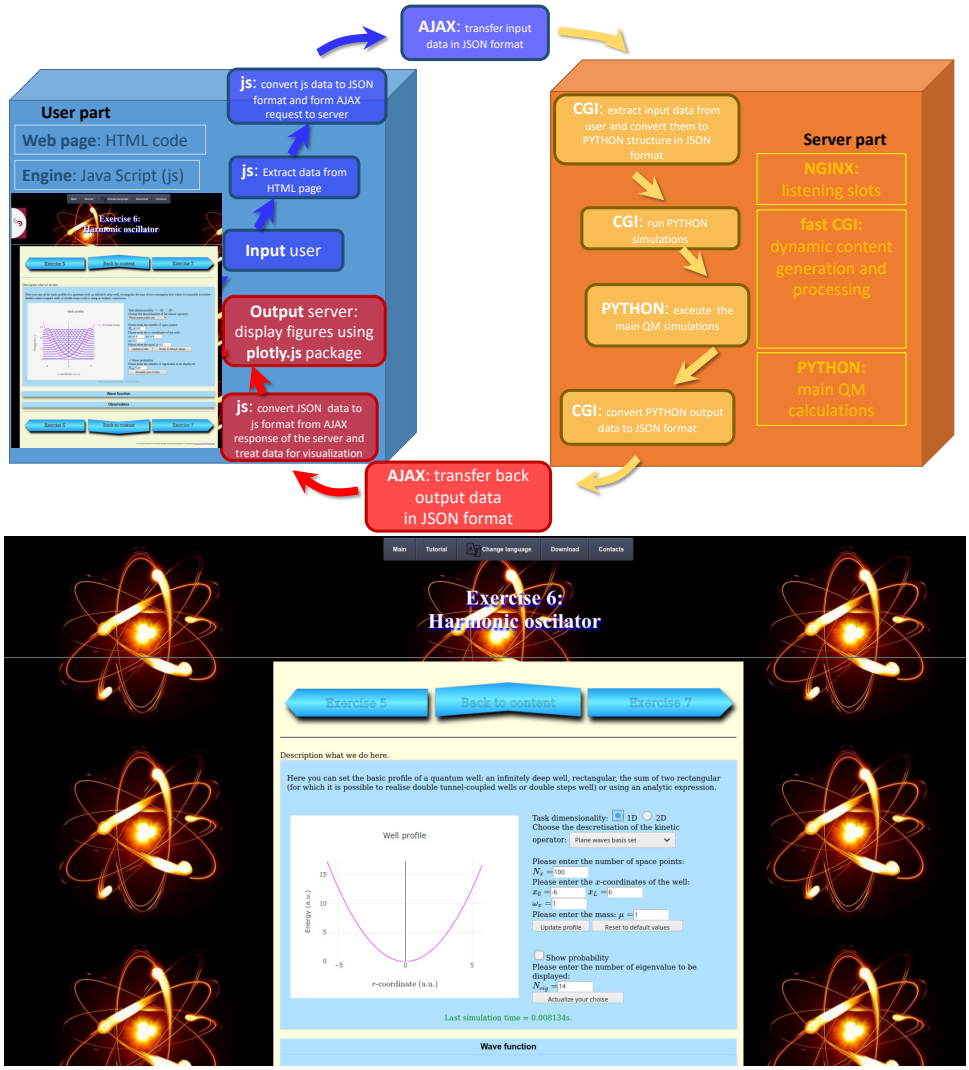

Figure IV.4: Logical structure of the interface of the learning environment in the upper panel. Lower panel shows the preliminary graphical environment for in-class activities on the topic of the harmonic oscillator (one of the topics listed non-exhaustively in Section IV.2.C). The figure shows the potential and several boxes to modify parameters of the problem and observables to watch ("measure") in the computer-modeled experiment. The lower part of the interface, allowing to visualize wave functions and different expectation values of observables, is not shown here to save space (see the online version

- Visualize wave functions, observables (energy, position, momentum,..) and test the Ehrenfest theorem.
- Download PYTHON codes or data such as the wave functions.
- Save figures and videos (wave packet propagation) for further utilizations.

The current interface can be used by instructors from other schools and universities

through our servers (CS or UCF) or in their own servers (online version). A stand-alone distribution (as an installation file) that can be installed on their own computers, as offline local use, was also developed for Linux and Windows operating systems. All these tools could be employed as course support.

IV.4 Concluding remarks

Based on codes carried out in my research activities, we developed an original tool to make teaching QM more efficient and accessible to undergraduate/graduate students (via online and blended modes). The idea of this project came from our experience of teaching at CS and UCF. The digital learning environment combines a set of PYTHON codes and a graphical interface gathering up a numerically-simulated experiments that demonstrate all topics of a standard QM course. The PYTHON codes are user-friendly, and the employed methods, namely, DVRs, permit to reconcile mathematical concepts of QM and programming. As for the web-interface, it allow users to manipulate with the codes, the wave functions, and observables. This pedagogical tool will be made available to the community either using our own servers (CS and UCF) or via a stand-alone distribution (as an installation file) that can be installed on other instructor's servers (online)/computers (offline) for their local use.

Further developments are planned in near future and would be a part of the NSF project on *Improving Undergraduate STEM Education*. Such developments will include preparation of (a) short lectures covering theoretical aspects of the QM concepts, (b) in-class activities and (c) laboratory assignments with and without the learning environment, (d) homework assignments. Some missing codes (in the list of QM topics above) should still be developed. Some other features that could be also considered are to integrate the developed tool either with (i) LMS (Learning Management System as Daskit that is available at CS) giving the possibility for the students to submit directly results of their experiental work (lab reports) or with (ii) a quantum chemistry packages (Molpro/Gaussian) for visualizing atomic/molecular orbitals and understanding the nature of the bonds (covalent, ionic) in a molecule.

Finally, we started testing the proposed teaching approach at CS in my quantum and statistical mechanics and research program classes. First feedback from students are positive which encourage us to accomplish tasks mentioned above. More tests are planned for the upcoming academic year. In parallel, this pedagogical tool will be tested in the Fall 2020 semester at the UCF Physics department in the class of undergraduate quantum mechanics taught by Prof. Kokoouline. Studies about the efficiency of the teaching strategies will be performed and published.

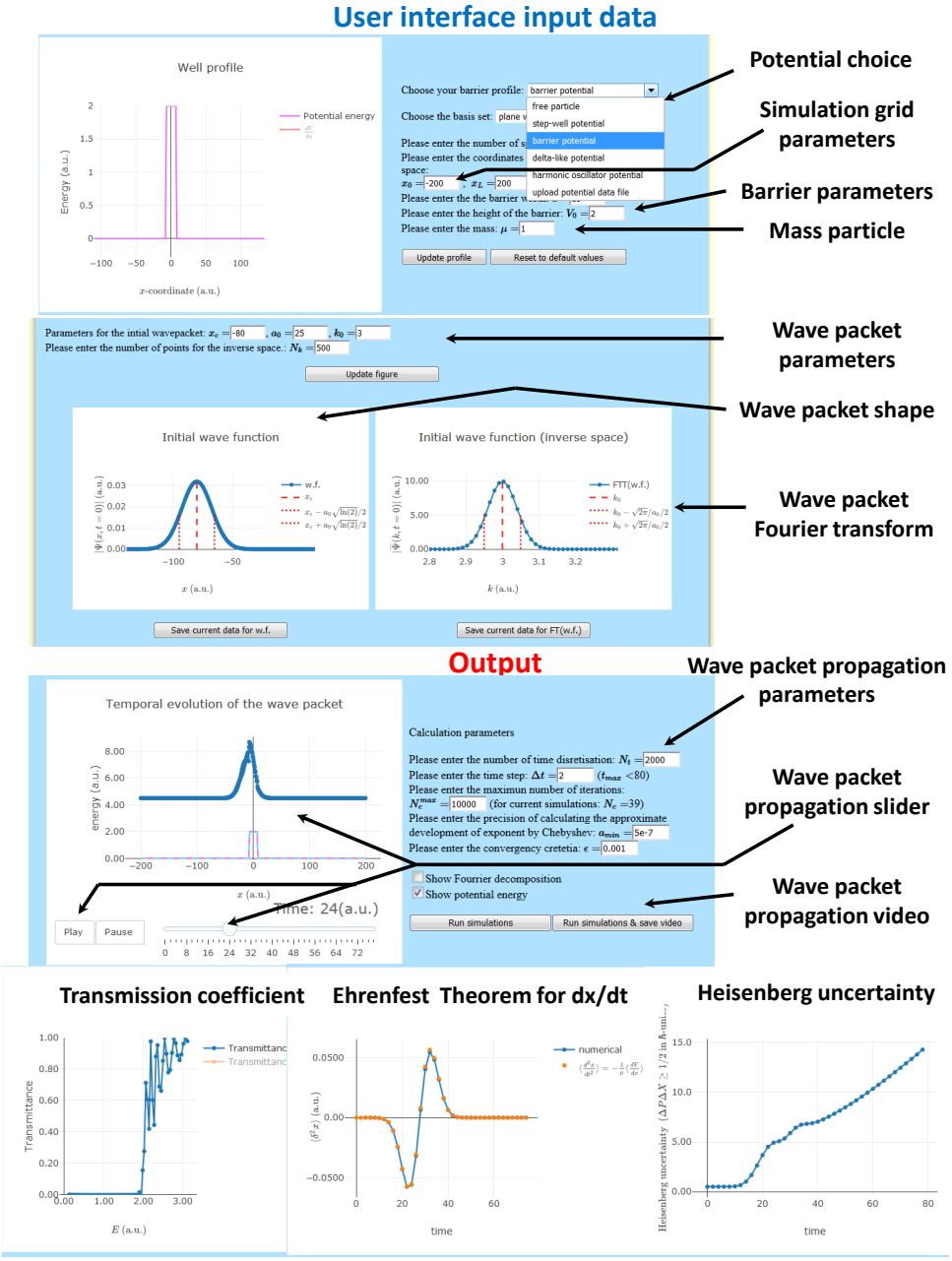

Figure IV.5: The draft version of the interface for wave packet propagation and the time-dependent Schrödinger equation. The students can choose one of the "standard" potentials (step-like, square well, etc.) to monitor the time-dependent evolution, or to use their own potential uploadable as a data file with values of the potential on a grid of points. Several observables can be monitored during the wave-packet propagation. Laboratory and homework assignments on the topic will be added later.

V – Conclusions and perspectives

V.1 Conclusions

The most relevant studies of my projects and supervisions (see CV in Appendix V.2.C) were described in the preceding chapters. I have made a significant contribution into the determination of reliable data for atomic and molecular reactions especially those involving electron-molecule collisions at low energy (see Figure.1). My students and I first focused on studying the simplest diatomic systems to benchmark our developed theoretical models, after which we worked on extending these models to large molecular ions and to the neutral species. Our theoretical models (depicted in Figures I.1 and II.1) are based on first principles. They employ the following: (i) the R-matrix method to compute *ab initio* electronic bound and continuum states, (ii) the vibrational frame transformation combined to, in case of ions, (iii) the closed-channel elimination procedure, in a spirit of molecular quantum defect theory, in order to construct an energy-dependent scattering matrix. This matrix describes interactions between vibronic channels of the target induced by the incident electron. For polyatomic molecules, an additional approximation of the theoretical methods was introduced: the use of the normal mode approximation for vibrational states of the target.

The proposed methods have allowed for computing ro-vibronic excitation (RVE) and dissociative recombination (DR) cross sections, as well as related rate coefficients, of various polyatomic systems of astrophysical (HeH^+, $CH_2NH_2^+$, NH_2CHOH^+), material development (BF_2^+) and atmospheric depollution (NO_2, N_2O) interest. Applications to ions with low-energy excited states were successful, as with CH^+. Such ions were known to be difficult to treat theoretically using previous theoretical methods. Certain precautions, nevertheless, were taken to extend the models to neutral molecules, especially on the use of frame transformation procedures. Our studies have afforded us, on one hand, to provide an upper limit for the total rate coefficient of DR (where data are not available) and on the other hand, to confirm previous calculations. These outcomes could be used for plasma models in planetary science, interstellar medium, and for technologies.

It has to be stressed that the developed theoretical approaches are general since they require only a method to determine the scattering or reaction matrices. This can be accomplished from the electron-scattering codes such as the U.K. R-matrix, used over this manuscript through the Quantemol-N suite, the complex Kohn method or the Schwinger variational principles. We are currently implementing our models as a module in Quantemol-N, to compute cross sections and related rate coefficients of VE and DR of polyatomic molecules

by electron impact; conducted in collaboration with Prof. Kokoouline from UCF and Dr Maria Tudorovskaya, scientific consultant form Quantemol team. We have also developed a complete course of undergraduate quantum mechanics, whose framework combines a set of PYTHON numerical codes and a graphical interface allowing students to prepare and run numerically-simulated experiments, demonstrating all topics of a standard QM course, usually covered in a formal mathematical approach. This project aims to address difficulties for undergraduate students in learning QM concepts. Further developments planned for the near future in both educational and research terms are stated thereafter.

V.2 Perspectives

My planned research program is a continuation of the previously-conducted studies. Figure V.1 resumes my plans for the next 4-year period, generally organized in three scientific work packages as follows.

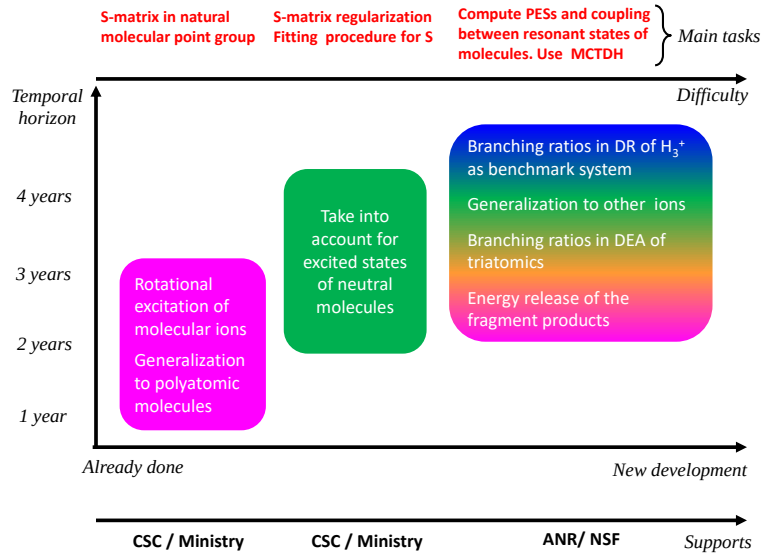

Figure V.1: *Schematic diagram summarizing the planned research program for the next 4-year period. Main tasks are listed with respect to their difficulties of realization.*

V.2.A Rotational excitations of molecular ions in their electronically-excited states

In many low-temperature ionized environments such as ISM, planetary atmospheres and technological plasmas, cross sections for vibronic excitations are important for understanding and modeling these environments, especially, when including the rotational structure of molecules in collisions with electrons. Therefore, I plan to extend the study of HeH^+, where we developed models for RE+VE of linear molecules, to CH^+ and include its rotational structure, in addition to its vibronic structure.

For this purpose, a complete rovibronic frame transformation (RVFT) is needed in combination with CCE-MQDT procedure to construct an energy-dependent scattering matrix in the laboratory frame. This matrix describes the interactions between rovibronic channels of CH^+ induced by the incident electron. Numerically, we obtain the body-frame scattering matrix (using the UK R-matrix code) in the subgroup C_{2v}, included in the natural $C_{\infty v}$ symmetry group of the ion. When various electronic states with different symmetries are included in the calculations, one needs to transform $\hat{S}^{C_{2v}}$ into $\hat{S}^{C_{\infty v}}$. This can be accomplished through the spherical harmonics transformation according to Tables I.1 and I.2.

The second step will generalize the developed model for linear molecules to asymmetric top polyatomic targets. This step is straightforward and should be carried out in the context of a Ph.D. research work funded by CSC or ministry (INTERFACES).

V.2.B Electronically-excited states of neutral molecules

As emphasized in the preceding chapters, the developed models are based on the approximation that the S-matrix for electron-molecules collisions is energy-independent, so far. This holds for ions when (i) the scattering electron energy is not large enough to excite the target ion electronically but also (ii) in absence of electronic resonances appearing when the potential energy surface (PES) of the doubly-excited neutral molecule (electron-ion system) crosses the ionic PES near the equilibrium geometry (CH^+ case for instance).

Fortunately, this assumption was fulfilled for e^-NO_2 and e^--N_2O collisions as revealed by a detailed analysis of eigenphase sums, so that the vibrational VFT could be accomplished. The S-matrix, however, does depend on the scattering electron energy for neutral molecules, in general.

Due to a variety of applications in plasma technology, the EE process including VE should be investigated. I am thus planning to extend the previous study on NO_2 making use of the method developed for CH^+. I identity three main tasks:

- Choosing a different normalization factor for the scattering electron wave function, the energy dependence of $\hat{S}$ can be removed. Then, the renormalized $\hat{\tilde{S}}$ is energy-independent so that VFT can be employed. After VFT, the renormalization factor is multiplied back, and the energy dependence is recovered to compute the cross sections.
- Another approach would be needed were there to exist electronic resonances or a sufficiently high total energy of the system for all collision channels to be open for ionization. Similar to the "closed-channel-elimination" procedure used for ions, I am planning to adapt this procedure in combination with the Breigt-Wigner formula so that the e^--NO_2 scattering physics below the first electronic state can be represented using an energy-independent multichannel scattering matrix evaluated above.
- To accomplish VFT in Eq.(II.17) within the preceding procedure, one has to evaluate the matrix elements $\langle\psi_1(\mathbf{q}_1)|\,\hat{S}\,|\psi_2(\mathbf{q}_2)\rangle$, where $\psi_1(\mathbf{q}_1)$ and $\psi_2(\mathbf{q}_2)$ represent, respectively, the harmonic vibrational functions depending on dimensionless normal coordinates of the ground and first electronically excited states of the target. Here also, a new development is required since the integration mentioned above runs over different coordinates.

To achieve these tasks, support will be asked from CSC/Ministry for hiring a PhD student.

V.2.C Branching ratios

Besides the DR process mentioned in the preceding chapters, branching ratios (BR) in dissociation of polyatomic molecules and negative ions after a collision of a molecular ion or a neutral molecule with an electron are also important data. Experimental determination of BR for certain systems is possible but expensive. From the theoretical point of view, a similar situation is observed: There are studies in which the DR branching ratios were determined, albeit with a highly unsatisfactory theoretical description. Hence, there is a clear need for a reliable theoretical approach towards determining of BR with respect to electronic and vibrational excitation of products. My long term project will address this issue.

In collaboration with Prof. Kokoouline (UCF), we plan to develop a simple theoretical method to determine the BR in DR of small polyatomic ions. We benefit from the study of DR in H_3^+ (of astrophysical interest) in which e^-−H_3^+ wave functions are explicitly computed, available, and could be analyzed in the asymptotic region, where the branching ratios should be evaluated. Thus, all the information about the scattering is accessible, particularly how much of the outgoing flux goes into dissociative channels within a finite region of space. Projecting this wave function on each rovibrational level of the H_2+H of H+H+H fragmentation yields the current density associated to each channel leading to BR. The development of a detailed theoretical approach for BR in a benchmark system as H_3^+ will help us to understand the main pathways that produce different products H_2+H/H+H+H. We expect that this approach could be further applied to other ions.

Analogously, the electron-neutral molecules collisions may lead to DEA process, in competition with VE, RE or EE. Also, the DEA branching ratios can be as important as the overall DEA cross sections for plasma modeling. Treating the complete DEA of triatomic molecules, which is the work being focused on this part, is theoretically and computationally challenging. To do this, we will follow another strategy. After computing the PESs of the neutral and ion molecules, NO_2 and NO_2^- for instance using MOLPRO, we will employ the MCTDH (Multi-channel Configuration Time-Dependent Hartree) method in order to propagate the wavepacket on these PESs. At the end of the propagation, the wavepacket is projected onto vibrational and electronic states of the final products and DEA cross sections and BR can be evaluated.

These proposed works will be carried out with the help of collaborations: Profs. Ioan Schneider and Khalid Hassouni who have a large expertise on the plasma modelling. New collaborations may be built with Dr. Asa Larson from Stockholm university for MCTDH method through Dr. Samantha Douguet. This could be a part of projects such as ANRs, NSF and NASA.

Appendix – CV, publications and communications

.1 Curriculum Vitae

Contact	CentraleSupélec	Position Associate professor (MdC HDR)
	Laboratoire LGPM	☎ +33 (1) 7531-6603
	3 Rue Joliot-Curie	✉ mehdi.ayouz@centralesupelec.fr
	91190 - Gif-Sur-Yvette- France	⌨ research.centralesupelec.fr/mehdi.ayouz/
Research area	Fundamental elementary processes involving electron and molecules collisions	

Education

Université Sorbonne (France)
Habilitation in Physics (Habilitation à Diriger des Recherches en physique)
Subject : Theoretical description of electron-driven processes in astrophysical and technological plasmas: Applications for development of materials, waste treatment processes, and atmospheric depollution, **2020**
Keywords: Quantum defect theory, R-matrix method, electron-molecules scattering, rovibronic frame transformation, rovibronic excitation, dissociative recombination, plasma applications

Université Paris-Sud XI (France)
Ph.D. in Physical Science
Subject : Theoretical study of the dynamics of small quantum systems : structure and dynamics of the formation of H_3^- in the interstellar medium (ISM), **2010**
Supervisors: Olivier Dulieu and Jacques Robert
Keywords: negative ion, hyperspherical coordinates, collision theory, ISM, cross sections, radiative association, molecular dynamics, *ab intio* calculations

Université Pierre et Marie Curie Paris VI (France)
Master in Fundamental Physics, **2007**

Université Pierre et Marie Curie Paris VI (France)
Bachelor in Applied Physics, **2003**

École Centrale Paris then **CentraleSupélec** (France)
Assistant professor (Maître de Conférence-LRU), **since 2012**

Employment

Université Villetaneuse Paris 13 (LSPM)
Post-doctoral Position, **2011-2012**
Subject: Cross sections electron-molecule for cold plasma applications
Keywords: R-matrix, electron-molecule collisions, *ab initio* calculations

Marquette University (Wisconsin. US)
Post-doctoral Position, **2010-2011**
Subject: Dynamics of the formation and destruction of the ozone molecule in the atmosphere

Keywords: *ab initio*, molecular dynamics, collision theory, hyperspherical coordinates

---

Teaching activities

Assistant professor (**since 2012**)
- Quantum and statistical physics, Bachelor I and II courses, Course Member
- Software development in PYTHON, Bachelor I course, Course Member
- Quantum numerical physics, Bachelor I course, Course Co-responsible
- Heat transfer, Bachelor I and III courses, Course Member
- Transfers science (fluid mechanics), Bachelor I course, Course Member
- Numerical experiment in physics, Bachelor III course, Course Member
- Material and biomaterial science laboratory, Bachelor I course, Course Co-responsible
- Challenges of the 21st Century: Team Project, Bachelor I course, Course Co-responsible
- Workshops on professional development and leadership, Bachelor I course, Course Member
- Student projects, Bachelor I and II (100-150h)

Part-time teacher (**2012-present**)
- Tutor in C/C++ programming and numerical simulation, Master I, Université Villetaneuse, Course Responsible (30h/year)

Part-time teacher (**2011-2012**)
- Tutor in numerical experiment for fluid mechanics, Bachelor I, Université Villetaneuse-Sup Galilee (integrated engineering school), ENER1A (28h/year)

Teaching instructor (**2007-2010**)
- Tutor in Physics, Bachelor I course, Course member of competitive examinations of medicine (PCEM)
- Tutor in Physics, Bachelor III course, Course Member

Part-time teacher (**2005-2007**)
- Tutor in statistics and computing, Bachelor I course, Université Marne La Vallée (48h/year)

Administrative activities

Centralesupélec

- Co-responsible of master *Procédés, Energies Renouvelables et Géosciences*, **Since 2019**
- Member of steering committee of Projects (*Pôles projets*), **Since 2018**. *Industrial/institutional partners* : ArcelorMittal, IAEA, EDF, Citelum, NASA, CEA, CNES, Observatoire de Paris, ARD, Veolia, INERIS, Efficacity, ANFR, Pneupur, UCF, ARCEP, Recub, Transaud, MssMat, LSPM, MAS, fluidyn, Suez, ADIONICS
- Member of physics teaching team of Centralesupélec competitive entrance exam (university stream), **Since 2018**
- Member of steering committee of research program (*Parcours recherche*), **Since 2016**

École Centrale Paris

- Participation to working groups on pedagogical activities of projects and laboratories in the context of the new engineering curriculum of Centralesupélec, **2015-2018**
- Member of the steering committee of projects (*Projet Enjeu Environnement*), **2013-2018**
- Committee member of laboratory activities (*Activités expérimentales*), **2013-2018**

Reaserch activities

Projects participation

1 Fulbright, *A study of electron-driven processes in the interstellar medium*, **2020-**

2 eMol-Programme National "Physique et Chimie du Milieu Interstellaire", *Collisions électron/molécule dans les milieux interstellaires : recombinaison dissociative, attachement dissociatif et excitation ro-vibrationnelle*, **2020**

3 ANR-MONA, *From MOlecules to NAnoparticles Coupling experiments and modeling for unraveling the complex physico-chemistry of hydrocarbon*, **2019-**

4 EnsPhyQ-IDEX Paris-Saclay, *Enseigner la physique quantique autrement : une approche numérique opensource*, **2018-**

5 EDriNOx-Thomas Jefferson Funds "Make our Planet Great Again", *Electron-driven reactivity of NO_x molecules by electron impact : the NO_2/N_2O prototype for control and reduction of atmospheric pollution*, **2018-**

6 NSF-PHY-1806915, *Fundamental processes in formation, dynamics, and destruction of molecular ions in cold plasma and ion traps*, **2017-**

7 Chateaubriand, *Development of theoretical methods to study two classes of elementary process in the interstellar medium : low-energy collisions involving three atoms and collisions of electrons with molecules*, **2017-2018**

8 PicoLIBS-ANR-10-LABEX-09-01, *Analyse de Composition Multi-élémentaire par la Technique LIBS Laser- Induced Breakdown Spectroscopy Picoseconde*, **2014-2017**
9 FEDER CO_2-VIRIDIS, *Valorisation du CO_2 par procédés catalytiques assistés par plasma*, **2018-2019**
10 *Other participations* : ANR-10-EQPX-37 MATMECA "Investissements d'avenir" program (**2019**), Lasips-*Symbio-reactor* (**2014-2015**)

Other funds
Chinese Scholarship Council (CSC), "*Accueil des chercheurs étrangers*" program of CentraleSupélec, "*Séjour à l'étranger 2019*" program of école doctorale INTERFACES of Université Paris-Saclay, école doctorale SMEMAG

Jury participation
- Member of Ph.D. committee of David Lapierre at Université de Reims. *Subject* : *Méthodes de calcul de paramètres pour la spectroscopie dynamique moléculaire : étude théorique et applications*, **2019**
- Member of section committee of assistant professor "Maître de Conference " at École Centrale Paris, **2014**

Reaserch activities

Journal reviewing
- Journal of Chemical Physics
- Physical Chemistry Chemical Physics

Other information
- 10-year experience in parallel computing MPI/OpenMP on supercomputers at NERSC (www.nersc.gov) and IDRIS (www.idris.fr)
- Use quantum chemistry softwares MOLPRO and GAUSSIAN, and scattering UK R-matrix code (Quantemol-N suite)
- Development of a complete course of undergraduate quantum mechanics based on numerical experiments available on http://prd-mecaqu.centralesupelec.fr/index.html (*beta version*)
- Published cross sections of vibrational (de)excitaiton of HeH^+ by electron impact were included in the IAEA database https://www-amdis.iaea.org/DATASETS/e_HeH/
- Member of the American Physical Society (APS)
- Member of *Société Française de Physique* (SFP)
- Committee organization of an international conference "Eurodrying'2013" at Paris

Collaborations

- Prof. V. Kokoouline at University of Central Florida (FL,US);
- Dr. Samantha Fonseca Dos Santo at Rollins College (FL,US);
- Dr. Nicolas Douguet at Kennesaw State University (Ga, US);
- Prof. Ioan Schneider at Université du Havre (France);
- Dr. János Zsolt Mezei at Institute for Nuclear Research (Hungary);
- Prof. Khalid Hassouni at LSPM (Université Villetaneuse);
- Profs. M. Raoult and O. Dulieu at Laboratoire Aimé Cotton (France);
- Prof. Dmitri Babikov at Marquette University (WI, US)

Internships positions held

Reaserch activities

- Société Générale Bank, Summer **2007**
- Laboratoire Aimé Cotton (Paris sud). *Subject* : "Dynamique des systèmes à N corps: Application aux collisions atomes/molécules", (Master) **2007**
- Institut d'Optique (École polytechnique Palaiseau). *Subject* : "Condensat de Bose-Einstein", (Master) **2006**
- Laboratoire de physique quantique (ESPCI). *Subject* : "Microscopie à force atomique dynamique", (Master) **2005-2006**
- Laboratoire de physique nucléaire et des hautes énergies (Université Paris VI). *Subject* : "Violation de la conjugaison de charge et de la parité sur les mésons B_0", (Bachelor) **2004-2005**
- Laboratoire Kastler Brossel (Université Paris VI). *Subject* : "Spectroscopie par rayon X de l'argon", (Bachelor) **2003-2004**

Doctoral Thesis Supervised

Students supervision

- Dr. Xianwu Jiang. *Hydrocarbon molecules databases for waste treatment applications.* Co-supervised with Prof. P. Cortona (Centralesupélec), **2017-2020**. Supervision rate : 90%. 1 published article + 1 in progress
- Hainan Liu. *Cross sections for excitation of NO_x molecules by electron impact for control and reduction of atmospheric pollution by NO_2.* Co-supervised with Prof. P. Cortona (Centralesupélec), **2017-2020**. Supervision rate : 90%. 1 published article + 1 submitted
- Abdillah Abdoulanziz, *Collision électron-molécules : étude des mécanismes réactionnels et applications.* Co-supervised with Prof. I. Schneider (Université du havre), **2017-**. Supervision rate : 30%. 1 published article
- Emerance DJUISSI, *Cinétique électronique dans les plasmas de bord: collisions avec cations d?hydrures, de nitrures et de gaz rares.* Co-supervised with Prof. I. Schneider (Université du Havre), **2018-**. Supervision rate : 20%
- Dr. Li Gong, *Continuous annealing of Advanced High Strength Steels used to reduce the weight of car body in the context of greenhouse gas emissions reduction.* Co-supervised with Prof. M-L. Giorgi (Centralesupélec), **2016-2020**. Supervision rate : 20%. 1 published article

- Dr. Chi Hong Yuen. *Theoretical studies of collisions involving three bodies and electron-molecules collisions relevant to astrophysical and atmospheric conditions.* Co-supervised with Prof. V. Kokoouline (University of Central Florida), **2014-2020**. Supervision rate : 30%. 3 published articles
- Mathilde Louërat, *Modélisation par la méthode Lattice Boltzmann de la diffusion de chaleur et d'humidité dans des matériaux biosourcés à partir de leur morphologie 3D.* Co-supervised with Prof. P. Perré (Centralesupélec), **2013-2017**. Supervision rate : 40%. 1 published article
- Huan Du, *Observation et modélisation de la croissance de Postia placenta : de l'échelle discrète de la colonie à l'échelle macroscopique.* Co-supervised with Prof. P. Perré (Centralesupélec), **2013-2017**. Supervision rate : 20%. 2 published articles

Post-doctoral Supervised

- Alexander Korovin, *Enseigner la physique quantique autrement : une approche numérique opensource (IDEX Paris Saclay).* **2019-2020**. Supervision rate : 100%

Internships Supervised

Students supervision

- Romain Piron, Bouthaina Houass and Jules Plaire (Centralesupélec research program), *PhyQApp : Smartphone/Tablet computer applications for learning quantum physics*, **2020**. Supervision rate : 100%
- Oscar Ambrois (Centralesupélec research program), *Calculation of the rotational and vibrational cross sections for plasma modelling*, **2020**. Supervision rate : 100%
- Malo Joly (Centralesupélec research program), *Cross sections for excitation and ionization of N_2O molecules by electron impact*, **2019**. Supervision rate : 100%
- Firas Dhaha (Centralesupélec research program), *Calcul de Section efficace pour la modélisation du plasma*, **2018**. Supervision rate : 100%
- Jesus Monserrat (ERASMUS), *Databases for modeling emission of NO_2 molecule for control/reduction of atmospheric pollution*, **2016**. Supervision rate : 100%
- Timothée Metthey, *Modélisation Lattice Boltzmann de la diffusion dans les matériaux*, **2015**. Supervision rate : 100%
- Benoît Guillemain, *Simulation par modèle continu des transferts dans un plasma dipolaire d'hydrogène par COMSOL.* Co-supervised with Prof. K. Hassouni (Université Paris 13), **2012**. Supervision rate : 50%
- Raphael Lopes, *Détermination du moment dipolaire de H_3^- pour le calcul des moments de transition radiatifs.* Co-supervised with V. Kokoouline (Université Paris-sud/UCF), **2010**. Supervision rate : 50%

1 Publications - Scientific outreach

23 PUBLICATIONS IN REFEREED AND 4 IN NON-REFEREED JOURNALS, 20 COMMUNICATIONS (WITH 3 INVITED), 2 TEXTBOOKS

A Referred journals

2020

Liu, H., Santos, S. F. d., Yuen, C. H., Cortona, P., Ayouz, M., and Kokoouline, V. (2020b). Vibrational excitation of n_2O by an electron impact and the role of the renner-teller effect in the process. *Phys. Rev. A*, 102:032808

Gong, L., Ruscassier, N., Ayouz, M., Haghi-Ashtiani, P., and Giorgi, M.-L. (2020). Analytical model of selective external oxidation of fe-mn binary alloys during isothermal annealing treatment. *Corrosion Science*, 166:108454

2019

Ayouz, M. A., Yuen, C. H., Balucani, N., Ceccarelli, C., Schneider, I. F., and Kokoouline, V. (2019). Dissociative electron recombination of NH_2CHOH^+ and implications for interstellar formamide abundance. *Monthly Notices of the Royal Astronomical Society*, 490(1):1325–1331

Ayouz, M. and Kokoouline, V. (2019). Cross sections and rate coefficients for rovibrational excitation of heh^+ isotopologues by electron impact. *Atoms*, 7(3)

Yuen, C. H., Ayouz, M. A., Balucani, N., Ceccarelli, C., Schneider, I. F., and Kokoouline, V. (2019). Dissociative recombination of $CH_2NH_2^+$: a crucial link with interstellar methanimine and Titan ammonia. *Monthly Notices of the Royal Astronomical Society*, 484(1):659–664

Mezei, Z. J., Chakrabarti, K., Epée Epée, M. D., Motapon, O., Yuen, C. H., Ayouz, M. A., Douguet, N., Fonseca dos Santos, S., Kokoouline, V., and Schneider, I. F. (2019). Electron-induced excitation, recombination, and dissociation of molecular ions initiating the formation of complex organic molecules. *ACS Earth and Space Chemistry*, 3(11):2376–2389

Jiang, X., Yuen, C. H., Cortona, P., Ayouz, M., and Kokoouline, V. (2019). Cross sections for vibronic excitation of ch^+ by low-energy electron impact. *Phys. Rev. A*, 100:062711

Liu, H., dos Santos, S. F., Yuen, C. H., Cortona, P., Kokoouline, V., and Ayouz, M. (2019). Theoretical study of electron-induced vibrational excitation of no_2. *Plasma Sources Science and Technology*, 28(10):105017

2018

Yuen, C. H., Ayouz, M., Endres, E. S., Lakhmanskaya, O., Wester, R., and Kokoouline, V. (2018). Quantum-tunneling isotope-exchange reaction $h_2 + d^- \rightarrow HD + h^-$. *Phys. Rev. A*, 97:022705

Khamesian, M., Ayouz, M., Singh, J., and Kokoouline, V. (2018). Cross sections and rate coefficients for rotational excitation of HeH^+ molecule by electron impact. *Atoms*, 6(3):49

Kokoouline, V., Ayouz, M., Mezei, J. Z., Hassouni, K., and Schneider, I. (2018). Theoretical study of dissociative recombination and vibrational excitation of BF_2^+ the ion by an electron impact. *Plasma Sources Sci. Technol.*, 27(11):115007

Louerat, M., Ayouz, M., and Perré, P. (2018). Heat and moisture diffusion in spruce and wood panels computed from 3-d morphologies using the lattice boltzmann method. *International Journal of Thermal Sciences*, 130:471 – 483

Du, H., Ayouz, M., Lv, P., and Perré, P. (2018). A lattice-based system for modeling fungal mycelial growth in complex environments. *Physica A: Statistical Mechanics and its Applications*, 511:191 – 206

2016 Ayouz, M. and Kokoouline, V. (2016). Cross sections and rate coefficients for vibrational excitation of HeH^+ molecule by electron impactukrm. *Atoms*, 4:30

Patrick, P., Giana, A., Mehdi, A., and Xavier, F. (2016). New modelling approaches to predict wood properties from its cellular structure: image-based representation and meshless methods. *Annals of Forest Science*, 73

Du, H., Lv, P., Ayouz, M., Besserer, A., and Perré, P. (2016). Morphological characterization and quantification of the mycelial growth of the brown-rot fungus postia placenta for modeling purposes. *PLoS ONE*, 11(9)::e0162469

2015 Perré, P., Pierre, F., Casalinho, J., and Ayouz, M. (2015). Determination of the mass diffusion coefficient based on the relative humidity measured at the back face of the sample during unsteady regimes. *Drying Technology*, 33(9):1068–1075

2013 Ayouz, M. and Babikov, D. (2013). Global permutationally invariant potential energy surface for ozone forming reaction. *J. Chem. Phys.*, 138(16):164311

Ayouz, M., Dulieu, O., and Robert, J. (2013). Resonant states of the h3–molecule and its isotopologues d2h–and h2d–. *J. Phys. Chem. A*, 117(39):9941–9949

2012 Ayouz, M., Mikhailov, I., Babikov, D., Raoult, M., Galtier, S., Dulieu, O., and Kokoouline, V. (2012). Potential energy and dipole moment surfaces of HCO^- for the search of H^- in the interstellar medium. *J. Chem. Phys.*, 136:224310

Ayouz, M. and Babikov, D. (2012). Improved potential energy surface of ozone constructed using the fitting by permutationally invariant polynomial function. *Advances in Physical Chemistry*, pages 1687–7985

2011 Ayouz, M., Lopes, R., Raoult, M., Dulieu, O., and Kokoouline, V. (2011). Formation of H_3^- by radiative association of H_2 and H^- in the interstellar medium. *Phys. Rev. A*, 83(5):052712

2010 Ayouz, M., Dulieu, O., Guérout, R., Robert, J., and Kokoouline, V. (2010). Potential energy and dipole moment surfaces of H_3^- molecule. *J. Chem. Phys.*, 132:194309

B Textbooks

2021 Mehdi Ayouz, Jean-Michel Gilet, Pierre-Eymeric Janolin and Viatcheslav Kokoouline *Toolbox for learning basic concepts of quantum physics : Fundamentals and Applications with Computer Codes* , Springer, in production

2020 Mehdi Ayouz, Jean-Michel Gilet, Pierre-Eymeric Janolin and Viatcheslav Kokoouline. *Les fondamentaux de la mécanique quantique sous PYTHON : rappel de cours et exercices d'application avec programmes inclus*, Ellipse edition, in press

C Non-Referred journals

2020 Liu, H., Santos, S. F., Yuen, C., Cortona, P., Kokoouline, V., and Ayouz, M. (2020a). Theoretical study of vibrational excitation and dissociative electron attachment of no_2 by an electron impact. *Journal of Physics: Conference Series*, 1412:172002

Jiang, X., Yuen, C., Cortona, P., Kokoouline, V., and Ayouz, M. (2020). Model for vibronic excitation of ch^+ by resonant scattering of electron. *Journal of Physics: Conference Series*, 1412:142031

2015 Dulieu, O., Ayouz, M., Raoult, M., Robert, J., and Kokoouline, V. (2015a). Could the H_3^- ion exist in interstellar medium? In *American Institute of Physics Conference Series*, volume 1642, pages 366–369

Dulieu, O., Ayouz, M., Raoult, M., Robert, J., and Kokoouline, V. (2015b). Could the H_3^- ion exist in interstellar medium? In *Proceedings of the International Conference of Computational Methods in Sciences and Engineering*, volume 0065-7727, pages 978–0–7354–1282–8

D Conference presentations

2021 Journée Initiatives Pédagogiques de l'Université Paris-Saclay, JIP 2020-2021, February 10, Institut d'Optique Graduate School (IOGS), France. *Enseigner la physique quantique (EnsPhyQ) autrement: approche numérique Opensource*

2020 The 51st Annual Meeting of the APS Division of Atomic, Molecular and Optical Physics June 1-5, Portland, Oregon. US. http://meetings.aps.org/Meeting/DAMOP20/Session/M05.8. *Cross sections for vibronic excitation and dissociative recombination of CH^+ by low-energy.* **Virtual RSVP**

2019 Challenges for Plasma and Catalysis, October 17-18, Le Havre, France. *Dissociative recombination and vibrational excitation of large molecules by electron impact.* **Invited**

The 50th Annual Meeting of the APS Division of Atomic, Molecular and Optical Physics APS Meeting, May 27-31, Milwaukee, Wisconsin, US. *Cross sections for vibronic excitations of CH^+ by low-energy.* Hainan LIU, Samantha Fonseca dos Santos, Chi Hong Yuen, Pietro Cortona, Viatcheslav Kokoouline and Mehdi Ayouz

Journée Initiatives Pédagogiques de l'Université Paris-Saclay, JIP 2019, November 28, Institut d'Optique Graduate School (IOGS), France. *Enseigner la physique quantique (EnsPhyQ) autrement: approche numérique Opensource*

2018 International Conference of Assistant professors, October 25, Russian cultural center, Paris, France. *Teaching quantum physics differently: an open source numerical approach.* **Invited**

The 49th Annual APS Division of Atomic, Molecular, and Optical Physics, May 28-June 1, Fort Lauderdale, US. http://meetings.aps.org/Meeting/DAMOP18/Content/3507. *Quantum tunneling isotope exchange reaction $H_2+D^- \rightarrow HD+H^-$* H. C. H. Yuen, M. Ayouz, E. S. Endres, O. Lakhamanskaya, R. Wester and V. Kokoouline

2017 The 48th Annual APS Division of Atomic, Molecular, and Optical Physics, June 5-9, Sacramento, California, US. http://meetings.aps.org/Meeting/DAMOP17/Content/3310. *Theoretical study of the $H_2+D^- \rightarrow HD+H^-$ reaction at low energies.* Chi Hong Yuen, Mehdi Ayouz, Viatcheslav Kokoouline

The 11th International Conference on Zinc and Zinc Alloy Coated, November 12-18, Tokyo, Japan. *Selective oxidation of Fe-Mn (1wt.%) binary alloy.* N. Ruscassier, Li Gong, M. Ayouz, T. Reiss, P. Haghi-Ashtiani and M-L. Girogi

2014 GDR, Nancy, November 13, France. *De l?expérimentation à l?échelle anatomique à la modélisation multi échelle des propriétés physiques du bois.* Mehdi Ayouz and Giana Perré.

2013 Eurodrying'2013, October 4th, Paris, France. *An original method for the determination of mass diffusion of hygroscopic materials in unsteady regime.* F. Pierre, M. Ayouz and P. Perré

2011 International conference on ozone. October 3-11, Reims, France. *Improved potential energy surface of ozone constructed using the fitting by permutationally invariant polynomial function.* **Invited**

The 42nd Annual Meeting of the APS Division of Atomic, Molecular and Optical Physics, June 13-17, Atlanta, Georgia, US. http://meetings.aps.org/Meeting/DAMOP11/Event/147334. *Radiative association of H_2 and H^- at low temperature : can we observe H_3^- in the interstellar medium ?*. Mehdi Ayouz, Olivier Dulieu, Maurice Raoult and Viatcheslav Kokoouline

2010 Meeting of division of atomic, molecular and optical physics of the French Physics Society, (PAMO), June 29-July 2, Orsay, France. http://www.pamojsm2010.fr/. *Étude théorique de la formation de l'ion moléculaire H_3^- : proposition d'observation de H^- dans le milieu interstellaire*, V. Kokoouline, M. Ayouz, M. Raoult, J. Robert, O.Dulieu

The 41st Annual Meeting of the APS Division of Atomic, Molecular and Optical Physics, May 25-29, Houston, Texas, US. http://meetings.aps.org/Meeting/DAMOP10/Session/C2.5. *Potential energy and dipole moment surfaces of H_3^- molecule.* Olivier Dulieu, Mehdi Ayouz, Romain Guérout, Jacques Robert, and Viatcheslav Kokoouline

Spectroscopy of Molecular Ions in the Laboratory and in (Extraterrestrial) Space, October 3-6 Kos, Greece. *Theoretical study of the H_3^- anion; proposal for its observation in the interstellar medium.* Mehdi Ayouz, Olivier Dulieu, Jacques Robert and Viatcheslav Kokoouline

DPG Spring Meeting of the Section AMOP, "Deutsche Physikalische Gesellschaft", March 8-12, Hanover, Germany. http://hannover10.dpg-tagungen.de/index.html. *Calculation of the structure of negative ion, and of its formation rate in the interstellar medium.* Mehdi Ayouz, Olivier Dulieu, Jacques Robert and Viatcheslav Kokoouline

The 10th European Conference on Atoms, Molecules and Photons, July 4-9, Salamanca, Spain. *Formation of H_3^- by radiative association of H_2 and H^- . Could H_3^- be observed in the interstellar medium ?*. V. Kokoouline, M. Ayouz, M. Raoult, J. Robert and O. Dulieu

2009 European Graduate College (EGC) on Cold atoms and molecules, June 29-July 02. Berlin, Germany. http://www.egc.uni-hannover.de/. *Low energy dynamics of H_3^- : a prototype for collisions between molecules and anions*

2008 European Graduate College (EGC) on Cold atoms and molecules, June 30-July 03, Gif Sur Yvette, France. http://n.saquet.free.fr/EGC2008/Home.html. *$N-$body systems dynamic: application at cold collision between atoms and molecules*

E Posters

2021 Processes in ATmospheric and AStrochemical environments, January 18-21, PATAS 2021 Virtual WG3 meeting. *Theoritical model for vibronic excitation and dissociative recombination of CH^+ by electron impact.* Mehdi Ayouz, Xianwu Jiang, Chi Hong Yuen and Viatcheslav Kokoouline

2021 Processes in ATmospheric and AStrochemical environments, January 18-21, PATAS 2021 Virtual WG3 meeting. *Electron induced reactivity of molecule cations: from mechanisms to new stateto-state cross sections and rate coefficients.* J.-Zs. Mezei, E. Djuissi, A. Abdoulanziz, C. Argentin, F. Iacob, N. Pop, A. Orban, K. Chacrabarti, D. Talbi, M. Ayouz, V. Kokoouline and I.-F. Schneider.

2020 The 51st Annual Meeting of the APS Division of Atomic, Molecular and Optical Physics, June 1-5, Portland, Oregon. US. *Theoretical study of vibrational (de-)excitation of NO_2 and N_2O by low-energy electron impact.* Hainan Liu, Mehdi Ayouz, Pietro Cortona, Samantha Fonseca dos Santos, Chi Hong Yuen and Viatcheslav Kokoouline

Physique et Chimie du Milieu Interstellaire (PCMI) biennal conference, July 6-9, Le Havre, France. *Cross sections for vibronic excitation of CH^+ by low-energy electron impact.* Xianwu Jiang, C. H. Yuen, P. Cortona, V. Kokoouline, M. Ayouz

2019 The 50th Annual Meeting of the APS Division of Atomic, Molecular and Optical Physics, May 27-31, Milwaukee, Wisconsin, US. *Dissociative recombination of $CH_2NH_2^+$ and $NH_2CH_2O^+$ ions.* Viatcheslav Kokoouline, Chi Hong Yuen, Ioan Schneider, Cecilia Ceccarelli, Nadia Balucani and Mehdi Ayouz

The 31st International Conference on Photonic, Electronic and Atomic Collisions, 23-30 July, Deauville, France. *Theoretical study of vibrational excitation and dissociative electron attachment of NO_2 by an electron impact.* Hainan Liu, Samantha Fonseca dos Santos, Chi Hong Yuen, Pietro Cortona, Viatcheslav Kokoouline and Mehdi Ayouz

The 31st International Conference on Photonic, Electronic and Atomic Collisions, 23-30 July, Deauville, France. *Model for vibronic excitation of CH^+ by resonant scattering of electron.* Xianwu Jiang, Chi Hong Yuen, Pietro Cortona, Viatcheslav Kokoouline and Mehdi Ayouz

2018 Intl'Conf. on Processing and Manufacturing of Advanced Materials, July 9-13, Paris, France. *Nucleation and Growth of MnO on Fe-Mn (1 wt.%) Binary Alloy.* Li Gong, Ruscassier Nathalie, Ayouz Mehdi and Giorgi Marie-Laurence

2015 Colloque de Recherche Inter Écoles Centrale, June 8-12, Lyon, France. *Modélisation et expérimentation à l?échelle microscopique de biomatériaux.* Huan Du, Mehdi Adrien Ayouz, Pin Lv and Patrick Perré

Colloque de Recherche Inter Écoles Centrale, June 8-12, Lyon, France. *Calcul de propriétés des matériaux par méthodes discrète MLattice Boltzmann.* M. Louërat, M. Ayouz and P. Perré

2013	Eurodrying'2013, October 4th, Paris, France. *Numerical simulation of diffusion in porous media using the Lattice Boltzmann Method.* Mehdi Ayouz and Patrick Perré
2011	The 42nd Annual Meeting of the APS Division of Atomic, Molecular and Optical Physics, June 13-17, Atlanta, Georgia, US. *Bound states, resonances, and formation of the H_3^- anion.* Viatcheslav Kokoouline, Mehdi Ayouz, Jacques Robert and Olivier Dulieu
2009	La Société Française de Physique, July 6-10, École polytechnique, Palaiseau, France
	Faraday Discussion, Cold and Ultracold Molecules, April 15-17, Durham University, U K.

atoms

MDPI

Article

Cross Sections and Rate Coefficients for Vibrational Excitation of HeH^+ Molecule by Electron Impact

Mehdi Ayouz [1,†] and Viatcheslav Kokoouline [2,*,†]

[1] Laboratoire de Genie des Procedes et des Materiaux, Ecole Centrale Paris, CentraleSupelec, campus de Chatenay-Malabry Grande Voie des Vignes F-92 295 Chatenay-Malabry Cedex, France; mehdi.ayouz@centralesupelec.fr

[2] Department of Physics, University of Central Florida, Orlando, FL 32816, USA

* Correspondence: viatcheslav.kokoouline@ucf.edu; Tel.: +1-407-823-5145

† These authors contributed equally to this work.

Academic Editor: Bastiaan J. Braams

Received: 11 November 2016; Accepted: 14 December 2016; Published: 20 December 2016

Abstract: Cross sections and thermally-averaged rate coefficients for vibration (de-)excitation of HeH^+ by an electron impact are computed using a theoretical approach that combines the multi-channel quantum defect theory and the UK R-matrix code. Fitting formulas with a few numerical parameters are derived for the obtained rate coefficients. The interval of applicability of the formulas is from 40 to 10,000 K.

Keywords: helium hydride ion; vibrational excitation; R-matrix; quantum-defect theory

1. Introduction

The hydrohelium (helium hydride) cation HeH^+ is an important species in the interstellar medium (ISM) [1] and in the chemistry of the planetary nebulae such as NGC 7027 [2–4]. It is one of the simplest molecular ions and the first one formed in the early universe [5]. In the ISM it is formed mainly in the process of radiative association of He and H^+ or of He^+ and H [6,7]. Due to the relatively large abundance of electrons and HeH^+ in the ISM, collisions of HeH^+ with electrons play a significant role, in particular, leading to dissociation (dissociative recombination) and rovibrational (de-)excitation of HeH^+. Other than in the ISM, the HeH^+ ion is also present in fusion reactors. Because it is one of the most abundant molecular ions near walls of the reactors, its contribution to the complete network of processes taking place in the reactors should be accounted for in fusion plasma modeling. In particular, cross sections for electron-HeH^+ collisions are needed.

A number of processes can occur when an electron collides with HeH^+. One of the most important processes is the dissociative recombination. Cross sections for this process were measured and calculated in several previous studies [8–13]. Another process, relevant for the ISM [14] and fusion reactors, in the vibrational excitation and (de)-excitation,

$$e^- + \mathrm{HeH}^+(v, j) \rightarrow e^- + \mathrm{HeH}^+(v', j')\,, \tag{1}$$

for which cross sections were calculated in a previous study [15] for the transitions between the three lowest vibrational levels $v = 0, 1, 2$. In that study, an R-matrix approach was employed to determine scattering matrices for fixed geometries. Rydberg series of vibrational and rotational resonances present in the spectrum of the $e^- - \mathrm{HeH}^+$ system were neglected. In this work we determine cross sections and rate coefficients for the process using an improved treatment, in which the Rydberg series of vibrational resonances in HeH are accounted for using the multichannel quantum defect theory (MQDT). Electron-impact transitions between the five lowest vibrational levels, $v = 0 - 4$, are considered.

The rest of the article is organized in the following way. The next section of the article discusses the theoretical approach used in the present calculation. In Section 3, the obtained rate coefficients for vibrational (de-)excitation are discussed and compared with the data available in literature. Section 4 concludes the study.

2. Theoretical Approach

2.1. Scattering Matrix for Fixed Geometries Of HeH^+

The theoretical model employed in the present study combines the UK R -matrix method [16,17] and the multi-channel quantum defect theory (MQDT) [18–20]. The electron scattering calculations were performed employing the Quantemol-N interface [21] to run the UK R-Matrix code [16,17]. The target HeH^+ ion was assumed to be in the ground electronic state $X^1\Sigma^+$.

In the R-matrix calculations, the target and the scattering wave functions were represented within a full CI treatment, i.e., by allowing all electrons to occupy all orbitals. The calculations were performed using the Gaussian basis set 6-311G*. The continuum orbitals of Faure et al. [22], representing the scattering electron, was included up to the g-wave. The R-matrix radius was set to $a_0 = 10$ bohrs. All generated states up to 25 eV were retained in the final close-coupling calculation. As the first electronically excited state, $A^1\Sigma^+$ correlated with H(1s) + $He^+(1s)$ is approximately 11 eV above the H^+ + He($1s^2$) dissociation limit for the $X^1\Sigma^+$ground state, the ground state is essentially isolated and non-adiabatic effects are expected to be small. Therefore, for low electron energy collisions (bellow 10 eV) only the lowest electronic state is open for ionization in $e^- - HeH^+$ collisions and the dimension of the geometry-fixed scattering matrix does not change with energy.

Wave functions of $e^- - HeH^+$ continuum states obtained in the R-matrix calculations have the following asymptotic behavior at large distances r between the electron and the target ion in channels open for ionization [16]

$$F_{ij}(r) \sim \frac{1}{\sqrt{k_i}} \left(\sin\theta_i(r)\delta_{ij} + \cos\theta_i(r) K_{ij}(R) \right) , \tag{2}$$

$$\theta_i(r) = k_i r - \frac{l_i \pi}{2} + \frac{\ln(2k_i r)}{k_i} + \arg\Gamma\left(l + 1 - \frac{i}{\pi} \right) , \tag{3}$$

where index i refers to the entrance channel before a collision and j refers to the outgoing channel after the collision. In the above equation, $K_{ij}(R)$ are the elements of the reactance matrix [16,20], which depend on the internuclear distance R. In the cross section calculation, the scattering matrix $\mathbf{S}(R)$ is needed, which is obtained from $\mathbf{K}(R)$ as

$$\mathbf{S}(R) = (\mathbf{1} + i\mathbf{K}(R))(\mathbf{1} - i\mathbf{K}(R))^{-1} . \tag{4}$$

Generally, for fixed geometries of the target and low collisional velocities, the matrices $\mathbf{S}(R)$ and $\mathbf{K}(R)$ depend weakly on energy. A sharper energy-dependence is observed only at certain higher energies, corresponding to positions of Rydberg states attached to excited electronic states of the ion. A convenient way to represent a weak or a strong energy dependence of the matrices is the eigenphase sum. Figure 1 shows eigenphase sums for three symmetries ($^2\Sigma^+$, $^2\Pi$, and $^2\Delta$) of the e^- + HeH^+ system and for several internuclear distances in HeH^+. The chosen interval of internuclear distances corresponds to the Franck-Condon region of the lowest vibrational level of HeH^+. The variation of the eigenphase sums for $^2\Pi$ and $^2\Delta$ is smooth for energies below 10 eV and does not change significantly with R. The $^2\Sigma^+$ eigenphase sums demonstrate a sharp energy dependence at certain energies, which corresponds to a resonant state of HeH with energy changing with the internuclear distance R.

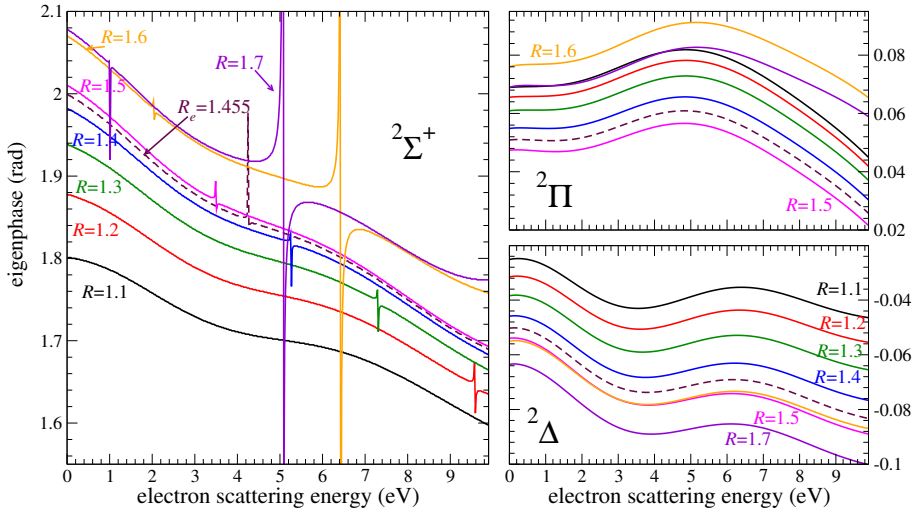

Figure 1. Eigenphase sum as a function of the electron scattering energy E_{el} (in eV) for several internuclear distances R (in units of bohr) for the $^2\Sigma^+$ (left panel), $^2\Pi$ (right upper panel), and $^2\Delta$ (right bottom panel) symmetries. The color scheme used to label different values of R is the same for all three panels. The dashed line represents the equilibrium internuclear distance $R_e = 1.445$ bohrs [15] of HeH^+.

2.2. HeH^+ Vibrational Dynamics

In calculations of the cross section for vibration (de-)excitations, vibrational wave functions of the target ion are needed in order to construct elements of the scattering matrix for transitions from one state v' to another v. We calculated vibrational wave functions $\psi_v(R)$ and energies ϵ_v by solving the Schrödinger equation for vibrational motion along R,

$$\left[-\frac{1}{2\mu}\frac{\partial^2}{\partial R^2} + V(R)\right]\psi_v(R) = \epsilon_v\psi_v(R)\,, \tag{5}$$

where μ the reduced mass and $V(R)$ is the internal potential of HeH^+. The above equation was solved using a DVR-type method [23]. In the numerical calculation, the distance R was varied from 0.5 to 20 bohrs. The potential energy curve $V(R)$ was calculated with the *ab initio* CCSD(T) method and the cc-pVQZ basis of Gaussian-type orbitals using the Molpro package [24]. Figure 2 shows the potential energy curve $V(R)$ and wave functions for four vibrational levels $v = 0, 1, 2, 8$. Energy differences for transitions $v \to v+1$ and rotational constants of the HeH^+ vibrational levels are listed in Table 1 and compared with previous benchmark calculations [25,26].

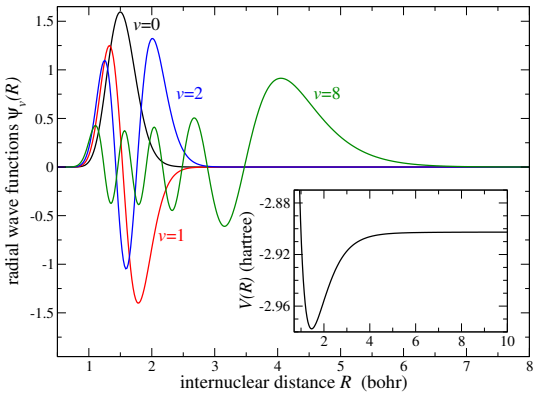

Figure 2. Wave functions $\psi_v(R)$ of the $v = 0, 1, 2$, and 8 vibrational states of the HeH^+ ion. The inset shows the potential energy curve $V(R)$ of the $X^2\Sigma^+$ electronic state of HeH^+ used in the calculation.

Table 1. The vibrational frequencies $\Delta_v = E_{v+1} - E_v$ for transitions $v \rightarrow v+1$ and rotational constants B_v obtained in the present study and compared with previous calculations. All values are in cm^{-1}.

Level v	Δ_v	Δ_v [26]	B_v	B_v [25]
0	2913	2911.0007	33.527	33.558
1	2607	2604.1676	30.816	30.839
2	2300	2295.5787	28.088	28.090
3	1988	1982.0562	25.305	25.301
4	1668	1660.3559	22.425	22.402
5	1339	1327.7860	19.394	19.344
6	1000	984.3599	16.151	16.058
7	660	639.1959	12.645	12.479
8	328	327.3615	8.813	8.621

2.3. The Scattering Matrix for an Electron Colliding with HeH^+

Once vibrational energies, wave functions, and geometry-fixed S-matrix are calculated, the scattering matrix describing the transition amplitude $S_{i',i}$ from one vibrational level v to another v' is obtained using the method of vibrational frame transformation [19,27]. The indexes i' and i enumerate vibrational states v, states of different electron angular momentum l, and its projections Λ on the molecular axis Z. Therefore, for the process

$$e^-(l,\Lambda) + \mathrm{HeH}^+(v) \longrightarrow e^-(l',\Lambda') + \mathrm{HeH}^+(v')\,, \tag{6}$$

the scattering matrix in the molecular frame coordinate system can be written as

$$\mathcal{S}_{\Lambda' v' l',\Lambda v l} = \left\langle \psi_{v'}(R) \left| S_{\Lambda' l',\Lambda l}(R) \right| \psi_v(R) \right\rangle\,, \tag{7}$$

where the brackets imply an integration over the vibrational coordinates. Many elements among $S_{\Lambda' v' l',\Lambda v l}$ are zero. In particular, the symmetry (one of the irreducible representations Γ of the $C_{\infty v}$ group) of the total e^- + HeH^+ system stays the same before and after a collision. Also, for low energies when there is only one electronic state $X^1\Sigma^+$ open for ionization, the $\mathcal{S}_{\Lambda' v' l',\Lambda v l}$ matrix is diagonal over Λ. Note that the matrix element $S_{\Lambda' l',\Lambda l}(R)$ in the above equation is obtained from R-matrix calculations for a given value of R. It represents the scattering amplitude when the electron scatters from one channel (Λl) to another $(\Lambda' l')$, while the nuclei do not have time to move. To evaluate the integral in Equation (7) the R-matrix calculations were performed for thirty values of R in the interval R = 1.0–3.9 bohrs with a step of 0.1 bohrs.

2.4. Elimination of Channels Closed for Ionization From the Scattering Matrix

The scattering matrix $\mathcal{S}$ of Equation (7) can be used for cross sections calculations only if the total energy of the system is high enough for all collision channels to be open for ionization. When some channels are closed, the scattering matrix should be modified applying the "closed-channel-elimination" procedure [20] and producing matrix $\mathcal{S}^{phys}(E)$ according to

$$\mathcal{S}^{phys}(E) = \mathcal{S}^{oo} - \mathcal{S}^{oc}\left[\mathcal{S}^{cc} - e^{-2i\beta(E)}\right]^{-1}\mathcal{S}^{co}\,. \tag{8}$$

The matrix $\mathcal{S}^{phys}(E)$ has $N_o \times N_o$ dimension, N_o being the number of channels open for ionization for a given total energy E of the system. The total energy could be written as a sum of the energy of the entrance channel E_i and the relative kinetic energy E_{el} of electron and the target ion: $E = E_i + E_{el}$. In the above equation, the matrices $\mathcal{S}^{oo}$, $\mathcal{S}^{oc}$, $\mathcal{S}^{cc}$ and $\mathcal{S}^{co}$are submatrices of the original matrix $\mathcal{S}$ [18,20], partitioned as

$$\mathcal{S} = \begin{pmatrix} \mathcal{S}^{oo} & \mathcal{S}^{oc} \\ \mathcal{S}^{co} & \mathcal{S}^{cc} \end{pmatrix}\,, \tag{9}$$

where the partition of the matrix elements in the "o"- and "c"-parts is made on the basis whether the corresponding channel, i or i', is open or closed for ionization for a given total energy E. The quantity $\beta(E)$ is a diagonal $N_c \times N_c$ matrix

$$\beta_{i'i}(E) = \frac{\pi}{\sqrt{2(E_i - E)}}\delta_{i'i}\,, \tag{10}$$

where E_i refers to energy of the corresponding closed channel i and $N_c = N - N_o$ is the number of closed channels. For a given vibrational quantum number v, channel energies are degenerate with respect to l and Λ. In principle, the channel energy E_i depends also on the electronic excitation of the target ion, but in this study the initial electronic state is $X^1\Sigma^+$ and collisional energies are too low to excite other electronic states.

3. Rate Coefficients and Cross Sections for Vibrational (De-)Excitation

Using the scattering matrix $\mathcal{S}^{phys}$, the cross section for electron-impact vibrational transition $v \to v'$ of the ion is [28]

$$\sigma_{v'v}(E_{el}) = \frac{\pi\hbar^2}{2m_e E_{el}} \sum_{\Lambda' l' \Lambda l} \left| \mathcal{S}^{phys}_{\Lambda' l' v', \Lambda l v} - \delta_{\Lambda l v, \Lambda' l' v'} \right|^2 , \tag{11}$$

where m_e is the reduced mass of the electron and the HeH^+ ion. It is also convenient to represent the cross section in the form

$$\sigma_{v'v}(E_{el}) = \frac{\pi}{k_{el}^2} P_{v'v}(E_{el})\,, \tag{12}$$

where k_{el} is the wave vector of the incident electron and $P_{v'v}(E_{el})$ could be viewed as the probability for vibrational (de-)excitation at collision energy E_{el}.

Figures 3 and 4 demonstrate, as examples, the cross sections of Equation (11) and the corresponding probabilities from Equation (12) for the $v = 3 \to v' = 0, 1, 2, 4$ transitions. At very low scattering energies, below 0.02 eV, the de-excitation cross sections are smooth functions inversely proportional to the incident energy of the electron as predicted by the Wigner threshold law. But at higher energies, especially, just below the energy of the each excited threshold, $v' = 4, 5, \cdots$, the (de-)excitation cross sections and probabilities demonstrate series of Rydberg resonances, where they vary significantly.

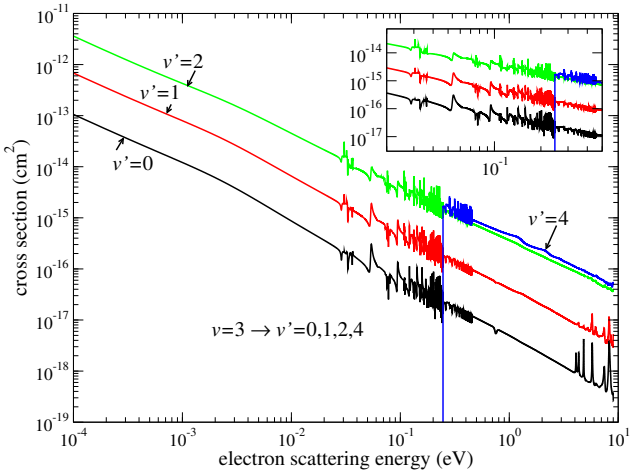

Figure 3. Cross sections of vibrational (de-)excitation from the vibrational level $v = 3$ to several other levels v'. The inset enlarges the region of Rydberg series of resonances close to the $v' = 4$ and $v' = 5$ ionization thresholds, situated at energy of 0.2465 and 0.4533 eV, respectively, above the $v = 3$ threshold.

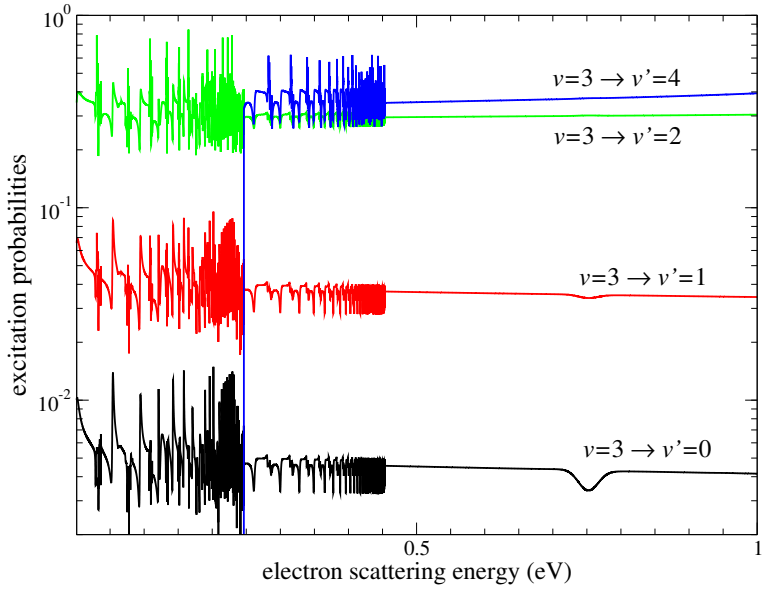

Figure 4. Probabilities $P_{v'v}(E_{el})$ for vibrational (de-)excitation from the vibrational level $v = 3$ to the $v' = 0, 1, 2, 4$ vibrational levels. Notice that the energy scale is linear in contrast to the logarithmic scale in Figure 3.

The thermally averaged rate coefficient $\alpha_{v' \leftarrow v}(T)$ (in atomic units) is obtained from the energy-dependent cross section of Equation (11),

$$\alpha_{v'v}(T) = \frac{8\pi}{(2\pi k_b T)^{3/2}} \int_0^\infty \sigma_{v'v}(E_{el}) e^{-\frac{E_{el}}{k_b T}} E_{el} dE_{el} \,, \tag{13}$$

where k_b is the Boltzmann coefficient and T is the temperature. Examples of obtained rate coefficients $\alpha_{v' \leftarrow v}(T)$ are shown in Figure 5.

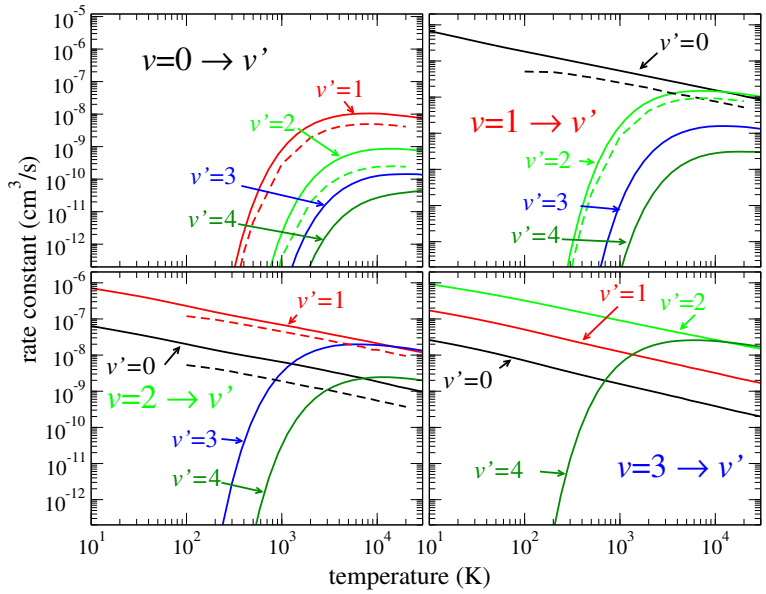

Figure 5. Thermally averaged rate coefficients for several (de-)excitation transitions obtained by direct integration using Equation (13). Vibrational transition $v \rightarrow v'$ labels are shown in each panel. Results of a previous calculation [15] are shown by dashed lines.

In order to simplify eventual applications of the calculated numerical coefficients $\alpha_{v'v}(T)$, the obtained numerical rate coefficients were fitted using the following analytical interpolation formula

$$\alpha^{fit}_{v'\leftarrow v}(T) = \frac{1}{\sqrt{T}} e^{-\frac{\Delta_{v'v}}{T}} P^{fit}_{v'v}(x), \tag{14}$$

where

$$P^{fit}_{v'v}(x) = a_0 + a_1 x + a_2 x^2 + a_3 x^3 \qquad \text{and} \qquad x = \ln(T). \tag{15}$$

with $P^{fit}_{v'v}(x) \approx P^{fit}_{vv'}(x)$. In equation (14), $\Delta_{v'v}$ is the threshold energy having the following expression:

$$\Delta_{v'v} = \begin{cases} E_{v'} - E_v > 0 & \text{for excitation}, \\ 0 & \text{for (de-)excitation}. \end{cases} \tag{16}$$

The coefficients a_i ($i = 0, 1, 2, 3$) are obtained for each pair of transitions $v' \leftrightarrow v$ from a numerical fit. The quantity $P^{fit}_{v'v}(x)$ in the above equation could be viewed as an averaged (de-)excitation probability that varies weakly with energy.

Figure 6 illustrates the rates coefficients for the $v = 3 \rightarrow v' = 0, 1, 2, 4$ transitions obtained numerically from Equation (13) and by the fit of Equation (14). Overall, the fitting curves agree well with the curves obtained numerically. The numerical values of a_i listed in the Table 2 are such that, when plugged into Equation (14), they give rate coefficients in units of $\mathrm{cm}^3 \cdot \mathrm{s}^{-1}$. The temperature in the fitting formulas of Equation (15) is in kelvin.

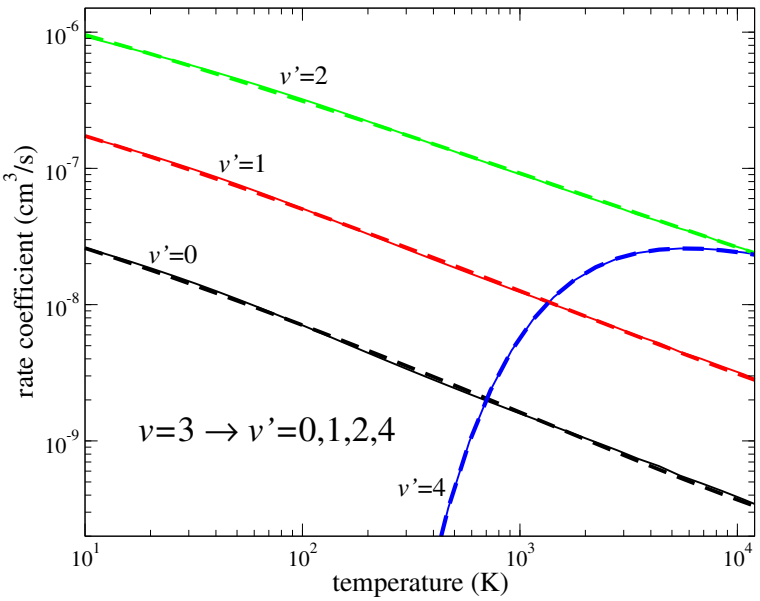

Figure 6. The figure demonstrates the quality of the fit of Equation (14): Numerical and fitted values are shown by solid and dashed lines respectively.

Table 2. Parameters a_0, a_1, a_2 and a_3 of the polynomial $P^{fit}_{v'v}(x) = P^{fit}_{vv'}(x)$ of Equation (14) for several pairs of initial and final vibrational level. The upper line in the header of the table specifies the pairs of initial and final vibrational levels for which the parameters are fitted. For convenience, we also specify (the second line of the header) the threshold energy $\Delta_{v'v}$ for excitation process of the corresponding pair. For all excitation and de-excitation processes, same parameters a_i are used in Equations (14) and (15) where the threshold for de-excitation is zero, $\Delta_{v'v} = 0$, as in Equation (16).

$v' - v$	0–1	0–2	0–3	0–4	1–2	1–3	1–4	2–3	2–4	3–4
$\Delta_{v'v}$ (K)	4191	7942	11251	14112	3751	7060	9920	3309	6169	2860
a_0	0.23e-5	0.20e-6	0.75e-7	0.11e-7	0.21e-5	0.47e-6	0.80e-7	0.24e-5	0.44e-6	0.28e-5
a_1	−0.11e-6	−0.20e-8	0.88e-8	0.31e-9	0.95e-7	0.62e-7	−0.71e-9	0.34e-6	−0.53e-8	0.16e-8
a_2	0.25e-8	0.10e-8	−0.28e-8	−0.24e-10	−0.18e-7	−0.16e-7	0.76e-9	−0.56e-7	0.40e-8	0.13e-7
a_3	0.85e-10	−0.11e-9	0.15e-9	−0.56e-12	0.79e-9	0.85e-9	−0.76e-10	0.22e-8	−0.36e-9	−0.92e-9

4. Conclusions and Discussion

In this study, cross sections and rate coefficients for electron-impact vibrational transitions in HeH^+ were computed for different combinations of the five lowest vibrational levels of HeH^+. The calculations were performed using the UK R-matrix package combined to the quantum-defect approach. The obtained thermally averaged rate coefficients were fitted with a simple analytical formula with four parameters. The numerical values of the fitting parameters are provided in Table 2. The obtained cross sections and rate coefficients could be used in modeling the hydrogen/helium plasma experiments as well as for modeling interstellar clouds and planetary atmospheres, where the HeH^+ ion is present.

The rotational structure of each vibrational level was neglected in the present approach such that the obtained cross sections and rate coefficients should be viewed as averaged over initial rotational states and summed over final rotational states of corresponding vibrational levels. Neglecting the rotational structure would correspond to an experiment for which the energy resolution is worse than a typical energy splitting between rotational levels. The rotational constants for the lowest vibrational levels of HeH^+ are in the interval 20–33 cm^{-1} (see Table 1). The energy resolution of existing experimental data on e^- + HeH^+ collisions is much worse [9]. Detailed rotational state-to-state thermally-averaged rate coefficients for rotational transitions without changing the vibrational state might be useful to model very cold environment, below 40 K. Due to this reason the rate coefficients obtained in the present study should not be viewed as accurate below 40 K. Theoretical rate coefficients for rotational excitation at low temperatures will be presented in a separate study.

It is worth stressing that narrow electronic resonances present in the $e - HeH^+$ spectrum (see Figure 1), around 1 eV and above, are taken into account only in a very crude manner. Namely, they produce scattering matrix $S(R)$ of Equation (4), which depends significantly on energy. Because the resonances are situated at relatively high energies and their widths are small (see, for example, the resonance at 4 eV for $R = 1.455$ bohrs in Figure 1), their effect is expected to be small on the obtained cross sections at low energies. The reason why the effect of such resonances is accounted for in a crude manner is because after the vibrational frame transformation of Equation (7), the resonances will be smeared out and will no appear in the excitation cross section. In a better treatment such resonances associated with HeH^* potential curves should be represented by one or several additional vibronic channels and would produce a few more additional resonances in the cross section for vibrational excitation. In the present treatment, the energy-dependence of $S(R)$, increases the excitation cross section near the corresponding energies but only on average, in a washed-out manner, without producing a few additional resonances. In any case, the effect of these resonances on the thermally-averaged rate coefficient is averaged out. A wider resonance appearing at large internuclear distances (for example, at 5 eV for $R = 1.7$ bohrs) could produce an important contribution to the vibrational excitation cross section at energies above 5 eV. A better treatment of the

vibrational excitation process accounting for electronic resonances is possible and will be developed in a further publication.

Acknowledgments: This work was supported by the National Science Foundation, Grant No. PHY-15-06391. V.K. acknowledges also a support from the Austrian-American Educational Commission.

Author Contributions: Authors contributed equally to this work.

Conflicts of Interest: The authors declare no conflict of interest.

References

1. Roberge, W.; Dalgarno, A. The formation and destruction of HeH^+ in astrophysical plasmas. *Astrophys. J.* **1982**, *255*, 489–496.
2. Dabrowski, I.; Herzberg, G. The predicted infrared spectrum of HeH^+ and its possible astrophysical importance. *Trans. N. Y. Acad. Sci.* **1977**, *38*, 14–25.
3. Black, J. Molecules in planetary nebulae. *Astrophys. J.* **1978**, *222*, 125–131.
4. Flower, D.; Roueff, E. On the formation and destruction of HeH^+ in gaseous nebulae and the associated infra-red emission line spectrum. *Astron. Astrophys.* **1979**, *72*, 361–366.
5. Lepp, S.; Stancil, P.; Dalgarno, A. Atomic and molecular processes in the early Universe. *J. Phys. B At. Mol. Opt. Phys.* **2002**, *35*, R57.
6. Zygelman, B.; Dalgarno, A. The radiative association of He^+ and H. *Astrophys. J.* **1990**, *365*, 239–240.
7. Kraemer, W.; Špirko, V.; Juřek, M. Formation of HeH^+ by radiative association of He^+ + H. An advanced ab initio study. *Chem. Phys. Lett.* **1995**, *236*, 177–183.
8. Strömholm, C.; Semaniak, J.; Rosén, S.; Danared, H.; Datz, S.; van der Zande, W.; Larsson, M. Dissociative recombination and dissociative excitation of $^4HeH^+$: Absolute cross sections and mechanisms. *Phys. Rev. A* **1996**, *54*, 3086–3094.
9. Tanabe, T.; Katayama, I.; Ono, S.; Chida, K.; Watanabe, T.; Arakaki, Y.; Haruyama, Y.; Saito, M.; Odagiri, T.; Hosono, K.; et al. Dissociative recombination of isotopes with an ultra-cold electron beam from a superconducting electron cooler in a storage ring. *J. Phys. B At. Mol. Opt. Phys.* **1998**, *31*, L297.
10. Larson, Å.; Orel, A. Wave-packet study of the products formed in dissociative recombination of HeH^+. *Phys. Rev. A* **2005**, *72*, 032701.
11. Takagi, H. Theoretical study of the dissociative recombination of HeH^+. *Phys. Rev. A* **2004**, *70*, 022709.
12. Larson, Å.; Nkambule, S.; Ertan, E.; Söder, J.; Orel, A.E. Studies of HeH: DR, RIP, VE, DE, PI, MN, ... *EPJ Web Conf.* **2015**, *84*, 03001.
13. Takagi, H.; Tashiro, M. Study on the dissociative recombination of HeH^+ by multi-channel quantum defect theory. *EPJ Web Conf.* **2015**, *84*, 02002.
14. Jimenez-Serra, I.; Martin-Pintado, J.; Viti, S.; Martin, S.; Rodriguez-Franco, A.; Faure, A.; Tennyson, J. The first measurements of the electron density enhancements expected in C-type shocks. *Astrophys. J. Lett.* **2006**, *650*, L135–L138.
15. Rabadán, I.; Sarpal, B.K.; Tennyson, J. Calculated rotational and vibrational excitation rates for electron-HeH^+ collisions. *Mon. Not. R. Astron. Soc.* **1998**, *299*, 171–175.
16. Tennyson, J. Electron–molecule collision calculations using the R-matrix method. *Phys. Rep.* **2010**, *491*, 29–76.
17. Carr, J.; Galiatsatos, P.; Gorfinkiel, J.; Harvey, A.; Lysaght, M.; Madden, D.; Mašín, Z.; Plummer, M.; Tennyson, J.; Varambhia, H. UKRmol: A low-energy electron-and positron-molecule scattering suite. *Euro. Phys. J. D* **2012**, *66*, 58.
18. Seaton, M.J. Quantum defect theory. *Rep. Prog. Phys.* **1983**, *46*, 167.
19. Greene, C.H.; Jungen, C. Molecular Applications of Quantum Defect Theory. *Adv. At. Mol. Phys.* **1985**, *21*, 51.
20. Aymar, M.; Greene, C.H.; Luc-Koenig, E. Multichannel Rydberg spectroscopy of complex atoms. *Rev. Mod. Phys.* **1996**, *68*, 1015.
21. Tennyson, J.; Brown, D.B.; Munro, J.J.; Rozum, I.; Varambhia, H.N.; Vinci, N. Quantemol-N: An expert system for performing electron molecule collision calculations using the R-matrix method. *J. Phys. Conf. Ser.* **2007**, *86*, 012001.

22. Faure, A.; Gorfinkiel, J.D.; Morgan, L.A.; Tennyson, J. GTOBAS: Fitting continuum functions with Gaussian-type orbitals. *Comput. Phys. Commun.* **2002**, *144*, 224.
23. Kokoouline, V.; Dulieu, O.; Kosloff, R.; Masnou-Seeuws, F. Mapped Fourier methods for long-range molecules: Application to perturbations in the Rb_2 (0_u^+) photoassociation spectrum. *J. Chem. Phys.* **1999**, *110*, 9865–9876.
24. Werner, H.J.; Knowles, P.J.; Lindh, R.; Manby, F.R.; Schütz, M.; Celani, P.; Korona, T.; Lindh, R.; Mitrushenkov, A.; Rauhut, G.; et al. MOLPRO, Version 2008.3, a Package of Ab Initio Programs, 2008.
25. Coxon, J.A.; Hajigeorgiou, P.G. Experimental Born-Oppenheimer Potential for the $X^1\Sigma^+$ Ground State of HeH^+: Comparison with the Ab Initio Potential. *J. Mol. Spectrosc.* **1999**, *193*, 306–318.
26. Stanke, M.; Kędziera, D.; Molski, M.; Bubin, S.; Barysz, M.; Adamowicz, L. Convergence of Experiment and Theory on the Pure Vibrational Spectrum of HeH^+. *Phys. Rev. Lett.* **2006**, *96*, 233002.
27. Jungen, C.; Atabek, O. Rovibronic interactions in the photoabsorption spectrum of molecular hydrogen and deuterium: An application of multichannel quantum defect methods. *J. Chem. Phys.* **1977**, *66*, 5584–5609.
28. Kokoouline, V.; Greene, C.H. Theory of dissociative recombination of D_{3h} triatomic ions applied to H_3^+. *Phys. Rev. Lett.* **2003**, *90*, 133201.

atoms

MDPI

Article

Cross Sections and Rate Coefficients for Rotational Excitation of HeH^+ Molecule by Electron Impact

Marjan Khamesian [1,†], Mehdi Ayouz [2,†], Jasmeet Singh [1,3,†] and Viatcheslav Kokoouline [1,*,†]

1 Department of Physics, University of Central Florida, Orlando, FL 32816, USA; khamesian.marjan@knights.ucf.edu (M.K.); jasmeet.singh@keshav.du.ac.in (J.S.)
2 LGPM, CentraleSupélec, Université Paris-Saclay, 8-10 rue Joliot-Curie, 91 190 Gif-sur-Yvette, France; mehdi.ayouz@centralesupelec.fr
3 Department of Physics, Keshav Mahavidyalaya, University of Delhi, Delhi 110 034, India
* Correspondence: Viatcheslav.Kokoouline@ucf.edu
† All authors contributed equally to this work.

Received: 2 July 2018; Accepted: 10 August 2018; Published: 3 September 2018

Abstract: Cross sections for rotational excitation and de-excitation of the HeH^+ ion by an electron impact are computed using a theoretical approach that combines the UK R-matrix code and the multi-channel quantum defect theory. The thermally-averaged rate coefficients derived from the obtained cross sections are fitted to an analytical formula valid for a wide range of temperatures.

Keywords: helium hydride ion; rotational excitation; R-matrix; quantum-defect theory

1. Introduction

Cross sections for the electronic, rotational, and vibrational excitation of molecules in collisions with electrons are important for understanding and modeling various plasma environments, such as the interstellar medium (ISM), planetary ionospheres and exospheres, in plasma processing and de-pollution technologies, and others. Measuring cross sections experimentally for such processes is usually difficult and expensive. However, theoretical methods for electron–molecule scattering together with abundant computational resources have made it possible to obtain reliable cross sections numerically, at least for diatomic and small polyatomic molecules.

The excitation of rotational and vibrational states of molecular ions has been studied theoretically for several decades. In particular, in one of the earliest studies of this kind, Boikova and Ob'edkov [1] considered the process using the Coulomb–Born approximation for the low-energy region. The first-order perturbation theory was applied, and a general analytical formula was derived in which dipole and quadrupole moments of the target ion determine the cross section for rotational excitation, while derivatives of the moments with respect to nuclear distances determine the cross section for vibrational excitation. The direct non-resonant excitation mechanism of the molecules was assumed to maintain the validity of the Born–Oppenheimer approximation for such processes. Later, Chu and Dalgarno [2] applied the same Coulomb–Born approximation to compute rate coefficients for the rotational excitation $j = 0 \to j' = 1$ of the CH^+ ion.

Flower [3] applied the semi-classical approximation and the time-dependent perturbation theory to the $j = 0 \to j' = 1$ transition for CH^+ and HeH^+. The rotation of the target molecule was quantised, while the motion of the incident electron was treated classically. The applicability of method is restricted to incident electron energies $E_{el} \gtrsim 2(E_{j'} - E_j)$, where E_j and $E_{j'}$ are the energies of the rotational states of the target ion.

In a series of publications, Rabadan et al. [4–6] modified the method developed by Chu and Dalgarno [2] for diatomic molecules. In their approach, the scattering matrix is obtained from first

principles using the R-matrix approach [7], rather than from the Coulomb–Born approximation. Similarly to Flower [3], cross sections for rotational excitation of CH^+ and HeH^+, as well as for NO^+ [4,5] are computed. However, as in the other studies mentioned above, the method does not account for near-threshold effects and assumes that different rotational levels are degenerate. In particular, it does not account for Rydberg resonances associated with closed rotational states of the neutral molecule, such as rotational Rydberg resonances of the HeH molecule in the case of e^--HeH^+ collisions. As it was shown later [8,9], this assumption is not appropriate if the incident electron couples strongly different rotational states of the target ion. In such a situation, the near-threshold effects should be accounted for to produce accurate rate coefficients at temperatures below 150 K. To address this problem, in Reference [10] the authors extrapolated the numerically-obtained cross sections down to the threshold using Wigner's threshold law, producing more accurate results compared to those obtained from a kinetic scaling of the previous -matrix study [6] on HeH^+ and CH^+. However, closed-channel effects associated with rotational resonances were still neglected in this study [10].

The theoretical method accounts for near-threshold effects, including rovibrational Rydberg resonances, and makes use of first-principle calculations (or experimental spectroscopic data if necessary), and is based on (1) the electron–molecule scattering matrix computed for fixed positions of nuclei (molecular-frame scattering matrix), (2) the idea of the rotational frame transformation [11], and (3) the molecular quantum defect theory (QDT) [12,13], which makes it possible to evaluate the scattering matrix in the laboratory frame (with respect to which the molecule rotates) and excitation cross sections. This method will be referred to below as the QDT method. It has been used in slightly different implementations in theoretical studies of rotational excitation for several molecular ions: H_2^+ [14,15], H_3^+ [16], HeH^+ [17], and CH^+ [18].

The molecular-frame scattering matrix in the QDT method can be evaluated in different ways. For example, in Reference [16], in calculations of the rotational excitation of H_3^+, the matrix was obtained by extrapolating quantum defects extracted from *ab initio* calculations of excited electronic states of H_3 for several internuclear geometries of the molecule. A similar method for the evaluation of the scattering matrix was used by Takagi et al. [19–22] in the study of the dissociative recombination of HeH^+. Another way to obtain the molecular-frame scattering matrix is to perform electron scattering calculations directly, using first principles. In a recent study [10], Čurík and Greene employed the molecular scattering matrix computed directly using the UK *R*-matrix method [7] in the calculation of the rotational excitation cross sections in e^--HeH^+ collisions.

In the present study, we discuss a general theoretical approach for the determination of rotational excitation cross sections for collisions of electrons with molecular ions at low scattering energies. A detailed derivation of the theory is presented for symmetric-top and linear target ions. A generalization to asymmetric top polyatomic targets is straightforward. We apply the method to the benchmark e^--HeH^+ system and compute cross sections and rate coefficients for excitation and de-excitation of the ion from the five lowest rotational states. The HeH^+ ion is one of the simplest molecular ions. It is present in helium-containing plasma, such as in fusion devices. It is thought to be the first molecule formed in the early Universe. It has also been suggested [23–27] that HeH^+ could be detected in planetary atmospheres, white dwarfs, and the interstellar medium. At low energies, e^--HeH^+ collisions can lead to dissociative recombination, rotational excitation, or dissociation recombination. The dissociative recombination of HeH^+ has been extensively studied both experimentally and theoretically [19–22,28]. There are no experimental measurements of cross sections for the rotational excitation of HeH^+, but there are a few previous theoretical studies [1,3,10,17]. Therefore, the present results can be compared with the previous calculations.

In the present study, essentially the same theoretical method as in Reference [17] is used to represent the rotational excitation of HeH^+, but the results for a larger number of rotational transitions in HeH^+ are obtained and an analytical fit of the thermally-averaged rate coefficients is performed, allowing the use of the data in plasma modeling.

The next section of the article presents the theoretical approach. In Section 3 we discuss the cross sections and rate coefficients obtained for the e^--HeH^+ collisions. Section 4 summarizes the obtained results. Finally, in Appendix A, details of the theoretical derivation of the main formulas of Section 2 are provided.

2. Theoretical Approach

A detailed derivation of the present theory is given in Appendix A. Here, we discuss only the main steps in the implementation of the approach.

As the first step in the calculation, the body-frame e^--HeH^+ reactance matrix $\hat{K}^\Lambda$ is determined. For rotational-excitation transitions without changing the vibrational state of the target, the reactance matrix can be evaluated using just one internuclear distance corresponding to the equilibrium position of the target ion, $R_{eq} = 1.445$ bohr for HeH^+. The ground electronic state of the HeH^+ ion is $X^1\Sigma^+$ with the Hartree–Fock electronic configuration of $1\sigma^2$. The matrix is obtained numerically using the UK R-matrix code [7,29]. Performing the scattering calculations, the R-matrix sphere of radius 10 bohr is used. Initially, several basis sets, including 6-311G*, DZP, and cc-pVTZ, were tested to investigate the stability of target properties such as dipole moment and ground state energy. Finally, the cc-pVTZ basis set was selected to perform the final calculations. A multicentered configuration interaction wave function expansion was used in the inner region, including two target states. The e^--HeH^+ reactance matrix is smooth at low electron energies, and the lowest electronic resonance appears at about 4 eV at geometries near the equilibrium.

At electron energies below the first excited electronic state of the target ion, different channels of the body-frame reactance matrix are labeled with partial wave labels, including the angular momentum quantum number l and its projection λ of the molecular axis. The matrix is block-diagonal, where each block corresponds to a given projection Λ of the total angular momentum (ion+electron) of the system. Thus, in practice, the body-frame reactance matrix is calculated separately for each Λ. At low scattering energies, below 10 eV, the target ion can only be in the ground electronic state $^1\Sigma^+$. Therefore, in the present calculations, the projection of the electronic angular momentum in a given channel is equal to Λ.

The reactance matrix is used to compute the body-frame scattering matrix

$$\hat{S}^\Lambda = \frac{\hat{1} + i\hat{K}^\Lambda}{\hat{1} - i\hat{K}^\Lambda}, \tag{1}$$

where $\hat{1}$ is the identity matrix. The laboratory-frame scattering matrix is then obtained by the transformation [30]

$$\mathcal{S}^J_{j'\mu' l';j\mu l} = \sum_{\lambda\lambda'} (-1)^{l'+\lambda'+l+\lambda} C^{j'\mu'}_{l'-\lambda' J\Lambda'} C^{j\mu}_{l-\lambda J\Lambda} S^\Lambda_{l'\lambda';l\lambda}, \tag{2}$$

where J is the total angular momentum of the e^--HeH^+ system, j, μ and j', μ' are the angular momenta with their projections on the molecular axis of the target before and after the rotational excitation of HeH^+, and $C^{j'\mu'}_{l'-\lambda' J\Lambda'}$ and $C^{j\mu}_{l-\lambda J\Lambda}$ are Clebsch–Gordan coefficients.

The total energy E of the system is the sum $E = E_{el} + E_{j\mu}$ of the relative kinetic energy E_{el} and the energy $E_{j\mu}$ of the initial state of the target. At a given energy E, the size N_o of the scattering matrix should be equal to the number of open channels with energies below E. Therefore, N_o varies with the energy depending on how many rotational states are open for a given E. However, the scattering matrix $\mathcal{S}^J$ in Equation (2) does not contain information about which channels are open or closed. The actual scattering matrix S^J with the correct energy dependence is obtained from $\mathcal{S}^J$ using the procedure of the closed-channel elimination [31,32] according to Equation (A15) of Appendix A. The resulting "physical" scattering matrix S^J represents properly rotational resonances associated with the closed rotational levels of the target.

Having the "physical" scattering matrix S^J, the cross section for the rotational excitation or de-excitation of the linear molecule by an electron impact is given as

$$\sigma_{j'\mu'\leftarrow j\mu}(E_{el}) = \frac{1}{2j+1}\frac{\pi}{k_j^2}\sum_{J,l,l'}(2J+1)\left|e^{i(l\pi/2+\sigma_l)}S^J_{j'\mu'l';j\mu l}e^{-i(l'\pi/2+\sigma_{l'})}\right|^2, \quad (3)$$

assuming that the initial $j\mu$ and final $j'\mu'$ rotational states are different (an inelastic process) and that the vibrational state is not changed during the process. In the above formula, σ_l is the Coulomb phase shift (see Equation (A5) in Appendix A).

3. Cross Sections and Rate Coefficients

Cross sections for electron impact transitions between the lowest five $j, j' = 0$–4 rotational states of HeH^+ were computed. Note that the only allowed projection μ in Equation (3) for HeH^+ in its ground electronic state is zero. Therefore, for scattering energies below the first excited ionization threshold of HeH^+, $\mu = \mu' = 0$ in Equation (3). Some examples are given in Figure 1. Solid lines in the figure represent the results obtained using the complete theoretical approach described in the previous section. The cross sections exhibit a strong resonant character. The resonances are produced by closed rotational states of the target. These resonances are washed out when thermally-averaged rate coefficients are computed. Therefore, in the calculation of the rate coefficients, one can use cross sections averaged over the resonances. Such averaged cross sections can be computed directly from the energy-independent scattering matrix $\mathcal{S}^J$, replacing in Equation (3) the matrix elements $S^J_{j'\mu'l';j\mu l}$ of the physical scattering matrix with the corresponding elements $\mathcal{S}^J_{j'\mu'l';j\mu l}$ of the energy-independent matrix. The cross sections calculated using the energy-independent scattering matrix are shown by dotted lines in Figure 1. Due to the overall $1/E_{el}$ dependence of the cross sections as a function of the collision energy, it is convenient to see the products $k_j^2\sigma_{j'\mu'\leftarrow j\mu}$, which could be viewed as excitation probabilities. They are shown in Figure 2. It is evident that the excitation probabilities obtained in the full treatment, including the closed-channel elimination, oscillate near the averaged value obtained in the treatment without considering the closed channels (i.e., from the energy-independent scattering matrix $\mathcal{S}^J$).

The obtained averaged rate coefficients are shown in Figure 3. They are compared with recently published data for the $j = 0 \leftrightarrow j'$ transitions: dotted lines are the calculations by Hamilton et al. [10] and the dashed lines are those of Čurík and Greene [17]. The agreement between the three sets of calculations are perfect to the $0 \leftrightarrow 2$ transitions, while for the $0 \leftrightarrow 1$ transitions the rate coefficients of Reference [10] are somewhat larger than the present result and the one from Reference [17]. For the $0 \leftrightarrow 3$ transitions, the coefficients of Reference [17] are somewhat larger than the present result and the one from Reference [10]. For the $0 \leftrightarrow 4$ transitions, the coefficients from the two other calculations agree with each other and are slightly larger than the present result.

The thermally averaged coefficients at low temperatures are sensitive to exact positions and widths of the lowest resonances, because the averaging integral over thermal velocities at low temperatures T is determined only by the small collision energies, $E_{el} \sim k_B T$. For example, the actual value of the cross sections for the $j = 1 \rightarrow j' = 0$ and $j = 2 \rightarrow j' = 1$ transitions in Figure 1 depends strongly on the position and the widths of the lowest resonances: at very low energies (below 2 meV), the cross sections are very different from the averaged ones shown with blue dotted lines. Therefore, the closed-channel elimination procedure is essential at low temperatures. Computationally, the procedure is not expensive if the number of channels is not very large (e.g., less than a thousand), and therefore, one can use the cross sections with all resonances in calculation of the rate coefficients for all temperatures.

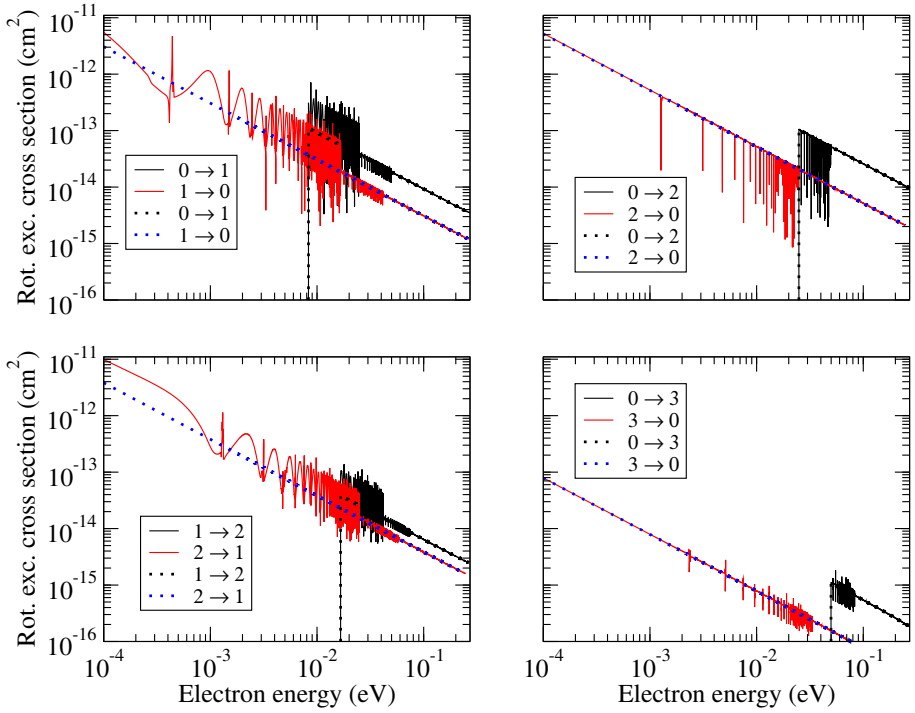

Figure 1. Rotational (de-)excitation cross sections for transitions between the four lowest rotational states of HeH^+. Solid lines represent the results obtained with the applied closed-channel elimination procedure of Equation (A14), while the dotted lines show the results for which the procedure was not applied.

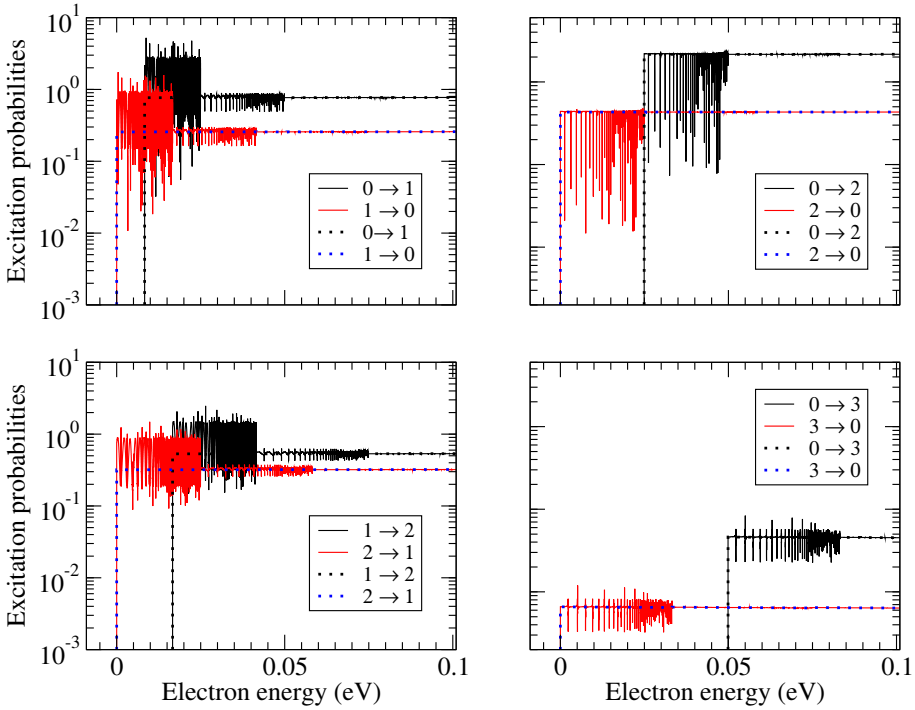

Figure 2. Rotational (de-)excitation probabilities for transitions between the four lowest rotational states of HeH^+. Solid lines represent the results obtained with the applied closed-channel elimination procedure, while the dotted lines show the results for which the procedure was not applied.

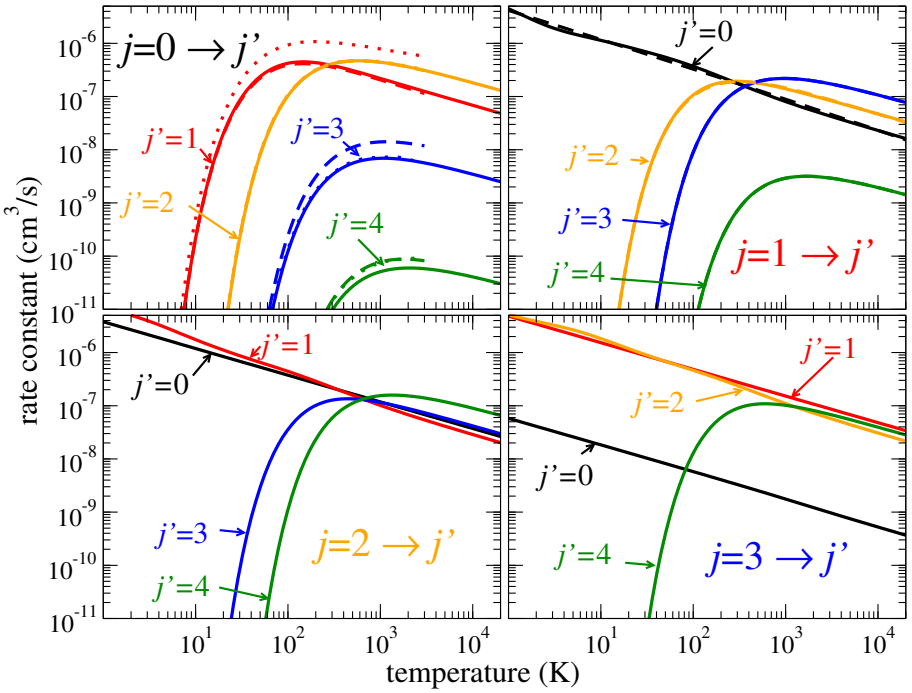

Figure 3. Rate coefficients (solid lines) for transitions from the four lowest rotational states of HeH^+, $j = 0, \cdots, 3$ rotational states. Dotted lines in the upper left panel are the calculations by Hamilton et al. [10], and the dashed lines are those of Čurík and Greene [17]. For the $0 \to 1$ transition, the dashed and solid lines overlap. For the $0 \to 2$ transition, the curves for all three calculations overlap. For the $0 \to 3$ transitions, the dotted and solid lines overlap. For the $0 \to 4$ transitions, the dotted and dashed lines overlap.

Due to the general $1/E_{el}$-dependence of cross sections $\sigma_{j' \leftarrow j}$, the calculated rate coefficients behave as $1/\sqrt{T}$ for de-excitation and $\exp\left(-\Delta_{j'\,j}/T\right)/\sqrt{T}$ for excitation transitions, where $\Delta_{j'\,j} = E_{j'\mu'} - E_{j\mu}$ (with $\mu = \mu' = 0$ for the present case) is the excitation energy. Therefore, similarly to References [16,33], for convenience of use, the rate coefficients are fitted to the formula

$$\alpha^{fit}_{j' \leftarrow j}(T) = \frac{1}{\sqrt{T}} e^{-\frac{\Delta_{j'j}}{T}} P^{fit}_{j'j}(x)\,, \tag{4}$$

where $P_{j'j}(T)$ are smooth functions of temperature and represented by the quadratic polynomial

$$P^{fit}_{j'j}(x) = a_0 + a_1 x + a_2 x^2 \qquad \text{and} \qquad x = \ln(T)\,, \tag{5}$$

where $\Delta_{j'j}$ is the threshold energy defined as

$$\Delta_{j'j} = \begin{cases} E_{j'} - E_j > 0 & \text{for excitation}\,, \\ 0 & \text{for (de-)excitation}\,. \end{cases} \tag{6}$$

The numerical parameters given in Table 1 are such that when used in Equations (4) and (5) along with the temperature T expressed in kelvin, the obtained numerical value of the rate coefficient in Equation (4) will be in units of cm^3/s.

Table 1. Parameters a_0, a_1, and a_2 of the polynomial $P_{jj'}^{fit}(x)$ of Equations (4) and (5) for several pairs of initial and final rotational states for de-excitation $j \leftarrow j'$ of HeH^+, with $j < j'$. The probabilities $P_{j'j}^{fit}(x)$ for the opposite (excitation) process, $j \rightarrow j'$, are obtained from $P_{jj'}^{fit}(x)$ multiplying them with the factor $(2j'+1)/(2j+1)$ (see Equation (7)). For convenience, we also specify (the second column) the threshold energy $\Delta_{j'j}$ in units of temperature (K) for the excitation process of the corresponding pair. For the de-excitation processes, $\Delta_{j'j} = 0$.

$j \leftarrow j'$	$\Delta_{j'j}$ (K)	a_0	a_1	a_2
$0 \leftarrow 1$	96	0.41×10^{-5}	-0.18×10^{-6}	-0.15×10^{-8}
$0 \leftarrow 2$	289	0.37×10^{-5}	-0.14×10^{-7}	0.85×10^{-9}
$0 \leftarrow 3$	578	0.57×10^{-7}	0.33×10^{-9}	-0.96×10^{-10}
$0 \leftarrow 4$	964	0.44×10^{-9}	-0.20×10^{-11}	0.77×10^{-12}
$1 \leftarrow 2$	192	0.73×10^{-5}	-0.83×10^{-6}	0.37×10^{-7}
$1 \leftarrow 3$	482	0.48×10^{-5}	-0.93×10^{-8}	0.38×10^{-9}
$1 \leftarrow 4$	868	0.75×10^{-7}	0.35×10^{-9}	-0.98×10^{-10}
$2 \leftarrow 3$	289	0.57×10^{-5}	-0.19×10^{-6}	-0.10×10^{-7}
$2 \leftarrow 4$	675	0.53×10^{-5}	0.61×10^{-9}	-0.39×10^{-9}
$3 \leftarrow 4$	385	0.32×10^{-5}	0.56×10^{-6}	-0.61×10^{-7}

Due to the detailed balance principle, the probabilities for the direct $P_{j'j}^{fit}(x)$ ($j' \leftarrow j$) and the inverse $P_{jj'}^{fit}(x)$ ($j \leftarrow j'$) processes are related to each other by the relative degeneracy factor

$$P_{j'j}^{fit}(x) = \frac{2j'+1}{2j+1} P_{jj'}^{fit}(x)\,. \tag{7}$$

The coefficients a_i ($i = 0, 1, 2$) are obtained numerically for each pair of transitions $j' \leftrightarrow j$ and are given in Table 1.

4. Conclusions

In this study, cross sections and thermally-averaged rate coefficients for electron impact rotational transitions in HeH^+ are computed for the five lowest rotational levels of HeH^+ using the UK *R*-matrix method combined with the multichannel quantum defect theory (MQDT). Our improved channel elimination procedure removes this ambiguity to evaluate accurate results at low energy (<0.01 eV). This and our previous study [33] make us believe that once the collisional excitation cross section data is available, the analysis of the intensities of infra-red and microwave regions can provide information for the diagnostics of tokamak, as well as the study of planetary atmospheres and of the interstellar medium.

With certain modifications accounting for a different threshold behavior of the cross section at low collision energies, the present theoretical approach can be extended for collisions between an electron and a neutral molecule. These developments will be published later.

Author Contributions: Methodology, M.A., M.K. and V.K.; Software, M.A., M.K. and J.S.; Validation, M.A., M.K., J.S. and V.K.; Investigation, M.A., M.K. and V.K.; Resources, V.K.; Writing-Original Draft Preparation, M.K., J.S. and V.K.; Writing-Review & Editing, M.A. and V.K.; Supervision, V.K.

Funding: This work was supported by the National Science Foundation, Grant No. PHY-15-06391 and the University Grant Commission (UGC), Government of India under Raman Post Doctoral Fellowship No. 5-159/2016 (IC).

Acknowledgments: V.K. acknowledges a support from the Austrian–American Educational Commission.

Conflicts of Interest: The authors declare no conflict of interest.

Appendix A

This section provides details on the formulas used for the cross section calculations. First, rotational and electronic states of the target ion are introduced as:

$$\phi_{j\mu m_j} = \sqrt{\frac{2j+1}{8\pi^2}} \left[D^j_{m_j\mu}(\Omega)\right]^* \omega(\mathbf{r_2}), \tag{A1}$$

where j, m_j, and μ are the angular momentum of HeH^+ and its projections in the laboratory frame (LF) and the molecular frame (MF), respectively. The function $\omega(\mathbf{r_2})$ specifies the two-electron wave function of HeH^+, which depends on μ. $D^j_{m_j\mu}(\Omega)$ is the Wigner function depending on three Euler angles, which are called collectively by symbol Ω. The vibrational state of the target ion is not specified (i.e., pure rotational transitions are considered). We assume that the incident electron plane wave propagates along the z-axis in the LF with a wave vector of magnitude k_j. The complete scattering wave function $\Psi_{j\mu m_j}$ of the system in the asymptotic region is given by the sum of the contributions due to the pure Coulomb field ψ_C and the short-range potential V_{sr}, representing the difference between the actual e^-+HeH^+ interaction and the Coulomb potential, as follows [34]:

$$\begin{aligned}\Psi_{j\mu m_j} \rightarrow \psi_C(k_j,\vec{r})\phi_{j\mu m_j} + \\ \tfrac{1}{r}\textstyle\sum_{j'\mu' m_{j'}} \exp\left[i(k_{j'}r - \eta' \ln\{2k_{j'}r\})\right] f_{j'\mu' m_{j'}\leftarrow j\mu m_j}(\vec{k}_{j'})\phi_{j'\mu' m_{j'}}\,,\end{aligned} \tag{A2}$$

where $\eta' = -1/(k_{j'}\hbar^2)$ is the Sommerfeld parameter. In the above expression, energetically open channels are labeled by the quantum numbers j' and μ'; $f_{j'\mu' m_{j'}\leftarrow j\mu m_j}(\vec{k}_j)$ denotes the differential amplitude for scattering from state $\{j,\mu,m_j\}$ to $\{j',\mu,m'_j\}$. The amplitude includes only the contributions due to V_{sr} . We assume that the incident wave in ψ_C is a plane wave for large r, such that the incident current density is k_j. Similar to Reference [30], channel functions with a definite total angular momentum $\vec{J} = \vec{l} + \vec{j}$ and its projection $M = m_l + m_j$ in the LF are introduced:

$$\Phi^{JM}_{j\mu l} = \sqrt{\frac{2j+1}{8\pi^2}}\omega(\mathbf{r_{N-1}}) \sum_{m_l=-l}^{l}\sum_{m_j=-j}^{j} C^{JM}_{lm_l jm_j}\left[D^j_{m_j\mu}(\Omega)\right]^* Y_{lm_l}(\hat{r})\,, \tag{A3}$$

where l and m_l are the incident electron angular momentum and its projection in the LF. The scattering state of Equation (A1) takes the form

$$\begin{aligned}\Psi_{j\mu m_j} \rightarrow \tfrac{2\pi i}{r\sqrt{k_j}} \textstyle\sum_{JM}\sum_{lm_l} Y_{lm_l}(\hat{k}_j) i^l e^{i\sigma_l} \sum_{j'l'} \frac{C^{JM}_{lm_l jm_j}}{\sqrt{k_{j'}}} \Phi^{JM}_{j'\mu' l'} \times \\ \left[\delta_{j'j}\delta_{\mu'\mu}\delta_{l'l} e^{-i\theta_{j'}(r)} - S^J_{j'\mu' l';j\mu l} e^{i\theta_{j'}(r)}\right]\,,\end{aligned} \tag{A4}$$

$$\text{with } \theta_{j'}(r) = k_{j'}r - \tfrac{l'\pi}{2} - \eta' \ln(2k_{j'}r) + \sigma_{l'} \text{ and } \sigma_{l'} = \arg\Gamma\left(l'+1+i\eta'\right)\,. \tag{A5}$$

The pure Coulomb scattering wave function can be written in a similar form:

$$\begin{aligned}\psi_C(k_j,\vec{r})\phi_{j\mu m_j} \rightarrow \tfrac{2\pi i}{r\sqrt{k_j}} \textstyle\sum_{JM}\sum_{lm_l} Y_{lm_l}(\hat{k}_j) i^l e^{i\sigma_l} \sum_{j'l'} \frac{C^{JM}_{lm_l jm_j}}{\sqrt{k_{j'}}} \Phi^{JM}_{j'\mu' l'} \times \\ \left[\delta_{j'j}\delta_{\mu'\mu}\delta_{l'l} e^{-i\theta_{j'}(r)} - \delta_{j'j}\delta_{\mu'\mu}\delta_{l'l} e^{i\theta_{j'}(r)}\right]\,.\end{aligned} \tag{A6}$$

The difference between Equations (A4) and (A6) gives the last term in Equation (A2):

$$\begin{aligned}\textstyle\sum_{m_{j'}} \exp\left[i(k_{j'}r - \eta' \ln\{2k_{j'}r\})\right] f_{j'\mu' m_{j'}\leftarrow j\mu m_j}(\vec{k}_{j'})\phi_{j'\mu' m_{j'}} = \\ \tfrac{2\pi i}{\sqrt{k_j}} \textstyle\sum_{JM}\sum_{lm_l} Y_{lm_l}(\hat{k}_j) i^l e^{i\sigma_l} \sum_{l'} \frac{C^{JM}_{lm_l jm_j}}{\sqrt{k_{j'}}} \Phi^{JM}_{j'\mu' l'} \left(\delta_{j'j}\delta_{\mu'\mu}\delta_{l'l} - S^J_{j'\mu' l';j\mu l}\right) e^{i\theta_{j'}(r)}\,.\end{aligned} \tag{A7}$$

Moving the exponent factor to the right-hand side, we obtain

$$\sum_{m_{j'}} f_{j'\mu' m_{j'} \leftarrow j\mu m_j}(\vec{k}_{j'}) \phi_{j'\mu' m_{j'}} = \frac{2\pi i}{\sqrt{k_j}} \sum_{JM} \sum_{lm_l} Y_{lm_l}(\hat{k}_j) \sum_{l'} \frac{C^{JM}_{lm_l jm_j}}{\sqrt{k_{j'}}} \Phi^{JM}_{j'\mu' l'} i^l e^{i\sigma_l} \left(\delta_{j'j} \delta_{\mu'\mu} \delta_{l'l} - S^J_{j'\mu' l';j\mu l} \right) e^{i\sigma_{l'}} i^{-l'} . \tag{A8}$$

Multiplying both sides of the above equation with $\phi_{j'\mu'\tilde{m}'_j}$, integrating over electronic coordinates $\mathbf{r_2}$ of the target and the angles Ω, we obtain the scattering amplitude for the transition $j\mu m_j \to j'\mu'\tilde{m}'_j$:

$$f_{j'\mu'\tilde{m}'_j \leftarrow j\mu m_j}(\vec{k}_{j'}) = \frac{2\pi i}{\sqrt{k_j}} \sum_{JM} \sum_{lm_l} Y_{lm_l}(\hat{k}_j) \sum_{l'm'_l} \frac{C^{JM}_{lm_l jm_j}}{\sqrt{k_{j'}}} C^{JM}_{l'm'_l j'\tilde{m}'_j} Y_{l'm'_l}(\theta\varphi) i^l e^{i\sigma_l} \left(\delta_{j'j} \delta_{\mu'\mu} \delta_{l'l} - S^J_{j'\mu' l';j\mu l} \right) e^{i\sigma_{l'}} i^{-l'} . \tag{A9}$$

To make notations slightly more uniform, in the equations below, we use symbol m'_j instead of $\tilde{m}'_j$. The cross section for rotational excitation $\sigma_{j'\mu'\leftarrow j\mu}(E_{el})$ averaged over initial projections m_j and summed over final projections $m'_j = \tilde{m}'_j$ is obtained as follows:

$$\sigma_{j'\mu'\leftarrow j\mu}(E_{el}) = \int \sin\theta d\theta d\varphi \, \frac{1}{2j+1} \frac{k_{j'}}{k_j} \sum_{m_j, m'_j} \left| f_{j'\mu' m'_j \leftarrow j\mu m_j}(\vec{k}_{j'}) \right|^2 , \tag{A10}$$

where $E_{el} = (\hbar k_j)^2/(2m)$ is the energy of the incident electron, and θ and ϕ are spherical angles of the wave vector $\vec{k}_{j'}$ of the scattered electron in the LF.

Below, we assume that the incident plane wave propagates along the z-axis of the LF (i.e., $Y_{lm_l}(\hat{k}_j) = \delta_{m_l,0}\sqrt{(2l+1)/(4\pi)}$ in Equation (A9)). Therefore, the number of summation indexes in Equation (A9) is reduced from six to five, over J, M, l, l', and m'_l. The square of the amplitude in Equation (A10) doubles the number of summation indexes. We will refer to the additional indexes as $\bar{J}, \bar{M}, \bar{l}, \bar{l}'$, and $\bar{m}_l{}'$. With the sums over m_j and m'_j in Equation (A10), the number of summation indexes becomes twelve. Due to the orthogonality of $Y_{l'm'_l}(\theta\varphi)$ and $Y_{\bar{l}'\bar{m}_l{}'}(\theta\varphi)$, the integral over θ and φ reduces the number of summation indexes to ten with $l' = \bar{l}'$ and $m'_l = \bar{m}_l{}'$. In the remaining ten-fold sum, the double sum over m'_j and m'_l is

$$\sum_{m'_l, m'_j} C^{JM}_{l'm'_l j'm'_j} C^{\bar{J}\bar{M}}_{l'm'_l j'm'_j} = \delta_{J,\bar{J}} \delta_{M,\bar{M}} , \tag{A11}$$

which reduces the number of indexes to $J, M, l, l', \bar{l}$, and m_j. Again, in the remaining sum (because $m_l = \bar{m}_l = 0$):

$$\sum_{m_j, M} C^{JM}_{l0jm_j} C^{JM}_{\bar{l}0jm_j} = \frac{2J+1}{2l+1} \delta_{l,\bar{l}} . \tag{A12}$$

With the above simplifications, the cross section of Equation (A10) becomes:

$$\sigma_{j'\mu'\leftarrow j\mu}(E_{el}) = \frac{1}{2j+1} \frac{\pi}{k_j^2} \sum_{J,l,l'} (2J+1) \left| e^{i(\sigma_l + l\pi/2)} S^J_{j'\mu' l';j\mu l} e^{i(\sigma_{l'} - l'\pi/2)} \right|^2 , \tag{A13}$$

assuming that the initial $j\mu$ and final $j'\mu'$ states are different (i.e., an inelastic process).

For a given total energy $E = E_{el} + E_{j\mu}$ of the e^--HeH^+ system, the size N_o of the matrix S^J in the formula above is equal to the number of open scattering channels with energies $E_{j'\mu'} < E$. However, the closed channels with $E_{j'\mu'} > E$, which are not included explicitly in Equation (A13), usually significantly influence the S-matrix and the cross section. Such closed channels are taken into

account using the "closed channel elimination" procedure [31,32]. The S-matrix in Equation (A13) is obtained from another matrix, having a larger number of channels, including the channels that are closed at given E. Namely, S^J in Equation (A13) is given by:

$$S^J = e^{i\hat{\eta}_c}\left[S^{oo} - S^{oc}\left(S^{cc} - e^{-2i\beta(E)}\right)^{-1} S^{co}\right] e^{i\hat{\eta}_c}\,, \tag{A14}$$

where $\hat{\eta}_c$ is a $N_o \times N_o$ [32] diagonal matrix with diagonal elements equal to the Coulomb phase shift in the corresponding channel, $[\hat{\eta}_c]_{i,i} = -\frac{l\pi}{2} - \eta\ln(2k_j r) + \sigma_l$. The matrices S^{oo}, S^{oc}, S^{cc}, and S^{co} are submatrices of the larger $N \times N$ S-matrix, which includes open and closed channels ($N \geq N_o$). The larger S-matrix, partitioned as:

$$\mathcal{S}^J = \begin{pmatrix} S^{oo} & S^{oc} \\ S^{co} & S^{cc} \end{pmatrix}\,, \tag{A15}$$

where the partition of the matrix elements in the "o"- and "c"-parts is made on the basis whether the corresponding channel, $j\mu$ or $j'\mu'$, is open or closed for ionization at the total energy E. The quantity $\beta(E)$ is a diagonal $N_c \times N_c$ matrix:

$$\beta_{j'\mu';j\mu}(E) = \frac{\pi}{\sqrt{2(E_{j\mu} - E)}}\delta_{j'j}\delta_{\mu'\mu}\,, \tag{A16}$$

and $N_c = N - N_o$ is the number of closed channels.

We assume that the initial and final vibrational states of the target ion are the same. In this situation, it is a good approximation to consider that the averaged internuclear distance in the target ion is unchanged during the rotational excitation process and is equal to the equilibrium distance R_e. The scattering matrix $\mathcal{S}^J$ in Equation (A15) is therefore obtained for a fixed geometry R_e in the basis of channel functions of Equation (A3). In the R-matrix calculation, the reactance matrix K is obtained in a different basis of functions $X^{JM}_{l\lambda}$ [30], in which the molecule is fixed in space (i.e., the body-fixed (BF) basis). The channel functions $X^{JM}_{l\lambda}$ transform into $\Phi^{JM}_{j\mu l}$ in the following way:

$$\Phi^{JM}_{j\mu l} = \sum_{\lambda} X^{JM}_{l\lambda}(-1)^{l+\lambda} C^{j\mu}_{l-\lambda J\Lambda}\,, \tag{A17}$$

where λ is the projection of the orbital momentum l of the incident electron on the molecular axis, and Λ is the projection of the total orbital momentum of all electrons on the molecular axis. For the HeH^+ ion in the ground electronic state, $\lambda = \Lambda$ and $\mu = 0$. The S-matrix obtained in the BF is diagonal over quantum numbers J and Λ. Therefore, the transformation between the S-matrices obtained in the two bases is given by:

$$\mathcal{S}^J_{j'\mu' l';j\mu l} = \sum_{\lambda\lambda'}(-1)^{l'+\lambda'+l+\lambda} C^{j'\mu'}_{l'-\lambda' J\Lambda'} C^{j\mu}_{l-\lambda J\Lambda} S^{\Lambda}_{l'\lambda';l\lambda}\,, \tag{A18}$$

where $S^{\Lambda}_{l'\lambda';l\lambda}$ is an element of the the BF S-matrix obtained from the reactance matrix K as:

$$\hat{S}^{\Lambda} = \frac{\hat{1} + i\hat{K}^{\Lambda}}{\hat{1} - i\hat{K}^{\Lambda}}\,, \tag{A19}$$

with $\hat{1}$ being the identity matrix and $\hat{K}^{\Lambda}$ is the reactance matrix obtained numerically using the UK R-matrix code.

References

1. Boikova, R.F.; Ob'edkov, V.D. Rotational and vibrational excitation of molecular ions by electrons. *Sov. Phys. JETP* **1968**, *27*, 772.
2. Chu, S.I.; Dalgarno, A. Rotational excitation of CH^+ by electron impact. *Phys. Rev. A* **1974**, *10*, 788. [CrossRef]
3. Flower, D. Electron collisional excitation of rotational transitions in CH^+ and HeH^+. *Astron. Astrophys.* **1979**, *73*, 237–239.
4. Rabadán, I.; Sarpal, B.K.; Tennyson, J. On the calculation of electron-impact rotational excitation cross sections for molecular ions. *J. Phys. B At. Mol. Opt. Phys.* **1998**, *31*, 2077. [CrossRef]
5. Rabadán, I.; Sarpal, B.K.; Tennyson, J. Calculated rotational and vibrational excitation rates for electron-HeH^+ collisions. *Mon. Not. R. Astron. Soc.* **1998**, *299*, 171–175. [CrossRef]
6. Rabadán, I.; Tennyson, J. ROTIONS: A program for the calculation of rotational excitation cross sections in electron—Molecular ion collisions. *Comput. Phys. Commun.* **1998**, *114*, 129–141. [CrossRef]
7. Tennyson, J. Electron—Molecule collision calculations using the R-matrix method. *Phys. Rep.* **2010**, *491*, 29–76. [CrossRef]
8. Faure, A.; Kokoouline, V.; Greene, C.H.; Tennyson, J. Near-threshold rotational excitation of molecular ions by electron impact. *J. Phys. B At. Mol. Opt. Phys.* **2006**, *39*, 4261. [CrossRef]
9. Faure, A.; Tennyson, J.; Kokoouline, V.; Greene, C.H. Rotational excitation of interstellar molecular ions by electrons. In *Journal of Physics: Conference Series*; IOP Publishing: Bristol, UK, 2009; Volume 192.
10. Hamilton, J.R.; Faure, A.; Tennyson, J. Electron-impact excitation of diatomic hydride cations—I. HeH^+, CH^+, ArH^+. *Mon. Not. R. Astron. Soc.* **2016**, *455*, 3281–3287. [CrossRef]
11. Chang, E.S.; Fano, U. Theory of electron-molecule collisions by frame transformations. *Phys. Rev. A* **1972**, *6*, 173. [CrossRef]
12. Greene, C.H.; Jungen, C. Molecular applications ofquantum defect theory. *Adv. At. Mol. Phys.* **1985**, *21*, 51–121.
13. Jungen, C. *Molecular Applications of Quantum Defect Theory*; Institute of Physics Publishing: Bristol, UK, 1996.
14. Motapon, O.; Pop, N.; Argoubi, F.; Mezei, J.Z.; Epée Epée, M.D.; Faure, A.; Telmini, M.; Tennyson, J.; Schneider, I.F. Rotational transitions induced by collisions of HD^+ ions with low-energy electrons. *Phys. Rev. A* **2014**, *90*, 012706. [CrossRef]
15. Epée Epée, M.D.; Mezei, J.Z.; Motapon, O.; Pop, N.; Schneider, I.F. Reactive collisions of very low-energy electrons with H_2^+ rotational transitions and dissociative recombination. *Mon. Not. R. Astron. Soc.* **2015**, *455*, 276–281. [CrossRef]
16. Kokoouline, V.; Faure, A.; Tennyson, J.; Greene, C.H. Calculation of rate constants for vibrational and rotational excitation of the H_3^+ ion by electron impact. *Mon. Not. R. Astron. Soc.* **2010**, *405*, 1195–1202.
17. Čurík, R.; Greene, C.H. Inelastic low-energy collisions of electrons with HeH^+: Rovibrational excitation and dissociative recombination. *J. Chem. Phys.* **2017**, *147*, 054307. [CrossRef] [PubMed]
18. Faure, A.; Halvick, P.; Stoecklin, T.; Honvault, P.; Epée Epée, M.; Mezei, J.; Motapon, O.; Schneider, I.; Tennyson, J.; Roncero, O.; et al. State-to-state chemistry and rotational excitation of CH^+ in photon-dominated regions. *Mon. Not. R. Astron. Soc.* **2017**, *469*, 612–620. [CrossRef] [PubMed]
19. Tanabe, T.; Katayama, I.; Ono, S.; Chida, K.; Watanabe, T.; Arakaki, Y.; Haruyama, Y.; Saito, M.; Odagiri, T.; Hosono, K.; et al. Dissociative recombination of HeH^+ isotopes with an ultra-cold electron beam from a superconducting electron cooler in a storage ring. *J. Phys. B At. Mol. Opt. Phys.* **1998**, *31*, L297. [CrossRef]
20. Takagi, H. Theoretical study of the dissociative recombination of HeH^+. *Phys. Rev. A* **2004**, *70*, 022709. [CrossRef]
21. Takagi, H. Cross sections of the processes induced by electron collisions with H_2^+, HeH^+, and their isotopes. *Fusion Sci. Technol.* **2013**, *63*, 406–412. [CrossRef]
22. Takagi, H.; Tashiro, M. Study on the dissociative recombination of HeH^+ by multi-channel quantum defect theory. In *EPJ Web of Conferences*; EDP Sciences: Les Ulis, France, 2015; Volume 84.
23. Dabrowski, I.; Herzberg, G. The predicted infrared spectrum of HeH^+ and its possible astrophysical importance. *Trans. N. Y. Acad. Sci.* **1977**, *38*, 14–25. [CrossRef]
24. Black, J. Molecules in planetary nebulae. *Astrophys. J.* **1978**, *222*, 125–131. [CrossRef]

25. Flower, D.; Roueff, E. On the formation and destruction of HeH^+ in gaseous nebulae and the associated infra-red emission line spectrum. *Astron. Astrophys.* **1979**, *72*, 361–366.
26. Roberge, W.; Dalgarno, A. The formation and destruction of HeH^+ in astrophysical plasmas. *Astrophys. J.* **1982**, *255*, 489–496. [CrossRef]
27. Harris, G.; Lynas-Gray, A.; Miller, S.; Tennyson, J. The role of HeH^+ in cool helium-rich white dwarfs. *Astrophys. J. Lett.* **2004**, *617*, L143. [CrossRef]
28. Guberman, S.L. Dissociative recombination without a curve crossing. *Phys. Rev. A* **1994**, *49*, R4277. [CrossRef] [PubMed]
29. Tennyson, J.; Brown, D.B.; Munro, J.J.; Rozum, I.; Varambhia, H.N.; Vinci, N. Quantemol-N: An expert system for performing electron molecule collision calculations using the R-matrix method. In *Journal of Physics: Conference Series*; IOP Publishing: Bristol, UK, 2007; Volume 86.
30. Douguet, N.; Fonseca dos Santos, S.; Raoult, M.; Dulieu, O.; Orel, A.E.; Kokoouline, V. Theory of radiative electron attachment to molecules: Benchmark study of CN^-. *Phys. Rev. A* **2013**, *88*, 052710. [CrossRef]
31. Seaton, M.J. Quantum defect theory. *Rep. Prog. Phys.* **1983**, *46*, 167. [CrossRef]
32. Aymar, M.; Greene, C.H.; Luc-Koenig, E. Multichannel Rydberg spectroscopy of complex atoms. *Rev. Mod. Phys.* **1996**, *68*, 1015. [CrossRef]
33. Ayouz, M.; Kokoouline, V. Cross Sections and Rate Coefficients for Vibrational Excitation of HeH^+ Molecule by Electron Impactukrm. *Atoms* **2016**, *4*, 30. [CrossRef]
34. Friedrich, H. *Scattering Theory*; Springer: Berlin/Heidelberg, Germany, 2013.

Cross sections for vibronic excitation of CH^+ by low-energy electron impact

Xianwu Jiang,[1] Chi Hong Yuen,[2] Pietro Cortona,[1] Mehdi Ayouz,[3] and Viatcheslav Kokoouline[2,*]

[1]*Laboratoire Structures, Propriétés et Modélisation des Solides de CentraleSupélec, CNRS-UMR8580, Université Paris-Saclay, 91190, Gif-sur-Yvette, France*

[2]*Department of Physics, University of Central Florida, 32816, Florida, USA*

[3]*Laboratoire Génie des Procédés et Matériaux EA 4038 de CentraleSupélec, Université Paris-Saclay, 91190, Gif-sur-Yvette, France*

(Received 26 September 2019; published 24 December 2019)

A theoretical approach for the electron-impact vibronic excitation of molecular ions with low-lying excited electronic states is described. In this approach, the fixed-nuclear *R*-matrix method is employed to compute electron-ion scattering matrices in the Born-Oppenheimer approximation. A vibronic frame transformation and the closed-channel elimination procedure in a spirit of molecular quantum defect theory are employed to construct an energy-dependent scattering matrix describing interactions between vibronic channels of the target ion induced by the incident electron. The obtained scattering matrix accounts for Rydberg series of vibronic resonances in the collisional spectrum. The approach is applied to the CH^+ ion of an astrophysical and technological interest. Cross sections for vibronic excitation for different combinations of initial and final vibronic states are computed. A good agreement between electronic-excitation cross sections, obtained using the quantum defect theory and in a direct *R*-matrix calculation, demonstrates that the present approach provides a reliable tool for determination of vibronic (de-)excitation cross sections for targets with low-energy electronic resonances. Such targets were difficult to treat theoretically using earlier methods.

DOI: 10.1103/PhysRevA.100.062711

I. INTRODUCTION

In many fields of research and applications, it is essential to have accurate cross sections for different processes taking place in collisions between molecular ions and electrons. Among such processes are electron-impact rotational (RE), vibrational (VE), and electronic (EE) excitation of the ions; dissociative recombination (DR); and photoionization and its inverse process, radiative recombination. Some cross sections could be obtained in experiments. However, for many processes, especially for the processes involving excited-state ions (ions here and below are assumed to be molecular ions, not atomic) or such ions as radicals, which are unstable in collisions with other species present nearby, an experimental approach is difficult or impossible. Even for stable ions in their ground quantum state, an experimental approach is often very expensive.

On the other hand, for theoretical approaches a significant complication in computation of the cross sections is the presence of vibrational and rotational degrees of freedom that have to be accounted for to obtain an accurate description of the processes. Electronic excitation and ionization of molecules can be treated theoretically, at least to some extent in the Born-Oppenheimer approximation or by taking into account the Franck-Condon factor. For other processes, such as rovibrational excitation or dissociative recombination, non-Born-Oppenheimer effects should be accounted for explicitly.

With modern development of electron-scattering methods and abundant computational resources, it became possible to compute, with an acceptable uncertainty, cross sections for many processes in electron-ion collisions. Significant progress was made for processes in diatomic ions formed by light elements: H_2^+ [1], HeH^+ [1], BeH^+ [2], BF^+ [3], CH^+ [4–7], SH^+ [8], N_2^+ [9–11], O_2^+ [12] with a few other diatomic ions, and the simplest triatomic ion H_3^+ with its isotopologs [13–17], where non-Born-Oppenheimer effects in electron-ion collisions were accurately accounted for, typically by using a quantum-defect approach combined with rotational and vibrational frame transformations. With some additional simplifications, such processes as rovibrational excitation and dissociative recombination were also successfully described theoretically for larger molecular ions: CH_3^+ [18], H_3O^+ [18,19], NH_4^+ [20], HCO^+ [21–27], BF_2^+ [28], N_2H^+ [27], $HCNH^+$ [29–32], $CH_2NH_2^+$ [33], and NH_2CHOH^+ [34].

Theoretically, non-Born-Oppenheimer couplings in electron-ion collisions are treated differently for the ions with low-energy electronic resonances appearing for geometries near the equilibrium of the target ion (in a fixed-nuclei picture) and for the ions without such low-energy electronic resonances. In the former case, usually the potential energy surface (PES) of the doubly excited neutral molecule crosses the ionic PES near the equilibrium geometry; in the latter case, there is no such a resonance PES. The ions of the first type usually (not always) have the first excited electronic state at a relatively low energy, below 5 eV; the ions of the second type have the first excited electronic state at a higher energy.

The presence of low-energy electronic resonances in the first type of the ions increases significantly compared to the ions of the second type, the DR, EE, VE, and RE cross sections at low collision energies. Because of the significant

*slavako@ucf.edu

difference in the physics of couplings in electron-ion collisions in the two types of the ions, one developed two types of approaches. The first approach, developed for DR, VE, and RE processes and originated from studies by O'Malley [35] and Bardsley [36–38], takes into account explicitly the PES crossing. The second approach, based mainly on studies by Lee [39], Jungen *et al.* [40,41], and Giusti [42] and employed when there is no PES crossing, accounts for the coupling between the incident electron and the rovibronic Rydberg resonances of the neutral molecule. In the absence of a PES crossing, such resonances are responsible for the major contribution to the DR cross section at low energies [13,42,43]. This is especially important for polyatomic ions, listed above. All these ions have a closed electronic shell, the first excited electronic state at a high energy, and no PES crossing near the equilibrium geometry of the ions.

There are situations where there is a PES crossing near the ion equilibrium geometry and, in addition, there are one or several low-energy electronic resonances in the collisional spectrum. Many open-shell ions are of this type, for example. The two approaches mentioned above are not able to describe satisfactory the DR and excitation processes. On the basis of an earlier theory suggested by Giusti [42,44], Jungen *et al.* have developed an efficient approach that can deal with such a situation. The approach was applied to several diatomic ions for which the dissociative electronic PES of the neutral molecule crosses the ionic PES near the ion equilibrium [6,45–47]. The approach is based on the quantum defect theory (QDT), where, in addition to one or several electronic states of the ion, the dissociative state is explicitly included into the coupling scheme [42,44]. Couplings between different electronic states of the target ion are derived from *ab initio* calculations of electronic (Rydberg) bound states of the neutral molecule. Couplings between the ionic and dissociative states are obtained from the autoionization widths of dissociative states of the neutral molecule (where autoionization is allowed). The widths are typically obtained in electron-scattering calculations.

The above theoretical approach is the only one able to describe non-Born-Oppenheimer effects on electron-ion collisions in the presence of coupled electronic channels of the target. One significant limitation of the approach is the difficulty in obtaining couplings between the electronic states. The procedure of diabatization of coupled Rydberg states obtained in *ab initio* calculations, used in the approach, is laborious, not unique, and sometimes not accurate. It becomes even more ambiguous and very complicated for polyatomic ions, such that an extension of the approach to polyatomic ions becomes impractical.

In this study, we propose another approach, which combines some of the original ideas from the molecular quantum defect theory [40,42,48], more recent DR and VE studies in polyatomic ions [14,21,25,27,43], and recent progress in electron-scattering calculations. The approach can be applied to determine EE, VE, RE, and DR cross sections for a wide range of small polyatomic ions, including the ions with one or several low-energy excited ionic and/or resonant states of the system. In this article, we focus on the VE process and, for the simplicity of discussion, on a particular case of a diatomic ion CH^+. However, the treatment can easily be applied to small polyatomic ions and, with some additions similar to Refs. [42,44], for the DR process.

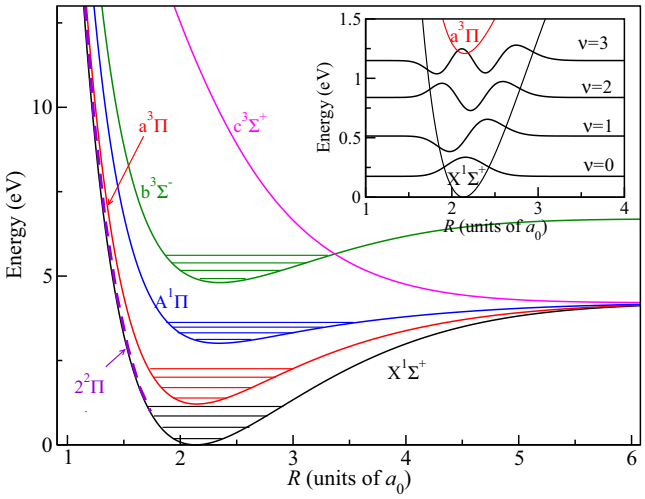

FIG. 1. Potential energy curves for the $X\,^1\Sigma^+$ (black curve), $a\,^3\Pi$ (red curve), $A\,^1\Pi$ (blue curve), $b\,^3\Sigma^-$ (green curve), and $c\,^3\Sigma^+$ (purple curve) electronic states of CH^+. Four lowest vibrational levels for the four lowest electronic states are shown by horizontal thin lines in potential wells of the states. The inset displays the four vibrational states $v = 0$–3 of the $X\,^1\Sigma^+$ state. The CH $2\,^2\Pi$ resonance state is plotted as thin dashed (violet) line. The CH $2\,^2\Pi$ resonance energies are obtained in fixed-nuclei R-matrix calculations at R varying from 1.137 to 1.737 bohrs with an interval of 0.1 bohrs.

II. ELECTRON-CH^+ COLLISIONS

Collisions of the CH^+ ion with electrons have been studied theoretically since, at least, 1951 [38,49–51]. The interest was motivated by the detection of the ion in diffuse interstellar clouds, made initially by Douglas and Herzberg [52] and by Adams [53] in 1941. These and later detections confirmed that CH^+ is ubiquitous as a major constituent of interstellar clouds. The ion is also an important intermediate in combustion and in the formation of large hydrocarbons in the interstellar medium (ISM). Reactive collisions of CH^+ with a low-energy electron determine the energy balance and evolution of low-temperature hydrocarbon plasmas such as in the ISM. The theoretical study of the e^--CH^+ collision system is thus of considerable astrophysical interest. Processes taking place in e^--CH^+ collisions are also of interest for technological plasmas: For example, they play an important role in plasma processing of diamond films [54] and at the edge plasma of fusion reactors [55], where graphite is used as plasma-facing material.

A theoretical description of low-energy e^--CH^+ collisions is complicated due to the presence of a low-energy electronic $2^2\Pi$ resonance and several low-energy excited electronic states of CH^+ [4,51,56] (see Fig. 1). The excited ionic states produce series of Rydberg resonances that influence all collisional processes. In this situation, the standard vibrational-frame-transformation approach by Chang and Fano [57], used in many theoretical studies on electron-molecule collisions [48,58], is not well adapted: The approach requires that

the scattering matrix or, alternatively, the matrix of quantum defects, obtained for fixed internuclear positions (in the Born-Oppenheimer approximation), to be a smooth function of the collision energy—ideally, to be energy independent. However, the presence of the $2\,^2\Pi$ resonance and the low-energy excited electronic states makes the fixed-nuclei scattering matrix to be strongly energy dependent.

The PES of the $2^2\Pi$ resonance crosses the PES of the ground electronic state $X\,^1\Sigma^+$ of the CH^+ ion slightly to the left of the CH^+ equilibrium geometry. As Giusti has pointed out [51], the electronic configuration of the resonance is mainly due to the coupling between the $3\sigma 1\pi(^1\Pi)4\sigma$ and $3\sigma 1\pi(^3\Pi)4\sigma$ orbitals of the $CH^+ + e^-$ system. The resonance at small internuclear distances has a Rydberg character and is produced by the $a\,^3\Pi$ and $A\,^1\Pi$ parent states of the CH^+ ion. These states are the first and second electronically excited states of the ion. Near and to the left of the crossing of the resonance and ionic $X\,^1\Sigma^+$ PES, the character of the resonance is mainly $3\sigma 1\pi(^1\Pi)4\sigma$ (see Fig. 1 of Ref. [51]). Therefore, the resonance could be included in the QDT description of the $CH^+ + e^-$ scattering if the $a\,^3\Pi$ and $A\,^1\Pi$ excited ionic states are accounted for in the complete scattering matrix. Of course, at low scattering energies at fixed geometries to the left of the crossing, these two electronic channels are closed for ionization and should be accounted for using the closed-channel elimination procedure [59], often employed in the QDT studies. Below, we describe in detail the developed theoretical approach.

III. QDT DESCRIPTION OF ELECTRONIC RESONANCES

In applications of the theoretical method presented below, one needs scattering matrices obtained numerically for fixed geometries of the target ion. The scattering matrices could be obtained in different ways. We used the UK R-matrix code [60]. The details of the numerical calculations using the R-matrix code for e^--CH^+ collisions are given in Sec. V.

As mentioned above, the geometry-fixed scattering matrix is strongly energy dependent for e^--CH^+ collisions. This is demonstrated in Fig. 2, showing derivatives of the eigenphase sums for the three symmetries $^2\Sigma^+$, $^2\Pi$, and $^2\Sigma^-$ of the e^--CH^+ system computed at the equilibrium with internuclear distance $R_e = 2.137$ bohrs. Several series of Rydberg resonances converge to the electronic states $a\,^3\Pi$ and $A\,^1\Pi$ as marked by the blue vertical lines in Fig. 2.

To describe low-energy electronic resonances in different e^--CH^+ scattering processes, we use the QDT approach and need an energy-independent scattering matrix, which includes not only the ground electronic state of CH^+ but a few more states that can produce resonances at scattering energies of the interest. In the e^--CH^+ case, low-energy resonances are well reproduced if one takes into account only three electronic states of the ion. Figure 2 shows derivatives of eigenphase sums in two calculations. In one calculation (black solid curves), only the three lowest $X\,^1\Sigma^+$, $a\,^3\Pi$, and $A\,^1\Pi$ states are included. In the second calculation (red dashed lines), 14 lowest states were included. As one can see, at low energies, below the $A\,^1\Pi$ ionization limit, the two calculations agree quite well with each other. In the second calculation with a larger number of ionic states, there are a few narrow

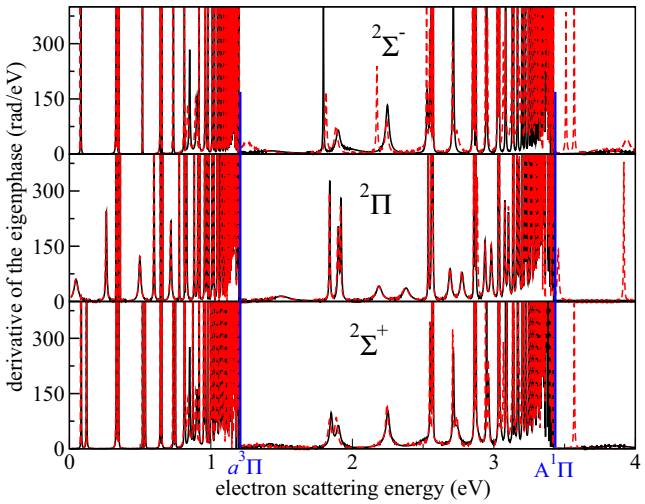

FIG. 2. Derivatives of the eigenphase sum for three symmetries $^2\Sigma^+$, $^2\Pi$, and $^2\Sigma^-$ of e^--CH^+ obtained for the equilibrium internuclear distance $R_e = 2.137$ bohrs in two different calculations: Black solid curves show the results obtained taking into account only three lowest electronic states of CH^+. Red dashed curves are obtained with 14 states. The differences between the curves are subtle and can hardly be seen in the figure.

resonances at low scattering energies that are not reproduced in the first, smaller calculation. These resonances are attached to very excited electronic states of the ion and do not influence significantly the low-energy spectrum.

Therefore, the electronic scattering matrix at low energies could well be represented by the three states $X\,^1\Sigma^+$, $a\,^3\Pi$, and $A\,^1\Pi$ of the ion. With this set of electronic states, the above-mentioned $2^2\Pi$ resonance is included in the scattering model.

In order to account for vibrational and rotational excitation of the target, the standard QDT approach is to use vibrational and rotational frame transformations [40,57]. The approach is applicable only if the electronic scattering matrix, obtained for a number of different geometries of the ion, is energy independent. As Fig. 2 shows, the e^--CH^+ scattering matrix depends strongly on energy below the $A\,^1\Pi$ ionization limit and cannot be immediately used in the frame transformation. A possible solution is to take the (almost) energy-independent scattering matrix, obtained at an energy above the $A\,^1\Pi$ ionization limit, and use it at energies below the limit. Therefore, the vibrational (and rotational) frame transformation is performed on a 3×3 electronic scattering matrix, which produces a $N \times N$ matrix with N vibronic (rovibronic) channels. Such a rovibronic scattering matrix is essentially energy independent and a QDT closed-channel elimination procedure [59,61] should be performed to obtain the physical energy-dependent matrix, which can be used to compute cross sections for various processes.

Before discussing the vibronic frame transformation applied to the e^--CH^+ collisions, we compare the fixed-nuclei electronic scattering matrices obtained (1) using the elimination procedure of the closed electronic states and by (2) a direct scattering R-matrix calculation at the same internuclear distance.

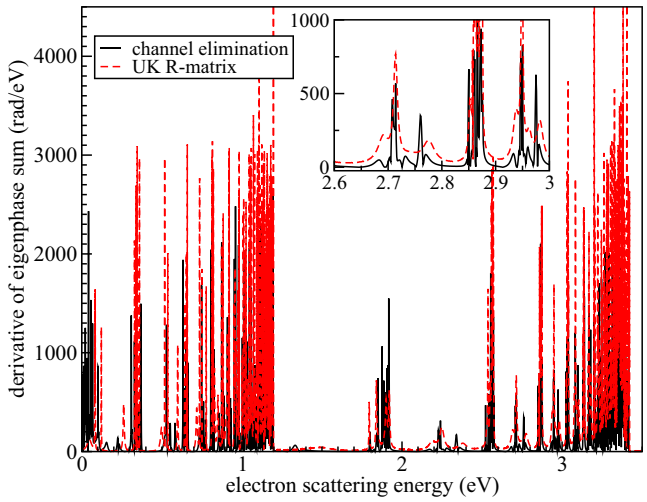

FIG. 3. Comparison of eigenphase-sum derivatives below the $A\,^1\Pi$ state obtained at a fixed CH^+ geometry in (1) the direct R-matrix calculations (red dashed curve) and using (2) the energy-independent 3×3 scattering matrix and the procedure of elimination of closed electronic channels (black solid curve). The inset shows an enlarged view for the 2.6- to 3.0-eV interval of energies.

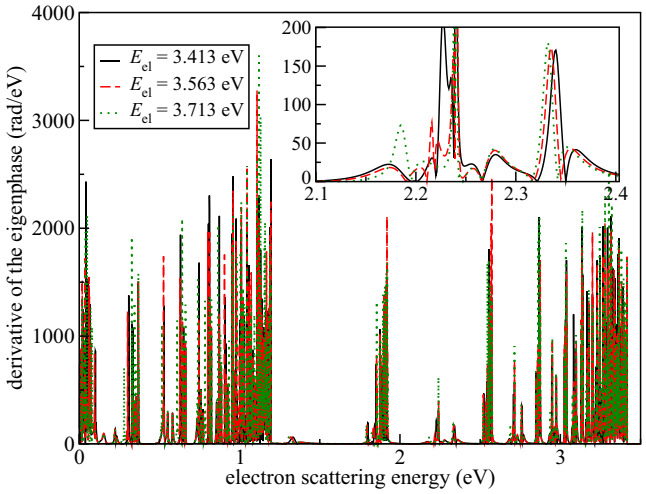

FIG. 4. Comparison of eigenphase-sum derivatives computed for a fixed CH^+ geometry using three different energy-independent 3×3 scattering matrices and the procedure of elimination of closed electronic channels. The three matrices are taken at energies 3.413 eV (black solid curve), 3.563 eV (red dashed curve), and 3.713 eV (green dotted curve). The inset shows an enlarged view for 2.1- to 2.4-eV energies.

The elimination of closed electronic channels at a geometry R is given by [59,61]

$$S^{\rm phys}(E_{\rm el}) = S^{oo} - S^{oc}[S^{cc} - e^{-2i\beta(E_{\rm el})}]^{-1}S^{co}\,, \qquad (1)$$

where $E_{\rm el}$ is the scattering energy and S^{oo}, S^{oc}, S^{cc}, and S^{co} are submatrices of the weakly dependent electronic scattering matrix (3×3 in the present case of the e^--CH^+ system),

$$S(E_{\rm el}) = \begin{pmatrix} S^{oo} & S^{oc} \\ S^{co} & S^{cc} \end{pmatrix}. \qquad (2)$$

Partition of matrix elements in the o and c parts is made on the basis of whether the corresponding channels are open or closed for excitation for the particular scattering energy $E_{\rm el}$. The quantity of $\beta(E_{\rm el})$ in Eq. (1) is a diagonal $N_c \times N_c$ matrix

$$\beta(E_{\rm el}, R) = \frac{\pi}{\sqrt{2[E_i(R) - E_{\rm el}]}}\delta_{i',i}, \qquad (3)$$

where $E_i(R)$ denotes the energy values of the ith electronic states at internuclear distance R.

Figure 3 shows derivatives of eigenphase sums obtained from the scattering matrices computed at the equilibrium distance R_e. The red dashed curve is the result from the R-matrix calculation; the black solid curve is the calculation using the energy-independent 3×3 electronic scattering matrix and the closed-channel elimination procedure. Overall, positions of the resonances in the two calculations are the same but widths in the R-matrix calculation are wider. This means that diagonal elements of the scattering matrices in the two calculations are very similar but the nondiagonal elements, responsible for channel couplings and widths of the resonances, are slightly different, suggesting that highly excited electronic states, neglected in the 3×3 channel elimination procedure, have non-negligible contributions to the coupling between the lowest channels.

The choice of the 3×3 scattering matrix used in the channel-elimination procedure is not unique, because the matrix depends on energy, even above the $A\,^1\Pi$ electronic state. To assess the result of uncertainty in the choice of the energy at which the 3×3 scattering matrix is taken, we plot in Fig. 4 eigenphase-sum derivatives obtained for 3×3 scattering matrices taken at three different energies above the $A\,^1\Pi$ state: at 3.413, 3.563, and 3.713 eV. Positions and the

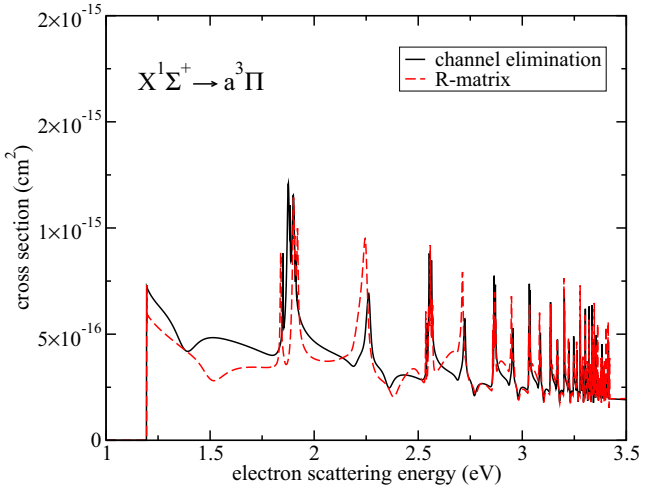

FIG. 5. Cross sections for the $X\,^1\Sigma^+ \rightarrow a\,^3\Pi$ electronic excitation of CH^+ at fixed geometry R_e obtained in the direct R-matrix calculations (red dashed curve) and using the QDT channel elimination procedure (black solid curve).

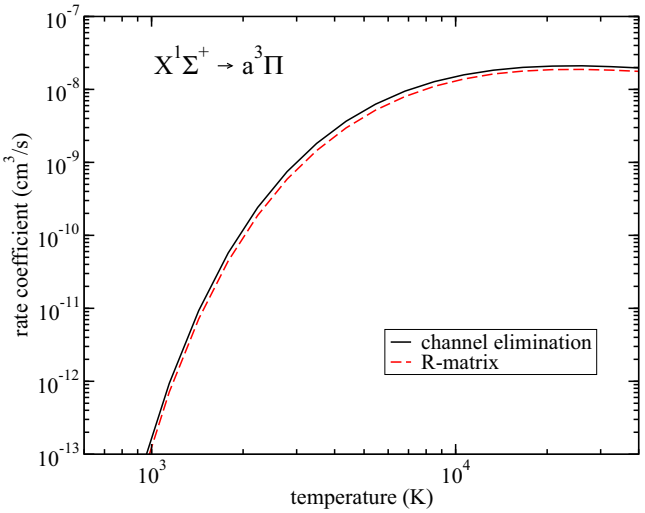

FIG. 6. The rate coefficients for the $X\,^1\Sigma^+ \rightarrow a\,^3\Pi$ electronic excitation of CH^+ at R_e obtained in the direct R-matrix calculations (red dashed curve) and the QDT channel elimination procedure (black solid curve).

widths of the resonances are nearly the same in the three calculations.

An important conclusion from the results discussed above is that the e^--CH^+ scattering physics below the $A\,^1\Pi$ state can be represented using an energy-independent multichannel scattering matrix evaluated at a higher energy, above the $A\,^1\Pi$ ionization limit in a combination with the closed-channel elimination.

A rough idea about the magnitude of cross sections for electron-impact electronic excitation of a molecule is obtained from a fixed-geometry calculation. Here, for a comparison between the QDT and direct R-matrix approaches, we present such excitation cross sections. The vibrational dynamics during the process is discussed in the next section.

Using the physical scattering matrix $S^{\rm phys}(E_{\rm el}, R_e)$ of Eq. (1) describing electronic transitions at the equilibrium geometry R_e of CH^+, the fixed-nuclei cross section of the electronic excitations from the $X\,^1\Sigma^+$ state to the $a\,^3\Pi$ state is computed in the QDT approach as [14]

$$\sigma_{i',i}(E_{\rm el}, R_e) = \frac{\pi\hbar^2}{2m_e E_{\rm el}} \times \sum_{l'm',lm} \left| S^{\rm phys}_{l'm'i',lmi}(E_{\rm el}, R_e) - \delta_{l'm'i',lmi} \right|^2, \quad (4)$$

where m_e is the reduced mass of electron and i and i' refer to the initial ($X\,^1\Sigma^+$ in this case) and final ($a\,^3\Pi$ here) electronic states. Indexes lm and $l'm'$ numerate initial and final angular momenta and their projections in the molecular reference frame (where *ab initio* calculations are performed). The cross section in the R-matrix approach is obtained by the same formula, except that the scattering matrix in the above equation is replaced with the one obtained directly in the R-matrix calculations at the corresponding energy $E_{\rm el}$.

Figure 5 compares the cross sections for the $X\,^1\Sigma^+ \rightarrow a\,^3\Pi$ transition obtained in the two approaches. The general agreement between the two curves is good, even for the widths of the resonances. One noticeable difference is in the position of the minimum near 1.5 eV: In the QDT calculations, it is shifted slightly to the left. The agreement is better at energies approaching the $a\,^3\Pi$ ionization limit.

Differences observed in the cross sections obtained by the two methods are smeared out in the thermally averaged rate coefficient

$$k_{i',i}(T, R_e) = \frac{8\pi}{(2\pi k_b T)^{3/2}} \int_0^\infty \sigma_{i',i}(E_{\rm el}, R_e) e^{\frac{-E_{\rm el}}{k_b T}} E_{\rm el} dE_{\rm el}, \quad (5)$$

computed from the cross sections. In the above equation, k_b is the Boltzmann coefficient and T is the temperature. The obtained rate coefficients, shown in Fig. 6, are in very good agreement with each other. This confirms that major couplings between electronic channels are accurately represented in the QDT approach and validates the approach.

IV. VIBRONIC EXCITATION

The energy-dependent physical scattering matrix for vibronic transitions is obtained in two steps. First, one computes the energy-independent vibronic scattering matrix assuming that all vibronic channels are open. In the second step, an

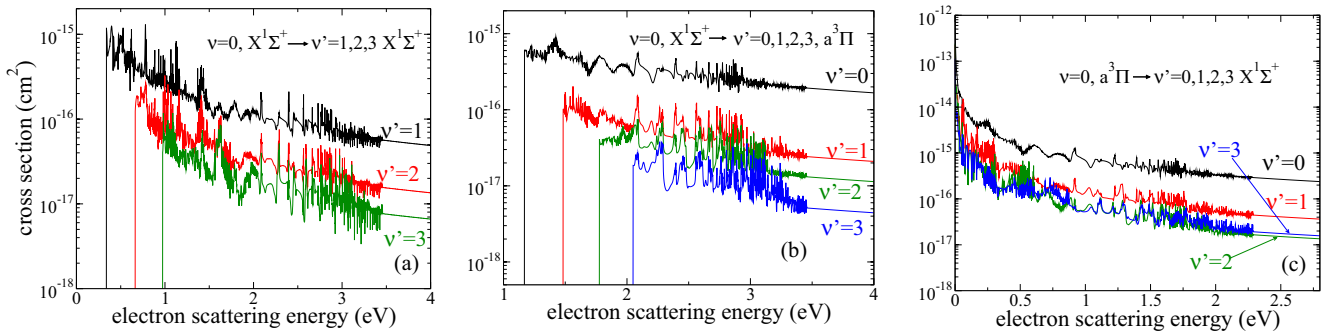

FIG. 7. Cross sections for vibronic excitations of CH^+ from the ground vibrational level $v = 0$ of the $X\,^1\Sigma^+$ state to $v = 1, 2, 3$ of the $X\,^1\Sigma^+$ state (left panel), to $v = 0, 1, 2, 3$ of the $a\,^3\Pi$ state (middle panel), and for vibronic de-excitations from the ground vibrational level $v = 0$ of $a\,^3\Pi$ to $v = 0, 1, 2, 3$ of the $X\,^1\Sigma^+$ state (right panel).

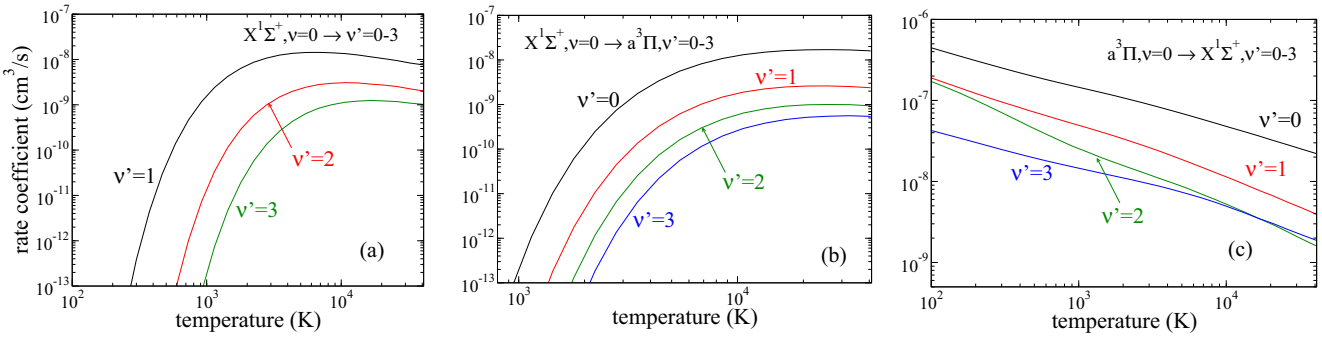

FIG. 8. Rate coefficients for same vibronic transitions as shown in Fig. 7.

elimination of closed vibronic channels is applied, producing the required energy-dependent vibronic scattering matrix.

The first step is performed by the vibronic frame transformation

$$S_{l'm'v'i',lmvi}(E_{\rm el}) = \langle \varphi_{v'i'}(R)|S_{l'm'i',lmi}(E_{\rm el},R)|\varphi_{vi}(R)\rangle, \quad (6)$$

where $\varphi_{vi}(R)$ and $\varphi_{v'i'}(R)$ are wave functions of the initial and final vibrational states. Index v or v' corresponds to the number of vibrational quanta in initial i or final i' electronic states. The brackets imply an integration over the vibrational coordinate R.

In the second step, the energy-dependent physical scattering matrix $S^{\rm phys}(E_{\rm el})$ is obtained by the QDT vibronic closed-channel elimination procedure, described by the same Eqs. (1) and (3), except that the energies $E_i(R)$ of closed channels are replaced with energies of vibronic channels E_{vi}, i.e.,

$$\beta(E_{\rm el}) = \frac{\pi}{\sqrt{2(E_{vi}-E_{\rm el})}}\delta_{v'i',vi}\,. \quad (7)$$

The cross sections $\sigma_{v'i',vi}(E_{\rm el})$ for vibronic excitation or de-excitation of CH^+ are computed using Eq. (4), where $S^{\rm phys}_{l'm'i',lmi}(E_{\rm el},R_{\rm e})$ is replaced with $S^{\rm phys}_{l'm'v'i',lmvi}(E_{\rm el})$.

Figure 7 illustrates cross sections obtained for different combinations of initial and final vibronic states. Figure 7(a) shows results for pure vibrational excitations between levels of the ground electronic state $X\,^1\Sigma^+$. As expected, the cross section for the transition with $\Delta v = 1$ is the largest one between inelastic processes. Figure 7(b) gives cross sections from the ground vibronic state $X\,^1\Sigma^+$, $v = 0$ to several vibrational levels of the $a\,^3\Pi$ state. Since the potential curves of the $X\,^1\Sigma^+$ and $a\,^3\Pi$ states have similar shapes near the equilibrium, the largest $X\,^1\Sigma^+ \to a\,^3\Pi$ cross section is expected to be for $\Delta v = 0$, as the present calculation indeed demonstrated. Figure 7(c) gives cross sections for the de-excitation process $a\,^3\Pi$, $v = 0 \to X\,^1\Sigma^+$, $v' = 0-3$.

Cross sections for vibronic excitations were recently estimated by Chakrabarti *et al.* [5] using a rough theoretical approach, in which cross sections for electronic excitations computed at the CH^+ equilibrium geometry were multiplied with Franck-Condon overlaps for various combinations of initial and final vibrational levels to obtain the cross sections for vibronic transitions. In that study, vibronic Feshbach resonances as well as differences in vibrational excitation energies were neglected. The cross sections obtained in Ref. [5] differ significantly—more than an order of magnitude for several transitions—from the present results. We attribute the disagreement to the mentioned approximations employed in Ref. [5]: (1) neglected differences in vibrational excitation threshold energies, (2) neglected dependence of e^--CH^+ scattering parameters with the internuclear distance, and (3) the neglected resonances in closed vibronic channels.

Thermally averaged rate coefficients $k_{v'i',vi}(T)$ for these vibronic (de-)excitations from 10 to 10 000 K are then computed using Eq. (5), where $\sigma_{i',i}(E_{\rm el},R_{\rm e})$ is substituted with $\sigma_{v'i',vi}(E_{\rm el})$. Figure 8 shows computed rate coefficients for the same transitions as the cross sections in Fig. 7.

As in previous studies [62–65] and for convenience of use, the computed thermally averaged rate coefficients $k_{v'i'\leftarrow vi}$ were fitted using the following analytical formula,

$$k^{\rm fit}_{v'i'\leftarrow vi}(T) = \frac{1}{\sqrt{T}}e^{-\frac{\Delta_{v'i',vi}}{T}}P^{\rm fit}_{v'i',vi}(x), \quad (8)$$

where $P^{\rm fit}_{v'i',vi}(x)$ is a quadratic polynomial

$$P^{\rm fit}_{v'i',vi}(x) = a_0 + a_1x + a_2x^2 \quad \text{and} \quad x = \ln(T) \quad (9)$$

with $P^{\rm fit}_{v'i',vi}(x) \approx P^{\rm fit}_{vi,v'i'}(x)$. This quantity could be viewed as the (de-)excitation probability. $\Delta_{v'i',vi}$ in Eq. (8) is the threshold energy defined as

$$\Delta_{v'i',vi} = \begin{cases} E_{v'i'} - E_{vi} > 0 & \text{for excitation,} \\ 0 & \text{for de-excitation.} \end{cases} \quad (10)$$

Numerically fitted parameters for vibronic transitions are given in Tables I–VI. When the parameters given in the tables are used in the fitting formulas of Eqs. (8) and (9) with T in K, obtained numerical values of rate coefficients will be in units

TABLE I. Parameters a_0, a_1, and a_2 of the polynomial $P^{\rm fit}_{vi,v'i'}(x)$ of Eqs. (8) and (9) for several pairs of initial and final vibrational levels of the ground electronic state $X\,^1\Sigma^+$ of CH^+. We specify the threshold energy $\Delta_{v'i',vi}$ for the excitation process in the pair $v'i'$, vi in the second column of each table. For the de-excitation process, $\Delta_{vi,v'i'} = 0$.

$v'i' \leftrightarrow vi$	$\Delta_{v'i',vi}$ (K)	a_0	a_1	a_2
$10 \leftrightarrow 00$	3 934	2.90×10^{-6}	-1.20×10^{-7}	2.30×10^{-9}
$20 \leftrightarrow 00$	7 700	1.10×10^{-6}	1.60×10^{-8}	-6.60×10^{-9}
$30 \leftrightarrow 00$	11 299	2.90×10^{-7}	5.00×10^{-8}	-5.10×10^{-9}
$20 \leftrightarrow 10$	3 766	7.85×10^{-7}	2.17×10^{-7}	-1.22×10^{-8}
$30 \leftrightarrow 10$	7 365	4.57×10^{-7}	1.02×10^{-7}	-8.64×10^{-9}
$30 \leftrightarrow 20$	3 599	2.39×10^{-6}	2.51×10^{-8}	-5.26×10^{-9}

TABLE II. Same as Table I for the electronic state $a\,^3\Pi$.

$v'i' \leftrightarrow vi$	$\Delta_{v'i',vi}$ (K)	a_0	a_1	a_2
$11 \leftrightarrow 01$	3 633	5.43×10^{-6}	4.68×10^{-7}	-4.41×10^{-8}
$21 \leftrightarrow 01$	7 039	2.01×10^{-6}	5.14×10^{-9}	-3.18×10^{-9}
$31 \leftrightarrow 01$	10 216	1.17×10^{-6}	-3.37×10^{-8}	-2.65×10^{-9}
$21 \leftrightarrow 11$	3 405	7.53×10^{-6}	6.95×10^{-8}	-2.30×10^{-8}
$31 \leftrightarrow 11$	6 583	2.99×10^{-6}	3.58×10^{-8}	-2.48×10^{-9}
$31 \leftrightarrow 21$	3 178	6.55×10^{-6}	2.04×10^{-7}	-8.40×10^{-9}

of cm^3/s. In the tables, the electronic states are numerated with index i (or i') with $i = 0$ corresponding to $X\,^1\Sigma^+$, $i = 1$ to $a\,^3\Pi$, and $i = 2$ to $A\,^1\Pi$.

V. CALCULATIONS OF ELECTRONIC STRUCTURE, SCATTERING, AND VIBRATIONAL DYNAMICS OF THE PROCESS

In this section, we provide details about numerical calculations of the vibrational wave functions of the ion and *ab initio* calculations performed for the bound electronic states of the ion and the e^--CH^+ scattering.

The configuration of the ground electronic state $X\,^1\Sigma^+$ of CH^+ is $1\sigma^2 2\sigma^2 3\sigma^2$ in the $C_{\infty v}$ symmetry group of the ion. The potential energy curves $V(R)$ of CH^+ were calculated using the C_{2v} symmetry group with a multireference configuration interaction (MRCI) method and the `cc-pV5Z` basis set using the MOLPRO code [66]. We kept the 1σ orbital of carbon doubly occupied and used 14 orbitals, i.e., 2σ-7σ, 1π-3π, and 1δ as the complete active space (CAS). The calculated potential energy curves of the $X\,^1\Sigma^+$, $a\,^3\Pi$, $A\,^1\Pi$, $b\,^3\Sigma^-$, and $c\,^3\Sigma^+$ electronic states are shown in Fig. 1. The $X\,^1\Sigma^+$, $a\,^3\Pi$, $A\,^1\Pi$, and $c\,^3\Sigma^+$ curves correlate with the $C^+(^2P) + H(^2S)$ dissociation limit at large internuclear distances.

In order to determine the vibrational energies E_v and the corresponding vibrational wave functions $\varphi_v(R)$ within these electronic states of CH^+, we solved the Schrödinger equation for vibrational motion along R

$$\left[-\frac{\hbar^2}{2\mu}\frac{d^2}{dR^2} + V(R)\right]\varphi_v(R) = E_v\varphi_v(R), \tag{11}$$

using a discrete variable representation (DVR) method [67]. In the above equation, μ denotes the reduced mass of CH^+. The lowest four vibrational energy levels $v = 0, 1, 2, 3$ of the $X\,^1\Sigma^+$ state are listed in Table VII. As one can see, the present computed energies agree well with the theoretical calculations by Biglari *et al.* [68].

TABLE III. Same as Table I for the electronic state $A\,^1\Pi$.

$v'i' \leftrightarrow vi$	$\Delta_{v'i',vi}$ (K)	a_0	a_1	a_2
$12 \leftrightarrow 02$	2 290	5.44×10^{-6}	1.74×10^{-7}	-1.09×10^{-8}
$22 \leftrightarrow 02$	4 271	2.16×10^{-6}	-1.24×10^{-8}	-6.08×10^{-10}
$32 \leftrightarrow 02$	5 971	1.49×10^{-6}	-8.82×10^{-9}	5.33×10^{-10}
$22 \leftrightarrow 12$	1 981	1.33×10^{-5}	-1.13×10^{-7}	-3.47×10^{-10}
$32 \leftrightarrow 12$	3 680	7.74×10^{-6}	8.39×10^{-9}	-8.35×10^{-10}
$32 \leftrightarrow 22$	1 699	3.48×10^{-6}	-1.17×10^{-8}	6.50×10^{-10}

TABLE IV. Same as Table I for vibronic transitions $vX\,^1\Sigma^+ \leftrightarrow v'a\,^3\Pi$.

$v'i' \leftrightarrow vi$	$\Delta_{v'i',vi}$ (K)	a_0	a_1	a_2
$01 \leftrightarrow 00$	13 572	5.10×10^{-6}	-1.20×10^{-8}	2.30×10^{-9}
$11 \leftrightarrow 00$	17 205	3.50×10^{-7}	2.70×10^{-7}	-2.20×10^{-8}
$21 \leftrightarrow 00$	20 610	5.00×10^{-7}	3.80×10^{-9}	-3.80×10^{-10}
$31 \leftrightarrow 00$	23 788	2.00×10^{-7}	5.70×10^{-8}	-5.70×10^{-9}
$01 \leftrightarrow 10$	9 638	4.90×10^{-7}	2.57×10^{-7}	-1.84×10^{-8}
$11 \leftrightarrow 10$	13 271	4.30×10^{-6}	5.30×10^{-8}	-2.80×10^{-9}
$21 \leftrightarrow 10$	16 677	7.13×10^{-7}	1.72×10^{-8}	-6.09×10^{-10}
$31 \leftrightarrow 10$	19 854	6.00×10^{-7}	1.98×10^{-8}	-5.12×10^{-10}
$01 \leftrightarrow 20$	5 872	7.06×10^{-7}	1.55×10^{-7}	-1.78×10^{-8}
$11 \leftrightarrow 20$	9 505	1.93×10^{-6}	-3.01×10^{-8}	-5.86×10^{-9}
$21 \leftrightarrow 20$	12 910	3.97×10^{-6}	-7.95×10^{-8}	6.09×10^{-9}
$31 \leftrightarrow 20$	16 088	9.13×10^{-7}	2.49×10^{-8}	-2.09×10^{-9}
$01 \leftrightarrow 30$	2 273	3.24×10^{-7}	4.24×10^{-8}	-2.23×10^{-9}
$11 \leftrightarrow 30$	5 906	8.23×10^{-7}	1.61×10^{-8}	-3.03×10^{-9}
$21 \leftrightarrow 30$	9 311	1.77×10^{-6}	-1.22×10^{-8}	-4.08×10^{-9}
$31 \leftrightarrow 30$	12 489	3.31×10^{-6}	-4.24×10^{-8}	3.17×10^{-10}

The e^--CH^+ scattering calculations were carried out using the UK R-matrix code [60,69] with the help of the Quantemol-N interface [70]. The `cc-pVQZ` basis set and CAS configuration interaction (CI) method in the C_{2v} Abelian subgroup were used in the calculations. The inner orbital $1a_1{}^2$ of CH^+ was frozen, and four external electrons were distributed in the space of the $[2a_1, 3a_1, 4a_1, 5a_1, 6a_1, 7a_1, 8a_1, 1b_1, 2b_1, 3b_1, 1b_2, 2b_2, 3b_2, 1a_2]$ orbitals ($2\sigma, 3\sigma, 4\sigma, 5\sigma, 6\sigma, 7\sigma, 1\pi, 2\pi, 3\pi, 1\delta$ in $C_{\infty v}$ symmetry group). We chose an R-matrix sphere of radius 13 bohrs and continuum Gaussian-type orbitals with partial waves $l \leqslant 4$. The two different R-matrix calculations described in Sec. III closed-coupling expansions with 3 and 14 lowest electronic states of CH^+ were used for constructing the total wave functions for the e^--CH^+ system. In the

TABLE V. Same as Table I for vibronic transitions $vX\,^1\Sigma^+ \leftrightarrow v'A\,^1\Pi$.

$v'i' \leftrightarrow vi$	$\Delta_{v'i',vi}$(K)	a_0	a_1	a_2
$02 \leftrightarrow 00$	34 147	3.30×10^{-6}	-2.10×10^{-7}	9.90×10^{-9}
$12 \leftrightarrow 00$	36 437	1.70×10^{-6}	-7.70×10^{-8}	2.90×10^{-9}
$22 \leftrightarrow 00$	38 418	6.70×10^{-7}	-1.20×10^{-8}	4.70×10^{-10}
$32 \leftrightarrow 00$	40 117	3.40×10^{-7}	-2.70×10^{-9}	1.50×10^{-10}
$02 \leftrightarrow 10$	30 213	1.21×10^{-6}	4.41×10^{-8}	-3.94×10^{-9}
$12 \leftrightarrow 10$	32 503	8.20×10^{-7}	-2.90×10^{-8}	-9.71×10^{-10}
$22 \leftrightarrow 10$	34 484	1.01×10^{-6}	2.69×10^{-9}	-3.61×10^{-10}
$32 \leftrightarrow 10$	36 183	7.74×10^{-7}	1.83×10^{-8}	-9.69×10^{-10}
$02 \leftrightarrow 20$	26 446	4.39×10^{-7}	2.69×10^{-8}	-1.11×10^{-9}
$12 \leftrightarrow 20$	28 737	1.17×10^{-6}	-2.14×10^{-8}	7.31×10^{-10}
$22 \leftrightarrow 20$	30 718	2.36×10^{-7}	8.67×10^{-10}	-5.88×10^{-11}
$32 \leftrightarrow 20$	32 417	3.82×10^{-7}	-5.63×10^{-9}	3.06×10^{-10}
$02 \leftrightarrow 30$	22 847	4.27×10^{-7}	-1.51×10^{-8}	-5.84×10^{-11}
$12 \leftrightarrow 30$	25 138	1.46×10^{-6}	2.16×10^{-8}	-2.89×10^{-9}
$22 \leftrightarrow 30$	27 119	7.21×10^{-7}	1.48×10^{-9}	-3.23×10^{-10}
$32 \leftrightarrow 30$	28 818	1.19×10^{-6}	-1.90×10^{-8}	1.04×10^{-9}

TABLE VI. Same as Table I for vibronic transitions $va\,^3\Pi \leftrightarrow v'A\,^1\Pi$.

$v'i' \leftrightarrow vi$	$\Delta_{v'i',vi}$ (K)	a_0	a_1	a_2
02 ↔ 01	20 575	3.28×10^{-6}	4.81×10^{-8}	-7.56×10^{-9}
12 ↔ 01	22 865	7.02×10^{-7}	2.32×10^{-9}	-1.11×10^{-9}
22 ↔ 01	24 846	5.83×10^{-7}	-4.73×10^{-9}	-2.56×10^{-11}
32 ↔ 01	26 545	4.43×10^{-7}	2.81×10^{-9}	-1.53×10^{-10}
02 ↔ 11	16 941	5.03×10^{-6}	2.61×10^{-7}	-1.85×10^{-8}
12 ↔ 11	19 232	1.08×10^{-6}	1.17×10^{-8}	-3.14×10^{-9}
22 ↔ 11	21 213	1.52×10^{-6}	-4.00×10^{-9}	-3.32×10^{-10}
32 ↔ 11	22 912	6.47×10^{-7}	-3.27×10^{-9}	1.69×10^{-10}
02 ↔ 21	13 536	1.39×10^{-6}	1.24×10^{-7}	-6.56×10^{-9}
12 ↔ 21	15 826	3.69×10^{-6}	-1.94×10^{-8}	9.08×10^{-10}
22 ↔ 21	17 807	7.26×10^{-7}	-2.50×10^{-8}	1.19×10^{-9}
32 ↔ 21	19 507	5.32×10^{-7}	6.38×10^{-9}	-3.78×10^{-10}
02 ↔ 31	10 358	1.30×10^{-6}	-9.89×10^{-8}	2.13×10^{-9}
12 ↔ 31	12 649	2.41×10^{-6}	7.13×10^{-8}	-5.00×10^{-9}
22 ↔ 31	14 630	1.54×10^{-6}	9.42×10^{-9}	-6.05×10^{-10}
32 ↔ 31	16 329	1.08×10^{-6}	-1.35×10^{-9}	4.25×10^{-11}

vibrational frame transformation of Eq. (6), the electron scattering calculations were performed in the interval between 1.537 and 3.937 bohrs with a step of 0.1 bohrs along the internuclear coordinate R.

VI. CONCLUSIONS

In conclusion, cross sections and rate coefficients for vibronic excitation and de-excitation of CH^+ by electron impact were computed in a framework using first principles only. The theoretical approach combines fixed-nuclei scattering matrices obtained for a number of internuclear distances using the UK R-matrix code, the vibronic frame transformation, and the QDT closed-channel elimination procedure. The approach is validated in model calculations for electronic excitation, performed for a single fixed internuclear distance of the target, comparing the results from a direct R-matrix calculation and the QDT channel elimination procedure. The main advantage of this method compared with the previous state of theory is that it can be applied to collisions of electrons with molecular ions with low-lying excited electronic states, including open-shell ions. The approach is quite general and can be applied for a number of different processes, taking place in collisions of molecular ions with electrons, including rovibronic excitation, dissociative excitation (DE), photoionization, and dissociative recombination (DR).

TABLE VII. Comparison of the four lowest vibrational energy levels (in eV) of the $X\,^1\Sigma^+$ state obtained in this study with the calculations by Biglari *et al.* [68].

Ref.	$v = 0$	$v = 1$	$v = 2$	$v = 3$
Biglari *et al.* [68]	0.175218	0.514360	0.838974	1.149288
This work	0.175189	0.514102	0.838515	1.148720
Relative error	0.017%	0.050%	0.055%	0.054%

In this study, we took into account only the electronic and vibrational structure of the target ion. The rotational structure of each vibrational level was neglected. The description of the rotational structure and couplings could be included into the treatment in the same way as was made in many previous treatments (see, for example, Ref. [65] and references therein). Therefore, the obtained cross sections and rate coefficients should be viewed as averaged over initial rotational states and summed over final rotational states of the corresponding vibrational levels. The inclusion of the rotational structure and couplings is important if one needs rotationally resolved cross sections or thermally averaged rate coefficients at temperatures T comparable or smaller than the CH^+ rotational constant, i.e., at $T \lesssim 20$ K. An extension of this method to include nuclear rotation will be discussed in a later publication.

ACKNOWLEDGMENTS

This work acknowledges support from the National Science Foundation, Grant No. PHY-1806915, China Scholarship Council, and the Thomas Jefferson Fund of the Office for Science and Technology of the Embassy of France in the United States. It has also received funding from the program "Accueil des chercheurs étrangers" of CentraleSupélec and "Séjour à l'étranger 2019" of École doctorale INTERFACES of Université Paris-Saclay.

[1] H. Takagi, Fusion Sci. Technol. **63**, 406 (2013).
[2] V. Laporta, K. Chakrabarti, R. Celiberto, R. Janev, J. Z. Mezei, S. Niyonzima, J. Tennyson, and I. Schneider, Plasma Phys. Controlled Fusion **59**, 045008 (2017).
[3] N. Pop, Z. Mezei, O. Motapon, S. Niyonzima, K. Chakrabarti, F. Colboc, R. Boată, M. D. E. Epée, and I. F. Schneider, AIP Conf. Proc. **1796**, 020014 (2017).
[4] L. Carata, A. E. Orel, M. Raoult, I. F. Schneider, and A. Suzor-Weiner, Phys. Rev. A **62**, 052711 (2000).
[5] K. Chakrabarti, A. Dora, R. Ghosh, B. Choudhury, and J. Tennyson, J. Phys. B: At., Mol. Opt. Phys. **50**, 175202 (2017).
[6] K. Chakrabarti, J. Z. Mezei, O. Motapon, A. Faure, O. Dulieu, K. Hassouni, and I. F. Schneider, J. Phys. B: At., Mol. Opt. Phys. **51**, 104002 (2018).
[7] Z. J. Mezei, M. D. Epée Epée, O. Motapon, and I. F. Schneider, Atoms **7**, 82 (2019).
[8] D. Kashinski, D. Talbi, A. Hickman, O. Di Nallo, F. Colboc, K. Chakrabarti, I. Schneider, and J. Z. Mezei, J. Chem. Phys. **146**, 204109 (2017).
[9] S. L. Guberman, J. Phys. Chem. A **111**, 11254 (2007).
[10] D. A. Little, K. Chakrabarti, J. Z. Mezei, I. F. Schneider, and J. Tennyson, Phys. Rev. A **90**, 052705 (2014).
[11] M. Fifirig, Mol. Phys. **112**, 1910 (2014).
[12] S. L. Guberman, Science **278**, 1276 (1997).
[13] V. Kokoouline, C. H. Greene, and B. D. Esry, Nature (London) **412**, 891 (2001).
[14] V. Kokoouline and C. H. Greene, Phys. Rev. Lett. **90**, 133201 (2003).

[15] S. Fonseca dos Santos, V. Kokoouline, and C. H. Greene, J. Chem. Phys. **127**, 124309 (2007).
[16] L. Pagani, C. Vastel, E. Hugo, V. Kokoouline, C. H. Greene, A. Bacmann, E. Bayet, C. Ceccarelli, R. Peng, and S. Schlemmer, Astron. Astrophys. **494**, 623 (2009).
[17] C. Jungen and S. T. Pratt, Phys. Rev. Lett. **102**, 023201 (2009).
[18] N. Douguet, A. E. Orel, C. H. Greene, and V. Kokoouline, Phys. Rev. Lett. **108**, 023202 (2012).
[19] N. Douguet, A. Orel, I. Mikhailov, I. F. Schneider, C. H. Greene, and V. Kokoouline, J. Phys. Conf. Ser. **300**, 012015 (2011).
[20] N. Douguet, V. Kokoouline, and A. E. Orel, J. Phys. B: At. Mol. Opt. Phys. **45**, 051001 (2012).
[21] I. A. Mikhaylov, V. Kokoouline, A. Larson, S. Tonzani, and C. H. Greene, Phys. Rev. A **74**, 032707 (2006).
[22] N. Douguet, V. Kokoouline, and C. H. Greene, Phys. Rev. A **77**, 064703 (2008).
[23] C. Jungen and S. T. Pratt, J. Chem. Phys. **129**, 164311 (2008).
[24] N. Douguet, V. Kokoouline, and C. H. Greene, Phys. Rev. A **80**, 062712 (2009).
[25] C. Jungen and S. T. Pratt, J. Chem. Phys. **133**, 214303 (2010).
[26] V. Kokoouline, N. Douguet, and C. H. Greene, Chem. Phys. Lett. **507**, 1 (2011).
[27] S. Fonseca dos Santos, N. Douguet, V. Kokoouline, and A. E. Orel, J. Chem. Phys. **140**, 164308 (2014).
[28] V. Kokoouline, M. Ayouz, J. Z. Mezei, K. Hassouni, and I. F. Schneider, Plasma Sources Sci. Technol. **27**, 115007 (2018).
[29] A. Hickman, R. Miles, C. Hayden, and D. Talbi, Astron. Astrophys. **438**, 31 (2005).
[30] V. Ngassam, A. E. Orel, and A. Suzor-Weiner, J. Phys. Conf. Ser. **4**, 224 (2005).
[31] V. Ngassam and A. E. Orel, Phys. Rev. A **75**, 062702 (2007).
[32] N. Douguet, S. F. dos Santos, V. Kokoouline, and A. Orel, EPJ Web Conf. **84**, 07003 (2015).
[33] C. Yuen, M. Ayouz, N. Balucani, C. Ceccarelli, I. Schneider, and V. Kokoouline, Mon. Not. R. Astron. Soc. **484**, 659 (2019).
[34] M. Ayouz, C. Yuen, N. Balucani, C. Ceccarelli, I. Schneider, and V. Kokoouline, Mon. Not. R. Astron. Soc. **490**, 1325 (2019).
[35] T. F. O'Malley, Phys. Rev. **150**, 14 (1966).
[36] J. N. Bardsley, J. Phys. B: At. Mol. Phys. **1**, 365 (1968).
[37] J. Bardsley, J. Phys. B: At. Mol. Phys. **1**, 349 (1968).
[38] J. Bardsley and B. Junker, Astrophys. J. **183**, L135 (1973).
[39] C. M. Lee, Phys. Rev. A **16**, 109 (1977).
[40] C. Jungen and O. Atabek, J. Chem. Phys. **66**, 5584 (1977).
[41] Ch. Jungen and D. Dill, J. Chem. Phys. **73**, 3338 (1980).
[42] A. Giusti-Suzor, J. N. Bardsley, and C. Derkits, Phys. Rev. A **28**, 682 (1983).
[43] V. Kokoouline and C. H. Greene, Phys. Rev. A **68**, 012703 (2003).
[44] A. Giusti, J. Phys. B: At. Mol. Phys. **13**, 3867 (1980).
[45] O. Motapon, M. Fifirig, A. Florescu, F. W. Tamo, O. Crumeyrolle, G. Varin-Bréant, A. Bultel, P. Vervisch, J. Tennyson, and I. Schneider, Plasma Sources Sci. Technol. **15**, 23 (2005).
[46] J. Z. Mezei, R. Backodissa-Kiminou, D. Tudorache, V. Morel, K. Chakrabarti, O. Motapon, O. Dulieu, J. Robert, W.-Ü. L. Tchang-Brillet, A. Bultel *et al.*, Plasma Sources Sci. Technol. **24**, 035005 (2015).
[47] M. Sommavilla, F. Merkt, J. Z. Mezei, and C. Jungen, J. Chem. Phys. **144**, 084303 (2016).
[48] C. Jungen, *Molecular Applications of Quantum Defect Theory* (Institute of Physics, Bristol, UK, 1996).
[49] D. R. Bates and L. Spitzer Jr., Astrophys. J. **113**, 441 (1951).
[50] M. Krauss and P. Jlienne, Astrophys. J. **183**, L139 (1973).
[51] A. Giusti-Suzor and H. Lefebvre-Brion, Astrophys. J. **214**, L101 (1977).
[52] A. Douglas and G. Herzberg, Astrophys. J. **94**, 381 (1941).
[53] W. S. Adams, Astrophys. J. **93**, 11 (1941).
[54] K. Hassouni, F. Silva, and A. Gicquel, J. Phys. D. **43**, 153001 (2010).
[55] https://euro-fusion.org/jet/
[56] H. Takagi, N. Kosugi, and M. Le Dourneuf, J. Phys. B: At., Mol. Opt. Phys. **24**, 711 (1991).
[57] E. Chang and U. Fano, Phys. Rev. A. **6**, 173 (1972).
[58] C. H. Greene and C. Jungen, Adv. At. Mol. Phys. **21**, 51 (1985).
[59] M. Aymar, C. H. Greene, and E. Luc-Koenig, Rev. Mod. Phys. **68**, 1015 (1996).
[60] J. Tennyson, Phys. Rep. **491**, 29 (2010).
[61] M. J. Seaton, Rep. Prog. Phys. **46**, 167 (1983).
[62] V. Kokoouline, A. Faure, J. Tennyson, and C. H. Greene, Mon. Not. R. Astron. Soc. **405**, 1195 (2010).
[63] M. Ayouz and V. Kokoouline, Atoms **4**, 30 (2016).
[64] M. Khamesian, M. Ayouz, J. Singh, and V. Kokoouline, Atoms **6**, 49 (2018).
[65] M. Ayouz and V. Kokoouline, Atoms **7**, 67 (2019).
[66] H.-J. Werner, P. J. Knowles, G. Knizia, F. R. Manby, and M. Schütz, WIREs Comput. Mol. Sci. **2**, 242 (2012).
[67] V. Kokoouline, O. Dulieu, R. Kosloff, and F. Masnou-Seeuws, J. Chem. Phys. **110**, 9865 (1999).
[68] Z. Biglari, A. Shayesteh, and A. Maghari, Comput. Theor. Chemy. **1047**, 22 (2014).
[69] J. M. Carr, P. G. Galiatsatos, J. D. Gorfinkiel, A. G. Harvey, M. A. Lysaght, D. Madden, Z. Masin, M. Plummer, J. Tennyson, and H. N. Varambhia, Eur. Phys. J. D **66**, 58 (2012).
[70] J. Tennyson, D. B. Brown, J. J. Munro, I. Rozum, H. N. Varambhia, and N. Vinci, J. Phys. Conf. Ser. **86**, 012001 (2007).

Vibrational excitation of N_2O by an electron impact and the role of the Renner-Teller effect in the process

Hainan Liu,[1] Samantha Fonseca dos Santos,[2] Chi Hong Yuen,[3] Pietro Cortona,[1] Mehdi Ayouz,[4,*] and Viatcheslav Kokoouline[3]

[1]*Université Paris-Saclay, CentraleSupélec, CNRS, Laboratoire SPMS, 91190 Gif-sur-Yvette, France*
[2]*Department of Physics, Rollins College, Winter Park, Florida 32789, USA*
[3]*Department of Physics, University of Central Florida, Orlando, Florida 32816, USA*
[4]*Université Paris-Saclay, CentralSupélec, LGPM, 91190 Gif-sur-Yvette, France*

(Received 25 May 2020; accepted 21 August 2020; published 11 September 2020)

Cross sections and rate coefficients for vibrational excitation and de-excitation of the N_2O molecule by a low-energy electron for transitions between the lowest vibrational levels are computed using a first-principles approach. The present theoretical approach employs the normal-mode approximation for the description of target vibrational states, the vibrational frame transformation to compute amplitudes of vibrational transitions, and the *R*-matrix method to compute *ab initio* electronic bound and continuum states. It was found that the nonadiabatic Renner-Teller effect, which couples partial waves of the incident electron with degenerate bending vibrations of N_2O, is responsible for the excitation of the bending mode. Theoretical results obtained agree reasonably well with available experimental data at low energies. Thermally averaged rate coefficients are computed for temperatures in the 10–10 000 K range.

DOI: 10.1103/PhysRevA.102.032808

I. INTRODUCTION

Vibrational (de-)excitation by electron impact is a process in which an electron scatters off a molecule and exchanges energy with it in a way that leaves the molecular target in a different vibrational state. For N_2O, vibrational (de-)excitation can be depicted by

$$e^- + N_2O(v_i) \rightarrow e^- + N_2O(v_i'), \tag{1}$$

where v_i and and v_i' denote the initial and final vibrational states of N_2O, respectively.

Due to the importance of nitrous oxide (N_2O) in a plethora of research fields ranging from astrochemistry [1–3] to low-temperature plasma technology [4] and medicine [5], different electron-N_2O collisional processes have been experimentally and theoretically explored over the years. Differential and integrated cross sections for elastic and certain inelastic processes have been measured by several groups [6–26]. Although the experimental investigations generally agree on the position of an observed resonance near 2.3–2.5 eV, they disagree on the assignment for the symmetry of the resonant state. Furthermore, there is also disagreement with respect to a second resonance observed around or above 8.0 eV. On the theoretical side, the earlier studies by Morgan [27], Sarpal *et al.* [28], and Bettega *et al.* [29] aimed at clearly specifying the nature of the two resonances observed in the experiments. Morgan and Sarpal *et al.* employed the *R*-matrix method with different models to study electron scattering by N_2O in its equilibrium geometry. They obtained a resonance near 2.3 eV with $^2\Pi$ symmetry. Later, using a slight modification of the Schwinger multichannel method of incorporating polarization effects, Bettega [29] was able to reproduce the experimental features between the two resonances.

To our knowledge, no theoretical vibrational cross sections have been reported to date, while several experimental cross sections have: by Hayashi and Akashi [30], Kitajima *et al.* [18], Allan and Skalický [21], and Nakamura [22]. A compilation of their work can be found in a recent review [31]. Hayashi and Akashi presented cross sections for electron-induced vibrational excitations from electron swarm parameters in pure N_2O. Kitajima *et al.* as well as Allan and Skalický measured absolute differential cross sections for vibrationally inelastic electron scattering with a range of electron scattering energies from the threshold region up to 20 eV. Allan and Skalický reported measurements for only one scattering angle, 135°, and multiplied each of the measured differential cross sections by the factor 4π to estimate the integral cross section. Nakamura [22] derived cross sections for vibrational excitation from swarm parameters.

The present work represents the first theoretical vibrational excitation (VE) study of N_2O by electron impact. We present cross sections and rate coefficients for transitions between ground and first vibrational states of N_2O using the theoretical and computational formalism recently employed to study the VE of NO_2 [32]. The rotational structure is neglected in the present study.

The paper is organized as follows. The next section, Sec. II, describes the theoretical approach and computational details employed in our calculations. In Sec. III, the results obtained numerically are analyzed using the model of Renner-Teller coupling for linear molecules. In Sec. IV, the obtained VE

*mehdi.ayouz@ecp.fr

cross sections and corresponding rate coefficients are shown and discussed. Section V presents uncertainty estimations of the present approach, and the last section, Sec. VI, is devoted to our conclusions.

II. THEORETICAL APPROACH

Our approach can be summarized as follows. We start by characterizing the molecular target according to its equilibrium geometry, vibrational frequencies, and dipole moment value at equilibrium: features that can be obtained by performing *ab initio* electronic bound molecular states calculations. We proceed by performing *ab initio* electronic continuum molecular states calculations to obtain a scattering matrix at different molecular geometries along the vibrational normal-mode coordinates. We then transform the scattering matrix into the basis of vibrational states of the target molecule. Finally, we compute the vibrational (de-)excitation cross sections from the transformed scattering matrix.

The approach used in our study has been previously described and applied to the NO_2 molecule [32], and a more detailed narrative of the simplified model on which our approach is based can be found in Refs. [33,34]. Therefore, we limit the description presented in this section to the main ingredients of the theoretical formalism—the normal-mode approximation and the vibrational frame transformation—and to the computational details of our calculations.

At low energies around the equilibrium position, the potential energy curve of the most rigid molecules is fairly well described by the quadratic potential of a harmonic oscillator. In our approach, we describe vibrational wave functions of the molecular target using the normal-mode approximation. The approximation allows us to perform a significant part of the calculations analytically. For molecules of astrophysical and low-temperature plasma interest, like N_2O, only the lowest vibrational levels are significantly populated at low temperatures and the range of scattering energies needed to study vibrational excitation is within the validity of the normal-mode model.

After computing the scattering matrix, we perform a vibrational frame transformation [35] to change the scattering matrix obtained for clumped nuclei for a number of molecular geometries to the vibrating-molecule picture that the electron sees when it is at large electronic distances.

The clumped nuclei basis of asymptotic channels is denoted by the channel quantum numbers $\{l, \lambda\}$ that label the angular momentum of the incoming and outgoing electrons and their respective projections on the z axis in the molecular frame coordinate system. The three axes of the molecular coordinate system are chosen along the principal axes on the inertia of the molecule, such that the quantization axis (the z axis) is directed along the molecular axis in calculations for linear geometries. For bent geometries of the molecule, the z axis is perpendicular to the plane of the molecule, with the x axis aligned along the axis of the smallest moment of inertia. In Sec. III we introduce another set of quantum numbers $\{l, \tilde{\lambda}\}$ and corresponding channel functions, which replace the spherical harmonic Y_l^{λ} with their real-valued combinations of $Y_l^{\pm\lambda}$. The target vibrational wave functions are labeled by the $\{\nu_i, \nu_i'\}$ set of quantum numbers.

The vibrational frame transformation of the scattering matrix elements is given by

$$S^{\nu_i'\nu_i}_{l'\lambda',l\lambda} = \langle \chi_{\nu_i'}(\mathbf{q}) | S_{l'\lambda',l\lambda}(\mathbf{q}) | \chi_{\nu_i}(\mathbf{q}) \rangle, \tag{2}$$

where $\mathbf{q}$ collectively represents the normal-mode coordinates and the index i denotes the vibrational mode. N_2O has three normal modes of vibration, namely, NO stretching, the doubly degenerate bending mode, and NN stretching, represented by ν_1, ν_2, and ν_3, respectively. The physical meaning of an element of the transformed scattering matrix is the scattering amplitude from one vibrational state, $\chi_{\nu_i}(\mathbf{q})$, of the target molecule to another, $\chi_{\nu_i'}(\mathbf{q})$. The vibrational frame transformation of Eq. (2) can only be performed if the fixed-nuclei S-matrix element, $S_{l'\lambda',l\lambda}$, is a smooth function of the incident electronic energy [36]. This means, in particular, that for this approach to be applicable, the fixed-nuclei S matrix should not have low-energy electronic resonances. As discussed above, the lowest electronic resonance in e^--NO_2 collisions occurs at collision energies of about 2.5 eV.

The cross section $\sigma_{\nu_i'\nu_i}$ for vibrational (de-)excitation can be obtained from the corresponding matrix element $S^{\nu_i'\nu_i}_{l'\lambda',l\lambda}$ by the expression

$$\sigma_{\nu_i'\nu_i}(E_{\rm el}) = \frac{\pi\hbar^2}{2m_e E_{\rm el}} \sum_{l'\lambda',l\lambda} \left| S^{\nu_i'\nu_i}_{l'\lambda',l\lambda} - \delta^{\nu_i'\nu_i}_{l'\lambda',l\lambda} \right|^2, \tag{3}$$

where m_e and $E_{\rm el}$ are, respectively, the reduced mass of the electron-N_2O system and the energy of the incident electron. Although the fixed-nuclei scattering matrix $S_{l'\lambda',l\lambda}(\mathbf{q})$ is weakly dependent on the energy, the remaining energy dependence introduces an ambiguity in the choice of the matrix in the integrand of Eq. (2). In the present calculation, we choose the following procedure: Integrating over the normal mode $\mathbf{q}$ in Eq. (2) for a given energy $E_{\rm el}$ of the electron in the incident channel (see the above equation) and at each integration point $\mathbf{q}$, the scattering matrix $S_{l'\lambda',l\lambda}(\mathbf{q})$ is taken from the R-matrix calculations performed at this particular fixed-nuclei geometry $\mathbf{q}$ and the electron scattering energy $E_{\rm el}$. Because the energy dependence of the fixed-nuclei scattering matrix is weak below 2.5 eV, the corresponding uncertainty of the final cross section is much smaller than the uncertainty related to the choice of the *ab initio* model (discussed below).

The cross section of Eq. (3) for vibrational excitation does not account for the rotational structure and can be compared with experiments or used in applications where the rotational structure of the initial and final vibrational levels is not important or not resolved. This is, generally, the case for most current experiments (including swarm measurements) and plasma applications at room or higher temperatures: With the rotational N_2O constant of 0.419 01 $\mathrm{cm}^{-1} = 5.195\times10^{-5}$ eV [37] at 300 K, at least 25 rotational states are significantly populated.

Computational details

At its equilibrium geometry, N_2O has a linear asymmetric "N-N-O" molecular structure, described by the $C_{\infty v}$ symmetry point group with the group electronic state of the $^1\Sigma^+$ symmetry. The equilibrium geometry and the normal-mode coordinates with corresponding frequencies were computed

TABLE I. Energies $\hbar\omega_i$ (in eV) of N_2O normal modes obtained in the present study and compared with experimental data from Ref. [38].

Mode (ν_i)	Degeneracies	Symmetry	$\hbar\omega_i$	
			Experimental	Calculated
NO stretching (ν_1)	1	Σ^+	0.1610	0.1622
Bending (ν_2)	2	Π	0.0739	0.0761
NN stretching (ν_3)	1	Σ^+	0.2830	0.2849

with the MOLPRO suite [39] using the complete active space self-consistent field (CASSCF) method and the cc-pVTZ basis set [40] centered on each atom. N_2O has 22 electrons in a closed-shell electronic ground-state configuration given by

$$^1\Sigma^+: 1\sigma^2 2\sigma^2 3\sigma^2 4\sigma^2 5\sigma^2 6\sigma^2 1\pi^4 7\sigma^2 2\pi^4.$$

In the calculations preserving the $C_{\infty v}$ symmetry group, the 10 electrons which occupy the lowest five σ molecular orbitals were kept frozen and the remaining 12 electrons were allowed to distribute themselves according to symmetry and spin restrictions in the complete active space (CAS) formed by the remaining $6\sigma 1\pi 7\sigma 2\pi$ ground-configuration orbitals and the next three molecular orbitals, 8σ, 9σ, and 3π, which are empty in the ground configuration. Because available quantum chemistry codes cannot handle continuous groups like $C_{\infty v}$, the calculations were performed in the C_{2v} group for the geometries describing NO and NN stretching displacements. For geometries breaking the $C_{\infty v}$ symmetry group—the bending-mode displacements—the same 10 electrons were kept frozen in the lowest 5 a' orbitals and the remaining 12 electrons were distributed in the 6–12 a' and 1–3 a'' orbitals of the corresponding C_s symmetry group.

Upon optimization of the equilibrium geometry, the N-N and N-O bond lengths were found to be 1.131 and 1.186 Å, respectively, in good agreement with the experimental values, 1.128 and 1.184 Å [38]. Table I reports a comparison between the obtained normal-mode frequencies and the available experimental data [38]. Our frequencies agree with the experimental references with a difference of less than 3%.

After characterizing the equilibrium geometry and normal-mode frequencies with MOLPRO [39], we carried out calculations of the potential energy of the ground electronic state of N_2O and calculations of continuum states using the U.K. *R*-matrix code [41] with the Quantemol-N suite [42]. For consistency with the MOLPRO calculations, we have used the same basis set and CAS. However, Quantemol-N does not have CASSCF built into it, and a series of convergence tests showed that the available complete active space configuration interaction (CAS-CI) model with the Hartree-Fock orbitals built with MOLPRO gave the best results. Figure 1 displays the ground-state electronic potential energy curves of N_2O for each normal mode obtained with Quantemol-N. For comparison, we also show the potential energy curves of harmonic oscillators generated with the frequencies obtained from MOLPRO. The Quantemol-N potential energy curves agree reasonably well with the potential energies calculated in the harmonic approximation. Small discrepancies are attributed to the anharmonicity of the actual N_2O potential. The permanent electric dipole moment of the target molecule obtained from the *R*-matrix calculation is 0.1 D, which is considered to be in satisfactory agreement with the experimental value, 0.16 D [38].

Using the molecular orbitals obtained from the structure calculations and the continuum Gaussian-type orbitals with partial waves up to $l \leqslant 4$, we performed the electronic continuum molecular states calculations with Quantemol-N. The radius of the *R*-matrix sphere was set to be 11 bohr. All the electronic states of the target below the cutoff energy, 16 eV, have been included in the close-coupling expansion. From the scattering calculations we can obtain the eigenphase sums and the reactance matrix (*K* matrix) at clumped nuclei.

Figure 2 displays the eigenphase sum of different irreducible representations at equilibrium and at displacements

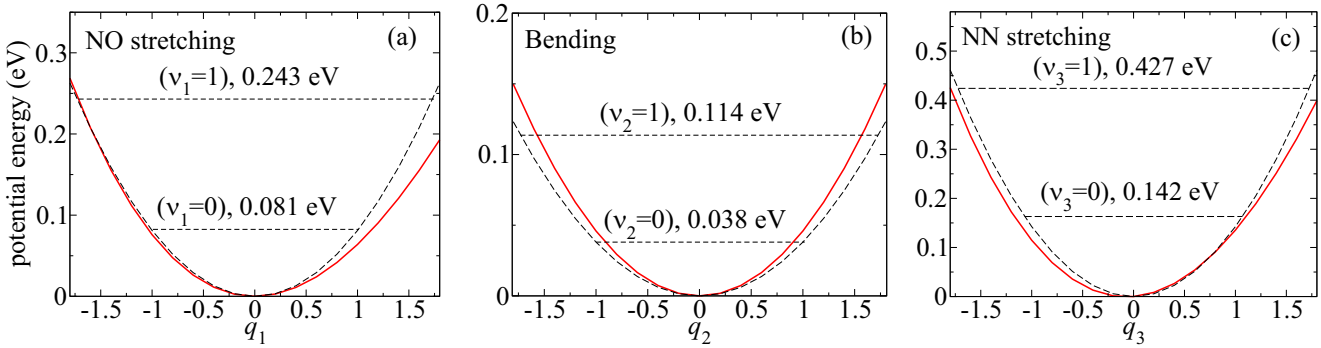

FIG. 1. Potential energy curves for the ground electronic state of N_2O as a function of the (a) NO stretching, (b) bending, and (c) NN stretching normal-mode coordinates. The abscissa axes represent dimensionless normal-mode coordinates. In each panel, only one mode is varied, while the other modes are kept fixed at their equilibrium positions. Solid red curves show the actual potential energies obtained from the *R*-matrix code, while dashed black curves represent energies calculated in the harmonic approximation, i.e., simply $\sim\frac{\hbar\omega_i}{2}q_i^2$. Dashed horizontal lines denote the energies of vibrational states.

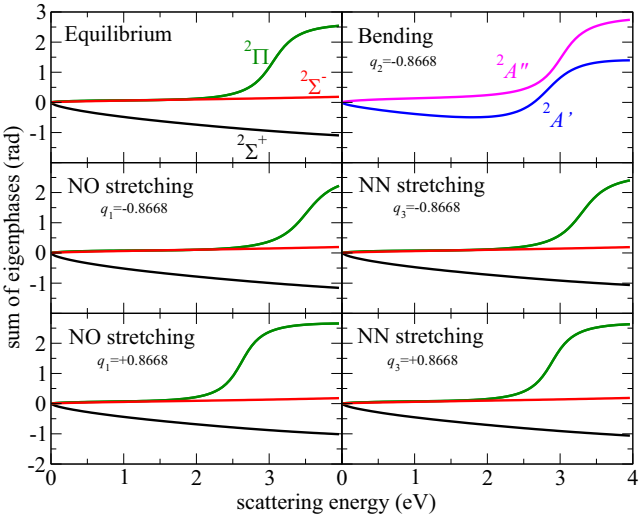

FIG. 2. Sum of eigenphases as a function of the electron scattering energy for equilibrium geometry and displacements $q_i = \pm 0.8668$ (dimensionless) along each normal mode. Due to the symmetry of the bending mode, the eigenphase sums of $q_2 = +0.8668$ and $q_2 = -0.8668$ are the same. The curves are color-coded according to the different symmetries of the $e^- + N_2O$ system.

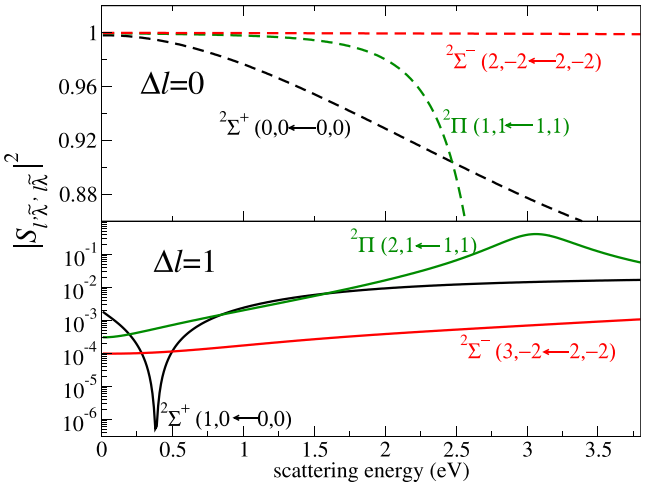

FIG. 3. Largest S-matrix elements (absolute values squared, $|S_{l'\tilde{\lambda}',l\tilde{\lambda}}|^2$) computed at the N_2O equilibrium geometry as a function of the scattering energy. Top: Couplings between channels with $\Delta l = 0$ in dashed curves. Bottom: Couplings between channels with $\Delta l = 1$ in solid curves.

away from the equilibrium along each normal-mode coordinate. We obtained the position and width of calculated resonances by fitting the eigenphase sum to a Breit-Wigner form. At equilibrium, the lowest resonance is found at 3.0 eV and has $^2\Pi$ symmetry. To compare with the available experimental data (the resonance around 2.3–2.5 eV [21,43]), the zero-point energy $\hbar(\omega_1 + 2\omega_2 + \omega_3)/2 = 0.3$ eV of the ground vibrational level should be accounted for. Therefore, in the present calculation, the energy of the resonance is 2.7 eV above the ground vibrational level. The difference from the experimental position of the resonance is attributed to the large uncertainty associated with the Born-Oppenheimer approximation used to identify the energy of the resonance in the theoretical calculation: The position of the resonance depends strongly on the choice of the fixed geometry near the N_2O equilibrium at which the scattering calculations were performed. In addition, the width (about 1 eV) of this shape resonance is larger than the difference between the experimental and the theoretical results.

The K matrix obtained from the scattering calculations was used to compute the clumped-nuclei scattering matrix (S matrix). Figure 3 displays selected dominant elements (the absolute value squared) of the S matrix at equilibrium geometry. In the figure (as well as in Fig. 4), the indices $\tilde{\lambda}$ refer to real-valued combinations of spherical harmonics $Y_l^{\pm\lambda}$ with positive and negative projections λ. The real-valued harmonics $Y_{l\tilde{\lambda}}$ with positive $\tilde{\lambda}$ transform as cosine-type functions with respect to the rotational angle ϕ about the axis z perpendicular to the plane of the molecule, while the harmonics with negative λ transform as sine-type functions. Except for the $S_{10,00}$ element, all other elements behave smoothly with the electronic energy below the first resonance. The minimum is observed near 0.4 eV for the $10 \leftarrow 00$ transition.

Although the $S_{10,00}$ element has a strong energy dependence, which breaks the condition of the applicability of the vibrational frame transformation (the energy dependence should be smooth), its contribution to the VE cross section in Eq. (3) is negligible compared to that of the dominant terms (diagonal over $l\tilde{\lambda}$), and therefore, it does not compromise the present theoretical approach. The vibrationally transformed S matrix is calculated according to Eq. (2), where the integration over vibrational coordinates is performed numerically using a Gaussian-Legendre quadrature with 10 points.

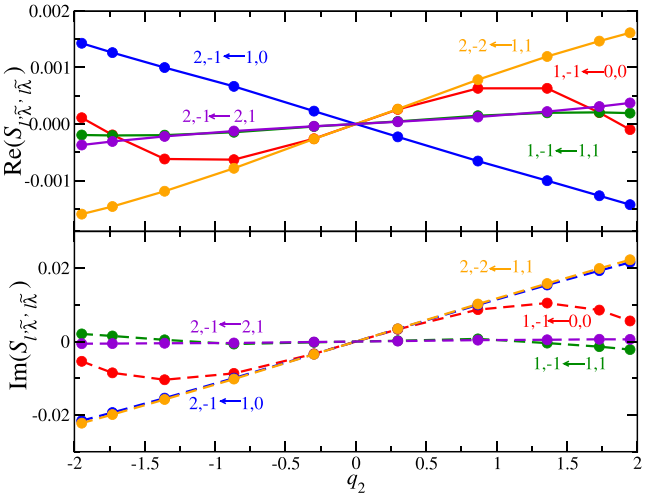

FIG. 4. Largest fixed-nuclei S-matrix elements as a function of the bending coordinate q_2, computed for scattering energy 0.26 eV. The upper (lower) panel shows the real (imaginary) part of the S-matrix elements. Couplings $l'\tilde{\lambda}' \leftarrow l\tilde{\lambda}$ between different partial waves, represented by real-valued harmonics $Y_{l,\tilde{\lambda}}$, are labeled by curves of different colors.

III. RENNER-TELLER COUPLING IN N_2O VIBRATIONAL EXCITATION BY ELECTRONS

It is instructive to analyze the dependence of major coupling elements of the scattering matrix as a function of the normal coordinates, especially for the bending mode. For the NO and NN stretching modes, the main contribution to the VE cross section is due to variation of the diagonal elements of the scattering matrix with low l.

In constrast, for the bending mode, the major contribution is due to the q_2 dependence of nondiagonal elements between the $^2\Sigma^+$ and the $^2\Pi$ states of the $e^- + N_2O$ system near the linear geometry. This is the Renner-Teller coupling, whose effect on electron-molecule collisions has been discussed in several previous studies [33,44–48]. For a linear triatomic (and larger) molecule with a ground electronic state of $^1\Sigma$ symmetry, the Renner-Teller effect couples σ and π partial waves of the incident electron with vibrational bending motion of the target molecule.

Due to the symmetry of the bending mode, all matrix elements $S_{l'\tilde{\lambda}',l\tilde{\lambda}}$ are symmetric or antisymmetric with respect to the change in the sign $q_2 \to -q_2$ of the displacement along the bending mode. The elements which are symmetric, such as diagonal and some nondiagonal elements, do not contribute to the vibrational excitation by one quantum of the bending mode. For an element $S_{l'\tilde{\lambda}',l\tilde{\lambda}}$ to be antisymmetric with respect to the $q_2 \to -q_2$ operation, one of $\tilde{\lambda}'$ and $\tilde{\lambda}$ should be negative, with the other positive or 0. In addition, there is a selection rule regarding the elements that do not vanish: For displacements along q_2, both spherical harmonics in $S_{l'\tilde{\lambda}',l\tilde{\lambda}}$ should be of a' or a'' irreducible representations of the C_s symmetry group (of the bent molecule). Figure 4 shows the largest (in magnitude) antisymmetric S-matrix elements as a function of the bending coordinate.

In Fig. 4, we see that most of the elements are linear with the q_2 coordinate, with the notable exception of $S_{1-1,00}$, which has a strong cubic dependence q_2^3. We attribute the significant cubic contribution to the coupling to the fact that the $s\sigma$ partial wave penetrates closer to the N_2O core electrons such that the linear approximation for the coupling between the $Y_{0,0}$ and the $Y_{1,-1}$ harmonics is no longer valid and higher terms are needed if a Taylor expansion is used to represent the coupling.

The linear dependence of the coupling between partial wave components in a linear molecule for small displacements along the bending coordinate is one of the main characteristics of the Renner-Teller effect. The effect cannot be easily observed in e^--N_2O scattering experiments, but it manifests itself in the bound states of the e^--N_2O system: Due to the degeneracy of the $^2\Pi$ electronic state of the e^--N_2O complex and the degenerate bending mode of N_2O, the relatively strong Renner-Teller coupling results in a bending configuration of the equilibrium geometry of the N_2O^- anion [49,50].

IV. CROSS SECTIONS AND RATE COEFFICIENTS

We calculated the vibrational (de-)excitation cross sections for transitions between the ground and the first excited vibrational states for each of the normal modes. Figure 5 displays a comparison of the theoretical $1 \leftarrow 0$ VE cross sections with the available experimental data [21,22,30], mentioned in Sec. I. None of the three experimental data resolve the $\nu_1 = 1/\nu_2 = 2$ and $\nu_3 = 1/\nu_1 = 2$ thresholds, i.e., the experimental cross section for the excitation of the NO mode ($\nu_1 = 0 \to 1$) includes also a contribution for the transition $\nu_2 = 0 \to 2$, and the cross section for the excitation of the NN mode includes a contribution for the $\nu_1 = 0 \to 2$ transition. But these additional contributions are expected to be significantly smaller due to the vibrational propensity rule: The transitions with a change of only one vibrational quantum are the largest. There is a significant disagreement between the experimental data, up to a factor of 20–50 for certain energies. On the other hand, the theoretical results also do not agree better with one or another experiment: For the NO stretching mode [Fig. 5(a)], the theory agrees better with the experiment by Hayashi [30]. For the bending mode [Fig. 5(b)], the theory agrees better with the other two experiments, although the agreement is quite poor. Note that the integral cross sections presented by Allan and Skalický [21] were obtained from the measured differential cross sections. Finally, for the NN stretching mode [Fig. 5(c)], the theory again agrees better with the data of Hayashi [30].

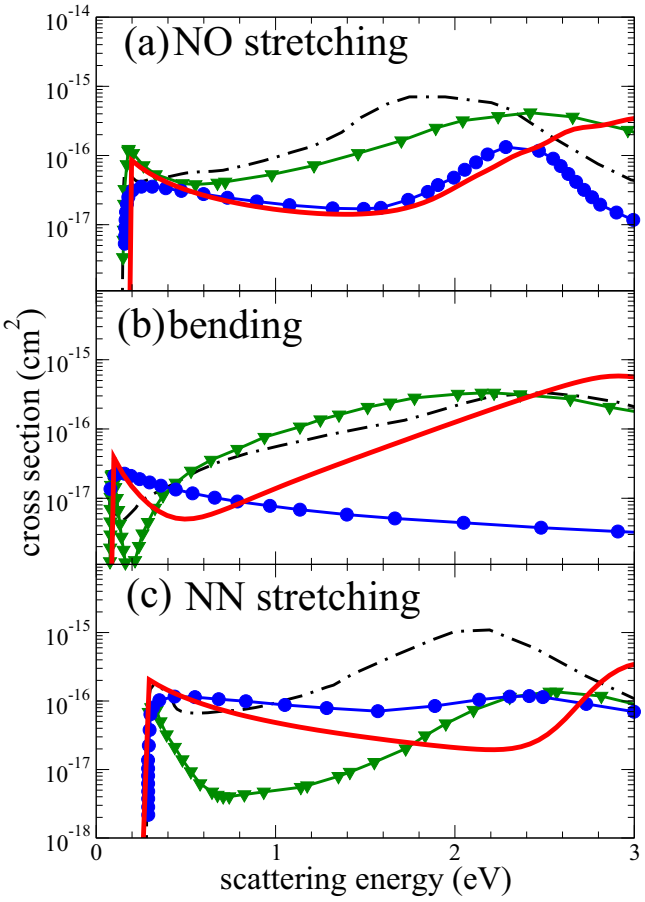

FIG. 5. Comparison of the present theoretical results with the available experimental cross sections for the vibrational $v = 0 \to v' = 1$ excitation of the (a) NO stretching, (b) bending, and (c) NN stretching modes. The experimental results are taken from Hayashi [30,31] (solid line with circles), Allan and Skalický [21] (solid line with triangles), and Nakamura [22] (dashed-dotted line).

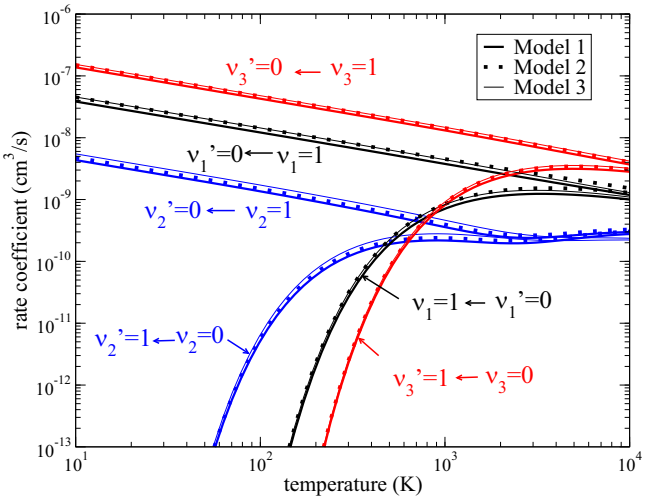

FIG. 6. Thermally averaged rate coefficients for excitation and de-excitation transitions between the ground and the first excited vibrational states of the NO stretching mode (black curves), bending mode (blue curves), and NN stretching mode (red curves). Vibrational (de-)excitations are labeled $\nu_i' \leftarrow \nu_i$. To provide an idea of the uncertainty of the present results, we also plotted the results of calculations with model 2 (dotted lines) and model 3 (thin lines). The three calculations produce curves that are almost indistinguishable.

In a recent review article [31], the swarm data of Nakamura [22], shown by the dashed-dotted lines in Fig. 5, were recommended as the most accurate among the available experimental cross sections. However, it should be stressed that the recommended swarm data may not be very accurate because of an ambiguity in their interpretation [22] (see the discussion in Secs. 3.3 and 3.5 in Ref. [31]). Therefore, the recommended experimental data should have a relatively large uncertainty and could be improved in a more accurate future experiment.

The present theoretical cross sections are expected to be valid only for energies below the energy of the $^2\Pi$ resonance mentioned above, i.e., below 2.3 eV. They are included in the Supplemental Material to this paper [51].

Thermally averaged rate coefficients $\alpha_{\nu_i'\nu_i}(T)$ for vibrational excitation are obtained from the cross sections of Eq. (3) using the standard formula

$$\alpha_{\nu_i'\nu_i}(T) = \frac{8\pi}{(2\pi k_B T)^{\frac{3}{2}}} \int_0^\infty \sigma_{\nu_i'\nu_i}(E_{\rm el}) e^{-\frac{E_{\rm el}}{k_B T}} E_{\rm el} {\rm d}E_{\rm el}, \quad (4)$$

where k_B is the Boltzmann constant and T is the temperature. The computed rate coefficients are shown in Fig. 6 in different colors.

For convenient use in plasma models, the computed coefficients were also fitted using the analytical formula employed in our previous studies [36,52,53],

$$\alpha^{\rm fit}_{\nu_i'\nu_i}(T) = \frac{1}{\sqrt{T}} e^{-\frac{\Delta_{\nu_i'\nu_i}}{T}} P^{\rm fit}_{\nu_i'\nu_i}(x), \quad (5)$$

where $P^{\rm fit}_{\nu_i'\nu_i}(x)$ is a quadratic polynomial,

$$P^{\rm fit}_{\nu_i'\nu_i}(x) = a_0 + a_1 x + a_2 x^2 \quad \text{and} \quad x = \ln(T), \quad (6)$$

TABLE II. Parameters a_0, a_1, and a_2 of the polynomial $P^{\rm fit}_{\nu_i'\nu_i}(x)$ in Eqs. (5) and (6) for transitions between the ground and the first vibrational states in each normal mode. We specify the excitation threshold energies $\Delta_{\nu_i'\nu_i}$ of Eq. (7) in the second column. The threshold $\Delta_{\nu_i'\nu_i} = 0$ for the de-excitation process.

$1 \leftrightarrow 0$	$\Delta_{\nu_i'\nu_i}$ (K)	a_0	a_1	a_2
NO stretch	1888	1.22×10^{-7}	6.60×10^{-11}	-3.14×10^{-11}
Bending	885	1.37×10^{-8}	-2.50×10^{-11}	4.40×10^{-12}
NN stretch	3316	4.34×10^{-7}	7.42×10^{-10}	-5.20×10^{-10}

where $P^{\rm fit}_{\nu_i'\nu_i}(x) \approx P^{\rm fit}_{\nu_i'\nu_i}(x)$ can be viewed as the excitation and de-excitation probabilities, with $\Delta_{v'i',vi}$ being the threshold energy, defined as

$$\Delta_{\nu_i'\nu_i} = \begin{cases} E_{\nu_i'} - E_{\nu_i} > 0 & \text{for excitation,} \\ 0 & \text{for de-excitation.} \end{cases} \quad (7)$$

The numerically fitted parameters for vibrational excitation are listed in Table II. When the parameters listed in the table are used in the fitting formulas of Eqs. (5) and (6) with the temperature in kelvins, the obtained numerical values of the rate coefficients will be in units of $\rm cm^3/s$.

V. UNCERTAINTY ESTIMATIONS

We have performed a number of calculations to assess the uncertainty of the obtained theoretical results. There are two main sources of uncertainty in the present theoretical approach. The first is the accuracy of the fixed-nuclei S-matrix elements computed for the polar molecule (with a small dipole moment) in the limited basis of spherical harmonics. It has been discussed by Liu [32]. The uncertainty associated with this approximation was estimated to be of the order of 6% for NO_2 [32]. It should not be larger for N_2O because it has a smaller dipole moment so that the couplings between partial waves induced by the permanent dipole moment of this molecule have a weaker effect on the final cross sections. Therefore, it is reasonable to assume that the corresponding uncertainty in the present case is below 6%.

The second source of uncertainty derives from the particular scattering model used in the calculation. The uncertainty can be assessed by performing a complete calculation with different parameters of the model. With the parameters discussed in Sec. II, referred to as model 1, we obtained the results shown above. In the second calculation, with model 2, the CAS in the configuration calculation was the same as in model 1 but a larger basis set, cc-pVQZ, was used. Finally, in the model 3 calculation the electronic basis set remained cc-pVTZ, but the CAS was reduced compared to that in model 1: 12 electrons were placed in frozen orbitals and the remaining 10 electrons in the lowest orbitals were allowed to be freely distributed in the active space. The rate coefficients obtained in the three models are shown in Fig. 6. The difference in the rate coefficients produced in the three models is about 6%. Consequently, the overall uncertainty of the present theoretical result is estimated to be below 12%.

VI. CONCLUSIONS

In this study, we computed cross sections for vibrational (de-)excitations of N_2O by a low-energy electron using (a) the normal-mode approximation to describe the vibrational states of the target molecule, (b) the *R*-matrix method to evaluate the fixed-nuclei electron-N_2O scattering matrices, and (c) the vibrational frame transformation to evaluate the amplitudes for vibrational transitions. In this approach, we neglected the rotational structure of each vibrational level, which corresponds to the situation where the rotational structure is not resolved in the initial and final states of the target molecule.

The computed results show a reasonable agreement with experimental data for the NO and NN stretching modes. For the bending mode the agreement is rather poor at energies above 0.4 eV. It was found that Renner-Teller coupling is responsible for the excitation of the bending mode, as was expected from general theoretical considerations. We are quite confident about the present theoretical cross sections for the bending mode because the numerical calculations of the fixed-nuclei scattering matrix fit well to the theory of Renner-Teller coupling. It should be stressed here that the most reliable experimental cross section for the bending mode by Nakamura [22,31] was obtained from swarm data and a direct measurement of the differential cross section at a single scattering angle by Allan and Skalický [21] and, therefore, may have a large uncertainty. This suggests that a better direct measurement of vibrational excitation in N_2O, at least for a few energies, is needed.

ACKNOWLEDGMENTS

This work was supported by the China Scholarship Council, the Thomas Jefferson Fund of the Office for Science and Technology of the Embassy of France in the United States, and National Science Foundation Grant No. PHY-1806915. It also received funding from the programs "Accueil des chercheurs étrangers" of CentraleSupélec and "Séjour à l'étranger 2019" of école doctorale INTERFACES of Université Paris-Saclay.

[1] L. M. Ziurys, A. Apponi, J. Hollis, and L. Snyder, Astrophys. J. **436**, L181 (1994).
[2] C. S. Jamieson, C. J. Bennett, A. M. Mebel, and R. I. Kaiser, Astrophys. J. **624**, 436 (2005).
[3] W.-C. Wang and N. D. Sze, Nature **286**, 589 (1980).
[4] N. Gherardi, S. Martin, and F. Massines, J. Phys. D: Appl. Phys. **33**, L104 (2000).
[5] Í. O'Sullivan and J. Benger, Emerg. Med. J. **20**, 214 (2003).
[6] A. Zecca, I. Lazzizzera, M. Krauss, and C. E. Kuyatt, J. Chem. Phys. **61**, 4560 (1974).
[7] R. I. Hall, A. Chutjian, and S. Trajmar, J. Phys. B: At. Mol. Opt. Phys. **6**, L365 (1974).
[8] E. Märk, T. D. Märk, Y. B. Kim, and K. Stephan, J. Chem. Phys. **75**, 4446 (1981).
[9] C. K. Kwan, Y. F. Hsieh, W. E. Kauppila, S. J. Smith, T. S. Stein, M. N. Uddin, and M. S. Dababneh, Phys. Rev. Lett. **52**, 1417 (1984).
[10] C. Szmytkowski, G. Karwasz, and K. Maciag, Chem. Phys. Lett. **107**, 481 (1984).
[11] L. Andric and R. Hall, J. Phys. B: At. Mol. Phys. **17**, 2713 (1984).
[12] D. Cubric, D. Cvejanovic, J. Jureta, S. Cvejanovic, P. Hammond, G. C. King, and F. H. Read, J. Phys. B: At. Mol. Phys. **19**, 4225 (1986).
[13] B. Marinkovic, C. Szmytkowski, V. Pejcev, D. Filipovic, and L. Vuskovic, J. Phys. B: At. Mol. Opt. Phys. **19**, 2365 (1986).
[14] W. M. Johnstone and W. R. Newell, J. Phys. B: At. Mol. Opt. Phys. **26**, 129 (1993).
[15] A. Zecca, J. C. Nogueira, G. P. Karwasz, and R. S. Brusa, J. Phys. B: At. Mol. Opt. Phys. **28**, 477 (1995).
[16] I. Iga, M. V. V. S. Rao, and S. K. Srivastava, J. Geophys. Res. E **101**, 9261 (1996).
[17] M. Kitajima, Y. Sakamoto, S. Watanabe, T. Suzuki, T. Ishikawa, H. Tanaka, and M. Kimura, Chem. Phys. Lett. **309**, 414 (1999).
[18] M. Kitajima, Y. Sakamoto, R. J. Gulley, M. Hoshino, J. C. Gibson, H. Tanaka, and S. J. Buckman, J. Phys. B: At. Mol. Opt. Phys. **33**, 1687 (2000).
[19] S. A. Rangwala, E. Krishnakumar, and S. V. K. Kumar, Phys. Rev. A **68**, 052710 (2003).
[20] A. Zecca, G. P. Karwasz, R. S. Brusa, and T. Wroblewski, Int. J. Mass Spectrom. **223-224**, 205 (2003).
[21] M. Allan and T. Skalický, J. Phys. B: At. Mol. Opt. Phys. **36**, 3397 (2003).
[22] Y. Nakamura, in *Proceedings of the 28th ICPIG*, edited by Institute of Plasma Physics AS CR (Czech Republic, Prague, 2007), pp. 224–226.
[23] H. Kawahara, D. Suzuki, H. Kato, M. Hoshino, H. Tanaka, O. Ingólfsson, L. Campbell, and M. J. Brunger, J. Chem. Phys. **131**, 114307 (2009).
[24] Y. Itikawa, At. Data Nucl. Data Tables **14**, 1 (1974).
[25] M. Kumar, Y. Kumar, N. Tiwari, and S. Tomar, J. At. Mol. Sci. **4**, 30 (2013).
[26] D. Nandi, V. S. Prabhudesai, and E. Krishnakumar, Phys. Chem. Chem. Phys. **16**, 3955 (2014).
[27] L. A. Morgan, C. J. Gillan, J. Tennyson, and X. Chen, J. Phys. B: At. Mol. Opt. Phys. **30**, 4087 (1997).
[28] B. K. Sarpal, K. Pfingst, B. M. Nestmann, and S. D. Peyerimhoff, J. Phys. B: At. Mol. Opt. Phys. **29**, 857 (1996).
[29] M. H. F. Bettega, C. Winstead, and V. McKoy, Phys. Rev. A **74**, 022711 (2006).
[30] M. Hayashi and K. Akashi, *Handbook of Plasma Material Science* (Ohm, Tokyo, 1992).
[31] M.-Y. Song, J.-S. Yoon, H. Cho, G. P. Karwasz, V. Kokoouline, Y. Nakamura, and J. Tennyson, J. Phys. Chem. Ref. Data **48**, 043104 (2019).
[32] H. Liu, S. F. dos Santos, C. H. Yuen, P. Cortona, V. Kokoouline, and M. Ayouz, Plasma Sources Sci. Technol. **28**, 105017 (2019).

[33] S. F. dos Santos, N. Douguet, V. Kokoouline, and A. Orel, J. Chem. Phys. **140**, 164308 (2014).
[34] V. Kokoouline, M. Ayouz, J. Z. Mezei, K. Hassouni, and I. F. Schneider, Plasma Sources Sci. Technol. **27**, 115007 (2018).
[35] E. Chang and U. Fano, Phys. Rev. A **6**, 173 (1972).
[36] X. Jiang, C. H. Yuen, P. Cortona, M. Ayouz, and V. Kokoouline, Phys. Rev. A **100**, 062711 (2019).
[37] G. Herzberg, *Electronic Spectra and Electronic Structure of Polyatomic Molecules*, Vol. 2 (Krieger, Malabar, FL, 1991).
[38] R. D. Johnson, *Computational Chemistry Comparison and Benchmark Database, NIST Standard Reference Database 101* (National Institute of Standards and Technology, Gaithersburg, Maryland, 2002), https://doi.org/10.18434/T47C7Z.
[39] H.-J. Werner, P. J. Knowles, G. Knizia, F. R. Manby, and M. Schütz, WIREs Comput. Mol. Sci. **2**, 242 (2012).
[40] R. A. Kendall, T. H. Dunning Jr., and R. J. Harrison, J. Chem. Phys. **96**, 6796 (1992).
[41] J. Tennyson, Phys. Rep. **491**, 29 (2010).
[42] J. Tennyson, D. B. Brown, J. J. Munro, I. Rozum, H. N. Varambhia, and N. Vinci, J. Phys.: Conf. Ser. **86**, 012001 (2007).
[43] A. Moradmand, A. L. Landers, and M. Fogle, Phys. Rev. A **88**, 012713 (2013).
[44] I. A. Mikhaylov, V. Kokoouline, A. Larson, S. Tonzani, and C. H. Greene, Phys. Rev. A **74**, 032707 (2006).
[45] N. Douguet, V. Kokoouline, and C. H. Greene, Phys. Rev. A **77**, 064703 (2008).
[46] N. Douguet, V. Kokoouline, and C. H. Greene, Phys. Rev. A **80**, 062712 (2009).
[47] N. Douguet, A. Orel, I. Mikhailov, I. F. Schneider, C. H. Greene, and V. Kokoouline, J. Phys.: Conf. Ser. **300**, 012015 (2011).
[48] N. Douguet, S. F. dos Santos, V. Kokoouline, and A. Orel, EPJ Web Conf. **84**, 07003 (2015).
[49] D. G. Hopper, A. C. Wahl, R. L. Wu, and T. O. Tiernan, J. Chem. Phys. **65**, 5474 (1976).
[50] G. S. Tschumper and H. F. Schaefer III, J. Chem. Phys. **107**, 2529 (1997).
[51] See Supplemental Material at http://link.aps.org/supplemental/10.1103/PhysRevA.102.032808 for the cross-section data.
[52] V. Kokoouline, A. Faure, J. Tennyson, and C. H. Greene, Mon. Not. R. Astron. Soc. **405**, 1195 (2010).
[53] M. Ayouz and V. Kokoouline, Atoms **4**, 30 (2016).

Plasma Sources Science and Technology

PAPER

Theoretical study of dissociative recombination and vibrational excitation of the BF_2^+ ion by an electron impact

To cite this article: Viatcheslav Kokoouline *et al* 2018 *Plasma Sources Sci. Technol.* **27** 115007

IOP Publishing Plasma Sources Science and Technology

Plasma Sources Sci. Technol. **27** (2018) 115007 (6pp) https://doi.org/10.1088/1361-6595/aae6f7

Theoretical study of dissociative recombination and vibrational excitation of the BF_2^+ ion by an electron impact

Viatcheslav Kokoouline[1,7], Mehdi Ayouz[2], János Zsolt Mezei[3,4,5,7], Khalid Hassouni[4] and Ioan F Schneider[5,6]

[1] Department of Physics, University of Central Florida, Orlando, FL 32816, United States of America
[2] LGPM, CentraleSupelec, Université Paris-Saclay, 8-10 Rue Joliot Curie, F-91190 Gif-sur-Yvette, France
[3] Institute for Nuclear Research, Hungarian Academy of Sciences, H-4001 Debrecen, Hungary
[4] Laboratoire des Sciences des Procédés et des Matériaux, CNRS-UPR3407, Université Paris 13, F-93430 Villetaneuse, France
[5] Laboratoire Ondes et Milieux Complexes CNRS-UMR6294, Université du Havre, F-76058 Le Havre, France
[6] Laboratoire Aimé Cotton CNRS-UMR9188, Université Paris-Sud, ENS Cachan, Université Paris-Saclay, F-91405 Orsay, France

E-mail: Viatcheslav.Kokoouline@ucf.edu and mezei.zsolt@atomki.mta.hu

Received 9 July 2018, revised 17 September 2018
Accepted for publication 9 October 2018
Published 7 November 2018

Abstract

Cross-sections for dissociative recombination and electron-impact vibrational excitation of the BF_2^+ molecular ion are computed using a theoretical approach that combines the normal modes approximation for the vibrational states of the target ion and use of the UK R-matrix code to evaluate electron–ion scattering matrices for fixed geometries of the ion. Thermally-averaged rate coefficients are obtained from the cross-sections for temperatures in the 10–3000 K range.

Keywords: non-equilibrium plasmas, plasma immersion ion implantation, electron molecular cation reactive collisions, dissociative recombination, vibrational excitation, vibrational frame transformation, R-matrix theory

1. Introduction

Non-equilibrium plasmas produced by electrical discharges in BF_3-containing feed gas are of continually increasing interest for a large number of applications. In particular, BF_3 is very often the boron carrier when plasmas are used for material processing [1–3]. Basically, BF_3 plasmas are used either for (i) the synthesis of ultra-hard boron compounds, e.g. boron carbides [1], (ii) the deposition of boron nitride, an advanced material with a large number of functionalities [2], and (iii) p-type doping by boron in the semi-conductor and photo-voltaic industries [3, 4]. As far as doping applications are concerned, plasma immersion ion implantation (PIII) processes are probably one of the most promising in terms of cost and technical performance [4, 5]. These processes make use of very low pressure, very high density magnetized plasmas generated in a BF_3-containing feed gas. Depending on the level of the power coupled to the plasma, several cations—BF_3^+, BF_2^+, BF^+, B^+—and anions—e.g. F^-—may be produced [6, 7]. The positive ions are then extracted from the source to an implantation chamber where the processed silicon substrate is submitted to very high negative voltage pulses. These pulses result in a large acceleration of the positive ions that are implanted in the substrate, which results in the doping of the latter. The implantation depth depends on the nature and the energy distribution of the ions impinging the substrate, while the doping level depends on the ion flux and, consequently, on the plasma density. The plasma density and the relative predominance of the different ions are determined by the ionization kinetics in the source region. The plasma sources used in PIII processes are usually magnetized [8]. The ambipolar diffusion in the radial direction

[7] Authors to whom any correspondence should be addressed.

that is perpendicular to the magnetic field is strongly reduced with respect to the parallel diffusion. Under typical plasma conditions used in PIII processes, i.e., $B \approx 100-500$ G and $p \approx 1$ Pa, electron cyclotron frequency in the GHz range, while the electron-neutral momentum transfer collision frequency is in the MHz range, according to equation (5.4.5) of [9] the diffusion coefficient in the radial direction is reduced by approximately 6 orders of magnitude with respect to the parallel diffusion coefficient. The characteristic time estimated for perpendicular diffusion for typical PIII reactor geometries is at the order of 100 s, while the dissociative recombination (DR) characteristic time is around 0.1 s. Following a similar procedure, one can easily show that mutual neutralization is also likely to dominate diffusion losses provided the negative ion density is of the same order of magnitude as the electron density, i.e. moderately electronegative plasmas. It appears, therefore, that under PIII discharge conditions, positive ion losses at the reactor wall are dominated by their DR with electrons and by their neutralization through collisions with negative ions. The investigation of DR of molecular ions is therefore of major interest for these processes. This is especially the case with BF_2^+, which is often the major ion in BF_3-containing plasma in discharge conditions corresponding to PIII process [5]. This study is a continuation of a previous work performed in the theoretical framework of the multichannel quantum defect theory on the DR and competitive processes of BF^+ [10].

The article is organized as follows. After the Introduction, section 2 describes the theoretical approach used in the present calculation. In section 3, the obtained cross-sections and the corresponding rate coefficients are displayed and discussed. Section 4 concludes the study.

2. Theoretical approach

2.1. Dissociative recombination and vibrational excitation cross-section formulas

Since the basic formalism used in our model is presented in detail in [11, 12], we restrict ourselves here to underlining its major ideas. The molecular cation under study, BF_2^+, is linear in its equilibrium geometry.

The theoretical model starts with the following assumptions (see for example [12]): (i) the rotation of the molecule is neglected, (ii) the cross-section is averaged over the autoionizing resonances, (iii) the autoionization lifetime is assumed to be much longer than the predissociation lifetime and (iv) the harmonic approximation is used to describe the vibrational state of the core ion. Using (i)–(iv) and applying the frame transformation, the DR cross-section is given by equation (13) of [12], in which the scattering matrix elements were expanded to first order in the normal coordinates. The cross-section for vibrational excitation (VE) of the mode i is written as

$$\sigma_i^{\mathrm{VE}}(E_{\mathrm{el}}) = \frac{\pi\hbar^2}{4\,mE_{\mathrm{el}}} g_i \sum_{ll'\lambda\lambda'} \left| \frac{\partial S_{l\lambda,l'\lambda'}}{\partial q_i} \right|^2 \theta(E_{\mathrm{el}} - \hbar\omega_i). \quad (1)$$

Here q_i, $\hbar\omega_i$ and g_i ($i = 1, 2, 3$) are respectively the dimensionless coordinate, the energy and the degeneracy of the mode i. The degeneracy is two for the bending mode 2 and one for the symmetric and asymmetric stretching modes. $S_{l\lambda,l'\lambda'}$ is an element of the fixed-nuclei scattering matrix for electron–BF_2^+ collisions with initial channel (λl) and exit channel ($\lambda' l'$), l being the electron angular momentum and λ its projection on the molecular axis. Finally, m is the reduced mass of the electron–ion system, E_{el} the incident energy of the electron and θ the Heaviside step function. The present theoretical approach can describe the (de-)excitation process changing only one quantum in each normal mode of the target ion. (De-)excitation cross-sections for changing two or more quanta in a mode are much smaller (the propensity rule) and are neglected in this study. In the present case, the initial state of the ion is the ground vibrational level, so the electron can only be captured into the first excited vibrational state of each normal mode.

The situation is similar if the electron energy is not sufficient to excite the ion and then to leave it. In such a situation, the present model suggests that the probability of excitation of the ion by the electron is described by the same physics, but instead of leaving the vibrationally excited ion, the electron is captured in a Rydberg resonance attached to that vibrational state, excited by the electron. If the electron is captured by the ion, the system will most likely dissociate, rather then autoionize. Correspondingly, the cross-section for DR is then obtained [12] as

$$\sigma^{\mathrm{DR}}(E_{\mathrm{el}}) = \frac{\pi\hbar^2}{4\,mE_{\mathrm{el}}} \sum_{i=1}^{3} g_i \sum_{ll'\lambda\lambda'} \left| \frac{\partial S_{l\lambda,l'\lambda'}}{\partial q_i} \right|^2 \theta(\hbar\omega_i - E_{\mathrm{el}}). \quad (2)$$

Here i runs over all three modes: two stretching modes ν_1 and ν_3 (symmetric and asymmetric) with respective frequencies ω_1 and ω_3 and corresponding coordinates q_1 and q_3, and a doubly degenerate transverse mode ν_2 with a lower frequency ω_2 and coordinates (q_{2x}, q_{2y}).

To calculate the derivative of the scattering matrix $\partial S_{l\lambda,l'\lambda'}/\partial q_i$ with respect to the normal coordinate q_i, the scattering matrix is evaluated for two values of q_i keeping the other normal coordinates $q_{i'}$ fixed at $q_{i'} = 0$.

The elements $S_{l\lambda,l'\lambda'}(\vec{q})$ of the scattering matrix $\hat{S}(\vec{q})$ at a given geometry $\vec{q}$ specified by four normal coordinates $\vec{q} = \{q_1, q_2, q_3, q_4\} = \{q_1, q_{2x}, q_3, q_{2y}\}$ are computed from the reactance matrix $\hat{K}$, obtained numerically as discussed below:

$$\hat{S} = \frac{\hat{1} + i\hat{K}}{\hat{1} - i\hat{K}}, \quad (3)$$

where $\hat{1}$ is the identity matrix.

2.2. The properties of the BF_2^+ ion and the scattering calculations

The main electronic ground state configuration $^1\Sigma_g^+$ of the ion in its natural point group symmetry $D_{\infty h}$ is $(1\sigma_u^+)^2$ $(1\sigma_g^+)^2$ $(2\sigma_g^+)^2$ $(2\sigma_u^+)^2$ $(3\sigma_g^+)^2$ $(4\sigma_g^+)^2$ $(3\sigma_u^+)^2$ $(1\pi_u^-)^2$ $(1\pi_u^+)^2$ $(1\pi_g^-)^2$ $(1\pi_g^+)^2$. The normal coordinates and the related frequencies are obtained using the cc-pVTZ basis set centered on each atom

Table 1. Vibrational frequencies (in cm^{-1}) obtained in this study and compared with previous data available in literature.

Mode	Symmetric stretching	Bending	Asymmetric stretching		
Symmetry	Σ_g^+	Π_u^+ and Π_u^-	Σ_u^+		
	ω_1	ω_2	ω_3	Method	References
	1062.8	469.2	2146.1	CI/cc-pVTZ	This work
	1023	443	2088	MP2	[14]
	1030	450		CI	[15]
			2 026.1 ± 0.2	Exp.	[16]

and including *s*, *p* and *d* orbitals. Performing configuration interaction (CI) calculations in the D_{2h} symmetry group, using the MOLPRO suite of codes [13], we found that the equilibrium geometry of the ion has a B–F distance of 1.2215 Å. Table 1 gives the vibrational frequencies obtained from CI calculations using the cc-pVTZ basis set, and compares with the data available in literature.

The electron-scattering calculations were performed using the UK R-Matrix code [17, 18] with the Quantemol-N interface [19]. The calculations were performed in the abelian subgroup D_{2h} and the target BF_2^+ ion was assumed to be in its ground electronic state. In our CI model, we freeze 10 electrons in the core $1a_g$, $2a_g$, $3a_g$, $1b_{2u}$, $2b_{2u}$, while the remaining 12 electrons are kept free in the active space of the $4a_g$, $5a_g$, $1b_{3u}$, $2b_{3u}$, $3b_{2u}$, $4b_{2u}$, $1b_{1g}$, $1b_{1u}$, $2b_{1u}$, $1b_{3g}$ molecular orbitals. A total of eight electronic excited target states are represented by 1844 configuration state functions (CSFs) for the ground state. All the generated states up to 16 eV were retained in the final close-coupling calculation. We used an R-matrix sphere of radius 10 bohrs and continuum Gaussian-type orbitals with partial waves up to $l < 4$. In the following, this calculation will be referred to CAS_1.

Initially, several basis sets—including DZP and cc-pVTZ—were tested to investigate the stability of the target properties such as polarizability and ground state energy and, finally, we chose the cc-pVTZ basis set in order to perform the scattering calculations. Since the first electronically excited state $^3\Sigma_g^-$ is approximately 13 eV above the dissociation limit for the ground state, this latter state is essentially isolated and the non-adiabatic effects are expected to be small. Therefore, for low electron energy collisions, i.e. below 10 eV, only the ground electronic state is open for ionization in e–BF_2^+ collisions, and the dimension of the geometry-fixed scattering matrix remains the same at low collision energies.

At low collision energies the fixed-nuclei scattering matrix depends only weakly on energy. A sharper energy-dependence is observed at certain relatively high energies, corresponding to positions of Rydberg states attached to the excited electronic states of the ion. A quantity convenient for the analysis of the energy dependence of the scattering matrix is the eigenphase sum. Figure 1 displays the eigenphase sum for three different geometries corresponding to a small displacement from equilibrium along each normal mode of the BF_2^+ ion. Bending and asymmetric stretching mode calculations were performed in the C_{2v} abelian subgroup, while for the symmetric mode the group D_{2h} was used in the calculations. The variation of the eigenphase sums is smooth for energies below 6 eV. Above this value, a sharp energy dependence at certain energies is observed due to the presence of electronic Rydberg resonances attached to closed ionization limits.

3. Cross-sections and rate coefficients

For convenience, we introduce the quantities

$$P_i = \frac{g_i}{2} \sum_{ll'\lambda\lambda'} \left| \frac{\partial S_{l\lambda,l'\lambda'}}{\partial q_i} \right|^2, \tag{4}$$

which could be interpreted as the probability of excitation of the vibrational mode *i*, and list them in table 2. Figure 2 shows the weak dependence of those quantities on energy and, therefore, they could be used as constants in calculations of the thermally-averaged rate coefficients.

Using P_i, the cross-sections of equations (1) and (2) are written as

$$\sigma_i^{\rm VE}(E_{\rm el}) = \frac{\pi\hbar^2}{2\,mE_{\rm el}} P_i\,\theta(E_{\rm el} - \hbar\omega_i), \tag{5}$$

$$\sigma^{\rm DR}(E_{\rm el}) = \frac{\pi\hbar^2}{2\,mE_{\rm el}} \sum_{i=1}^{3} P_i\,\theta(\hbar\omega_i - E_{\rm el}). \tag{6}$$

Figure 3 illustrates the DR cross-section $\sigma^{\rm DR}(E_{\rm el})$ computed based on equation (5). At very low scattering energies, i.e. below 0.02 eV, the DR cross-section is a smooth function inversely proportional to the incident energy of the electron, as predicted by the Wigner threshold law, whereas at higher energies, it exhibits a drop at each vibrational threshold.

Due to the simple analytical form of the cross-sections, the corresponding rate coefficients are easily evaluated from the general expression

$$\alpha(T) = \frac{8\pi}{(2\pi k_{\rm b}T)^{3/2}} \int_0^\infty \sigma(E_{\rm el}) \exp\left(-\frac{E_{\rm el}}{k_b T}\right) E_{\rm el}\,{\rm d}E_{\rm el}, \tag{7}$$

giving

$$\alpha_i^{\rm VE}(T) = \sqrt{\frac{2\pi}{k_{\rm b}T}}\,\frac{\hbar^2}{m^{3/2}}\,P_i \exp\left(-\frac{\hbar\omega_i}{k_{\rm b}T}\right), \tag{8}$$

$$\alpha^{\rm DR}(T) = \sqrt{\frac{2\pi}{k_{\rm b}T}}\,\frac{\hbar^2}{m^{3/2}} \sum_{i=1}^{3} P_i \left[1 - \exp\left(-\frac{\hbar\omega_i}{k_{\rm b}T}\right)\right]. \tag{9}$$

where $k_{\rm b}$ is the Boltzmann coefficient and T is the temperature. The thermally-averaged rate coefficients for DR and VE are shown in figure 4.

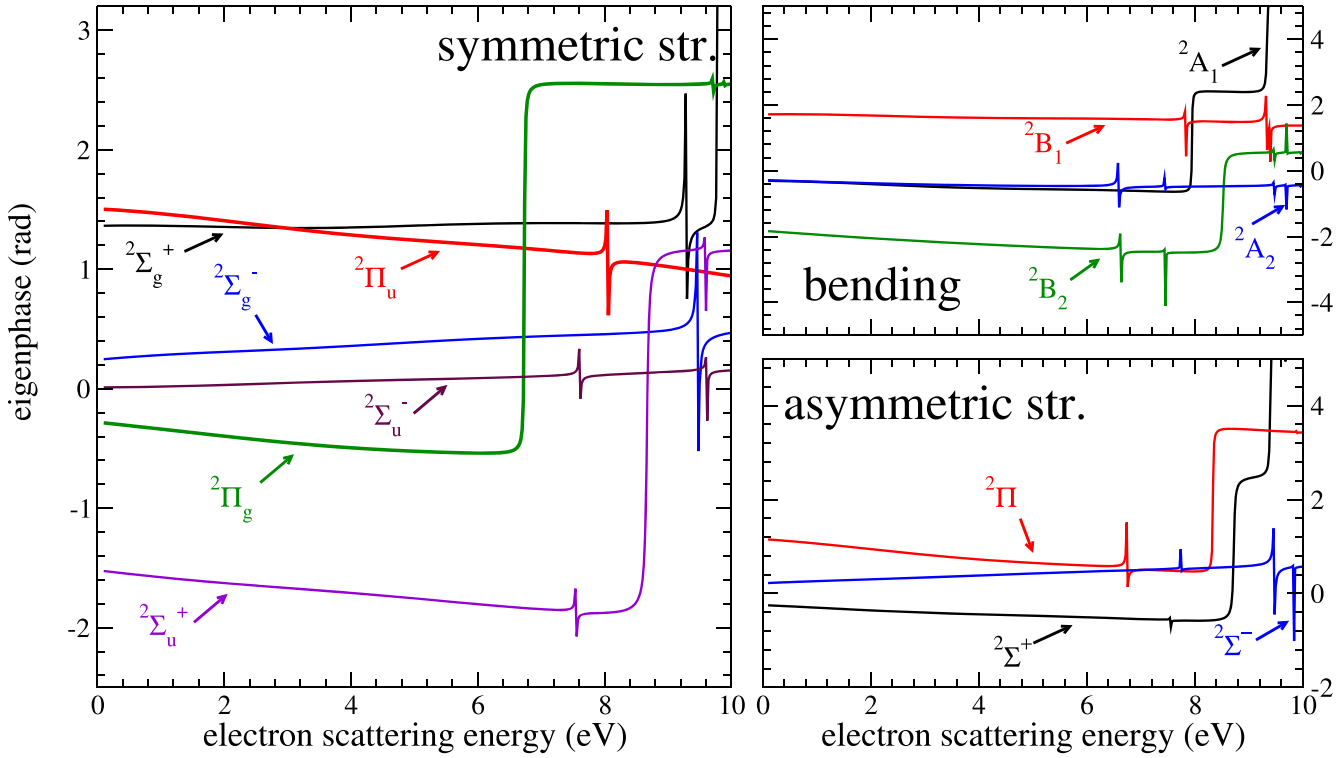

Figure 1. Eigenphase sums as a function of the electron-scattering energy E_{el} for $q_i = 0.01$ (dimensionless) for the symmetric stretching (left panel), bending (right upper panel), and asymmetric stretching (right bottom panel) modes. The curves of different colors correspond to different symmetries of the e^-–BF_2^+ system.

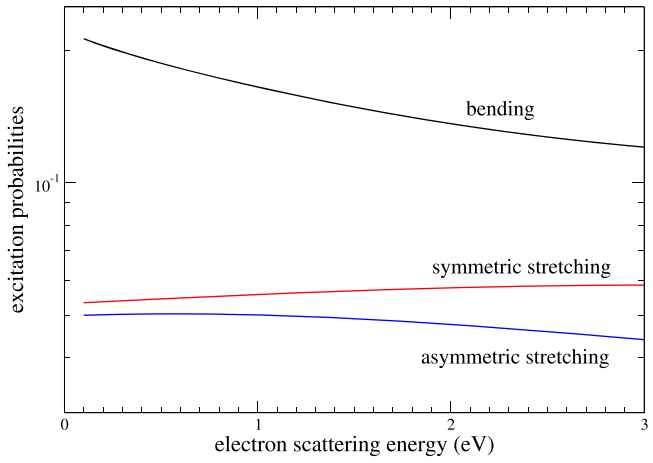

Figure 2. VE of BF_2^+: probabilities corresponding to the normal vibrational modes of the target ion.

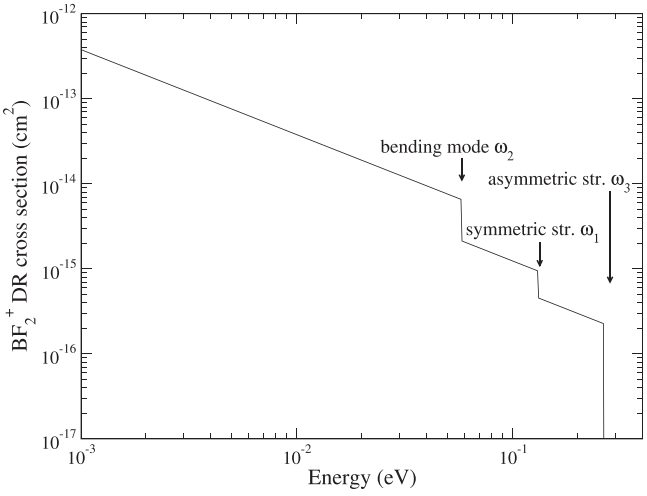

Figure 3. Cross-section for the DR of BF_2^+. The lowest vibrational threshold of each normal mode is indicated by arrows.

Table 2. Parameters of equations (8) and (9) calculated at $E = 0.1$ eV collision energy.

Mode i	P_i
symmetric stretching	0.053
bending	0.20
asymmetric stretching	0.05

In order to access the uncertainty of the present theoretical model, we have performed a complete calculation of the DR and VE rate coefficients using different basis sets and orbital spaces in the electron-scattering calculations. The calculations were performed for three sets of parameters (1) the CAS_1 with the cc-pVTZ basis set, mentioned above; (2) a calculation (referred here as cc-pVTZ CAS_2) similar to (1) but with a smaller orbital space, where 8 electrons are kept free in the active space; and (3) a calculation (referred here as cc-pVQZ CAS_1) similar to (1) but with the larger basis cc-pVQZ. The results are shown in figure 4. The difference between the rate coefficients produced in the three calculations for the DR process and the VE of the asymmetric stretching and bending modes is about 4%. The uncertainty of the rate coefficient for the VE of the symmetric stretching

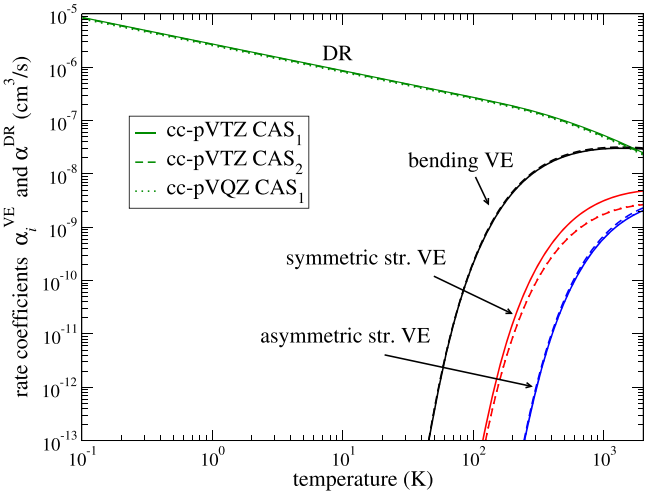

Figure 4. DR and VE of BF_2^+: rate coefficients—equations (8) and (9). To give an idea of the uncertainty of the present results, we also plotted the results of two calculations with the cc-pVTZ CAS_2 (dashed line) and the cc-pVQZ CAS_1 (dotted line) sets of parameters of the model. For the VE of the symmetric stretching mode, the cc-pVTZ CAS_2 and cc-pVQZ CAS_1 curves are indistinguishable and slightly below the cc-pVTZ CAS_1 curve. For the remaining three processes, the three calculations produce curves which are almost indistinguishable in the figure.

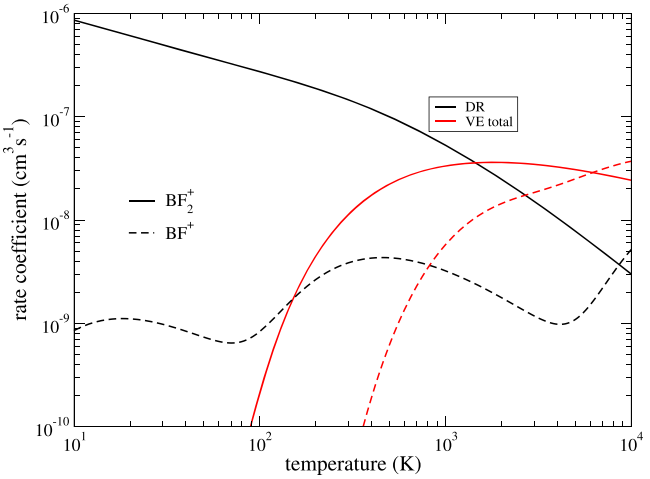

Figure 5. Relative importance of the DR and VE of BF_2^+, with respect to those of BF^+.

mode is larger, varying in the interval 10%–40% for different temperatures. Notice that the overall probability for the symmetric stretching excitation is much smaller than the probabilities for other modes and DR.

4. Conclusions and discussions

In this study, cross-sections and rate coefficients for DR and VE of BF_2^+ by electron-impact were obtained using a theoretical approach that combines the normal modes approximation for the vibrational states of the target ion, the vibrational frame transformation, and the UK R-matrix code. The thermally-averaged rate coefficients have a simple analytical form.

The obtained thermally-averaged rate coefficients are relevant for the kinetic modeling of molecule based cold non-equilibrium plasmas, in the context of a complete lack of other theoretical or experimental data on these processes for this cation, and are ready to be used in the modeling of fluorine/boron plasma for etching or implantation processes. Indeed, we are presently able to make important statements on the relative importance of BF_2^+ with respect to BF^+ on the population and excitation balance. In particular, as shown in figure 5, the DR of BF_2^+ strongly dominates that of BF^+ below 7000 K, and the VE displays the same feature below 5000 K.

The rotational structure of the target ion and of the neutral molecule was neglected in the present approach, which implies that the obtained cross-sections and rate coefficients should be viewed as averaged over initial rotational states and summed over final rotational states of the corresponding initial and final vibrational levels (for VE) or dissociative states (for DR). Purely rotational transitions, i.e. without changing the vibrational state, might be useful to model very cold environments, below 40 K, which is not the case for the presently investigated BF_3 plasma. Moreover BF_2^+ has no permanent dipole, so the rotational transitions are likely to have very small cross-sections.

Acknowledgments

This work was supported by the National Science Foundation, Grant No PHY-1806915.

Ioan F. Schneider and János Zsolt Mezei are grateful for generous financial support from La Région Haute-Normandie, via the GRR Electronique, Energie et Matériaux and the project BIOENGINE, from the Fédération de Recherche 'Energie, Propulsion, Environnement', and from the LabEx EMC^3 and FEDER via the projects PicoLIBS (ANR-10-LABEX-09-01), EMoPlaF and CO_2-VIRIDIS.

They acknowledge support from the CNRS via the GdR THEMS, IAEA (Vienna) via the Coordinated Research Project 'Light Element Atom, Molecule and Radical Behaviour in the Divertor and Edge Plasma Regions', the Programme National 'Physique et Chimie du Milieu Interstellaire' (PCMI) of CNRS/INSU with INC/INP co-funded by CEA and CNES, and Fédération de Recherche 'Fusion par Confinement Magnétique' (CNRS and CEA).

János Zsolt Mezei and Khalid Hassouni acknowledge support from USPC via ENUMPP and Labex SEAM.

Ioan F Schneider thanks Laboratoire Aimé Cotton for its outstanding hospitality.

ORCID iDs

János Zsolt Mezei https://orcid.org/0000-0002-7223-5787

References

[1] Sennikov P G, Kornev R A and Shishkin A I 2017 *Plasma Chem. Plasma Process.* **37** 997
[2] Torigoe M, Teii K and Matsumoto S 2016 *IEEE Trans. Plasma Sci.* **44** 3219
[3] Gonzatti F, Milesi F, Delaye V, Duchaine J, Torregrosa F, Etienne H and Yckache K 2011 *AIP Conf. Proc.* **1321** 27
[4] Duchaine J, Milesi F, Coquand R, Barraud S, Reboh S, Gonzatti F, Mazen F and Torregrosa F 2012 *AIP Conf. Proc.* **1496** 71
[5] Young D L, Nemetti W, La Salvia V, Page M R, Theingi S, Aguiar J, Lee B G and Stardins P 2016 *Sol. Energy Mater. Sol. Cells* **158** 68
[6] Farber M M and Srivastava R D 1984 *J. Chem. Phys.* **81** 241
[7] Yong-Ki K and Irikura K K 2000 *AIP Conf. Proc.* **543** 220
[8] Stewart R A and Lieberman M A 1991 *J. Appl. Phys.* **70** 3481
[9] Lieberman M A and Lichtenberg A J 2005 *Principles of Plasma Discharges and Materials Processing* (Hoboken, New Jersey: John Wiley & Sons, Inc.)
[10] Mezei J Z *et al* 2016 *Plasma Sources Sci. Technol.* **25** 055022
[11] Douguet N, Orel A, Mikhailov I, Schneider I F, Greene C H and Kokoouline V 2011 *J. Phys.: Conf. Series* **300** 012015
[12] Fonseca dos Santos S, Douguet N, Kokoouline V and Orel A E 2014 *J. Chem. Phys.* **140** 164308
[13] Werner H-J *et al* 2012 *WIREs Comput. Mol. Sci.* **2** 242
[14] Pyykko P and Zhao Y 1990 *J. Chem. Phys.* **94** 7753
[15] Perić M and Peyerimhoff S 1993 *Mol. Phys.* **78** 877
[16] Jacox M E and Thompson W E 1995 *J. Chem. Phys.* **102** 4747
[17] Tennyson J 2010 *Phys. Rep.* **491** 29
[18] Carr J, Galiatsatos P, Gorfinkiel J, Harvey A, Lysaght M, Madden D, Mašín Z, Plummer M, Tennyson J and Varambhia H 2012 *Euro. Phys. J.* D **66** 58
[19] Tennyson J, Brown D B, Munro J J, Rozum I, Varambhia H N and Vinci N 2007 *J. Phys. Conf. Series* **86** 012001

Bibliography

[o20,] 56

[mot, 1966] (1966). Book Review: The theory of atomic collisions. N. F. MOTT and H. S. MASSEY, 3rd ed. (Clarendon Press: Oxford University Press, London, 1965. xxii-858 p. 120s). *Nuclear Physics*, 81(2):673–673. 2

[Adamovich et al., 2017] Adamovich, I., Baalrud, S. D., Bogaerts, A., Bruggeman, P. J., Cappelli, M., Colombo, V., Czarnetzki, U., Ebert, U., Eden, J. G., Favia, P., Graves, D. B., Hamaguchi, S., Hieftje, G., Hori, M., Kaganovich, I. D., Kortshagen, U., Kushner, M. J., Mason, N. J., Mazouffre, S., Thagard, S. M., Metelmann, H.-R., Mizuno, A., Moreau, E., Murphy, A. B., Niemira, B. A., Oehrlein, G. S., Petrovic, Z. L., Pitchford, L. C., Pu, Y.-K., Rauf, S., Sakai, O., Samukawa, S., Starikovskaia, S., Tennyson, J., Terashima, K., Turner, M. M., van de Sanden, M. C. M., and Vardelle, A. (2017). The 2017 plasma roadmap: Low temperature plasma science and technology. *Journal of Physics D: Applied Physics*, 50(32):323001. viii

[Allan and Skalický, 2003] Allan, M. and Skalický, T. (2003). Structures in elastic, vibrational, and dissociative electron attachment cross sections in N_2O near threshold. *J. Phys. B: At., Mol. Opt. Phys.*, 36(16):3397. 60, 61

[Amitay et al., 1996] Amitay, Z., Zajfman, D., Forck, P., Hechtfischer, U., Seidel, B., Grieser, M., Habs, D., Repnow, R., Schwalm, D., and Wolf, A. (1996). Dissociative recombination of CH^+: Cross section and final states. *Physical Review A*, 54(5):4032. 29

[Anicich, 1993] Anicich, V. G. (1993). Evaluated bimolecular ion-molecule gas phase kinetics of positive ions for use in modeling planetary atmospheres, cometary comae, and interstellar clouds. *J. Phys. Chem. Ref. Data*, 22(6):1469–1569. 30

[Arthurs et al., 1960] Arthurs, A. M., Dalgarno, A., and Bates, D. R. (1960). The theory of scattering by a rigid rotator. *Proceedings of the Royal Society of London. Series A. Mathematical and Physical Sciences*, 256(1287):540–551. 2

[Aymar et al., 1996] Aymar, M., Greene, C. H., and Luc-Koenig, E. (1996). Multichannel Rydberg spectroscopy of complex atoms. *Rev. Mod. Phys.*, 68:1015. 6, 11, 13, 14, 42

[Ayouz et al., 2020] Ayouz, M., Gillet, J.-M., Janolin, P.-E., and Kokoouline, V. (2020). *Les fondamentaux de la mécanique quantique sous Python*. Ellipse. 76, 79

[Ayouz et al., 2022] Ayouz, M., Gillet, J.-M., Janolin, P.-E., and Kokoouline, V. (2022). *Toolbox for learning basic concepts of quantum physics*. Springer. 76

[Ayouz and Kokoouline, 2016] Ayouz, M. and Kokoouline, V. (2016). Cross sections and rate coefficients for vibrational excitation of HeH^+ molecule by electron impactukrm. *Atoms*, 4:30. 17, 18, 77

[Ayouz and Kokoouline, 2019] Ayouz, M. and Kokoouline, V. (2019). Cross sections and rate coefficients for rovibrational excitation of heh^+ isotopologues by electron impact. *Atoms*, 7(3). 18

[Ayouz et al., 2019] Ayouz, M. A., Yuen, C. H., Balucani, N., Ceccarelli, C., Schneider, I. F., and Kokoouline, V. (2019). Dissociative electron recombination of NH_2CHOH^+ and implications for interstellar formamide abundance. *Monthly Notices of the Royal Astronomical Society*, 490(1):1325–1331. 30, 66

[Baeva et al., 2002] Baeva, M., Pott, A., and Uhlenbusch, J. (2002). Modelling of NOxremoval by a pulsed microwave discharge. *Plasma Sources Science and Technology*, 11(2):135–141. vii

[Bartschat and Kushner, 2016] Bartschat, K. and Kushner, M. J. (2016). Electron collisions with atoms, ions, molecules, and surfaces: Fundamental science empowering advances in technology. *Proceedings of the National Academy of Sciences*, 113(26):7026–7034. vii

[Baye, 2006] Baye, D. (2006). Lagrange-mesh method for quantum-mechanical problems. *Phys. Status Solidi B*, 243(5):1095–1109. 77

[Benoit and Abouaf, 1991] Benoit, C. and Abouaf, R. (1991). *Chem. Phys. Lett.*, 177(6):573–578. 44

[Black, 1978] Black, J. (1978). Molecules in planetary nebulae. *Astrophys. J.*, 222:125. 15

[Boeuf et al., 2011] Boeuf, J. P., Hagelaar, G. J. M., Sarrailh, P., Fubiani, G., and Kohen, N. (2011). Model of an inductively coupled negative ion source: II. application to an ITER type source. *Plasma Sources Science and Technology*, 20(1):015002. vii

[Bohr et al., 2014] Bohr, A., Paolini, S., Forrey, R. C., Balakrishnan, N., and Stancil, P. C. (2014). A full-dimensional quantum dynamical study of h2+h2 collisions: Coupled-states versus close-coupling formulation. *The Journal of Chemical Physics*, 140(6):064308. 2

[Born and Oppenheimer, 1927] Born, M. and Oppenheimer, R. (1927). Zur quantentheorie der molekeln. *Annalen der Physik*, 389(20):457–484. 2

[Boudaïffa et al., 2000] Boudaïffa, B., Cloutier, P., Hunting, D., Huels, M. A., and Sanche, L. (2000). Resonant formation of dna strand breaks by low-energy (3 to 20 ev) electrons. *Science*, 287(5458):1658–1660. vii

[Britt and Humble, 2017] Britt, K. A. and Humble, T. S. (2017). High-performance computing with quantum processing units. *J. Emerg. Technol. Comput. Syst.*, 13(3). 75

[Bulgac and Forbes, 2013] Bulgac, A. and Forbes, M. M. (2013). Use of the discrete variable representation basis in nuclear physics. *Phys. Rev. C*, 87:051301. 78

[Bundaleska et al., 2013] Bundaleska, N., Tatarova, E., Dias, F. M., da Silva, M. L., Ferreira, C. M., and Amorim, J. (2013). Air-water 'tornado'-type microwave plasmas applied for sugarcane biomass treatment. *Journal of Physics D: Applied Physics*, 47(5):055201. vii

[Burke et al., 2007] Burke, P., Noble, C., and Burke, V. (2007). R-matrix theory of atomic, molecular and optical processes. *Advances in Atomic Molecular and Optical Physics*, 54:237. 5

[Burke and Robb, 1976] Burke, P. and Robb, W. (1976). The r-matrix theory of atomic processes. volume 11 of *Advances in Atomic and Molecular Physics*, pages 143 – 214. Academic Press. 5

[Burke and Tennyson, 2005] Burke, P. and Tennyson, J. (2005). R-matrix theory of electron molecule scattering. *Molecular Physics*, 103(18):2537–2548. 5

[Burke, 2011] Burke, P. G. (2011). *R-Matrix Theory of Atomic Collisions: Application to Atomic, Molecular and Optical Processes*, volume 61. Springer Science & Business Media. 3

[Burke et al., 1971] Burke, P. G., Hibbert, A., and Robb, W. D. (1971). Electron scattering by complex atoms. *Journal of Physics B: Atomic and Molecular Physics*, 4(2):153–161. 5

[Burke et al., 1977] Burke, P. G., Mackey, I., and Shimamura, I. (1977). R-matrix theory of electron-molecule scattering. *Journal of Physics B: Atomic and Molecular Physics*, 10(12):2497–2512. 5, 41

[Cai et al., 2015] Cai, X.-D., Wu, D., Su, Z.-E., Chen, M.-C., Wang, X.-L., Li, L., Liu, N.-L., Lu, C.-Y., and Pan, J.-W. (2015). Entanglement-based machine learning on a quantum computer. *Phys. Rev. Lett.*, 114:110504. 75

[Carata et al., 2000] Carata, L., Orel, A., Raoult, M., Schneider, I., and Suzor-Weiner, A. (2000). Core-excited resonances in the dissociative recombination of CH^+ and CD^+. *Physical Review A*, 62(5):052711. 29

[Carr et al., 2012] Carr, J. M., Galiatsatos, P. G., Gorfinkiel, J. D., Harvey, A. G., Lysaght, M. A., Madden, D., Masin, Z., Plummer, M., Tennyson, J., and Varambhia, H. N. (2012). Ukrmol: a low-energy electron- and positron-molecule scattering suite. 66:58. 5

[Carr et al., 2009] Carr, L. D., DeMille, D., Krems, R. V., and Ye, J. (2009). Cold and ultracold molecules: science, technology and applications. *New J. Phys.*, 11:055049. 75

[Chakrabarti et al., 2018a] Chakrabarti, K., Mezei, J. Z., Motapon, O., Faure, A., Dulieu, O., Hassouni, K., and Schneider, I. (2018a). Dissociative recombination of the CH^+ molecular ion at low energy. *Journal of Physics B: Atomic, Molecular and Optical Physics*, 51(10):104002. 29

[Chakrabarti et al., 2018b] Chakrabarti, K., Mezei, J. Z., Motapon, O., Faure, A., Dulieu, O., Hassouni, K., and Schneider, I. F. (2018b). Dissociative recombination of the CH^+ molecular ion at low energy. *Journal of Physics B: Atomic, Molecular and Optical Physics*, 51(10):104002. 12, 23

[Chang and Fano, 1972] Chang, E. and Fano, U. (1972). Theory of electron-molecule collisions by frame transformations. *Phys. Rev. A*, 6(1):173. 8

[Chase, 1956] Chase, D. M. (1956). Adiabatic approximation for scattering processes. *Phys. Rev.*, 104:838–842. 2

[Chung et al., 2016] Chung, H.-K., Braams, B. J., Bartschat, K., Császár, A. G., Drake, G. W. F., Kirchner, T., Kokoouline, V., and Tennyson, J. (2016). Uncertainty estimates for theoretical atomic and molecular data. *Journal of Physics D: Applied Physics*, 49(36):363002. 14, 43

[Clough and Thrush, 1967] Clough, P. and Thrush, B. A. (1967). *Trans. Faraday Soc.*, 63:915–925. 44

[Collin, 1959] Collin, J. (1959). Ionization and dissociation of molecules by monoenergetic electrons. iii. on the existence of a bent excited state of no2+. *J. Chem. Phys.*, 30(6):1621–1621. 44

[Čurík and Greene, 2017] Čurík, R. and Greene, C. H. (2017). Inelastic low-energy collisions of electrons with heh^+: Rovibrational excitation and dissociative recombination. *J. Chem. Phys.*, 147(5):054307. 20

[da Costa et al., 2015] da Costa, R. F., Varella, M. T. d. N., Bettega, M. H., and Lima, M. A. (2015). Recent advances in the application of the schwinger multichannel method with pseudopotentials to electron-molecule collisions. *The European Physical Journal D*, 69(6):159. 3

[Dabrowski and Herzberg, 1977] Dabrowski, I. and Herzberg, G. (1977). The predicted infrared spectrum of heh^+ and its possible astrophysical importance. *Trans. N. Y. Acad. Sci.*, 38(1 Series II):14. 15

[Deslauriers and Wieman, 2011] Deslauriers, L. and Wieman, C. (2011). Learning and retention of quantum concepts with different teaching methods. *Phys. Rev. ST Phys. Educ. Res.*, 7:010101. 75

[Dickinson and Certain, 1968] Dickinson, A. S. and Certain, P. R. (1968). Calculation of matrix elements for one-dimensional quantum-mechanical problems. *J. Chem. Phys.*, 49(9):4209–4211. 77

[Douglas and Herzberg, 1941] Douglas, A. E. and Herzberg, G. (1941). Note on ch^+ in interstellar space and in the laboratory. *apj*, 94:381. Provided by the SAO/NASA Astrophysics Data System. 20

[Douguet et al., 2015a] Douguet, N., dos Santos, S. F., Kokoouline, V., and Orel, A. (2015a). Simplified model to describe the dissociative recombination of linear polyatomic ions of astrophysical interest. In *EPJ Web of Conferences*, volume 84, page 07003. EDP Sciences. 3

[Douguet et al., 2015b] Douguet, N., Fonseca dos Santos, S., Kokoouline, V., and Orel, A. (2015b). Simplified model to describe the dissociative recombination of linear polyatomic ions of astrophysical interest. *EPJ Web of Conferences*, 84:07003. 61

[Douguet et al., 2015c] Douguet, N., Fonseca dos Santos, S., Raoult, M., Dulieu, O., Orel, A. E., and Kokoouline, V. (2015c). Theoretical study of radiative electron attachment to CN, C_2H, and C_4H radicals. *The Journal of chemical physics*, 142(23):234309. 3

[Douguet et al., 2008a] Douguet, N., Kokoouline, V., and Greene, C. H. (2008a). Theoretical rate of dissociative recombination of hco^+ and dco^+ ions. *Phys. Rev. A*, 77:064703. 12

[Douguet et al., 2008b] Douguet, N., Kokoouline, V., and Greene, C. H. (2008b). Theoretical rate of dissociative recombination of HCO^+ and DCO^+ ions. *Phys. Rev. A*, 77:064703. 61, 65

[Douguet et al., 2009a] Douguet, N., Kokoouline, V., and Greene, C. H. (2009a). Theory of dissociative recombination of a linear triatomic ion with permanent electric dipole moment: Study of hco^+. *Phys. Rev. A*, 80:062712. 12

[Douguet et al., 2009b] Douguet, N., Kokoouline, V., and Greene, C. H. (2009b). Theory of dissociative recombination of a linear triatomic ion with permanent electric dipole moment: Study of HCO^+. *Phys. Rev. A*, 80:062712. 61

[Douguet et al., 2012a] Douguet, N., Kokoouline, V., and Orel, A. E. (2012a). Breaking a tetrahedral molecular ion with electrons: study of NH_4^+. *J. Phys. B: At. Mol. Opt. Phys.*, 45:051001. 33, 70

[Douguet et al., 2011] Douguet, N., Orel, A., Mikhailov, I., Schneider, I. F., Greene, C. H., and Kokoouline, V. (2011). The role of the Jahn-Teller coupling in dissociative recombination of H_3O^+ and H_3^+ ions. *J. Phys.: Conf. Series*, 300(1):012015. 61

[Douguet et al., 2012b] Douguet, N., Orel, A. E., Greene, C. H., and Kokoouline, V. (2012b). Theory of dissociative recombination of highly-symmetric polyatomic ions. *Phys. Rev. Lett.*, 108:023202. 12, 33, 65, 68, 70

[Duchaine et al., 2012] Duchaine, J., Milesi, F., Coquand, R., Barraud, S., Reboh, S., Gonzatti, F., Mazen, F., and Torregrosa, F. (2012). Plasma immersion ion implantation for sub-22 nm node devices : Fd-soi and tri-gate. *AIP Conf. Proc.*, 1496:71. vii, 63

[Dulieu et al., 1997] Dulieu, O., Kosloff, R., Masnou-Seeuws, F., and Pichler, G. (1997). Quasibound states in long-range alkali dimers: Grid method calculations. *J. Chem. Phys.*, 107(24):10633–10642. 77

[Fano, 1970] Fano, U. (1970). Quantum Defect Theory of l Uncoupling in H_2 as an Example of Channel-Interaction Treatment. *Phys. Rev. A*, 2:353. 2

[Flower and Roueff, 1979] Flower, D. and Roueff, E. (1979). On the formation and destruction of HeH^+ in gaseous nebulae and the associated infra-red emission line spectrum. *Astron. Astrophys.*, 72:361. 15

[Fonseca dos Santos et al., 2014a] Fonseca dos Santos, S., Douguet, N., Kokoouline, V., and Orel, A. (2014a). Scattering matrix approach to the dissociative recombination of hco+ and n2h+. *J. Chem. Phys.*, 140(16):164308. 61, 66, 70

[Fonseca dos Santos et al., 2014b] Fonseca dos Santos, S., Douguet, N., Kokoouline, V., and Orel, A. E. (2014b). Scattering matrix approach to the dissociative recombination of hco+ and n2h+. *The Journal of Chemical Physics*, 140(16):164308. 12

[Fonseca dos Santos et al., 2014] Fonseca dos Santos, S., Douguet, N., Kokoouline, V., and Orel, A. E. (2014). Scattering matrix approach to the dissociative recombination of HCO^+ and N_2H^+. *J. Chem. Phys.*, 140:164308. 33

[Fox, 1960] Fox, R. (1960). *J. Chem. Phys.*, 32(1):285–287. 44

[Frisch, 2004] Frisch, M. J., i. (2004). *Gaussian 03, Revision D.02*. Gaussian, Inc., Wallingford CT. 40

[Garrod et al., 2008] Garrod, R. T., Weaver, S. L. W., and Herbst, E. (2008). Complex chemistry in star-forming regions: An expanded gas-grain warm-up chemical model. *The Astrophysical Journal*, 682(1):283–302. viii

[Gherardi et al., 2000] Gherardi, N., Martin, S., and Massines, F. (2000). A new approach to sio2 deposit using a n2-sih4-n2o glow dielectric barrier-controlled discharge at atmospheric pressure. *J. Phys. D: Appl. Phys.*, 33(19):L104. 56

[Gonzatti et al., 2010] Gonzatti, F., Milesi, F., Delaye, V., Duchaine, J., Torregrosa, F., Etienne, H., and Yckache, K. (2010). Plasma immersion ion implantation applied to n^+p junction realisation in 4h-sic. *AIP Conf. Proc.*, 1321:27. vii, 63

[Green, 1975] Green, S. (1975). Rotational excitation in h2–h2 collisions: Close-coupling calculations. *The Journal of Chemical Physics*, 62(6):2271–2277. 2

[Greene et al., 1979] Greene, C., Fano, U., and Strinati, G. (1979). General form of the quantum-defect theory. *Phys. Rev. A*, 19:1485–1509. 12, 43

[Greene and Jungen, 1985] Greene, C. H. and Jungen, C. (1985). Molecular applications ofquantum defect theory. *Adv. At. Mol. Phys.*, 21:51. 43

[Greene et al., 1982] Greene, C. H., Rau, A. R. P., and Fano, U. (1982). General form of the quantum-defect theory. II. *Phys. Rev. A*, 26:2441. 43

[Gupta et al., 2019] Gupta, D., Song, M.-Y., Choi, H., Kwon, D.-C., Baluja, K. L., and Tennyson, J. (2019). R-matrix study for electron scattering of beryllium dihydride for fusion plasma. *Journal of Physics B: Atomic, Molecular and Optical Physics*, 52(6):065204. 5

[Hagelaar et al., 2011] Hagelaar, G. J. M., Fubiani, G., and Boeuf, J.-P. (2011). Model of an inductively coupled negative ion source: I. general model description. *Plasma Sources Science and Technology*, 20(1):015001. vii

[Ham, 1955] Ham, F. S. (1955). The quantum defect method11this article is an expansion of a paper by h. brooks and f. s. ham which has been submitted for publication to the physical review (1955). it has been drawn for the most part from the present author's doctoral thesis (harvard university, cambridge, mass., 1954, unpublished). volume 1 of *Solid State Physics*, pages 127 – 192. Academic Press. 11

[Hamilton et al., 2016] Hamilton, J. R., Faure, A., and Tennyson, J. (2016). Electron-impact excitation of diatomic hydride cations–I. HeH^+, CH^+, ArH^+. *Mon. Not. R. Astron. Soc.*, 455(3):3281. 20

[Harris et al., 1965] Harris, D. O., Engerholm, G. G., and Gwinn, W. D. (1965). Calculation of matrix elements for one-dimensional quantum-mechanical problems and the application to anharmonic oscillators. *J. Chem. Phys.*, 43(5):1515–1517. 77

[Hayashi and Akashi, 1992] Hayashi, M. and Akashi, K. (1992). Handbook of plasma material science. 60, 61

[Hopper et al., 1976] Hopper, D. G., Wahl, A. C., Wu, R. L., and Tiernan, T. O. (1976). Theoretical and experimental studies of the n2o- and n2o ground state potential energy surfaces. implications for the o-+ n2→ n2o+ e and other processes. *J. Chem. Phys.*, 65(12):5474–5494. 61

[J. B. A. Mitchell and A. I. Florescu-Mitchell, 2005] J. B. A. Mitchell, O. N. G. A. J. L. . L. C. R.-R. A. S. L. H. A. and A. I. Florescu-Mitchell, A. E. O. (2005). Dissociative Recombination of Rare-Gas Hydride Ions:I NeH^+. *J. Phys. B: At. Mol.Opt.Phys.*, 38:693. 12

[Jamieson et al., 2005] Jamieson, C. S., Bennett, C. J., Mebel, A. M., and Kaiser, R. I. (2005). Investigating the mechanism for the formation of nitrous oxide [n2o (x $1\sigma+$)] in extraterrestrial ices. *Astrophys. J.*, 624(1):436. 56

[Janežič et al., 1995] Janežič, D., Venable, R. M., and Brooks, B. R. (1995). Harmonic analysis of large systems. iii. comparison with molecular dynamics. *Journal of Computational Chemistry*, 16(12):1554–1566. 40

[Jiang et al., 2019] Jiang, X., Yuen, C. H., Cortona, P., Ayouz, M., and Kokoouline, V. (2019). Cross sections for vibronic excitation of ch^+ by low-energy electron impact. *Phys. Rev. A*, 100:062711. 20, 24, 26

[Jimenez-Serra et al., 2006] Jimenez-Serra, I., Martin-Pintado, J., Viti, S., Martin, S., Rodriguez-Franco, A., Faure, A., and Tennyson, J. (2006). The first measurements of the electron density enhancements expected in C-type shocks. *Astrophys. J. Lett.*, 650(2):L135–L138. 15

[Johnson III, 2010] Johnson III, R. D. (2010). Nist computational chemistry comparison and benchmark database, nist standard reference database number 101. *NIST, Gaithersburg, MD.* 45, 57

[Khamesian et al., 2018] Khamesian, M., Ayouz, M., Singh, J., and Kokoouline, V. (2018). Cross sections and rate coefficients for rotational excitation of heh+ molecule by electron impact. *Atoms*, 6(3). 18

[Kiser and Hisatsune, 1961] Kiser, R. W. and Hisatsune, I. (1961). *J. Phys. Chem.*, 65(8):1444–1446. 44

[Kohnle et al., 2015] Kohnle, A., Baily, C., Campbell, A., Korolkova, N., and Paetkau, M. J. (2015). Enhancing student learning of two-level quantum systems with interactive simulations. *American Journal of Physics*, 83(6):560–566. 75

[Kokoouline et al., 2018] Kokoouline, V., Ayouz, M., Mezei, J. Z., Hassouni, K., and Schneider, I. (2018). Theoretical study of dissociative recombination and vibrational excitation of BF_2^+ the ion by an electron impact. *Plasma Sources Sci. Technol.*, 27(11):115007. 66, 67, 73

[Kokoouline et al., 2011] Kokoouline, V., Douguet, N., and Greene, C. H. (2011). Breaking bonds with electrons: Dissociative recombination of molecular ions. *Chem. Phys. Lett.*, 507:1. 28

[Kokoouline et al., 1999] Kokoouline, V., Dulieu, O., Kosloff, R., and Masnou-Seeuws, F. (1999). Mapped Fourier methods for long-range molecules: Application to perturbations in the Rb_2 (0_u^+) photoassociation spectrum. *J. Chem. Phys.*, 110(20):9865. 77

[Kokoouline and Greene, 2001] Kokoouline, V. and Greene, C. H. (2001). Mechanism for the destruction of h_3^+ ions by electron impact. 412:891. 12

[Kokoouline and Greene, 2005] Kokoouline, V. and Greene, C. H. (2005). Theoretical study of the H_3^+ dissociative recombination process. *J. Phys. Conf. Series*, 4:74. 29

[Kolobov, 2009] Kolobov, V. I. (2009). Simulations of non-equilibrium plasmas: Atomic and molecular data needs. *Fusion Science and Technology*, 55(2T):30–37. viii

[Kosloff, 1988] Kosloff, R. (1988). Time-dependent quantum-mechanical methods for molecular dynamics. *J. Phys. Chem.*, 92:2087. 77

[Kosloff, 1994] Kosloff, R. (1994). Propagation methods for quantum molecular dynamics. *Annual Review of Physical Chemistry*, 45(1):145–178. 79

[Kraemer et al., 1995] Kraemer, W., Špirko, V., and Juřek, M. (1995). Formation of heh^+ by radiative association of he^++ h. an advanced ab initio study. *Chem. Phys. Lett.*, 236(1):177–183. 15

[Krijtenburg-Lewerissa et al., 2017] Krijtenburg-Lewerissa, K., Pol, H. J., Brinkman, A., and van Joolingen, W. R. (2017). Insights into teaching quantum mechanics in secondary and lower undergraduate education. *Phys. Rev. Phys. Educ. Res.*, 13:010109. 75

[Lane, 1980] Lane, N. F. (1980). The theory of electron-molecule collisions. *Rev. Mod. Phys.*, 52:29–119. 2

[Leforestier et al., 1991] Leforestier, C., Bisseling, R., Cerjan, C., Feit, M., Friesner, R., Guldberg, A., Hammerich, A., Jolicard, G., Karrlein, W., Meyer, H.-D., Lipkin, N., Roncero, O., and Kosloff, R. (1991). A comparison of different propagation schemes for the time dependent schrödinger equation. *Journal of Computational Physics*, 94(1):59 – 80. 79

[Leonardi et al., 1996] Leonardi, E., Petrongolo, C., Hirsch, G., and Buenker, R. J. (1996). *J. Chem. Phys.*, 105(20):9051–9067. 46, 53

[Lepp et al., 2002] Lepp, S., Stancil, P., and Dalgarno, A. (2002). Atomic and molecular processes in the early universe. *J. Phys. B: At., Mol. Opt. Phys.*, 35(10):R57. vii, 15

[Liu et al., 2019] Liu, H., dos Santos, S. F., Yuen, C. H., Cortona, P., Kokoouline, V., and Ayouz, M. (2019). Theoretical study of electron-induced vibrational excitation of no_2. *Plasma Sources Science and Technology*, 28(10):105017. 43, 49, 50, 55

[Liu et al., 2020] Liu, H., dos Santos, S. F., Yuen, C. H., Cortona, P., Kokoouline, V., and Ayouz, M. (2020). Vibrational excitation of n_2o by an electron impact and the role of renner-teller coupling. *submitted to Phys. Rev. A*. 43, 61

[Loupas and Gorfinkiel, 2019] Loupas, A. and Gorfinkiel, J. D. (2019). Shape and core-excited resonances in electron scattering from alanine. *The Journal of Chemical Physics*, 150(6):064307. 5

[Loupas et al., 2018] Loupas, A., Lozano, A. I., Blanco, F., Gorfinkiel, J. D., and García, G. (2018). Cross sections for electron scattering from thiophene for a broad energy range. *The Journal of Chemical Physics*, 149(3):034304. 5

[Lucamarini et al., 2009] Lucamarini, M., Di Giuseppe, G., and Tamaki, K. (2009). Robust unconditionally secure quantum key distribution with two nonorthogonal and uninformative states. *Phys. Rev. A*, 80:032327. 75

[M and E, 1993] M, P. B. and E, S. S. (1993). *Non-Thermal Plasma Techniques for Pollution Control (NATO-ASI Series G)*. (Berlin: Springer. vii

[M. Farber and Srivastava, 1984] M. Farber, M. and Srivastava, R. D. (1984). *J. Chem. Phys*, 81(1):241. 63

[McElroy et al., 2013] McElroy, D., Walsh, C., Markwick, A., Cordiner, M., Smith, K., and Millar, T. (2013). The umist database for astrochemistry 2012. *Astron. Astrophys.*, 550:A36. 30

[McGuire and Kouri, 1974] McGuire, P. and Kouri, D. J. (1974). Quantum mechanical close coupling approach to molecular collisions. jz -conserving coupled states approximation. *The Journal of Chemical Physics*, 60(6):2488–2499. 2

[McKagan et al., 2008] McKagan, S. B., Perkins, K. K., Dubson, M., Malley, C., Reid, S., LeMaster, R., and Wieman, C. E. (2008). Developing and researching phet simulations for teaching quantum mechanics. *American Journal of Physics*, 76(4):406–417. 75

[McKagan et al., 2010] McKagan, S. B., Perkins, K. K., and Wieman, C. E. (2010). Design and validation of the quantum mechanics conceptual survey. *Phys. Rev. ST Phys. Educ. Res.*, 6:020121. 75

[Mezei et al., 2015] Mezei, J. Z., Backodissa-Kiminou, R. D., Tudorache, D. E., Morel, V., Chakrabarti, K., Motapon, O., Dulieu, O., Robert, J., Tchang-Brillet, W.-U. L., Bultel, A., Urbain, X., Tennyson, J., Hassouni, K., and Schneider, I. F. (2015). Dissociative recombination and vibrational excitation of co^+: model calculations and comparison with experiment. *Plasma Sources Science and Technology*, 24(3):035005. 12

[Mezei et al., 2019] Mezei, Z. J., Epée Epée, M. D., Motapon, O., and Schneider, I. F. (2019). Dissociative recombination of CH^+ molecular ion induced by very low energy electrons. *Atoms*, 7(3):82. 29

[Mikhailov et al., 2006a] Mikhailov, I. A., Kokoouline, V., Larson, A., Tonzani, S., and Greene, C. H. (2006a). Renner-teller effects in hco^+ dissociative recombination. *Phys. Rev. A*, 74:032707. 12

[Mikhailov et al., 2006b] Mikhailov, I. A., Kokoouline, V., Larson, A., Tonzani, S., and Greene, C. H. (2006b). Renner-Teller effects in HCO^+ dissociative recombination. *Phys. Rev. A*, 74:032707. 33, 61, 65, 70

[Millar et al., 2017] Millar, T. J., Walsh, C., and Field, T. A. (2017). Negative ions in space. *Chemical Reviews*, 117(3):1765–1795. PMID: 28112897. vii

[Misra et al., 2016] Misra, N., Schlüter, O., and Cullen, P. J. (2016). *Cold plasma in food and agriculture: Fundamentals and applications*. Academic Press. vii

[Molek et al., 2007] Molek, C. D., McLain, J. L., Poterya, V., and Adams, N. G. (2007). A remeasurement of the products for electron recombination of N_2H^+ using a new technique: No signficant NH+N production. *J. Phys. Chem. A*, 111:6760–6765. 45

[Monnerville and Robbe, 1994] Monnerville, M. and Robbe, J. M. (1994). Optical potential coupled to discrete variable representation for calculations of quasibound states: Application to the co($b^1\sigma^+$-$d'^1\sigma^+$) predissociating interaction. *J. Chem. Phys.*, 101(9):7580–7591. 79

[Moulane, Y. et al., 2018] Moulane, Y., Mezei, J. Zs., Laporta, V., Jehin, E., Benkhaldoun, Z., and Schneider, I. F. (2018). Reactive collision of electrons with co+ in cometary coma. *A&A*, 615:A53. 12

[Mukherjee and Mukherjee, 2015] Mukherjee, T. and Mukherjee, M. (2015). Low-energy positron–nitrogen-molecule scattering: A rovibrational close-coupling study. *Phys. Rev. A*, 91:062706. 2

[Müller and Wiesner, 2002] Müller, R. and Wiesner, H. (2002). Include interpretation in introductory quantum mechanics courses. *American Journal of Physics*, 70(9):887–887. 75

[Munjal et al., 2009] Munjal, H., Baluja, K., and Tennyson, J. (2009). *Phys. Rev. A*, 79(3):032712. 44

[Nakamura, 2007] Nakamura, Y. (2007). Electron swarm parameters in pure n2o and in dilute n2o-ar mixtures and electron collision cross sections of n2o molecule. *Proc. of the 28th ICPIG*, page 224. 60

[Novotný et al., 2009] Novotný, O., Motapon, O., Berg, M. H., Bing, D., Buhr, H., Fadil, H., Grieser, M., Hoffmann, J., Jaroshevich, A. S., Jordon-Thaden, B., Krantz, C., Lange, M., Lestinsky, M., Mendes, M., Novotny, S., Orlov, D. A., Petrignani, A., Schneider, I. F., Orel, A. E., and Wolf, A. (2009). Dissociative recombination of CF^+: Experiment and theory. *Journal of Physics: Conference Series*, 192:012021. 12

[Pelicon and Razpet, 2003] Pelicon, P. and Razpet, A. (2003). Neutral molecules in tokamak edge plasma - role of vibrationally excited hydrogen molecules. 37

[Rabadán et al., 1998] Rabadán, I., Sarpal, B. K., and Tennyson, J. (1998). Calculated rotational and vibrational excitation rates for electron-HeH^+ collisions. *Mon. Not. R. Astron. Soc.*, 299(1):171. 16, 19

[Rangwala et al., 2003] Rangwala, S. A., Krishnakumar, E., and Kumar, S. (2003). *Phys. Rev. A*, 68(5):052710. 44

[Roberge and Dalgarno, 1982] Roberge, W. and Dalgarno, A. (1982). The formation and destruction of heh^+ in astrophysical plasmas. *Astrophys. J.*, 255:489. 15

[Rydberg, 1890] Rydberg, J. R. (1890). Xxxiv. on the structure of the line-spectra of the chemical elements. *The London, Edinburgh, and Dublin Philosophical Magazine and Journal of Science*, 29(179):331–337. 11

[Sadaghiani and Pollock, 2015] Sadaghiani, H. R. and Pollock, S. J. (2015). Quantum mechanics concept assessment: Development and validation study. *Phys. Rev. ST Phys. Educ. Res.*, 11:010110. 75

[Samukawa et al., 2012] Samukawa, S., Hori, M., Rauf, S., Tachibana, K., Bruggeman, P., Kroesen, G., Whitehead, J. C., Murphy, A. B., Gutsol, A. F., Starikovskaia, S., Kortshagen, U., Boeuf, J.-P., Sommerer, T. J., Kushner, M. J., Czarnetzki, U., and Mason, N. (2012). The 2012 plasma roadmap. *Journal of Physics D: Applied Physics*, 45(25):253001. viii

[Sanz et al., 2012] Sanz, A. G., Fuss, M. C., Blanco, F., Sebastianelli, F., Gianturco, F. A., and Garcia, G. (2012). Electron scattering cross sections from hcn over a broad energy range (0.1-10000 ev): Influence of the permanent dipole moment on the scattering process. *The Journal of Chemical Physics*, 137(12):124103. 2

[Schneider and Rescigno, 1988] Schneider, B. and Rescigno, T. (1988). Complex kohn variational method: Application to low-energy electron-molecule collisions. *Physical Review A*, 37(10):3749. 3

[Schneider, 1975] Schneider, B. I. (1975). r-matrix theory for electron-molecule collisions using analytic basis set expansions. ii. electron-h_2 scattering in the static-exchange model. *Phys. Rev. A*, 11:1957–1962. 5

[Schneider and Hay, 1976] Schneider, B. I. and Hay, P. J. (1976). Elastic scattering of electrons from f_2: An r-matrix calculation. *Phys. Rev. A*, 13:2049–2056. 5

[Schwinger, 1947] Schwinger, J. (1947). A variational principle for scattering problems. In *Physical Review*, volume 72, pages 742–742. AMERICAN PHYSICAL SOC ONE PHYSICS ELLIPSE, COLLEGE PK, MD 20740-3844 USA. 3

[Seaton, 1966] Seaton, M. J. (1966). *Proc. Phys. Soc. London*, 88:801. 11, 12

[Seaton, 1983] Seaton, M. J. (1983). Quantum defect theory. *Rep. Prog. Phys.*, 46:167. 11, 13

[Sennikov et al., 2017] Sennikov, P. G., Kornev, R. A., and Shishkin, A. I. (2017). *Plasma Chem. Plasma Process.*, 37(4):997. 63

[Shomali et al., 2015a] Shomali, M., Opie, D., Avasthi, T., and Trilling, A. (2015a). *PLoS One*, 10(6):e0130043. 43

[Shomali et al., 2015b] Shomali, M., Opie, D., Avasthi, T., and Trilling, A. (2015b). Nitrogen dioxide sterilization in low-resource environments: A feasibility study. *PLOS ONE*, 10(6):1–11. vii

[Shor, 1995] Shor, P. W. (1995). Scheme for reducing decoherence in quantum computer memory. *Phys. Rev. A*, 52:R2493–R2496. 75

[Singh and Marshman, 2015] Singh, C. and Marshman, E. (2015). Review of student difficulties in upper-level quantum mechanics. *Phys. Rev. ST Phys. Educ. Res.*, 11:020117. 75

[Song et al., 2019] Song, M.-Y., Yoon, J.-S., Cho, H., Karwasz, G. P., Kokoouline, V., Nakamura, Y., and Tennyson, J. (2019). Cross sections for electron collisions with no, n2o, and no2. *J. Phys. Chem. Ref. Data*, 48(4):043104. 56, 60

[Stephan et al., 1980] Stephan, K., Helm, H., Kim, Y., Seykora, G., Ramler, J., Grössl, M., Märk, E., and Märk, T. (1980). *J. Chem. Phys.*, 73(1):303–308. 44

[Szalay, 1993] Szalay, V. (1993). Discrete variable representations of differential operators. *J. Chem. Phys.*, 99(3):1978–1984. 79

[Szmytkowski and Krzysztofowicz, 1992] Szmytkowski, Maciag, K. and Krzysztofowicz, A. (1992). *Chem. Phys. Lett.*, 190(1-2):141–144. 44

[Takagi et al., 1991] Takagi, H., Kosugi, N., and Le Dourneuf, M. (1991). Dissociative recombination of CH^+. *Journal of Physics B: Atomic, Molecular and Optical Physics*, 24(3):711. 29

[Takatsuka and McKoy, 1981] Takatsuka, K. and McKoy, V. (1981). Extension of the Schwinger variational principle beyond the static-exchange approximation. *Physical Review A*, 24(5):2473. 3

[Tal-Ezer and Kosloff, 1984] Tal-Ezer, H. and Kosloff, R. (1984). An accurate and efficient scheme for propagating the time dependent schrödinger equation. *The Journal of Chemical Physics*, 81(9):3967–3971. 80

[Tennyson, 2010] Tennyson, J. (2010). Electron–molecule collision calculations using the R-matrix method. *Phys. Rep.*, 491:29. 5, 6, 41, 42, 66

[Tennyson et al., 2007] Tennyson, J., Brown, D. B., Munro, J. J., Rozum, I., Varambhia, H. N., and Vinci, N. (2007). Quantemol-n: an expert system for performing electron molecule collision calculations using the r-matrix method. *J. Phys. Conf. Series*, 86(1):012001. 5

[Tolstikhin et al., 1998] Tolstikhin, O. I., Ostrovsky, V. N., and Nakamura, H. (1998). Siegert pseudostate formulation of scattering theory: One-channel case. *Physical Review A*, 58(3):2077. 9

[Torigoe et al., 2016] Torigoe, M., Teii, K., and Matsumoto, S. (2016). *IEEE Trans. Plasma Sci.*, 44(12):3219. 63

[Tschumper and Schaefer III, 1997] Tschumper, G. S. and Schaefer III, H. F. (1997). Predicting electron affinities with density functional theory: Some positive results for negative ions. *J. Chem. Phys.*, 107(7):2529–2541. 61

[van Dijk et al., 2009] van Dijk, J., Kroesen, G. M. W., and Bogaerts, A. (2009). Plasma modelling and numerical simulation. *Journal of Physics D: Applied Physics*, 42(19):190301. viii

[Vibok and Balint-Kurti, 1992] Vibok, A. and Balint-Kurti, G. (1992). Parametrization of complex absorbing potentials for time-dependent quantum dynamics. *The Journal of Physical Chemistry*, 96(22):8712–8719. 9

[Vuitton et al., 2006] Vuitton, V., Yelle, R., and Anicich, V. (2006). The nitrogen chemistry of titan's upper atmosphere revealed. *Astrophysics. J. Lett.*, 647(2):L175. 30

[Wakelam et al., 2012] Wakelam, V., Herbst, E., Loison, J.-C., Smith, I., Chandrasekaran, V., Pavone, B., Adams, N., Bacchus-Montabonel, M.-C., Bergeat, A., Béroff, K., et al. (2012). A kinetic database for astrochemistry (kida). *Astrophys. J., Suppl. Ser*, 199(1):21. 30

[Wang and Sze, 1980] Wang, W.-C. and Sze, N. D. (1980). Coupled effects of atmospheric n2o and o3 on the earth's climate. *Nature*, 286(5773):589–590. 56

[Werner et al., 2008] Werner, H.-J., Knowles, P. J., Lindh, R., Manby, F. R., Schütz, M., et al. (2008). MOLPRO, version 2008.3, a package of ab initio programs. 9, 41, 66

[Wigner, 1946] Wigner, E. P. (1946). Resonance reactions and anomalous scattering. *Phys. Rev.*, 70:15–33. 5

[Wigner and Eisenbud, 1947] Wigner, E. P. and Eisenbud, L. (1947). Higher angular momenta and long range interaction in resonance reactions. *Phys. Rev.*, 72:29–41. 5

[Yong-Ki and Irikura, 2000] Yong-Ki, K. and Irikura, K. K. (2000). *AIP Conf. Proc.*, 543:220. 63

[Young et al., 2016] Young, D. L., Nemetti, W., La Salvia, V., Page, M. R., Theingi, S., Aguiar, J., Lee, B. G., and Stardins, P. (2016). *Sol. Energy Mater. Sol. Cells*, 158:68. 63

[Yuen et al., 2019] Yuen, C. H., Ayouz, M. A., Balucani, N., Ceccarelli, C., Schneider, I. F., and Kokoouline, V. (2019). Dissociative recombination of $CH_2NH_2^+$: a crucial link with interstellar methanimine and Titan ammonia. *Monthly Notices of the Royal Astronomical Society*, 484(1):659–664. 30, 31, 32, 34

[Zammit et al., 2017] Zammit, M. C., Fursa, D. V., Savage, J. S., and Bray, I. (2017). Electron–and positron–molecule scattering: development of the molecular convergent close-coupling method. *Journal of Physics B: Atomic, Molecular and Optical Physics*, 50(12):123001. 2

[Zhou et al., 2010] Zhou, T., Huang, D., and Caflisch, A. (2010). Quantum mechanical methods for drug design. *Current Topics in Medicinal Chemistry*, 10(1):33–45. 75

[Zhu and Singh, 2012a] Zhu, G. and Singh, C. (2012a). Improving students' understanding of quantum measurement. i. investigation of difficulties. *Phys. Rev. ST Phys. Educ. Res.*, 8:010117. 75

[Zhu and Singh, 2012b] Zhu, G. and Singh, C. (2012b). Surveying students' understanding of quantum mechanics in one spatial dimension. *American Journal of Physics*, 80(3):252–259. 75

[Ziurys et al., 1994] Ziurys, L. M., Apponi, A., Hollis, J., and Snyder, L. (1994). Detection of interstellar n2o: A new molecule containing an no bond. *Astrophys. J.*, 436:L181–L184. 56

[Zygelman and Dalgarno, 1990] Zygelman, B. and Dalgarno, A. (1990). The radiative association of he^+ and h. *Astrophys. J.*, 365:239. 15